Universidad del País Vasco
Euskal Herriko Unibertsitatea

UNIVERSITY OF THE BASQUE COUNTRY

FACULTY OF ENGINEERING

DOCTORAL THESIS

Identification of the stress and relaxation level in people, based on the study and the advanced processing of physiological signals related to the activity of the autonomic nervous system

---

Author:
Unai ZALABARRIA

Supervisors:
Dr. Eloy IRIGOYEN
Dr. Raquel MARTÍNEZ

A thesis submitted in fulfillment of the requirements for the degree of Doctor of Philosophy

in the

Intelligent Control Research Group
Department of Systems Engineering and Automation

October 29, 2020

Universidad del País Vasco | Euskal Herriko Unibertsitatea

NAZIOARTEKO BIKAINTASUN CAMPUSA
CAMPUS DE EXCELENCIA INTERNACIONAL

TESI ZUZENDARIKIDEEN BAIMENA TESIA AURKEZTEKO	AUTORIZACIÓN DEL LOS CODIRECTORES DE TESIS PARA SU PRESENTACIÓN

Zuzendarikideen izen-abizenak /Nombre y apellidos de los codirectores:
ELOY IRIGOYEN GORDO* y RAQUEL MARTÍNEZ RODRÍGUEZ**

IFZ /NIF: 29141675P* y 78892778H**

Tesiaren izenburua / Título de la tesis:
IDENTIFICATION OF THE STRESS AND RELAXATION LEVEL IN PEOPLE, BASED ON THE STUDY AND THE ADVANCED PROCESSING OF PHYSIOLOGICAL SIGNALS RELATED TO THE ACTIVITY OF THE AUTONOMIC NERVOUS SYSTEM

Doktorego programa / Programa de doctorado:
INGENIERÍA DE CONTROL, AUTOMATIZACIÓN Y ROBÓTICA

Doktoregaiaren izen-abizenak / Nombre y apellidos del/la doctorando/a:
UNAI ZALABARRIA PENA

Unibertsitateak horretarako jartzen duen tresnak emandako ANTZEKOTASUN TXOSTENA ikusita, baimena ematen dugu goian aipatzen den tesia aurkez dadin, horretarako baldintza guztiak betetzen baititu.

Visto el INFORME DE SIMILITUD obtenido de la herramienta que a tal efecto pone a disposición la universidad, autorizamos la presentación de la tesis doctoral arriba indicada, dado que reúne las condiciones necesarias para su defensa.

Tokia eta data / Lugar y fecha:

ELOY IRIGOYEN GORDO - 29141675P
Firmado digitalmente por ELOY IRIGOYEN GORDO - 29141675P
Fecha: 2020.10.12 20:21:08 +02'00'

RAQUEL MARTINEZ RODRIGUEZ - 78892778H
Firmado digitalmente por RAQUEL MARTINEZ RODRIGUEZ - 78892778H
Nombre de reconocimiento (DN): c=ES, o=UPV - EHU, ou=Ziurtagiri Profesionala - Certificado Profesional, 2.5.4.97=VATES-Q4818001B, cn=RAQUEL MARTINEZ RODRIGUEZ - 78892778H, givenName=RAQUEL, sn=MARTINEZ RODRIGUEZ, serialNumber=78892778H
Fecha: 2020.10.13 17:07:35 +02'00'

Sin. / Fdo.: Tesiaren zuzendarikideak / Los codirectores de la tesis

Universidad del País Vasco Euskal Herriko Unibertsitatea | NAZIOARTEKO BIKAINTASUN CAMPUSA CAMPUS DE EXCELENCIA INTERNACIONAL

AUTORIZACIÓN DE LA COMISIÓN ACADÉMICA DEL PROGRAMA DE DOCTORADO

La Comisión Académica del Programa de Doctorado en INGENIERÍA DE CONTROL, AUTOMATIZACIÓN Y ROBÓTICA en reunión celebrada el día 20 de Octubre de 2020, ha acordado dar la conformidad a la presentación de la Tesis Doctoral titulada Identification of the stress and relaxation level in people, based on the study and the advanced processing of physiological signals related to the activity of the autonomic nervous system, dirigida por el Dr. Eloy Irigoyen Gordo y la Dra. Raquel Martínez Rodríguez y presentada por D. Unai Zalabarria Pena adscrito al Departamento de Ingeniería de Sistemas y Automática.

En Bilbao a 22 de Octubre de 2020

EL/LA RESPONSABLE DEL PROGRAMA DE DOCTORADO

Fdo.: MARCOS MUÑOZ MARGARITA - 16029464M

Firmado digitalmente por MARCOS MUÑOZ MARGARITA - 16029464M
Fecha: 2020.10.22 17:34:12 +02'00'

Universidad del País Vasco Euskal Herriko Unibertsitatea

NAZIOARTEKO BIKAINTASUN CAMPUSA
CAMPUS DE EXCELENCIA INTERNACIONAL

AUTORIZACIÓN DEL DEPARTAMENTO

El Consejo del Departamento de Ingeniería de Sistemas y Automática en reunión celebrada el día 27 de octubre de 2020, ha acordado dar la conformidad a la admisión a trámite de presentación de la Tesis Doctoral titulada: "Identification of the stress and relaxation level in people, based on the study and the advanced processing of physiological signals related to the activity of the autonomic nervous system", dirigida por el Dr. Eloy Irigoyen Gordo y la Dra. Raquel Martínez Rodríguez

---

y presentada por D. Unai Zalabarria Pena ante este Departamento.

En Bilbao, a 27 de octubre de 2020

VºBº DIRECTOR/A DEL DEPARTAMENTO

Fernando Artaza Fano

Firmado digitalmente por Fernando Artaza Fano
Fecha: 2020.10.28 13:37:32 +01'00'

Fdo.: FERNANDO ARTAZA FANO

SECRETARIO/A DEL DEPARTAMENTO

CASQUERO OYARZABAL OSCAR - 78896682N

Digitally signed by CASQUERO OYARZABAL OSCAR - 78896682N
Date: 2020.10.27 19:17:30 +01'00'

Fdo.: OSKAR CASQUERO OYARZABAL

ACTA DE GRADO DE DOCTOR O DOCTORA
ACTA DE DEFENSA DE TESIS DOCTORAL

DOCTORANDO DON. UNAI ZALABARRIA PENA

TITULO DE LA TESIS: IDENTIFICATION OF THE STRESS AND RELAXATION LEVEL IN PEOPLE, BASED ON THE STUDY AND THE ADVANCED PROCESSING OF PHYSIOLOGICAL SIGNALS RELATED TO THE ACTIVITY OF THE AUTONOMIC NERVOUS SYSTEM

El Tribunal designado por la Comisión de Postgrado de la UPV/EHU para calificar la Tesis Doctoral arriba indicada y reunido en el día de la fecha, una vez efectuada la defensa por el/la doctorando/a y contestadas las objeciones y/o sugerencias que se le han formulado, ha otorgado por_____la calificación de:
unanimidad ó mayoría

SOBRESALIENTE / NOTABLE / APROBADO / NO APTO

Idioma/s de defensa (en caso de más de un idioma, especificar porcentaje defendido en cada idioma):

Castellano _____

Euskera _____

Otros Idiomas (especificar cuál/cuales y porcentaje) _____

En _____a _____de _____de _____

EL/LA PRESIDENTE/A, EL/LA SECRETARIO/A,

Fdo.: Fdo.:

Dr/a: _____ Dr/a: _____

VOCAL 1º, VOCAL 2º, VOCAL 3º,

Fdo.: Fdo.: Fdo.:

Dr/a: _____Dr/a:_____Dr/a:_____

EL DOCTORANDO,

Fdo.: _____

"Things around you were not created by people much more intelligent than you."

The Author

UNIVERSITY OF THE BASQUE COUNTRY

Abstract

Faculty of Engineering

Department of Systems Engineering and Automation

Doctor of Philosophy

Identification of the stress and relaxation level in people, based on the study and the advanced processing of physiological signals related to the activity of the autonomic nervous system

by Unai ZALABARRIA

The World Health Organization refers to stress as the health epidemic of the 21st century. This fact is reflected in the statements of the European Commission in 2017, where it was reported that more than the half of the workers in the European Union work in stressful conditions, among which four out of ten cannot handle such stress properly. This activation state can lead to both physical and mental exhaustion, where the immune system is among the most affected. Consequently, people suffering from stress are more likely to get ill, being common certain chronic diseases such as cardiovascular diseases, diabetes and cancer, among others. This fact emphasizes the necessity of developing and implementing new methodologies to estimate the level of stress and relaxation in people, helping to regulate the pace of life in today's society and highlighting the importance of both physical and mental well-being to avoid further diseases.

The objective of this thesis is the development and implementation of intelligent algorithms for the real-time processing of non-invasively acquired physiological signals to automatically predict the continuous level of stress and relaxation in people. Thus, be able to identify the activity associated with the autonomic nervous system, responsible for the alterations caused in the homeostatic balance within the body. This goal resulted in a solution that goes from the analysis and processing of physiological signals to the design of an algorithm for real-time prediction of the level of stress and relaxation, which has subsequently been implemented in a functional low-cost hardware prototype. More precisely, the physiological records used to carry out this development are the electrocardiogram, the galvanic skin response and breathing due to their relation with the activity of the autonomic nervous system and the possibility of being acquired non-invasively.

The proposed methodology focuses on four main aspects. The first is the processing of physiological signals in short-term sliding windows, which contributes to improve the

techniques used for the extraction of heart period through the design of novel algorithms focused on the robust analysis of the electrocardiogram and blood pressure signals. In the second, the analysis, normalization and labeling of the extracted physiological parameters is carried out using original and validated methodologies. In the third aspect, the resulting data are subsequently employed for the design and training of intelligent systems through the implementation of supervised and unsupervised learning techniques in order to carry out a robust prediction of the level of stress and relaxation. Among the validated methods fuzzy logic, fuzzy rule-based supervised learning systems and artificial neural networks stand out. Finally, the development is successfully implemented in a portable low-cost hardware solution consisting of a physiological signal acquisition module and a server that processes and transfers the information to the client safely in real-time.

The proposed research resulted in a promising methodology for the quantification of autonomic nervous system activity in terms of stress and relaxation. Thus, validation results yielded a sensitivity of 98.02% and a specificity of 98.30% in the estimation of stress and relaxation level through the application of 21-fold cross-validation. These results support the effectiveness and robustness of the proposed methodology, which can lead to future research lines by applying the proposed solutions in different areas of biomedical engineering such as the estimation of emotional states based on the analysis of physiological signals.

UNIVERSIDAD DEL PAÍS VASCO

Resumen

Escuela de Ingeniería de Bilbao

Departamento de Ingeniería de Sistemas y Automática

Doctorado

Identificación del nivel de estrés y relajación en personas basada en el estudio y procesamiento avanzado de señales fisiológicas relacionadas con la actividad del sistema nervioso autónomo

por Unai ZALABARRIA

La Organización Mundial de la Salud calificó el estrés como la epidemia de salud del siglo XXI. Este hecho quedó reflejado en las declaraciones llevadas a cabo por la Comisión Europea en 2017, en donde se afirmó que más de la mitad de los trabajadores de la Unión Europea trabajan en un ambiente estresante, entre los cuales cuatro de cada diez no pueden gestionar ese estrés de manera adecuada. El estado de activación causado por el estrés puede dar lugar a un desgaste tanto físico como mental, en donde el sistema inmunológico es uno de los más afectados. Este factor da lugar a que las personas que sufren de estrés sean más propensas a enfermar, siendo comunes algunas enfermedades crónicas como las cardiovasculares, la diabetes y el cáncer, entre otras. Estos hechos resaltan la necesidad de desarrollar e implementar métodos de relajación que ayuden a regular el ritmo de vida de la población en la sociedad actual, dando especial importancia al bienestar tanto físico como mental de las personas, con el fin de evitar la aparición de enfermedades asociadas al estrés.

Teniendo en cuenta estas consideraciones, se ha definido como objetivo principal de esta tesis doctoral el desarrollo e implementación de algoritmos inteligentes capaces de procesar y predecir, de forma automática y en tiempo real, a partir de señales fisiológicas adquiridas de forma no invasiva, el nivel continuo de estrés y relajación en personas. De este modo, poder identificar la actividad asociada al sistema nervioso autónomo, que es uno de los principales responsables de las alteraciones causadas en el equilibrio homeostático del organismo. Dado que el estrés y la relajación están estrechamente ligados a la actividad del sistema nervioso autónomo, es importante estudiar en profundidad las reacciones fisiológicas debidas a esta actividad. El estudio llevado a cabo a lo largo de esta tesis ha dado lugar al diseño de soluciones novedosas, que van desde el análisis y procesamiento de señales fisiológicas hasta el desarrollo de algoritmos capaces de medir el nivel de estrés y relajación en tiempo real. Concretamente, se ha llevado a cabo el desarrollo de

algoritmos basados en técnicas de computación inteligente enfocados al procesamiento de señales fisiológicas adquiridas en entornos reales y no necesariamente controlados, los cuales han sido posteriormente implementados y validados en un prototipo hardware de bajo coste. El desarrollo ha concluido con la implementación de la solución propuesta en una plataforma hardware portable para la monitorización fisiológica del nivel de estrés y relajación, demostrando que es posible modelar la activación del sistema nervioso autónomo mediante el modelado de patrones fisiológicos utilizando técnicas de computación inteligente.

Con el fin de lograr el objetivo propuesto, esta tesis se compone de cuatro bloques principales u objetivos parciales, a lo largo de los cuales se lleva a cabo el procesamiento sistemático de los registros fisiológicos, el análisis y etiquetado de los parámetros extraídos, el estudio comparativo de los diferentes algoritmos inteligentes seleccionados y la implementación hardware de los algoritmos resultantes de todo el estudio realizado. El desarrollo propuesto se centra principalmente en el análisis de tres señales fisiológicas: el periodo cardíaco, la respuesta galvánica de la piel y la respiración. Estas señales han sido cuidadosamente seleccionadas debido a su estrecha relación con la actividad del sistema nervioso autónomo y por la posibilidad de ser adquiridas de forma no invasiva.

El primer bloque está enfocado al desarrollo de algoritmos para la extracción robusta del periodo cardíaco. Tal y como queda reflejado en el estado del arte, el tiempo entre latidos se puede obtener mediante el procesado de diferentes bioseñales. En ocasiones, estas señales están afectadas por artefactos que dan lugar a mediciones erróneas del periodo cardíaco, falseando la estimación de la actividad del sistema nervioso autónomo. Con el fin de robustecer la extracción del periodo cardíaco, en esta tesis se presentan dos algoritmos novedosos: uno para el procesamiento del electrocardiograma y el otro para el procesamiento de la presión arterial, siendo también aplicable este último algoritmo durante el procesamiento de señales pletismográficas.

El algoritmo desarrollado para la extracción del periodo cardíaco a partir de las señales electrocardiográficas está basado en la detección robusta de picos R. Esta tesis propone una metodología original para llevar a cabo una primera detección de los picos R mediante la medición del área por encima del complejo QRS. Los picos R detectados son posteriormente procesados de forma iterativa por tres novedosas máquinas de estados que corrigen los errores cometidos durante la primera detección mediante la inserción y eliminación de los picos R faltantes y sobrantes, respectivamente. Cada máquina de estados está compuesta por un conjunto de condiciones que evalúan la veracidad del periodo cardíaco en cada instante. Además, el algoritmo propuesto ha sido diseñado para llevar a cabo el procesamiento del electrocardiograma utilizando una ventana deslizante de 20 segundos, siendo así implementable en sistemas con funcionamiento en tiempo real. Los resultados obtenidos alcanzan una sensibilidad del 99.54 % y una precisión del 99.60 %, con un gasto computacional adecuado para su implementación en plataformas de bajas prestaciones. Estos resultados también avalan la fiabilidad del algoritmo a la hora de procesar ventanas de corta duración, ya que un pequeño error durante la detección de los

picos R puede dar lugar a alteraciones indeseadas en los parámetros derivados del periodo cardíaco. Este desarrollo ha dado lugar a una publicación en la prestigiosa revista *Applied Mathematics and Computation* (JCR: 3.472 - Q1) bajo el título de "*Online robust R-peaks detection in noisy electrocardiograms using a novel iterative smart processing algorithm*."

El algoritmo propuesto para la extracción del periodo cardíaco a partir de señales de presión arterial se basa en la estimación de la posición de los valles de la señal que preceden a cada latido para identificar cuando estos ocurren. Para ello, se han desarrollado algunas técnicas de procesamiento avanzado como el "método del cálculo diferencial de la interpolación móvil" y el "método mejorado del cálculo del valor máximo de la segunda derivada" para la eliminación robusta de la línea de base y la detección precisa de todos los valles presentes en la señal de presión arterial. Estos valles son posteriormente clasificados en valles correspondientes y no correspondientes a latidos del corazón a través del procesamiento inteligente de cinco parámetros característicos de la morfología de la señal. La clasificación se ha llevado a cabo utilizando una red neuronal artificial cuidadosamente optimizada, la cual combina a la entrada los cinco parámetros extraídos para clasificar los valles detectados y determinar si corresponden a latidos cardíacos. Este desarrollo se ha llevado a cabo utilizando registros de presión arterial de 10 segundos, alcanzando una sensibilidad del 99.17 % y una especificidad del 99.21 % en la detección de latidos del corazón. Debido a la similitud que existe entre la morfología de los registros de presión arterial y las señales fotopletismográficas, el algoritmo propuesto es potencialmente aplicable para procesar este segundo tipo de señales. Al igual que ocurre con el algoritmo de procesamiento del electrocardiograma, la capacidad de procesar ventanas de corta duración hace que el algoritmo desarrollado sea implementable en sistemas de ejecución en tiempo real. El trabajo realizado ha dado lugar a una segunda publicación en la conocida revista *Computer Methods and Programs in Biomedicine* (JCR: 3.632 - Q1) bajo el título de "*Diagnosis of atrial fibrillation based on arterial pulse wave foot point detection using artificial neural networks*."

En el segundo bloque se proponen varias metodologías novedosas para la normalización y etiquetado de los parámetros fisiológicos extraídos a partir del periodo cardíaco, la respuesta galvánica de la piel y la respiración. Este bloque empieza proponiendo un etiquetado binario (0-1) parcial de los intervalos claramente identificables como estados de estrés y de relajación, para posteriormente llevar a cabo una innovadora normalización y etiquetado completo y continuo de los registros. Con el fin de obtener unos parámetros fisiológicos normalizados que supriman las diferencias fisiológicas interpersonales, se ha diseñado una metodología original para la selección del método de normalización que mejor se ajusta a la naturaleza de cada parámetro. Para ello, se han evaluado algunos métodos de normalización existentes junto a otros propuestos en esta tesis mediante una función de coste especialmente diseñada para diferenciar estados de estrés y de relajación, siendo los métodos con el coste más pequeño los mejor adaptados para llevar a cabo la normalización del parámetro en cuestión. Además, se ha realizado una selección de los

parámetros más representativos de los estados de estrés y de relajación mediante un estudio exhaustivo de su distribución. Posteriormente se ha llevado a cabo un análisis de los componentes principales con el fin de eliminar la redundancia entre los parámetros más relevantes. Los componentes principales han sido finalmente implementados, junto a las etiquetas parciales (binarias), en un algoritmo de aprendizaje semisupervisado, dando como resultado un pseudoetiquetado continuo y completo de cada uno de los registros. Los resultados obtenidos se han validado frente a un segundo etiquetado parcial realizado por personal experto en el análisis de señales fisiológicas. Este segundo etiquetado no ha sido previamente utilizado durante el desarrollo propuesto en este bloque, únicamente se ha utilizado para llevar a cabo la validación de la metodología propuesta, alcanzando un 98.41 % de sensibilidad y un 99.32 % de especificidad en el pseudoetiquetado de los registros.

En el tercer bloque se hace uso de los componentes principales y del pseudoetiquetado completo y continuo obtenidos en el bloque anterior con el fin de entrenar y configurar diferentes algoritmos inteligentes basados en aprendizaje supervisado y no supervisado, y comparar la capacidad de predicción de cada uno de ellos a la hora de estimar el nivel de estrés y relajación para cada registro. Entre las técnicas validadas están la lógica difusa, las redes neuronales artificiales y varios sistemas de aprendizaje supervisado basados en reglas difusas, como son: *Wang and Mendel's technique*, *dynamic evolving neural-fuzzy inference system*, *hybrid neural fuzzy inference system* y *heuristics and gradient descent method*. Para evaluar cada uno de los métodos propuestos, en esta tesis se ha llevado a cabo un procedimiento original basado en el mapeo de los posibles valores de cada uno de los hiperparámetros de cada técnica mediante la implementación de una validación cruzada de 21 iteraciones. Los resultados obtenidos han dado lugar a una sensibilidad del 97.93 % y una especificidad del 97.92 % para las redes neuronales artificiales, las cuales presentan los resultados más estables y los tiempos de entrenamiento e inferencia más pequeños. Además, se ha llevado a cabo la evaluación de todas las posibles combinaciones de las tres señales fisiológicas utilizadas, demostrando que el periodo cardíaco y la respuesta galvánica de la piel combinadas obtienen los resultados más prometedores. La respiración, por su parte, ha demostrado que contribuye en la mejora de los resultados que cada una de las otras dos señales obtienen por separado.

El cuarto y último bloque describe la implementación hardware de los algoritmos desarrollados y validados a lo largo de esta tesis. Para ello, se ha diseñado una plataforma de adquisición portátil y con funcionamiento en tiempo real combinando de forma original distintos componentes de bajo coste fácilmente asequibles en el mercado. Además, se ha llevado a cabo la implementación de los algoritmos propuestos en un servidor de bajo coste y prestaciones, como es la plataforma Raspberry Pi. El servidor recibe las señales fisiológicas adquiridas de forma inalámbrica (Bluetooth) al mismo tiempo que extrae y procesa los parámetros fisiológicos a través de la red neuronal artificial previamente entrenada para finalmente obtener una medida continua del nivel de estrés y relajación. Los resultados obtenidos son enviados al cliente a través de la red (cable o Wi-Fi) utilizando el

protocolo gRPC, el cual permite implementar mecanismos de encriptación y autentificación para una mayor seguridad y protección de los datos. La concurrencia del sistema ha sido validada sometiendo tanto a la plataforma de adquisición como al servidor a pruebas de funcionamiento en tiempo real y obteniendo los tiempos que así lo avalan.

Tanto la implementación en el tercer bloque del modelo de lógica difusa para la estimación continua del nivel de estrés y relajación, como la implementación de los algoritmos propuestos en plataformas de bajo coste, han dado lugar a una tercera publicación en la conocida revista *IEEE Access* (JCR: 3.745 - Q1) bajo el título de "*A low-cost, portable solution for stress and relaxation estimation based on a real-time fuzzy algorithm*."

En definitiva, esta tesis aborda, a través de cuatro bloques bien definidos, la metodología para llevar a cabo el desarrollo completo de un sistema inteligente capaz de realizar una estimación continua del nivel de estrés y relajación en personas con distintas fisiologías mediante el procesamiento de parámetros extraídos a partir de señales fisiológicas adquiridas en tiempo real y de forma no invasiva. Durante el proceso, se han utilizado métodos del campo de la inteligencia computacional, entre los que se encuentran varios algoritmos de análisis supervisado, semisupervisado y no supervisado. Además, se han aportado nuevas metodologías tanto para el procesamiento de señales fisiológicas como para el normalizado, análisis y etiquetado de los parámetros extraídos de las mismas. También se ha hecho un uso original de los algoritmos de análisis semisupervisado para llevar a cabo el pseudoetiquetado de los registros, demostrando que es posible convertir unas etiquetas binarias y parciales en un etiquetado completo y de dominio continuo. Otra aportación realizada es la función de coste para la selección del mejor método de normalización. Además, también se ha propuesto otra función de coste customizada para el entrenamiento de la red neuronal artificial utilizada, la cual ha sido específicamente diseñada para este contexto. Tienen un peso relevante los resultados obtenidos durante la predicción del nivel de estrés y relajación para las distintas combinaciones de señales fisiológicas, ya que aportan información útil sobre la relación que guardan con la actividad del sistema nervioso autónomo. Por último, se ha hecho un esfuerzo considerable para llevar a cabo la implementación hardware del sistema, donde se han combinado distintos componentes para dar lugar a un dispositivo basado en tecnología IoT capaz de adquirir señales fisiológicas en tiempo real y de ejecutar los algoritmos propuestos de forma concurrente.

Cabe destacar que las diferencias fisiológicas entre individuos aún suponen un reto a la hora de normalizar los parámetros extraídos y poder diseñar algoritmos genéricos capaces de procesar estos parámetros de forma simultánea. Cada persona es diferente y esto se observa en las reacciones que tenemos cada uno ante la misma clase de eventos, tanto en el tipo como en la intensidad de la reacción. Esta tesis ha sabido abordar este reto de una forma original, ya que algunas señales pueden diferir en gran medida de otras debido a su morfología. El etiquetado de señales fisiológicas ha sido otro de los principales retos, para el cual cada señal se ha estudiado de forma individual tanto para llevar a cabo el etiquetado parcial de forma manual como para lograr el etiquetado completo y continuo mediante algoritmos de pseudoetiquetado.

Acknowledgements

I would first like to thank my first co-supervisor, Dr. Eloy Irigoyen, whose expertise was invaluable in formulating the research questions and methodology. Your insightful feedback pushed me to sharpen my thinking and brought my work to a higher level.

I would also like to thank my second co-supervisor, Dr. Raquel Martínez, for her valuable guidance throughout my studies. You provided me with the tools that I needed to choose the right direction and successfully complete my thesis.

I would like to acknowledge my colleagues from my internship at Auckland University of Technology for their wonderful collaboration. I would particularly like to single out my supervisor at the Institute of Biomedical Technologies, Dr. Andrew Lowe. I want to thank you for your support and for all of the opportunities I was given to further my research.

In addition, I would like to thank my family for their unconditional support. You are always there for me. Finally, I could not have completed this thesis without the support of my friends, who provided stimulating discussions as well as happy distractions to rest my mind outside of my research.

Contents

List of Figures

List of Tables

List of Algorithms

List of Abbreviations

WHO	World Health Organization
ANS	Autonomic nervous system
SNS	Sympathetic nervous system
PNS	Parasympathetic nervous system
GSR	Galvanic skin response
SCL	Skin conductance level
SCR	Skin conductance response
HP	Heart period
ECG	Electrocardiogram
BP	Blood pressure
OBP	Oscillometric blood pressure
LA	Left arm
RA	Right arm
LL	Left leg
PPG	Photoplethysmography
HRV	Heart rate variability
RSP	Breathing
PCA	Principal component analysis
PC	Principal component
FRBS	Fuzzy rule-based system
WM	Wang and Mendel's method
DENFIS	Dynamic evolving neural-fuzzy inference system
HyFIS	Hybrid neural fuzzy inference system
FS.HGD	Heuristics and gradient descent method
ECM	Evolving clustering method
ANN	Artificial neural network
SAM	Self-assessment manikin
UPV/EHU	University of the Basque Country
MITADB	MIT-BIH arrhythmia database
TP	True positive
TN	True negative
FP	False positive
FN	False negative
Pr	Precision
Se	Sensitivity

Sp	Specificity
Ac	Accuracy
F1	F1 score
SW	Sliding window
SM	State machine
BW	Baseline wander
CL	Cutting line
SI	Signal intensity
NI	Noise intensity
N	Neighbors
W	Duration of the QRS complex
PVC	Premature ventricular contraction
FPO	Oscillometric foot point
LSW	Long sliding window
SSW	Short sliding window
LTV	Long-term variation
STV	Short-term variation
MID	Moving interpolation difference
SDMM	Second derivative maximum method
ZCP	Zero-crossing point
MI	Minimum MID wave value
MA	Maximum MID wave value
HL	Hidden layer
MHP	Mean heart period
VHP	Variation of the heart period
IRRX	Irregularity index
NN50	Number of successive heart periods that differ by more than 50ms
PNN50	Percentage of NN50
RMS	Root mean square of the heart period
RMSSD	Root mean square of successive heart period differences
SDNN	Standard deviation of the heart period
SDSD	Standard deviation of successive heart period differences
SENN	Standard error of the heart period mean
HPHF	Heart period high frequency band
HPLF	Heart period low frequency band
HPVLF	Heart period very low frequency band
HPULF	Heart period ultra low frequency band
POSD1	Poincare plot standard deviation 1
POSD2	Poincare plot standard deviation 2
POSD12	Ratio between POSD1 and POSD2
DIS	Dispersion of points around diagonal line in poincaré plot
STEP	Mean stepping increment of inter-beat intervals

MGSR	Mean value of the galvanic skin response
VGSR	Variation in the galvanic skin response
AGSR	Differential area between the GSR signal and its first-order interpolation
RSPHF	Breathing high frequency band
RSPLF	Breathing low frequency band
RSPVLF	Breathing very low frequency band
RSPULF	Breathing ultra low frequency band
SDRSP	Standard deviation of the frequencies
CC	Cross correlation
HSCR	Product between SDRSP and RMS
CACO	Cardiac coherence
PIMF	Pi-shaped membership function
TRAPMF	Trapezoidal membership function
SMF	S-shaped membership function
ZMF	Z-shaped membership function
EMG	Electromyogram
EEG	Electroencephalogram
ST	Skin temperature
ACC	Acceleration
PCB	Printed circuit board
ArdN	Arduino Nano board
Fs	Sampling frequency
RPi3	Raspberry Pi 3
RPi4	Raspberry Pi 4
HW	Hardware device
RT	Real-time
P	Portable

Dedicated to my family and friends.

1 Introduction

1.1 Motivation

In recent years, more and more people and medical centers are using physiological records, mostly acquired non-invasively, to monitor the health status in real-time [1, 2]. These devices range from wearable gadgets (e.g., wrist-bands, T-shirts and watches) to standalone systems, very common in hospitals [3, 4]. In many cases, this follow-up can be critical to identify states that may be decisive to prevent various diseases such as those related to stress [5]. Relaxation is equally important as it is directly involved in therapies focused on the prevention of stress-related pathologies [6]. This fact is leading to the development of algorithms centered on the analysis of physiological parameters for the prediction of both stress and relaxation states [7, 8, 9, 10].

"Stress" was dubbed the "health epidemic of the 21st Century" by the World Health Organization (WHO) and it is estimated to cost American businesses up to $300 billion a year [11]. According to a statement from the European Commission in 2017, work-related stress is one of the most challenging and growing occupational safety and health concerns. Over half of European Union workers report that stress is common in their workplaces, and 4 out of 10 think that it is not well handled [12]. Moreover, it can cause various diseases including chronic illnesses (e.g. cardiovascular diseases, diabetes and some forms of cancer). All these circumstances increase economic costs, especially in developed countries [5].

The WHO defines Health as a state of complete physical, mental and social wellness, together with the absence of disease [13]. Considering the new paradigms focused on the search for people's wellness by means of positive psychology, many research lines have changed the focus on how people relax [14, 15]. Thus, the understanding and strengthening of the factors that allow individuals to prosper is proposed as a method to improve the quality of life of communities and societies. Therefore, pathologies caused by adverse living conditions can be prevented [16]. Relaxation techniques are, among others, the most widely used techniques to achieve a state of wellness [6, 17, 18].

In the literature, stress is defined as a general adaptation syndrome consisting of physiological and psychological components [11, 19, 20]. The term was first introduced by Hans Selye, the "father of stress", who noticed that patients with various diseases (i.e., hypertension, nephrosclerosis and the rheumatic diseases) may represent effects of the endocrine

reactions, present in the general adaptation syndrome [21, 5, 22]. Walter B. Cannon introduced and popularized the concepts of homeostasis and "fight or flight" that by now are well known and widely accepted [23, 22]. He asserted that not only physical emergencies but also psychological emergencies evoke release of adrenaline into the bloodstream, preparing the body to "fight" or "flight" [24, 11]. Benson introduced the concept of relaxation response, which refers to the physiological response during a state of relaxation [25]. Homeostasis, defined as the stability of the internal state, is the result of the activity of the autonomic nervous system (ANS) and the hypothalamic-pituitary-adrenal axis, that respond to stress as an attempt to relax or reestablish the balance on a psychophysiological level [26, 19, 27]. Thus, the relaxation response appears not only during states of relaxation, but also when the stressful event is over. This involves changes in cardiac activity, sweat gland activity and breathing [19]. Therefore, physiological signals, including heart period, galvanic skin response and chest measurements can provide insights into ANS activity and are considered reliable indicators of stress and relaxation [11, 28].

The possibility of quantifying ANS activity by observing variations in physiological signals has given rise to innovative areas of study, allowing researchers to directly assess the user's internal state. Moreover, the increasing availability of inexpensive and sophisticated measurement systems establishes the basis for novel research ideas and developments. Some of these areas have focused their effort on developing algorithms and methodologies to extract relevant physiological information in relation to the ANS activity [28, 29, 9]. Rosalind W. Picard introduced the concept of Affective Computing, which lays the foundations for physiological signal processing according to changes in the ANS [30]. Recent advances in the development of smaller and more precise sensors, which do not require gels, have made it possible to apply a wide range of wireless patient monitoring systems in conventional environments [31]. Some research lines have integrated these technologies in the development of low-cost portable devices capable of carrying out physiological signal processing for the detection of events related to ANS activity [3, 32, 2].

However, there is still a gap in research efforts moving from laboratory studies to real-world settings. Some of these challenges are related to the differences among the physiological signals of different individuals in the same stress and relaxation situations, including dispersed distributions and sample imbalance. This makes it difficult to generalize an algorithm that works properly with signals collected from different individuals [33]. Additionally, devices are increasingly becoming connected through IoT technologies. This has tremendous potential to make healthcare accessible to everyone and with reduced costs. Nevertheless, it also provides the opportunity for technology criminals to hack these devices. Thus, it is essential to consider security issues, as medical devices collect and exchange personal health data [34].

This thesis proposes an original solution based on the study and processing of physiological signals for the estimation of ANS activity in people in terms of stress and relaxation through the development and implementation of innovative algorithms based on computational intelligence. Several human physiological signals (i.e., heart period, galvanic

skin response and breathing) were studied with the aim of extracting parameters suitable for implementation in regression algorithms for advanced modeling of patterns related to the activity of the ANS, thus achieving an accurate estimate of the stress and relaxation level at each time. For this purpose, a novel framework for real-time ANS activity recognition based on patterns extracted from peripheral physiological signals was implemented, along with the design of a low-cost wireless prototype with reliable data communication that integrates the developed software. To this end, the author focused on three main aspects. First, existing physiological signal preprocessing techniques were improved. More precisely, an innovative algorithm for robust and real-time extraction of heart period in electrocardiographic and blood pressure signals was developed. Second, an original physiological signal processing methodology was proposed, where extracted parameters were studied with the aim of reducing the errors caused by individual differences and improving the regressive performance of stress and relaxation recognition algorithms. Finally, due to the efficiency, safety and versatility required from medical devices, a robust low-cost prototype based on IoT technologies was developed considering the safety measures needed to protect client information. A more detailed explanation of the proposed methods is covered further on in the following chapters.

1.2 Objectives

The main objective of this thesis is the development of an intelligent and integrated solution to predict the level of stress and relaxation in people based on advanced processing of parameters extracted from physiological signals closely related to the activity of the ANS (i.e., heart period, galvanic skin response and breathing). This solution covers the analysis, development and implementation on a hardware platform of the proposed methodology. To achieve this goal, the following partial objectives are defined:

- Design of accurate and computationally efficient algorithms for the preprocessing of signals extracted from the cardiovascular system in order to carry out a robust measurement of the heart period and the parameters derived from it.
- Analysis, normalization and labeling of the parameters extracted from non-invasively acquired heart period, galvanic skin response and breathing signals, according to their correlation with the activity of the ANS.
- Identification of patterns related to the activity of the ANS based on a comparative study of intelligent computing techniques.
- Implementation of the proposed algorithm in a low-cost portable hardware solution that fulfils the real-time concurrency and security requirements in order to validate the proposed methodology and apply the conducted study to real use cases.

1.3 Contributions

The development of this thesis resulted in the publications presented below.

1.3.1 Publications with impact factor

JCR: Web of Science

- Unai Zalabarria, Eloy Irigoyen, and Andrew Lowe. "Diagnosis of atrial fibrillation based on arterial pulse wave foot point detection using artificial neural networks". In: *Computer Methods and Programs in Biomedicine* 197 (Dec. 2020), p. 105681. DOI: 10.1016/j.cmpb.2020.105681 (JCR: 3.632 - Q1)
- Unai Zalabarria et al. "A Low-Cost, Portable Solution for Stress and Relaxation Estimation Based on a Real-Time Fuzzy Algorithm". In: *IEEE Access* 8 (2020), pp. 74118–74128. DOI: 10.1109/access.2020.2988348 (JCR: 3.745 - Q1)
- Unai Zalabarria et al. "Online robust R-peaks detection in noisy electrocardiograms using a novel iterative smart processing algorithm". In: *Applied Mathematics and Computation* 369 (Mar. 2020), p. 124839. DOI: 10.1016/j.amc.2019.124839 (JCR: 3.472 - Q1)
- A. Salazar-Ramirez et al. "An enhanced fuzzy algorithm based on advanced signal processing for identification of stress". In: *Neurocomputing* 271 (2018), pp. 48–57. ISSN: 0925-2312. DOI: 10.1016/j.neucom.2016.08.153 (JCR: 4.072 - Q1)

SJR: Scimago

- Unai Zalabarria et al. "Acquisition and Fuzzy Processing of Physiological Signals to Obtain Human Stress Level Using Low Cost Portable Hardware". In: *International Joint Conference SOCO'17-CISIS'17-ICEUTE'17 León, Spain, September 6–8, 2017, Proceeding*. Springer International Publishing, Aug. 2017, pp. 68–78. DOI: 10.1007/978-3-319-67180-2_7
- Unai Zalabarria et al. "Detection of Stress Level and Phases by Advanced Physiological Signal Processing Based on Fuzzy Logic". In: *International Joint Conference SOCO'16-CISIS'16-ICEUTE'16*. Springer International Publishing, Oct. 2016, pp. 301–312. DOI: 10.1007/978-3-319-47364-2_29

1.3.2 Publications without impact factor

- Unai Zalabarria et al. "Adquisición y procesamiento difuso de señales fisiológicas para la obtención del nivel de estrés utilizando hardware portable de bajo coste". In: *XIII Simposio CEA de Control Inteligente*. 2017, pp. 52–57
- Unai Zalabarria et al. "Detección del nivel y fases de estrés mediante procesamiento avanzado de señales fisiológicas basado en lógica difusa". In: *XII Simposio CEA de Control Inteligente*. 2016, pp. 31–36
- Unai Zalabarria et al. "Procesamiento robusto para el análisis avanzado de señales electrocardiográficas afectadas por perturbaciones". In: *Actas de las XXXVI Jornadas de Automática*. 2015, pp. 807–814

1.4 Thesis structure

Below, an overview of the thesis structure is presented, explaining in general terms the content of each chapter.

Chapter 2 is the state of the art, which is divided into five subsections to present the previous work that supports the current thesis. First introduces the principal mechanisms of human psychophysiology that influence the activity of the ANS, explaining how the body reacts against different events leading to states of stress and relaxation. This chapter also describes the experiment conducted for the collection of physiological records, which were used during the development and validation of the algorithms. In addition, the soft computing techniques employed during this thesis and the hardware used for the implementation of a final prototype are also included. Finally, the used evaluation tools are described.

Chapter 3 presents the proposed algorithms for an advanced extraction of the heart period during the preprocessing of electrocardiographic and blood pressure signals. Several new methodologies are presented to robustly process these signals, further improving the results obtained by existing methods. The proposed algorithms were designed to carry out the processing in relatively small context windows compared to other works, which makes them suitable for implementation in real-time systems.

In chapter 4, an original partial labeling of the physiological signals is performed together with the extraction of the parameters derived from such signals, which are representative of the ANS activity. A parameter normalization is also carried out by applying the most appropriate standardization techniques. For this purpose, a novel analysis comparing different normalization methods is performed, from which a selection of the most significant parameters is also conducted. The redundancy among the selected parameters is finally eliminated through the extraction of the principal components. These principal components are later used to complete the partial labeling through an original implementation of semi-supervised learning techniques.

Chapter 5 addresses the design, training and validation of a set of methods based on supervised and unsupervised learning techniques. Validated methods include fuzzy logic, artificial neural networks and fuzzy rule-based supervised learning systems, where a new customized loss function is proposed for the training of artificial neural networks. To perform an optimal training, a mapping of the hyperparameters of the supervised learning methods is performed, thus achieving a robust validation of each method through the application of cross-validation. The whole process is carried out in duplicate, using the normalized and unnormalized physiological parameters in order to compare the performance associated with the previously designed normalization mechanism.

Chapter 6 describes the implementation of the previously developed algorithms into an advanced IoT-based low-cost hardware prototype. On the one hand, a portable hardware for real-time acquisition of physiological signals and wireless transmission of the data is

presented. On the other hand, a server for the processing of the acquired physiological signals is introduced, in which the estimation of the stress and relaxation level is also performed. The whole process is embedded in a secure client-server connection, which is performed by means of communication protocols that guarantee the transmission of encrypted data.

Finally, chapter 7 discusses the conclusions of the solution presented in this thesis, as well as the resulting contributions. It also includes the future lines that may be carried out considering potential contributions that could be addressed in future developments.

2 State of the art

To introduce the preliminary works around which this thesis is built, the state of the art is divided into five subsections. In the first subsection, an introduction to human psychophysiology is conducted, explaining the different physiological reactions of the human body and its relationship with the autonomic nervous system. The second subsection presents the soft computing methods involved in the development of the proposed methodologies. The third subsection focuses on the data sets used for both the design and validation of the implemented algorithms. In the fourth subsection, the hardware devices used for the development of a functional prototype that executes the previously designed algorithms are introduced. Finally, the fifth subsection presents the evaluation tools used to validate the proposed algorithms. Next, the foundations of psychophysiology on which this study is supported are presented.

2.1 Foundations of psychophysiology

From the moment people began to experience themselves as an object of their own awareness, they have had the intuition that bodily changes were related to their moods, feelings and emotions. Psychophysiology was born as a branch of psychology dealing with the physiological basis of these psychological processes. Additionally, it is closely related to the experience and behaviour of organisms in the physical and social environment [44].

Rose [45] differentiated at least two components of the nervous system related to psychological states and physiological events, as illustrated in Figure 2.1: The central nervous system, consisting of the brain and spinal cord, and the peripheral nervous system, which its main function is to connect the central nervous system to the limbs and organs through the nerves and ganglia [46].

The peripheral nervous system is divided into the somatic nervous system and the autonomic nervous system (ANS), where the ANS exerts influence over the organ systems of the body to upregulate and downregulate various functions.

2.1.1 Autonomic nervous system

The ANS is also known as the vegetative nervous system, as it acts unconsciously and regulates bodily functions such as the heart period, digestion, respiratory rate, pupillary response, urination, and sexual arousal [47]. It is divided, in turn, into the sympathetic nervous system (SNS) and parasympathetic nervous system (PNS) [48]. The sympathetic

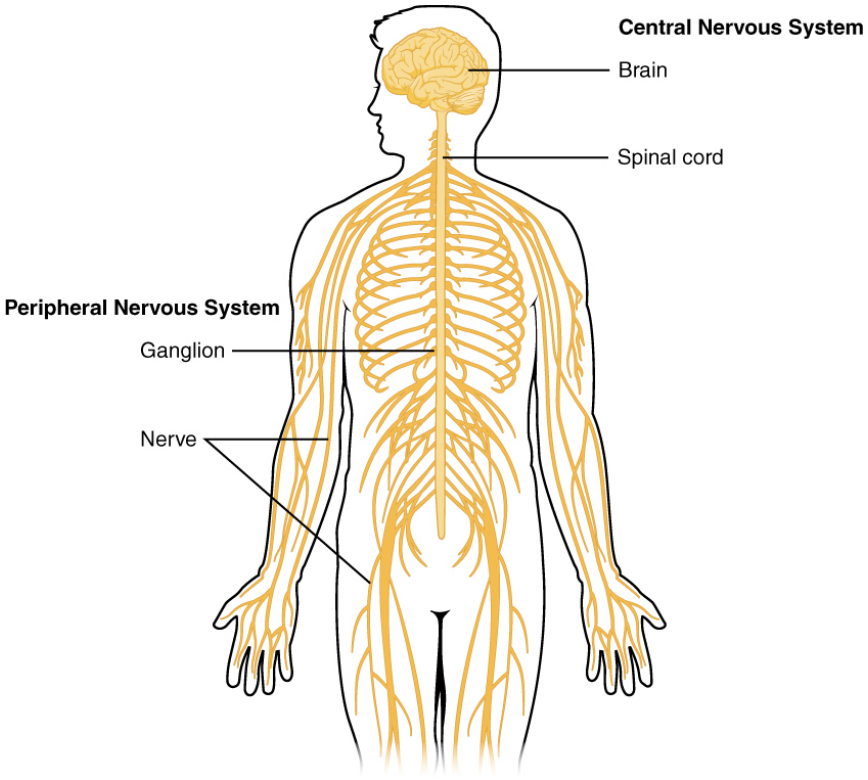

FIGURE 2.1: Schematic representation of the central nervous system in yellow and the peripheral nervous system in orange.
Source: openstax.org

system is associated with the "fight or flight" response, and parasympathetic activity is known as "rest and digest" [49]. The two aspects of the ANS can be considered as opposing functions that act to achieve homeostasis, which is regulated by the hypothalamus [26, 19, 50]. The activity of the SNS and PNS results in the physiological responses shown in Figure 2.2.

Sympathetic nervous system

During stressful situations, the SNS reacts by activating different effector organs in a coordinated manner. As the body prepares for "fight or flight", more oxygen needs to be inhaled and delivered to skeletal muscle. The respiratory, cardiovascular, electrodermal and musculoskeletal systems are all activated together. Additionally, sweating protects the body from the excess heat that comes from muscle contraction that causes the body to overheat [20, 19]. The digestive system shuts down so that blood is not absorbing nutrients when it should be delivering oxygen to skeletal muscles [51]. To coordinate all these responses, the connections in the sympathetic system diverge from a limited region of the central nervous system to a wide range of ganglia that project to the effector organs simultaneously. This phenomenon is illustrated in the diagram in Figure 2.3 [50]. The activation of the SNS causes a reaction commonly known as stress.

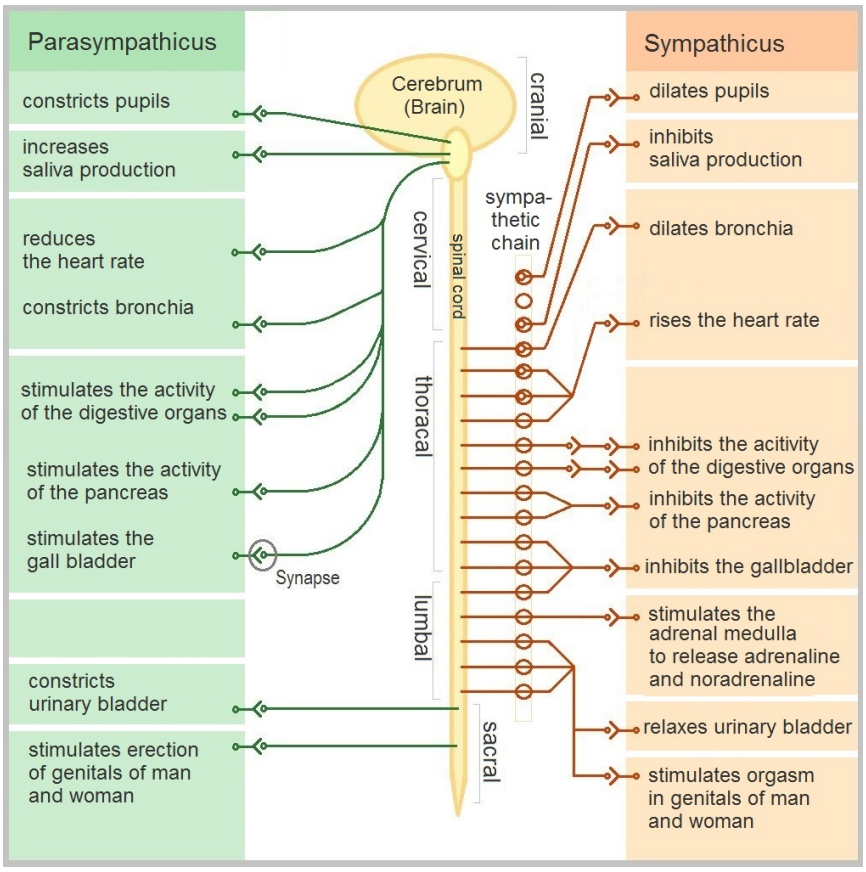

FIGURE 2.2: Physiological responses due to sympathetic and parasympathetic activity.
Source: Geo-Science-International

Stress

The first and most generic definition of stress is that proposed by Hans Selye: "Stress is the nonspecific response of the body to any demand" [5]. The terms of stress, "*general adaptation syndrome*" and "*general alarm reaction*" are synonymous. They all indicate a physiological response that occurs due stressful stimuli, helping the body to adapt to the situation through the activation of the ANS [21, 52].

In the book "*Stress in health and disease*", Selye underscored the fact that stress is part of everyday life and it is associated with a variety of diverse problems, such as emotional arousal, fatigue, mental or physical effort, burns, surgical trauma, fear, pain, frustration, concentration, the loss of blood, intoxication with environmental pollutants or drugs, or any kind of event that requires reformulating one's lifestyle [5].

Selye also established that some stress is essential and healthy, but too much stress can be harmful [53, 54]. Therefore, it is accepted that there are two types of stress, as described below [52].

- Eustress: it is considered as good stress because it is not harmful and it is essential for life, growth and survival. This type of stress allows organisms to face and adapt to changes and different situations.

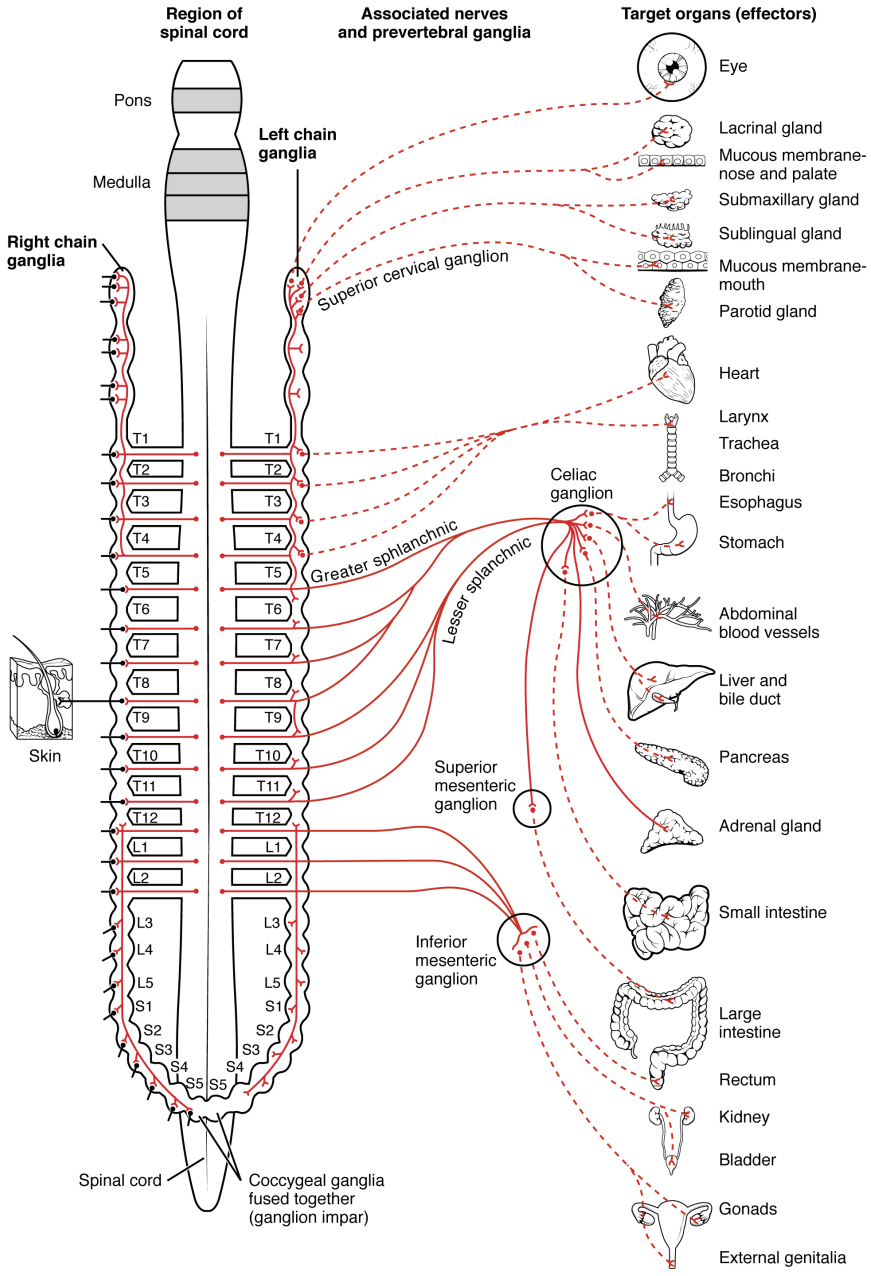

FIGURE 2.3: Connections of sympathetic branch of the ANS.
Source: opentextbc.ca

- Distress: it is considered a bad stress because it is harmful, pathological, destroys the organism, is accumulative, kills hippocampal neurons, contributes to produce mental pathologies, accelerates the aging process, etc.

In a healthy person, the performance level increases during eustress but decreases rapidly in the distress stage as illustrated in the human function curve in Figure 2.4 developed by Nixon [55]. In total, five stages of stress are differentiated:

1. Alarm stage: The organism prepares to “fight or flight”.
2. Resistance stage: Consists of continued sympathetic stimulation. The body is attempting to maintain homeostasis in the presence of the stressor which initiated

the alarm reaction.

3. Recovery stage: As the stress is brought under control, normal body function returns.

4. Adaptation stage: If the body does not proceed through to the recovery stage, the distress becomes chronic. At this stage the body prepares for a period of stress that can result in chronic diseases.

5. Exhaustion stage: The exhaustion stage occurs when the body finally gets drained due to the incapacity to recover from continuous stress.

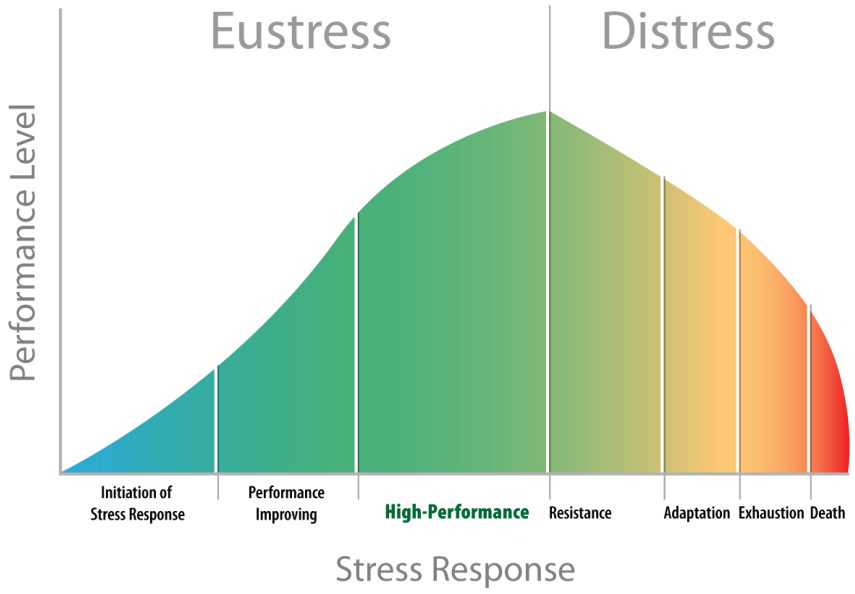

FIGURE 2.4: The human stress-performance curve.
Source: nutritionalbalancing.org

Parasympathetic nervous system

The parasympathetic division has the opposite role, counteracting the activity of the SNS. It restores the body to a state of calm and relaxation. When the external environment does not present any immediate danger, the body goes into rest mode and the digestive system is more active. It slows the heart rate, increases intestinal and gland activity and relaxes sphincter muscles in the gastrointestinal tract [49].The parasympathetic system can also be referred to as the craniosacral system because the preganglionic neurons are located in nuclei of the brainstem and the lateral horn of the sacral spinal cord, as illustrated in the scheme in Figure 2.5 [48, 50]. The activation of the PNS causes a reaction commonly known as relaxation.

Relaxation

Considering the new paradigms of positive psychology, many research lines have changed the focus in this area, looking for solutions centered on the wellness of people and analyzing how people relax [14, 15, 51, 56]. The idea of relaxation in psychology was popularized

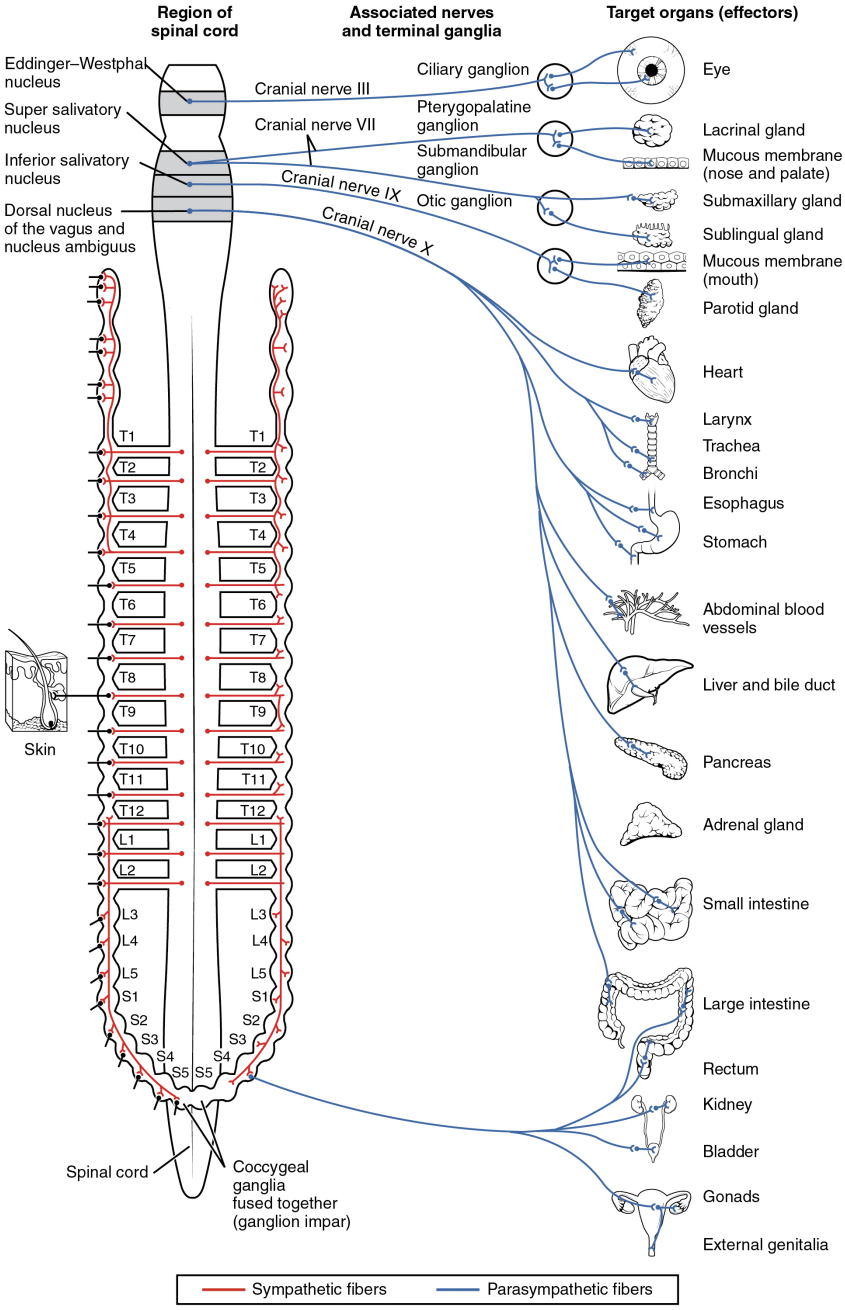

FIGURE 2.5: Connections of parasympathetic division of the ANS.
Source: opentextbc.ca

by Dr. Edmund Jacobson in his book "*Progressive Relaxation*" [57]. The feeling of the effect that PNS has on the organism is what it is feels as relaxation. This phenomenon is associated with a decrease in heart rate, blood pressure and breathing rate, normalization of blood sugar levels, increase of blood flow to major muscles, reduction of the activity of stress hormones and reduction of the muscle tension and chronic pain [49]. These changes that take place in the organism produce what Benson called a relaxation response [25].

2.1.2 Response systems

The body response is usually understood as the body's ability to react properly to the influence of both external and internal factors. The body response can range from a relaxing ("rest and digest") to a stressful ("fight or flight") response, affecting the physiology of the electrodermal, cardiovascular and respiratory systems [19, 49, 27]. Therefore, it is essential to study these systems to understand their responses to different stimuli, both stressful and relaxing, and determine which objective measures can be extracted to quantify the level of activity in each case.

Electrodermal system

Electrodermal activity, also named galvanic skin response (GSR), is one of the most used physiological signal in the field of psychophysiology [19]. It consists in the measurement of the continuous variations in the conductance of the skin, which fluctuates with the state of sweat glands [58].

There are two different types of sweat glands, as illustrated in Figure 2.6: eccrine glands, which open by a duct directly onto the skin surface, and apocrine glands, which open into the hair follicles. While eccrine glands produce sweat for thermal regulation, apocrine glands are related to hormone production. Although both types are almost all over the body, the eccrine gland concentration is bigger in the feet soles, hand palms and forehead. Furthermore, the glands located in the feet soles and hand palms are more related to psychological changes rather than thermal regulation [59].

Figure 2.6 shows the basic mechanisms involved in the electrodermal activity. The extreme outer layer of the skin, the epidermis, consists of a layer that serves to protect the internal organs. Below, the dermis contains the follicles, oil glands and sweat glands. Just below the dermis is the subcutaneous fat. The eccrine sweat gland consists of a compact coiled body, which is the secretory portion of the gland, and the sweat duct, the long tube which is the excretory portion of the gland. The sweat duct remains relatively straight and opens on the surface of the skin as a small pore [60].

As noted above, human body sweating, which is predominantly cholinergic, is regulated by the ANS. More specifically, palmar sweat gland activity increases when the sympathetic branch of the ANS is highly aroused, which in turn increases skin conductance. This is directly related to the fact that in a stress situation the secretory activity of the palms increases to provide a flexible adhesive surface that facilitates tactile acuity and grip of objects [62]. Hence, the GSR is a measure of the human SNS responses, which are directly related to some mental states, such as stress. Next, the most common GSR acquisition methods are presented, along with properties inherent to the signal itself.

Measurements

There are currently two predominant methods for GSR acquisition: measuring changes in electrical potential between two electrodes placed on the skin without applying any

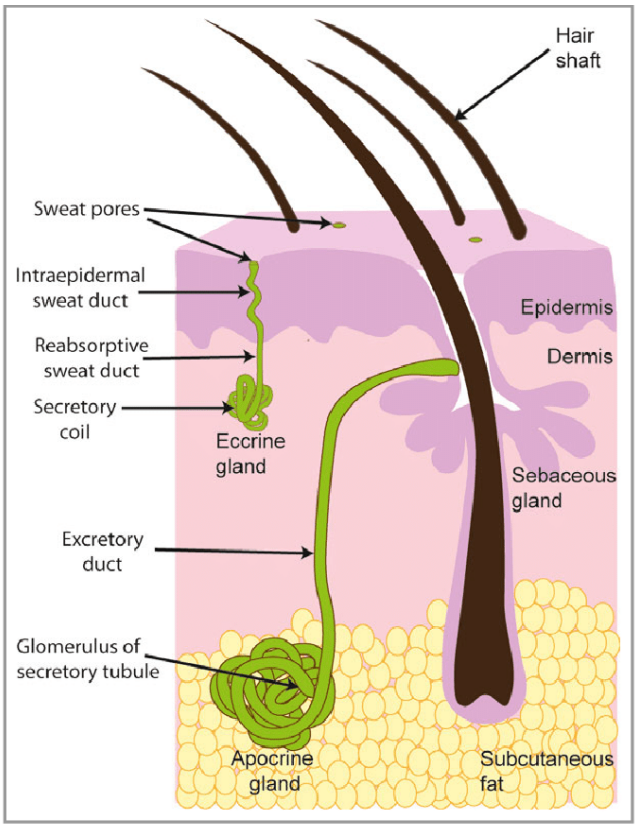

FIGURE 2.6: Anatomy of the sweat glands.
Source: Hu et al. [61]

external current as reported by Tarchanoff [63], or by applying a low electrical potential between the two electrodes [64]. Lykken and Venables [65] strongly recommend the direct measurement of skin conductance with a constant voltage system. Currently, most of the GSR recording systems on the market include constant voltage systems. Among these, there is a wide variety of new wearable healthcare devices, e.g., bracelets and watches [3]. Thus, this measure is usable in research activities, also in non-laboratory settings [7, 66, 1].

Due to the correlation between the activity of the SNS and the sweat glands of the hands, it is very common to acquire the GSR using sensors located in the palms as illustrated in Figure 2.7. It is usual to place the sensors in the distal phalanges of the non-dominant hand [19]. In this way, the dominant hand is available to carry out tasks if necessary.

In contrast to other physiological signals, GSR is cumulative. The moisture generated by sweat glands does not dissipate at the same rate at which it emanates, since it depends on the physical and environmental conditions. Therefore, under the same stress and relaxation states, the measured conductivity may vary the value depending on when the measurements are performed. Figure 2.8 illustrates this phenomenon, where the level of the GSR at the beginning and at the end of the signal (blue background) has different values, even belonging to an identical state of relaxation.

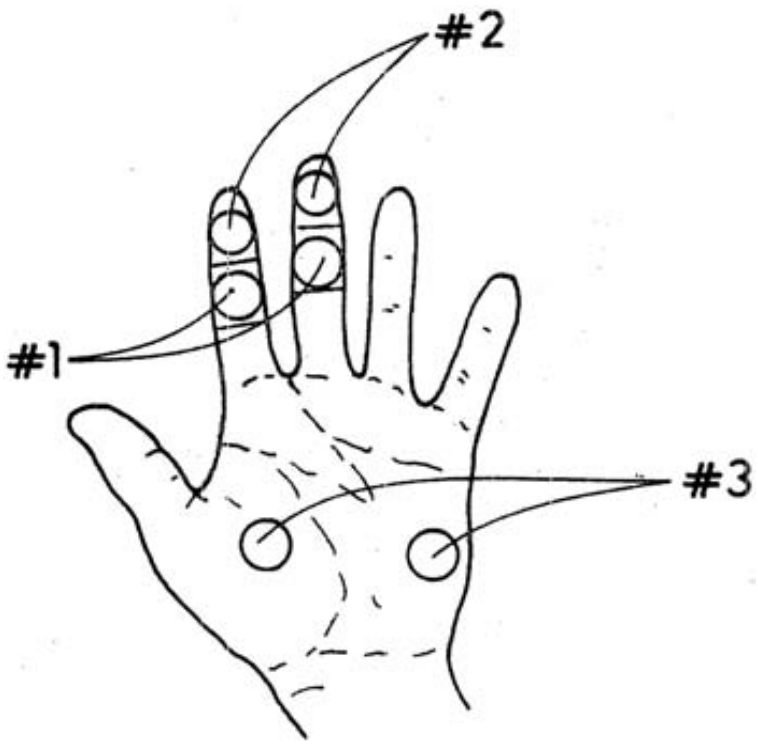

FIGURE 2.7: The three more common electrode placements for recording GSR.
Source: Cacioppo et al. [19]

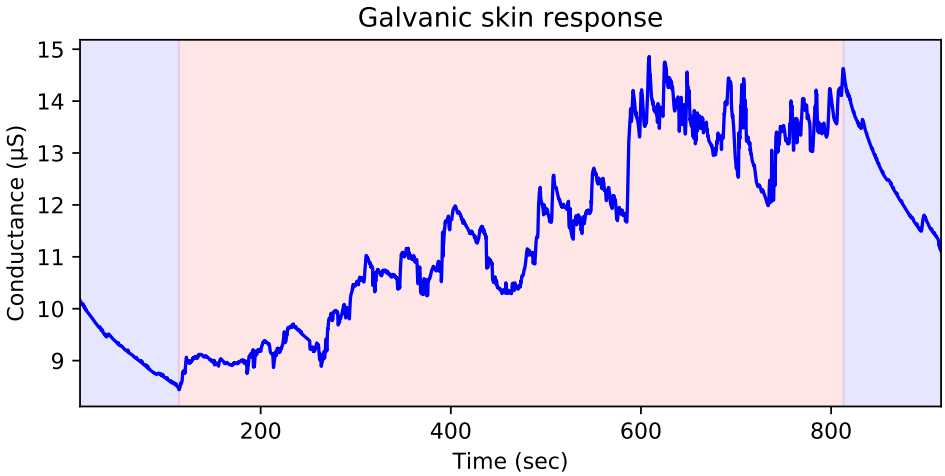

FIGURE 2.8: Electrodermal activity recorded during the relaxation-stress-relaxation stages of the experiment. Relaxation periods correspond to the blue background and stress periods to the red background.

The cumulative characteristic of the GSR signal results in the differentiation of two main components: the tonic component, that corresponds to the baseline or skin conductance level (SCL), and the phasic component, that refers to the variations around the baseline or skin conductance response (SCR) [19]. The tonic component is associated with the long-term variations of the moisture. On the contrary, the phasic component correspond to the short-term sweat bursts as a consequence of SNS activity. Thus, it is common to see a GSR

signal full of phasic components when the person goes into an alert state. This results in the following GSR features extraction.

Feature extraction

Considering the large variance in the raw GSR, it is necessary to normalize the signal both in an intrapersonal and interpersonal context. Analyzing the raw GSR, the distribution of the amplitude of the SCR and the SCL is positively skewed. Venables and Christie propose the standardization of the signal by calculating the logarithm according to equation 2.1 [67]. Figure 2.9 shows the difference between the original GSR signal in blue and the normalized GSR (GSR') in purple. After normalization, the slope of the GSR during relaxation states is equalized regardless of the level of humidity.

$$GSR' = log(GSR + 1.0) \tag{2.1}$$

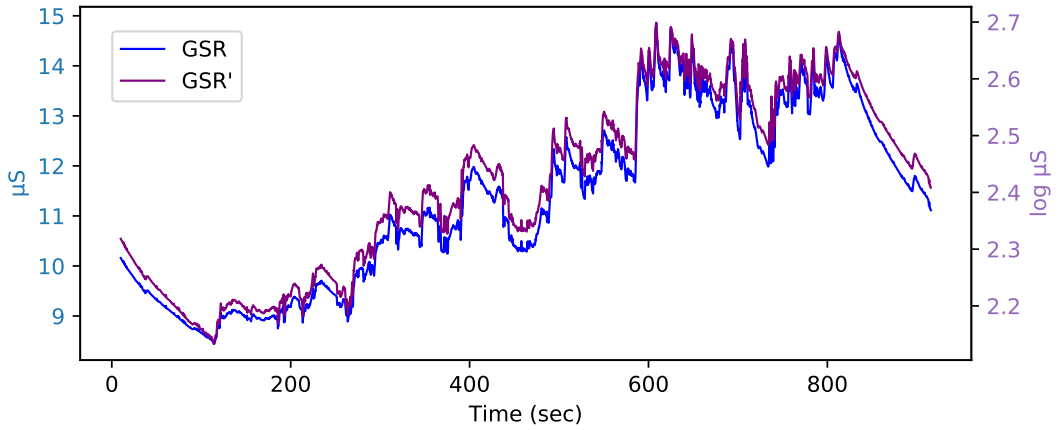

FIGURE 2.9: Electrodermal activity before (blue) and after (purple) applying equation 2.1.

Another issue is the standardization of GSR among different individuals, since signal values can vary significantly among different subjects. Lykken et al. proposed a method to fix the interindividual variance by ranging the signal between the maximum and the minimum value according to equation 2.2 [68].

$$GSR'' = \frac{GSR' - GSR'_{min}}{GSR'_{max} - GSR'_{min}} \tag{2.2}$$

The achievement of a homogeneous variance of the GSR across several individuals results in the extraction of high quality parameters for the design of generic algorithms. Typical features of the GSR are given in Table 2.1 for SCL and Table 2.2 for SCR, and shown graphically in Figure 2.10 extracted from [19].

TABLE 2.1: SCL features and definitions.

Feature	Definition
Mean SCL	Mean value of electrical conductivity of skin in a fixed window.
SCL slope	Slope of the SCL measured in a fixed window.
Standard deviation	Standard deviation of the SCL in a fixed window.
SCL amplitude	Difference between the maximum and minimum point in a fixed window.

TABLE 2.2: SCR features and definitions.

Feature	Definition
SCR frequency	Number of SCRs in a fixed window.
SCR amplitude	Phasic increase in a SCR.
SCR latency	Temporal interval between SCRs in a fixed window.
SCR rise time	Time between SCR initiation and SCR peak.
SCR half recovery time	Time between SCR peak and 50% recovery of SCR amplitude.
SCR slope	Rate of change of SCR amplitude.

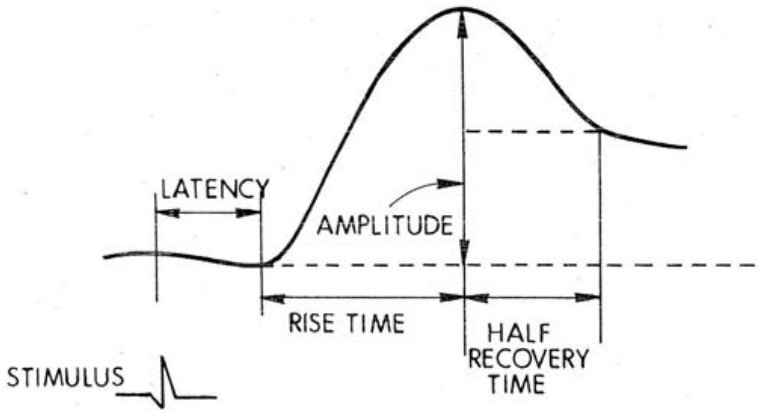

FIGURE 2.10: Graphical representation of principal GSR components.
Source: Cacioppo et al. [19]

Circulatory system

The circulatory system, also called the cardiovascular system, is essential for life. It transports nutrients through the bloodstream to every cell in the body and helps fight diseases and maintain homeostasis. It consists of the heart, which is a special cardiac muscle with properties different from skeletal muscles that pumps blood, and a closed system of vessels called veins, arteries and capillaries. While arteries are blood vessels responsible for transporting oxygenated blood from the heart to the rest of the body, the veins carry deoxygenated blood from the body back to the heart for reoxygenation. The heart provides a continuous flow of oxygen-rich blood by sending it into the lungs and then to the rest of the body, as illustrated in Figure 2.11 [19].

The cardiovascular system has a vital role in maintaining homeostasis, which depends on the continuous and controlled movement of blood through the thousands of miles of

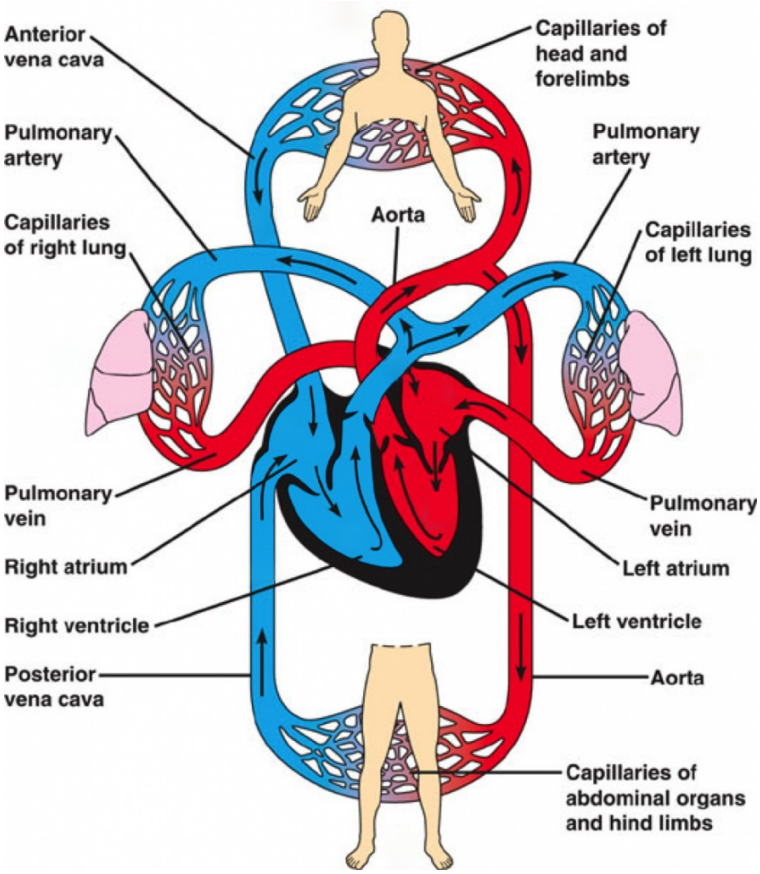

FIGURE 2.11: Body and pulmonary blood circulation scheme.
Source: quora.com (modified)

capillaries that reach every cell in the body [69]. There are numerous control mechanisms to help regulate the various tasks of the cardiovascular system that supply blood to specific areas of the body as needed. Those autoregulatory processes are associated with ANS and hormonal control [19].

The circulatory system is under control of both the sympathetic and parasympathetic branches of the ANS [19]. These control the heart period, dilatation of blood vessels and force of heart contraction and constriction [69]. Heart is partially controlled by the vagal tone, which is a fundamental component of the parasympathetic branch of the ANS that refers to the activity of the vagus nerve. While the neurons of both the sympathetic and parasympathetic system secret acetylcholine, the SNS release norepinephrine, which innervates cardiac activity [70]. The autonomic innervation of the heart is illustrated in Figure 2.12, extracted from [19].

Measurements

A wide variety of measures are used to assess the state of the cardiovascular system including cardiac cycle, blood flow, blood pressure (BP), vascular resistance and cardiac output [19].

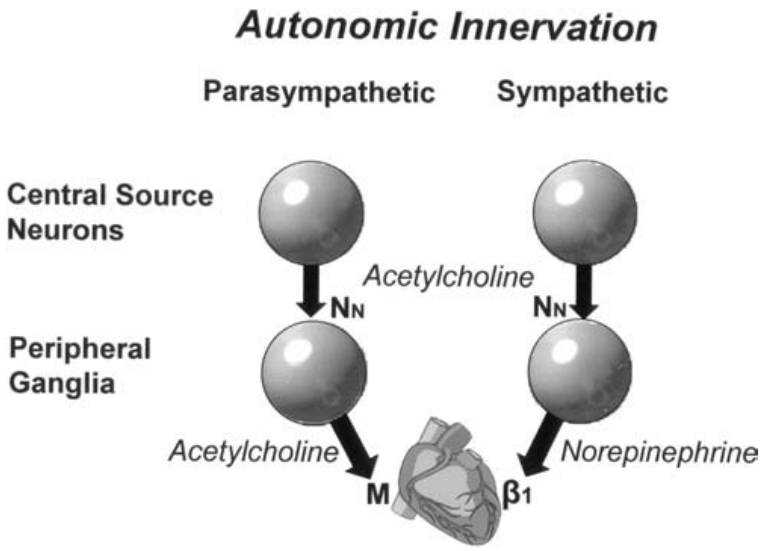

FIGURE 2.12: Scheme of the autonomic innervation of the heart.
Source: Cacioppo et al. [19]

One of the most commonly used parameter to estimate the activity of the ANS is the cardiac cycle, also known as heart period (HP), which is directly related to the sympathetic and parasympathetic branches of the ANS. This is defined as the performance of the human heart from one beat to the next. It consists of two periods: The first during the relaxation of the heart muscles, where the heart refills with blood (diastole). This is followed by a second period of robust contraction and pumping of blood (systole) [71]. This phenomenon is illustrated in the Wiggers diagram in Figure 2.13, which includes a graphic representation of various cardiovascular measures commonly used in the field of cardiac physiology.

There are different methods for the extraction of the HP, all based on the detection of events related to the appearance of beats in cardiovascular records. The most commonly used signals to perform this task are the electrocardiogram (ECG), BP and blood volume records, which not only include the HP but are also analysed to detect a wide variety of heart diseases [72, 73].

An important disadvantage of BP measurements is the limited acquisition time. The recording usually takes a few seconds. Furthermore, it is necessary to apply an external pressure to the body limb where the measurement is performed, which makes it an invasive method. To achieve a continuous monitoring and avoid the external invasive pressure, the assessment of blood volume based on a plethysmographic acquisition is among the most used methods for non-invasive acquisition [74].

Below, the main non-invasive techniques used in the acquisition of the ECG and the plethysmography, which are normally used in continuous monitoring, are presented.

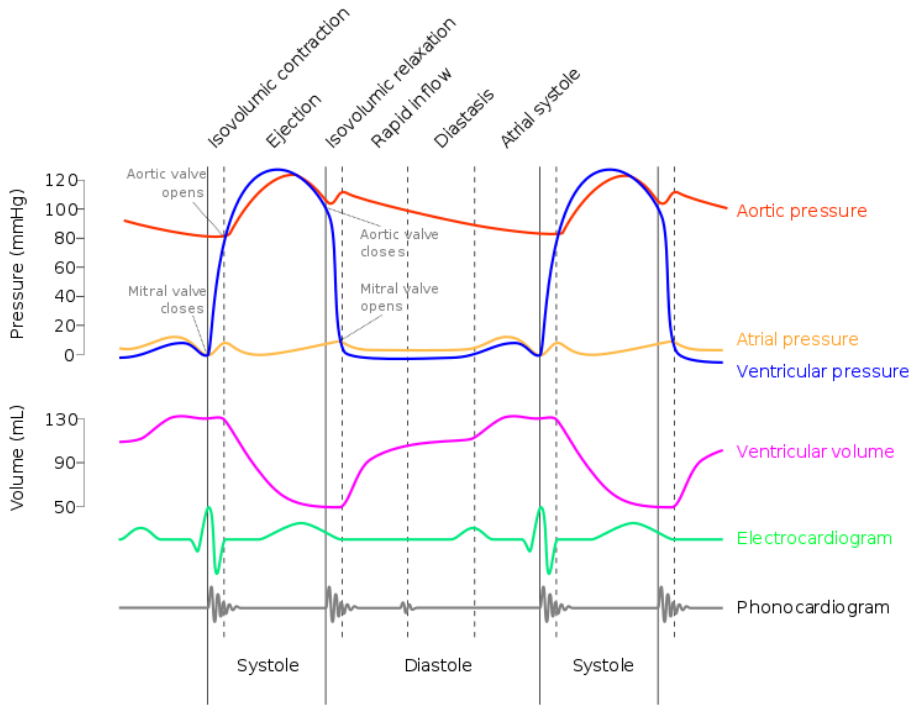

FIGURE 2.13: A Wiggers diagram showing the cardiac cycle events.
Source: Wikimedia (modified)

Electrocardiogram

Each heartbeat is caused by an electrical impulse that is normally generated in specialized cells of the upper right heart cavity (sinoatrial node cells). The ECG is a signal that records this electrical activity during the myocardial contraction of the heart [75, 76]. It is frequently used to detect heart problems and monitor the heart status in many situations. The electrical activity is measured from the patient's body surface using a set of electrodes.

The ECG is normally represented by the "standard 12-lead ECG", which gathers information from 12 different areas of the heart. Commonly, a total of 10 electrodes are used to form the 12 leads, as shown in Figure 2.14. The electrodes are placed on the skin of the chest and sometimes the limbs. Electric activity is recorded as waves on a graph, with different patterns corresponding to each electrical phase of the heartbeat [76]. An example of this type of graph is illustrated in Figure 2.15.

Among the most used non-invasive electrode configuration, the Einthoven's triangle stands out, which is illustrated in Figure 2.16. By convention, electrodes are located on the left arm (LA), right arm (RA) and left leg (LL). Even so, it can also be placed closer to the heart if necessary, around the chest, maintaining the same configuration with the heart at the centre.

In total, the following three leads are distinguished [77]:

- Lead I goes from the RA to the LA, with the negative electrode placed on the right

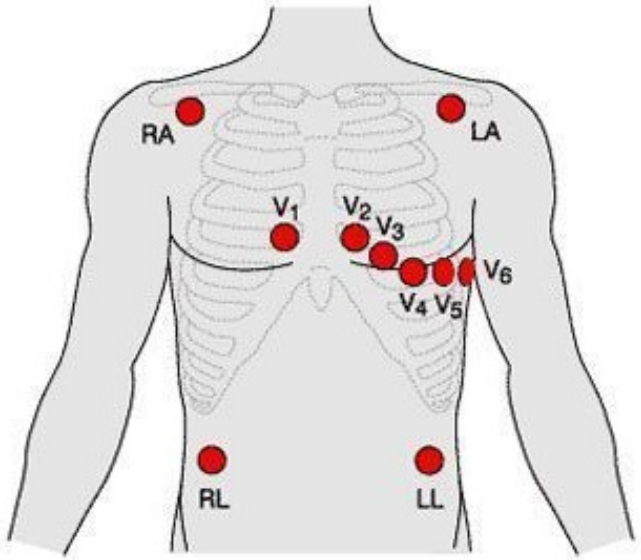

FIGURE 2.14: Location of the 10 electrodes in a standard 12-lead ECG.
Source: pinterest.com

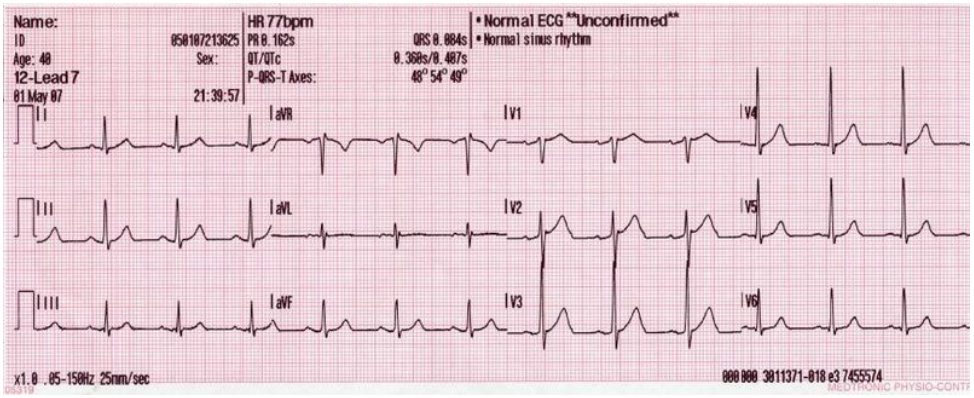

FIGURE 2.15: A standard 12-lead ECG example.
Source: Wikipedia

shoulder and the positive electrode placed on the left shoulder. It is calculated according to equation 2.3.

$$I = LA - RA \tag{2.3}$$

- Lead II goes from the RA to the LL, with the negative electrode on the right shoulder and the positive one on the LL. It is calculated according to equation 2.4.

$$II = LL - RA \tag{2.4}$$

- Lead III goes from the LA to the LL, with the negative electrode on the left shoulder and the positive one on the LL. It is calculated according to equation 2.5.

$$III = LL - LA \tag{2.5}$$

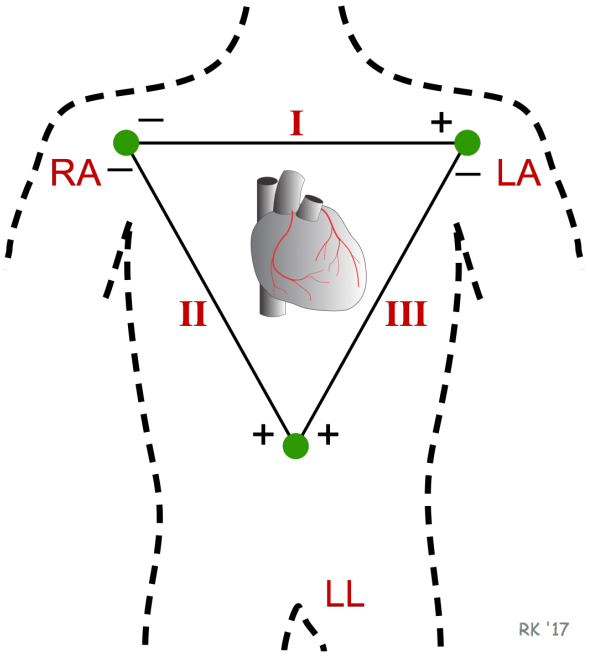

FIGURE 2.16: Einthoven's triangle.
Source: Klabunde [78]

For normal heart function, the ECG signal has the characteristic shape shown in Figure 2.17, where each heartbeat is composed of PQRST complexes. The R-peak located in the QRS complex is the most characteristic waveform and is usually employed as a reference for the heartbeat position [76]. The R-R interval extracted from two consecutive heartbeats corresponds to one HP.

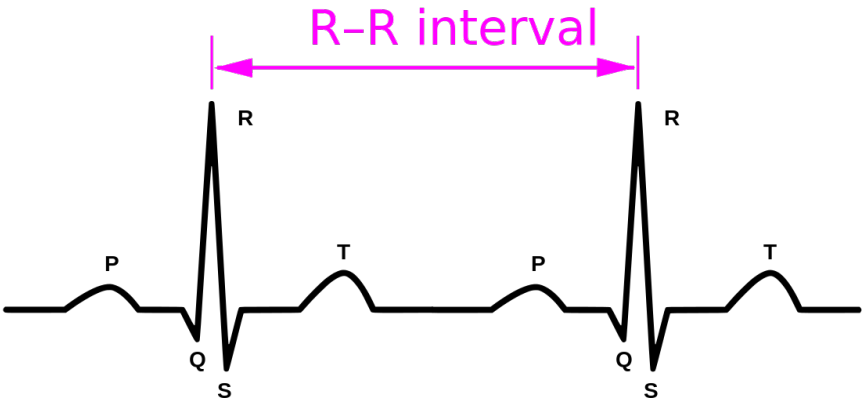

FIGURE 2.17: R-R interval measured between two PQRST complexes.
Source: kindpng.com

Numerous algorithms for ECG analysis based on different computing techniques have been developed during the last decades [79]: artificial neural networks [80], support vector machines [81], Hilbert transform [82], genetic algorithms [83], digital filters [84, 85, 86, 87, 88], k-means [89], wavelets [90, 91, 92, 93, 94, 95, 96], derivatives [97, 98], combined threshold methods [99] and moving averaging methods [100], among others.

Plethysmography

Plethysmography is defined as the measurement of volume changes in an organ or the entire body. Several techniques are used for the non-invasive analysis of the venous system. One of the most used is photoplethysmography (PPG). PPG is based on the use of a transducer, that emits infrared light from a led into the dermis, and a photodetector, that measures the scattered light and displays it as a line tracing. The amount of scattered light varies with the red blood volume [101].

Among the different measurements, finger PPG is a non-invasive method to record changes in blood flow. [102]. The pulsatile blood supply comes from the radial and ulnar artery over the palmar arch. The venous return is an almost laminar flow. The light is partly absorbed by arterial blood, which changes according to the heart activity. The photodetector receives the non-absorbed light on the other side of the finger and therefore produces a continuous pulse signal as illustrated in Figure 2.18.

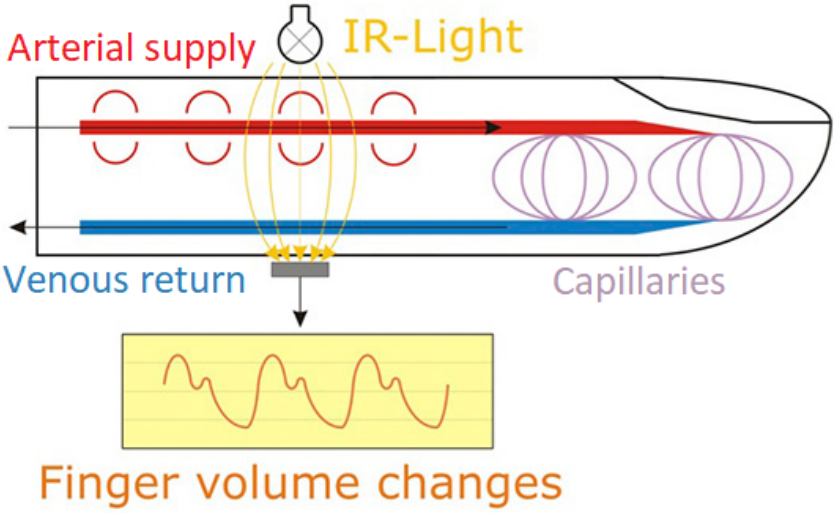

FIGURE 2.18: Finger PPG measurement scheme.
Source: cnsystems.com (modified)

The most commonly used reference to measure the HP in plethysmographic signals, as well as BP signals, is the foot point [103, 104]. From these, the foot to foot interval (F-F interval) is calculated as illustrated in Figure 2.19, which is equivalent to the HP measurement.

Several approaches have been proposed to locate foot points in both plethysmographic and BP signals, such as those reported in Kazabicus et al. [104]. Some of those methods include the bottom straight-line and forefront tangent intersection method, the second derivative maximum method, the wave foot polynomial approximation method and the tangent intersection foot-to-foot method, among others. For these methods, accuracy of the foot point estimation decreases proportionally to the signal-to-noise ratio.

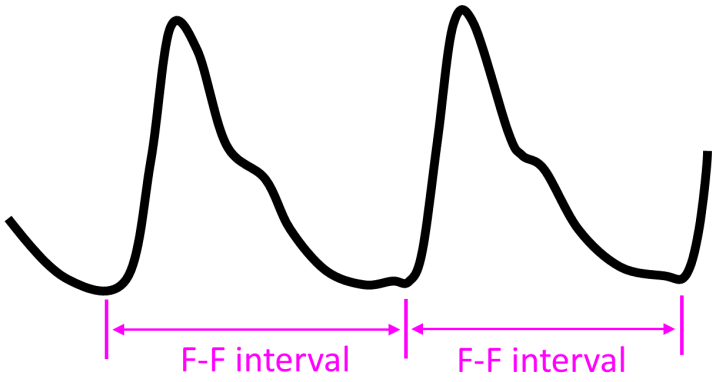

FIGURE 2.19: F-F interval measures in a plethysmographic signal.

Feature extraction

From previously extracted heartbeat references, both the R-R interval and the F-F interval are used to calculate the HP according to equations 2.6 and 2.7, respectively. *rpeaks* and *fpoints* correspond to the location on the temporal axis of the detected R-peaks and foot points, respectively. Figure 2.20 illustrates an example of the HP extracted from an ECG record.

$$HP_i = rpeaks_{i+1} - rpeaks_i \tag{2.6}$$

$$HP_i = fpoints_{i+1} - fpoints_i \tag{2.7}$$

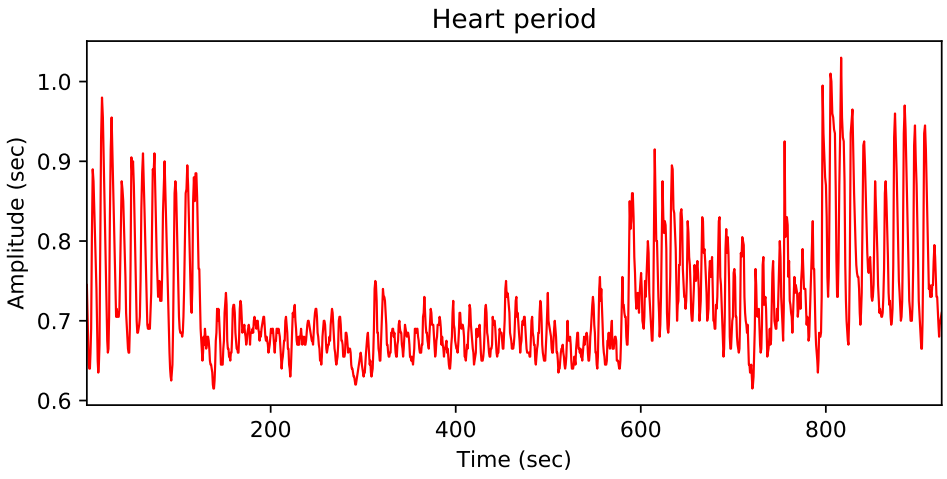

FIGURE 2.20: HP extracted from an ECG signal.

Traditionally, HP (in seconds) is generally converted to heart rate (in beats/minute or bpm). Those two parameters are not linearly related to each other. Berntson et al. [105] reviewed literature showing that the relationship between changes in the activity of the sympathetic and parasympathetic branches of the ANS and HP are more nearly correlated.

Heart rate variability (HRV) is also widely used in cardiovascular psychophysiology and is calculated according to equation 2.8. It represents the variation in the time interval between consecutive heartbeats. This phenomenon is illustrated in the top graph in Figure 2.21. HRV is reported to be an index of the influence of both the SNS and PNS. The parasympathetic influence is mediated by the release of acetylcholine by the vagus nerve, which is reflected in the high frequency band of HRV. The sympathetic influence, in contrast, is mediated by the release of norepinephrine and epinephrine reflected in the low frequency band of HRV as illustrated in the bottom graph in Figure 2.21 [106].

$$HRV_i = HP_{i+1} - HP_i \tag{2.8}$$

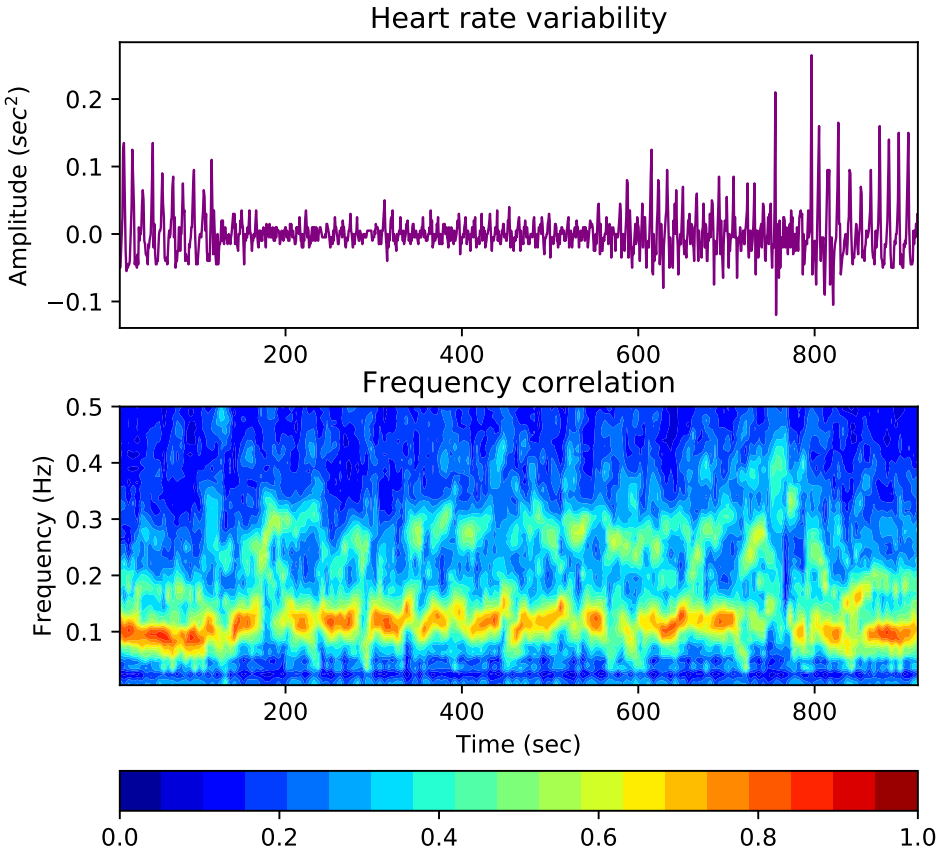

FIGURE 2.21: HRV obtained from previously calculated HPs (top graph) and the corresponding frequency correlation (bottom graph).

A wide range of parameters have been developed to assess a measure of HRV, including temporal-domain, frequency-domain and nonlinear metrics illustrated in Tables 2.3, 2.4 and 2.5, respectively [107, 108, 109].

Respiratory system

In psychophysiology, the respiratory system is often underestimated, but is remarkably complex and sensitive to a variety of psychological states. It consists on a series of organs

TABLE 2.3: HRV temporal-domain features and definitions.

Feature	Definition
SDNN	Standard deviation of the HP intervals.
SENN	Standard error of the mean, is an estimate of the standard deviation of the sampling distribution of means.
SDSD	Standard deviation of differences between adjacent HP intervals.
RMS	Root mean square of the HP intervals.
RMSSD	Square root of the mean squared successive HP differences.
IRRX	Irregularity index, which is the standard deviation divided by mean HP lying between the a^{th} and b^{th} percentile.
NN50	Number of successive differences of HPs which differ by more than 50ms.
pNN50	NN50 divided by the total number of HPs.

TABLE 2.4: HRV frequency-domain features and definitions.

Feature	Definition
HF	HRV power spectrum high frequency band (0.15 – 0.4Hz).
LF	HRV power spectrum low frequency band (0.04 – 0.15Hz).
VLF	HRV power spectrum very low frequency band (0.0033 – 0.04Hz).
ULF	HRV power spectrum ultra low frequency band (<0.0033Hz).

TABLE 2.5: HRV nonlinear features and definitions.

Feature	Definition
SD1	First standard deviation of the Poincaré plot, is related to the fast HP variability.
SD2	Second standard deviation of the Poincaré plot, is related to the long-term HP variability.

responsible for inhaling oxygen and exhaling carbon dioxide as illustrated in Figure 2.22. The primary organs of the respiratory system are the lungs, which consist of a pair of air-filled organs located on either side of the thorax. The trachea conducts inhaled air into the lungs through its tubular branches, called bronchi. The bronchi are divided into smaller and smaller branches, called bronchioles. The bronchioles eventually end in clusters of microscopic air sacs called alveoli [110].

The lungs work together with the circulatory system to pump oxygenated blood to all cells in the body. The blood, then, collects carbon dioxide and other waste products and transports them back to the lungs according to the previously shown in Figure 2.11.These materials are finally pumped out of the body when the person exhales [111].

The breathing or respiratory action (RSP) is partially influenced by the sympathetic and parasympathetic branches of the ANS and affects many other systems of the body [112]. It is mostly coupled to the cardiac output, changing heart period as a function of the respiratory cycle. This phenomenon is called respiratory sinus arrhythmia and is closely related to the cardiovascular system. In fact, the degree of dissociation between RSP and heart period is often used as an index of the vagal control of the heart [113].

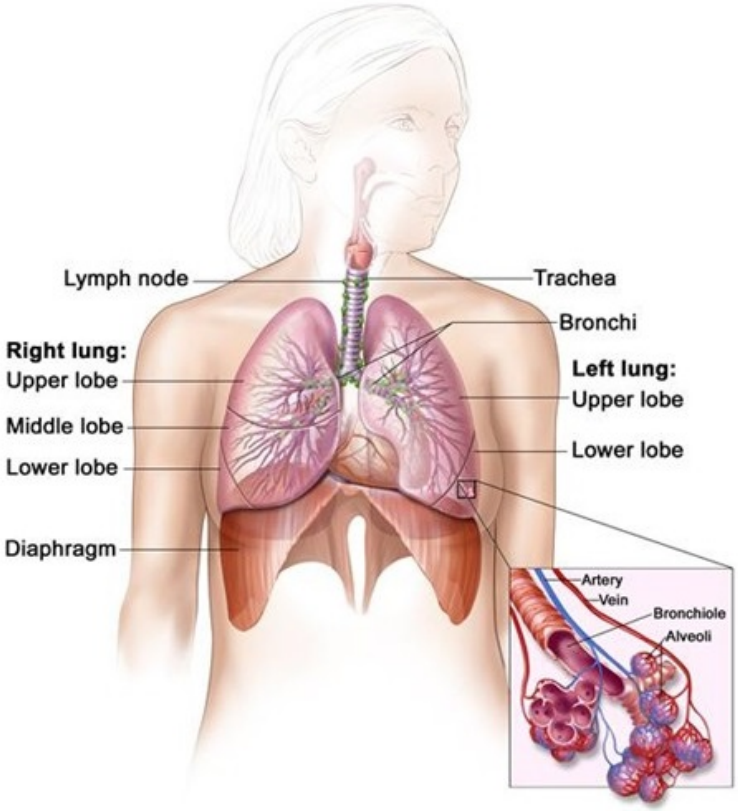

FIGURE 2.22: Anatomy of the respiratory system.
Source: Wikimedia

Measurements

Almost all measurements of lung function in medical settings are made using spirometry. The problem with this technique is that the patient is usually nose clipped and breathes through a tube placed into the mouth, which is psychologically invasive because it often centers the subject's attention on the process of breathing [114].

In research, it is common to use a respiratory belt to assess a continuous measurement of the volume of the thorax while the tasks of interest are performed. This method has the advantage of not invading the psychological dimensions of the task [19]. Nowadays, the most commonly used respiratory belt consists of a piezoelectric device. These are robust electromechanical systems that react to compression, providing reliable signals that can be incorporated into most electrophysiological recording systems. Figure 2.23 shows the placement in the chest of a common piezoelectric belt.

Piezoelectric sensors show almost zero deflection, giving an excellent linearity over a wide range of amplitude. As the subject inhales air, the volume of the chest increases and consequently stretches the device. The opposite occurs when exhaling air, resulting in the signal plotted in Figure 2.24.

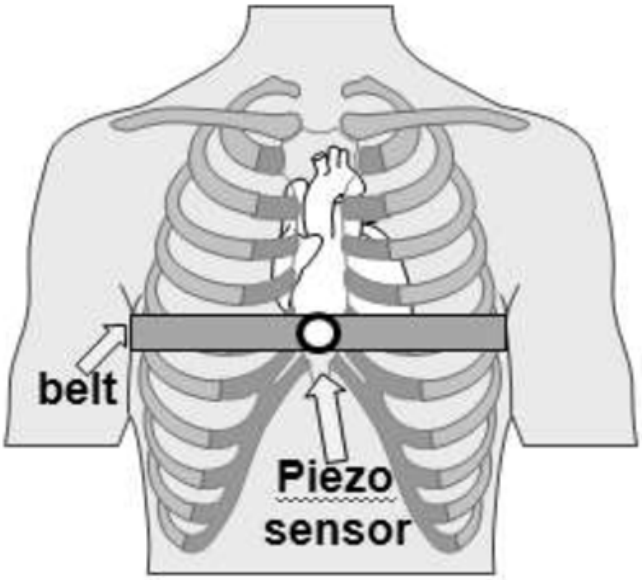

FIGURE 2.23: Piezoelectric belt placement.
Source: Bifulco et al. [115]

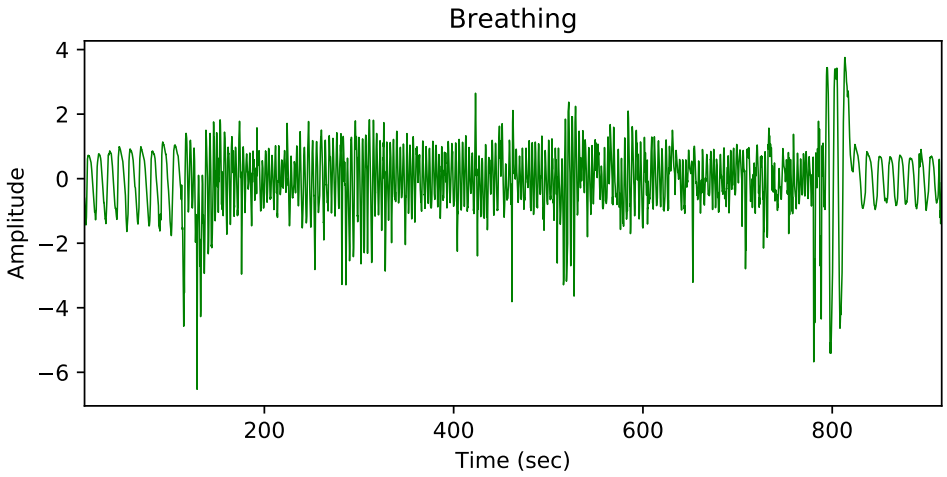

FIGURE 2.24: RSP signal recorded using a piezoelectric belt

Feature extraction

The extraction of features is mainly based on the analysis of the inspiration and exhalation periods. Exhalation peak is defined as the minima of the RSP waveform between two cycles and is labeled as “a” on the graph in Figure 2.25, extracted from [19]. Inspiration peak is the maxima and is labeled as “b.”

Table 2.6 shows the main parameters extracted from RSP, in which the respiratory rate in addition to the inspiration/exhalation volume and period are studied [19]. Furthermore, the frequency components of the signal have also been considered.

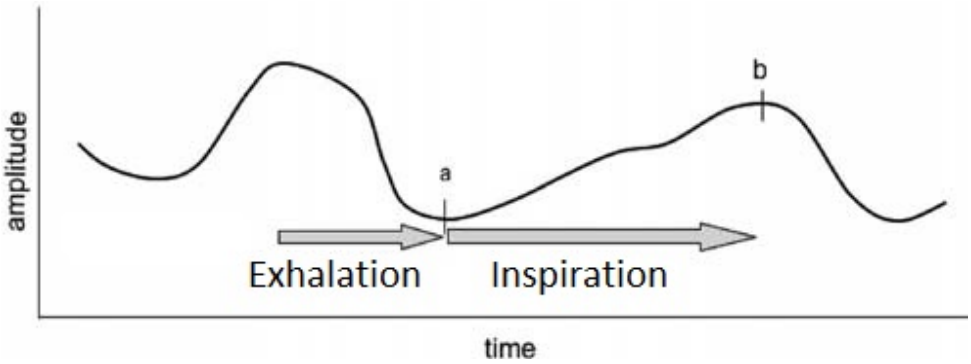

FIGURE 2.25: Inspiration and exhalation representation in a RSP signal extracted from a piezoelectric belt transducer.
Source: Cacioppo et al. [19]

TABLE 2.6: Features extracted from a RSP signal and definitions.

Feature	Definition
Breathing rate	Number of peaks per minute in a fixed window.
Inspiratory volume	Integration of the breathing signal during inspiration.
Expiratory volume	Integration of the breathing signal during exhalation.
Inspiration/Exhalation ratio	Relation between inspiration and exhalation volume.
Inspiratory duration	Duration of the inspiration.
Exhalatory duration	Duration of the exhalation.
Duration ratio	Relation between inspiration and exhalation duration.
Complexity	Spectral analysis combined with examination of the amplitudes of nondominant frequencies.

2.2 Soft computing

Soft computing is a field of artificial intelligence that includes methodologies based on ideas inspired by biology, psychology and linguistics to find solutions to problems with incomplete, uncertain or inaccurate information. These problems are characterized by the need to interact efficiently with complex systems when the available information is not enough. Soft computing is commonly used to control, analyze, and model complex systems, such as communications, robotics and healthcare applications. The scheme in Figure 2.26 illustrates the techniques and methods used throughout this thesis.

To present the algorithms used for the development of this thesis, subsection 2.2.1 focuses on the principal component analysis technique, implemented to reduce parameter dimensionality. In subsection 2.2.2, semi-supervised pseudo-labeling techniques are introduced, applied to carry out a continuous labeling of the records. Finally, subsections 2.2.3, 2.2.4 and 2.2.5 describe the algorithms used to carry out the predictions, i.e., fuzzy logic algorithm, fuzzy rule-based supervised learning methods and artificial neural networks.

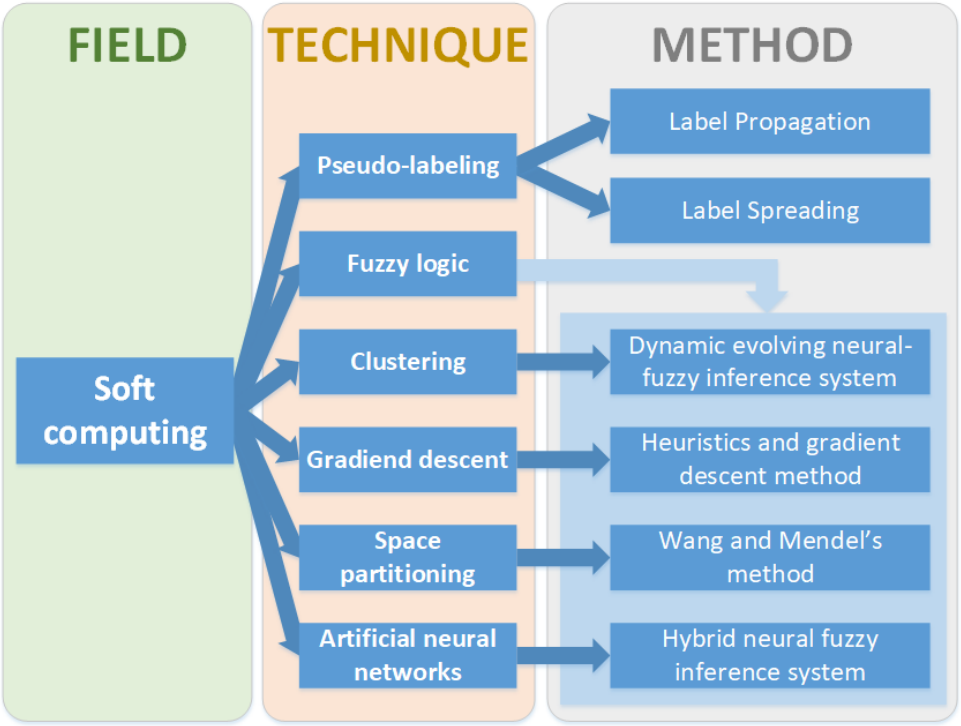

FIGURE 2.26: Schematic representation of the soft computing techniques and methods used throughout this thesis.

2.2.1 Principal component analysis

Principal component analysis (PCA) is a statistical technique used to identify the underlying dependencies of a data set. This technique significantly reduces the dimensionality of the data set by finding a new set of uncorrelated variables, smaller than the original one. PCA is commonly used for the compression of input data when there is redundancy due to the correlation of multiple features. During the process, most of the sample information is retained. The new set of uncorrelated variables, called principal components (PCs), should be able to explain most of the variance of the original variables [116]. Figure 2.27 depicts each step of the PCA that is explained in detail below.

Since PCA is frequently employed to reduce a multivariate data set while maintaining most of the information of the original data, it can also be implemented as a preprocessing approach of a soft computing method. However, since this process is irreversible, the reduction of the data should be done only for the inputs and not for the target variables.

1. *Subtraction of the mean from the data*

   In this first step, the mean ($\overline{x}$) is subtracted to each sample in the data set ($x^{(i)} = \{x_1^{(i)}, x_2^{(i)}, \ldots, x_p^{(i)}\}$) to carry out the normalization. Mean value is calculated according to equation 2.9, where n is the number of examples for a given data set. This results in a shift of data in all its dimensions, which now has an average of zero. The graph in Figure 2.28 shows the resulting normalized data for a hypothetical two-variable (x_1 and x_2) data set.

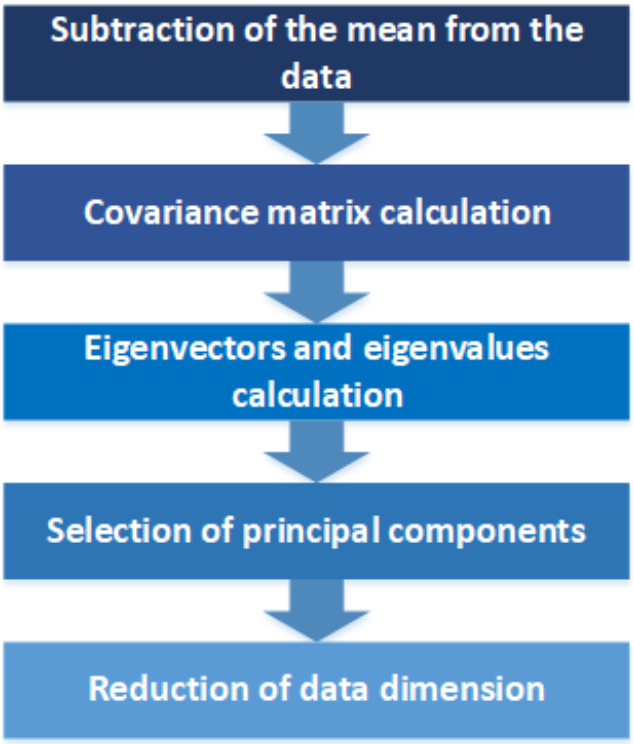

FIGURE 2.27: Steps of the PCA.

$$\overline{x} = \frac{1}{n}\sum_{i=1}^{n} x^{(i)} \tag{2.9}$$

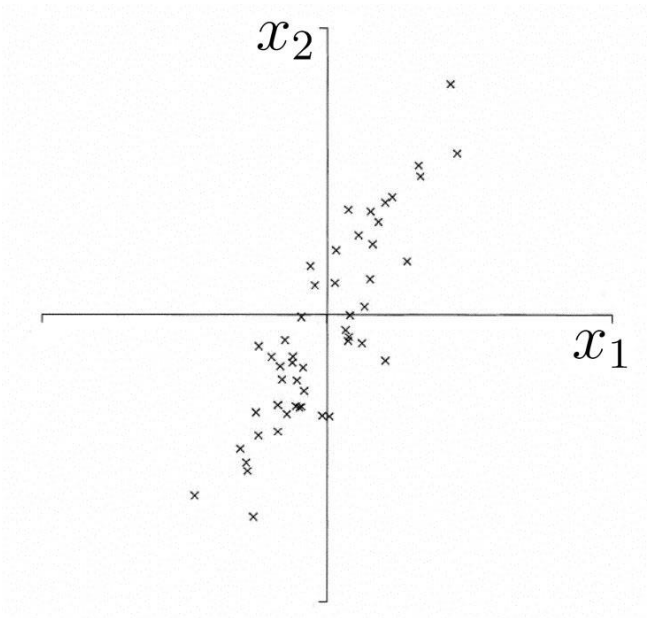

FIGURE 2.28: A two-variable random data set after mean subtraction.

2. *Covariance matrix*

The variance is a measure of the dispersion that represents the variability of the

data in relation to its mean. The covariance, however, is a measure that reflects the degree of combined variation of two different variables in relation to their respective means according to equation 2.10.

$$\Sigma_{jk} = \frac{1}{n}\sum_{i=1}^{n}\left(x_j^{(i)} - \overline{x}_j\right)\left(x_k^{(i)} - \overline{x}_k\right)^T \tag{2.10}$$

The resulting matrix is used to determine the linear dependencies between the different features to later reduce the dimensionality of the data set. The values corresponding to the diagonal of the covariance matrix represent the variance of each variable. Besides, the off-diagonal values represent the covariance between each pair of variables. If the covariance is positive for a given pair of variables, the value of both increase and decrease together, but if it is negative, then when the value of one variable increases the value of the other decreases, and vice versa.

3. *Eigenvectors and eigenvalues*

   Eigenvectors represent a particular case of multiplication between a matrix and a vector, resulting in a multiple of the original vector whose direction remains unchanged. The length of the vector can not remain the same after the transformation, which results in a factor called eigenvalue. Each eigenvector has an eigenvalue associated with it.

   Eigenvectors represent the directions in which the data has more variance and eigenvalues determine the amount of variance that the data set has in that direction. The number of eigenvectors or PCs that can be calculated for each data set is equal to the dimension of the data set.

   Let v be a vector and λ a scalar that satisfies $\Sigma v = \lambda v$, then λ is the eigenvalue associated with the eigenvector v of square matrix A. The eigenvalues of A are roots of the characteristic equation 2.11, where I is the identity matrix.

$$\det(A - \lambda I) = 0 \tag{2.11}$$

   Eigenvectors are subsequently calculated according to equation 2.12 once eigenvalues have been calculated. For each eigenvalue λ, we have:

$$(A - \lambda I)x = 0 \tag{2.12}$$

   where x is the eigenvector associated with eigenvalue λ.

   According to the two-variable example of the graph in Figure 2.29, the vector that determines the first PC (z_1) is the one that has the direction in which the observations have the largest variance. The projections of the observations on that direction correspond to the values of the first PC.

The second PC (z_2) also looks for a maximum variance, satisfying the condition of not being correlated with the first PC. The non-correlation between the PCs means that they are orthogonal to each other.

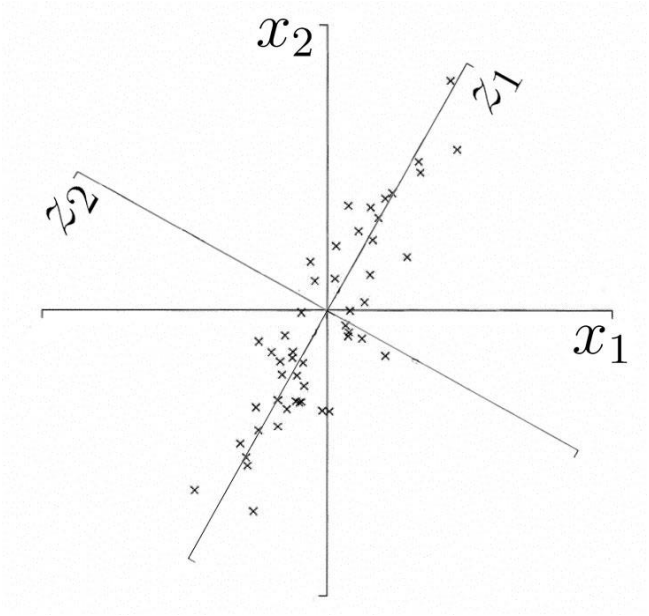

FIGURE 2.29: Eigenvector (or PC) representation.

4. *Principal components*

To carry out the reduction of the number of variables, it is necessary to perform a selection of the main eigenvectors, also known as PCs. The selection criterion is based on the amount of information that must be retained from the original data set, which is usually defined as a percentage. This criterion requires the definition of the cumulative explained variance (π) according to equation 2.13, which depends on the total variance of the data set (denominator) and the sum of the relative variance of each eigenvector up to the desired number of PCs (k) (numerator). The variance is determined by the eigenvalues, where p is the total number of eigenvalues/eigenvectors. The graph in Figure 2.30 shows an example of the cumulative explained variance depending on the number of PCs.

$$\pi_k = \frac{\sum_{i=1}^{k} \lambda_i}{\sum_{j=1}^{p} \lambda_j} \cdot 100 \ \ (\%) \tag{2.13}$$

A common way to select the number of PCs is to establish the amount of information that needs to be kept, considering that if the selected number of PCs decreases, the amount of saved information will be also reduced.

5. *Reduction of data dimension*

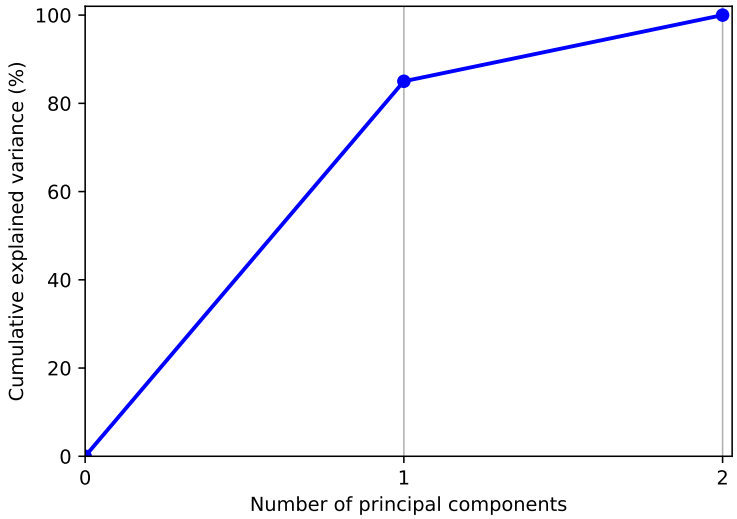

FIGURE 2.30: Cumulative variance chart.

Once the desired number of PCs is selected, the data is projected through the projection matrix (W) according to equation 2.14, where W is constructed from the eigenvectors selected in the previous step. The variance information lost during this process due to discarded components is irreversible, which means that the original data can not be recovered from the projection.

$$x^{(i)'} = x^{(i)} \cdot W \tag{2.14}$$

2.2.2 Pseudo-labeling

Pseudo-labeling is a branch of semi-supervised learning commonly used to classify the samples of a partially labeled data set. Among the most used methods, label propagation and label spreading stand out. The difference between both lies in the design of the transition matrix. Label propagation uses the graph Laplacian matrix while label spreading uses a modified version of the original graph and normalizes the edge weights by computing the normalized graph Laplacian matrix.

To further introduce both methods, N labeled points (denoted by -1 and +1) and M unlabeled points (denoted by 0) will be considered, being a sample label $y^{(i)} \in -1, +1, 0)$. The data set is defined according to equation 2.15. $G = \{V, E\}$ is the undirected graph based on a measure of geometric affinity among samples, where $V = v^{(1)}, v^{(2)}, \ldots, v^{(N+M)}$ is the set of vertices. Each vertex $v^{(i)}$ corresponds to a unique data point $x^{(i)}$. Further, each edge $(v_{(i)}, v_{(j)}) \in E$ of this graph is associated with a non-negative weight $w_{ij} \geq 0$, which measures the similarity between the nodes $v_{(i)}$ and $v_{(j)}$, and is computed using an appropriate kernel function. The affinity matrix $W = (w_{ij})_{i,j=1,2,\ldots,N+M}$ depends only on the sample values denoted by X, not on the labels. The graph in Figure 2.31 illustrates an example of a partially labeled data set with the corresponding affinity parameters [117].

$$\begin{cases} X = \{x^{(0)}, x^{(1)}, \ldots, x^{(N)}, x^{(N+1)}, \ldots, x^{(N+M)}\} \text{ where } x^{(i)} \in \mathbb{R}^k \\ Y = \{y^{(0)}, y^{(1)}, \ldots, y^{(N)}, 0, 0, \ldots, 0\} \text{ where } y^{(i)} \in \{0, +1, -1\} \end{cases} \tag{2.15}$$

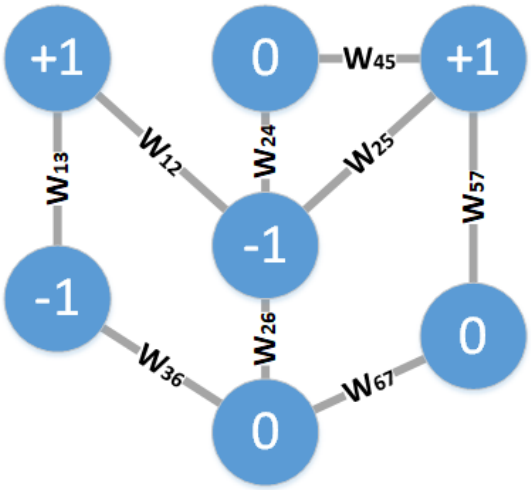

FIGURE 2.31: Example of a partially labeled data set with the corresponding affinity parameters. Labeled data is denoted by -1 and +1 and unlabeled data by 0.

Label propagation

Label propagation belongs to the family of semi-supervised algorithms based on a graphical representation of the data set. The basic principle behind the label propagation algorithm is that a single label can rapidly become dominant in a group of densely connected nodes. In contrast, labels will have trouble crossing sparsely connected areas. [118]. Densely connected groups of nodes will end up with the same label, being considered part of the same community as illustrated in Figure 2.32.

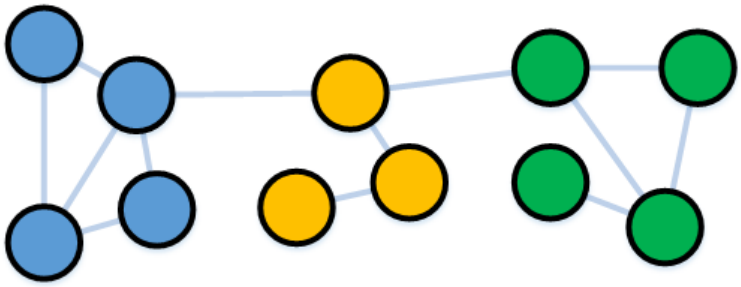

FIGURE 2.32: Connected group of nodes. Each color represents a label.

An interesting feature of label propagation is the possibility of assigning preliminary labels to the nodes. This fact provides the algorithm with clues to generate the groups, reducing the range of available solutions. Consequently, it allows the manual selection of some initial communities so that the rest of the communities can be found by means of a semi-supervised procedure.

As proposed by Zhu and Ghahramani [119], the steps of the label propagation algorithm are represented in the schematic in Figure 2.33, which are introduced below.

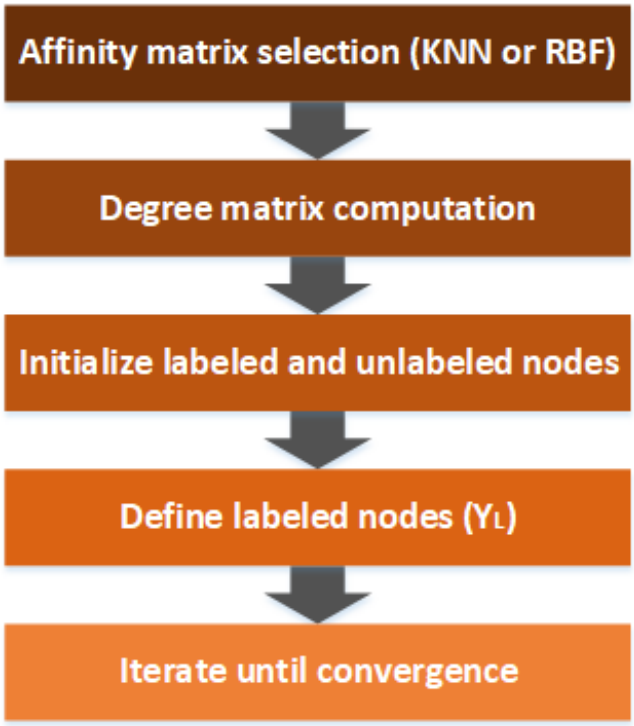

FIGURE 2.33: Steps of the label propagation algorithm.

1. *Affinity matrix selection*

   The affinity matrix is generally a square, symmetric matrix, whose dimensions have a size of $N+M$. The two most common methods used to obtain the weights of the affinity matrix are the K-nearest neighbors (kNN), according to equation 2.16, and the radial basis function kernel, according to equation 2.17.

$$w_{ij} = \begin{cases} 1 & \text{if } \; x^{(i)} \in kNN\left(x^{(j)}\right) \\ 0 & \text{otherwise} \end{cases} \tag{2.16}$$

$$w_{ij} = e^{-\gamma \| x^{(i)} - x^{(j)} \|^2} \tag{2.17}$$

2. *Degree matrix computation*

   To describe the basic label propagation algorithm, it is necessary to introduce the degree matrix (D), which is a diagonal matrix where each non-null element represents the degree of the corresponding vertex according to equation 2.18.

$$D = diag\left(\left|\sum_j w_{ij}\right| \;\; \forall \;\; i = 1 \,..\, N+M\right) \tag{2.18}$$

3. *Initialize labeled and unlabeled nodes* $\rightarrow Y^{(0)}$

This step refers to the initialization of Y at $t = 0$ according to the partially labeled and unlabeled nodes according to equation 2.19, where Y was previously defined in 2.15.

$$Y^{(0)} = Y = \{y^{(0)}, y^{(1)}, \ldots, y^{(N)}, 0, 0, \ldots, 0\} \tag{2.19}$$

4. *Define labeled nodes* $\rightarrow Y_L$

   The labeled nodes correspond to a subsection of Y, which contains only the nodes with defined labels as follows:

$$Y_L = \{y^{(0)}, y^{(1)}, \ldots, y^{(N)}\} \tag{2.20}$$

5. *Iterate until convergence*

   At every iteration, a propagation step is performed with both labeled and unlabeled data according to 2.21. The first command of 2.21 spreads each label from a node across its outgoing edges. For this purpose, the affinity matrix, which is normalized by the degree matrix, increases or decreases the effect of each weight. The second command of 2.21 resets all labeled samples to their original value to avoid changing the predefined labels.

$$\begin{cases} \tilde{Y}^{(t+1)} = D^{-1} W \tilde{Y}^{(t)} \\ \tilde{Y}_L^{(t+1)} = Y_L \end{cases} \tag{2.21}$$

   The algorithm reaches convergence when each node has the majority label of its neighbours. It stops when convergence is achieved or the maximum number of iterations defined by the user is reached. The final labels are obtained according to equation 2.22 (this equation is only applicable if the labeling is binary).

$$Y_{Final} = sign\left(\tilde{Y}^{(t_{end})}\right) \tag{2.22}$$

Label spreading

Label spreading algorithm was first proposed by Zhou et al. [120] and is closely related to label propagation algorithm. The steps of the label spreading algorithm are represented in the schematic in Figure 2.34, where steps 1, 2 and 4 are identical to steps 1, 2 and 3 of label propagation. In addition, label spreading uses the standardized Laplacian graph in step 3 defined in equation 2.23.

$$\mathscr{L} = D^{-1/2} W D^{-1/2} \tag{2.23}$$

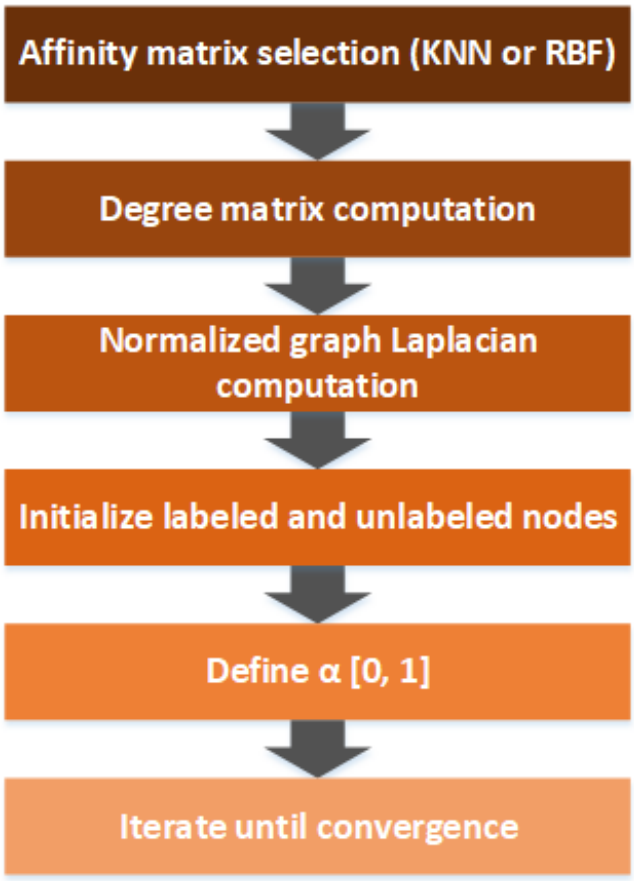

FIGURE 2.34: Steps of the label spreading algorithm.

Below, the additional steps 5 and 6 are presented. These stand out as the major difference between this method and label propagation.

1. *Define α*

   Label spreading includes a clamping factor α for the labeled samples. If $\alpha = 0$, the algorithm will always reset the labels (Y_L) to the original values (as in label propagation). If alpha is in the range (0, 1], the percentage of labels that are reset to their original values decreases progressively until $\alpha = 1$, where no labels are reset anymore.

2. *Iterate until convergence*

   At every iteration, a propagation step is performed according to equation 2.24.

$$\tilde{Y}^{(t+1)} = \alpha \mathscr{L} \tilde{Y}^{(t)} + (1-\alpha) Y^{(0)} \tag{2.24}$$

   The algorithm reaches convergence when each node has the majority label of its neighbours. It stops when convergence is achieved or the maximum number of iterations defined by the user is reached. The final labels are obtained according to equation 2.22, previously defined in label propagation.

2.2.3 Fuzzy logic

The fuzzy logic concept was first introduced in the fuzzy set theory by Zadeh [121], according to the premise that people make decisions based on imprecise and non-numerical information. However, human ability to make accurate statements based on such inaccurate information decreases as the analyzed system becomes more complex, requiring the implementation of intelligent methods capable of dealing with fuzzy data. While classical computer frameworks are better suited to traditional logic, some situations require intelligent systems to adapt to fuzzy, context-based concepts. This adaptation is very similar to the paradigm of human reasoning.

Fuzzy logic is a branch of soft computing based on the concept of "grade of belonging", which is defined through membership functions or fuzzy sets. Figure 2.35 illustrates a common example of fuzzy sets where "cold", "warm", and "hot" linguistic variables are represented by trapezoidal membership functions that determine the degree in which the temperature value belongs to each of these states.

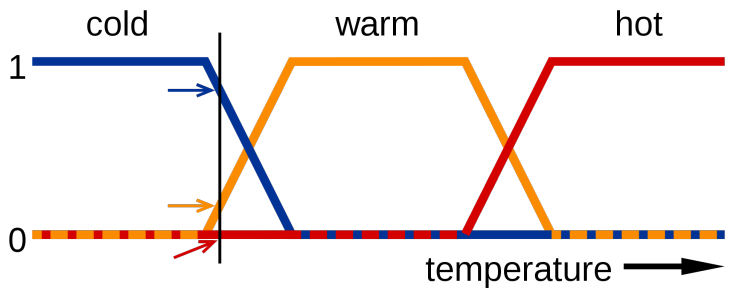

FIGURE 2.35: Example of "cold", "warm", and "hot" trapezoidal membership functions for a temperature input.
Source: Wikimedia

Thus, this methodology makes possible to handle vague or inaccurate information to obtain the status of a specific system. The kernel of this method consists of a set of rules extracted from expert knowledge. Unlike other methods, the knowledge implemented in fuzzy logic models is already known, since it has been previously defined by experts in the field. This fact makes the algorithm an unsupervised method that does not require labels to be tuned, thus being an advantage when using information that has not been previously labeled.

This method is divided into two main branches according to the methodologies proposed by Mamdani and Assilian [122] and Sugeno [123], respectively. While Mamdani systems have a more intuitive rule base suitable for applications where the rules are created from human expert knowledge, the defuzzification process of a Sugeno system is more computationally efficient, using a weighted average of a number of data points, rather than calculating the centroid of a two-dimensional area such as in the Mamdani method.

Figure 2.36 shows the basic scheme of a fuzzy algorithm where the system architecture consists of three main stages: fuzzification, inference and defuzzification.

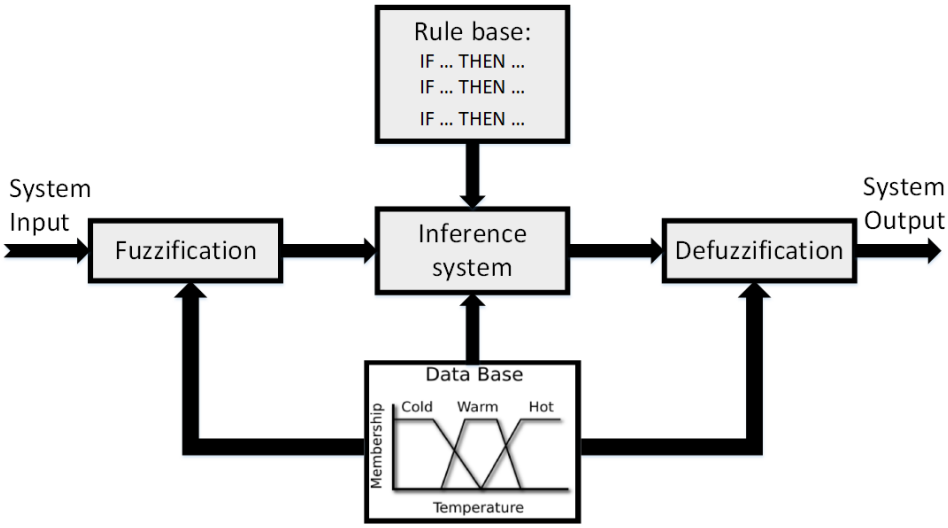

FIGURE 2.36: Basic scheme of a fuzzy algorithm.

1. *Fuzzification*

   Fuzzification is a process that consists of determining the possibility or degree of belonging of one variable to each of the membership functions of a fuzzy set. The degree of membership is within a range [0, 1], where zero is a null degree of membership to a linguistic variable and one is a total degree of membership. The membership functions can take any form (gaussian, triangular, sigmoid, step, and so on) depending on the data set and the context. Figure 2.37 illustrates an example of a set of triangular membership functions where the degree of membership is defined according to the value of each variable on the horizontal axis and the morphology of the corresponding membership function.

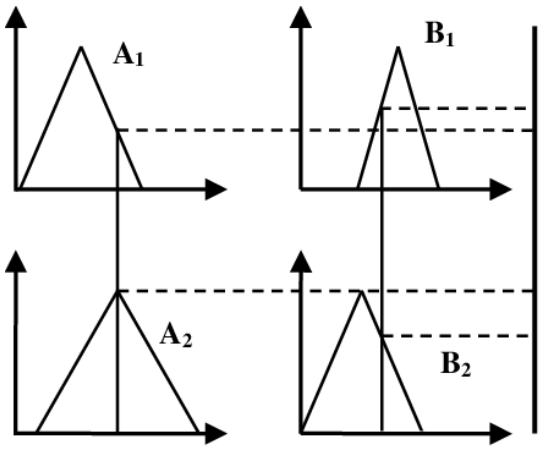

FIGURE 2.37: Example of triangular fuzzy membership functions.
Source: Nebot & Mugica [124] (modified)

2. *Inference system*

   In this step, several procedures are implemented to combine the degree of membership of the different variables and take decisions in a similar way to what is known as

logical reasoning. In fuzzy logic, the degrees of membership are combined through IF-THEN rules in order to reach a conclusion. This conclusion can result in an output fuzzy set, for the Mamdani method, or a discrete value, for the Sugeno method.

The set of rules is provided by experts in the field where the system is being applied by means of linguistic information. For this purpose, input fuzzy sets are combined using the logical operators AND, OR and NOT, as illustrated in Figure 2.38.

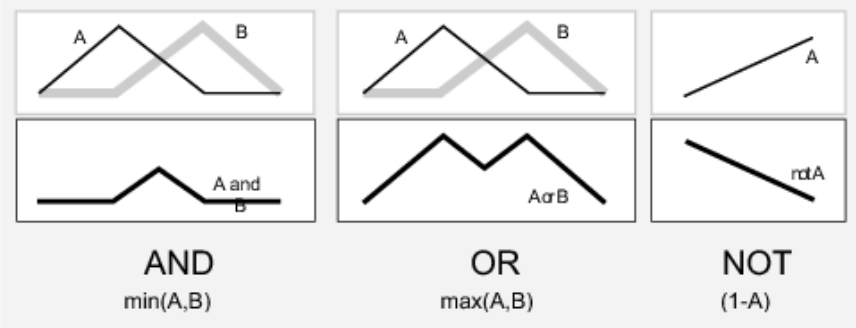

FIGURE 2.38: Fuzzy logic operators.
Source: quantdare.com

Figures 2.39 and 2.40 illustrate IF-THEN rules structure for the Mamdani and Sugeno methodologies, respectively. While in the Mamdani method the consequence is a fuzzy set, in the Sugeno method the consequence is a function of the variables used in the premise.

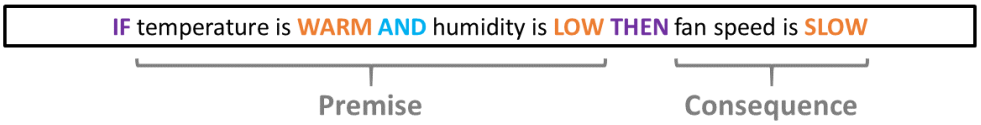

FIGURE 2.39: Mamdani rule structure.

FIGURE 2.40: Sugeno rule structure.

In Sugeno method, each rule generates two values: The first is the i^{th} rule output level (u_i), which is either a constant value or a linear function of the input values according to equation 2.25. x_j represents the j^{th} input value and $a_j^{(i)}$ the associated factor for the i^{th} rule. The second value is the rule firing strength (w_i), derived from the rule antecedent according to equation 2.26, where $F_j^{(i)}(x_j)$ is the membership function for input x_j in the i^{th} rule.

$$u_i = a_1^{(i)} x_1 + a_2^{(i)} x_2 + \ldots + a_k^{(i)} x_k + a_{k+1}^{(i)} \tag{2.25}$$

$$w_i = AndMethod\left(F_1^{(i)}(x_1), F_2^{(i)}(x_2), \ldots, F_k^{(i)}(x_k)\right) \tag{2.26}$$

3. *Defuzzification*

   In this last step, the fuzzy sets (Mandami) or discrete values (Sugeno) generated in the inference engine are combined to obtain a final numerical output value. In the Mamdani method, the most used technique to obtain this value is the calculation of the center of mass (centroid) of the area corresponding to the output fuzzy set according to equation 2.27, where $f(z_r)$ refers to the output fuzzy set, which depends on z_r. R refers to the selected resolution for the discrete calculation of the centroid.

$$out_M = \frac{\sum_{r=1}^{R} z_r \cdot f(z_r)}{\sum_{r=1}^{R} f(z_r)} \tag{2.27}$$

   In the Sugeno method, the weighted average over all rule outputs is calculated according to equation 2.28, where N_r is the number of rules. Figure 2.41 illustrates all the stages followed to implement the Sugeno and Mamdani fuzzy logic methods.

$$out_S = \frac{\sum_{i=1}^{N_r} u_i \cdot w_i}{\sum_{i=1}^{N_r} w_i} \tag{2.28}$$

2.2.4 Fuzzy rule-based supervised learning methods

Fuzzy rule-based systems (FRBSs) are methods that address complex real-world problems by applying concepts of fuzzy logic and supervised learning techniques. They are commonly used for classification and regression tasks. FRBSs are based on the fuzzy set theory, proposed by Zadeh [121] and previously explained in subsection 2.2.3. FRBSs are capable of generating the fuzzy rules and fuzzy sets automatically from labeled data by means of supervised learning techniques in situations where it is not possible to manually set up the fuzzy rules due to the absence of specialized knowledge. In this subsection, several fuzzy rule-based supervised learning methods are presented.

Among the methods proposed to perform the learning task throughout this thesis, Riza et al. [126] provide the appropriate tools to easily train and validate FRBS regression algorithms. Those methods, explained below, are Wang and Mendel's method (WM) [127], dynamic evolving neural-fuzzy inference system (DENFIS) [128], hybrid neural fuzzy inference system (HyFIS) [129] and heuristics and gradient descent method (FS.HGD) [130].

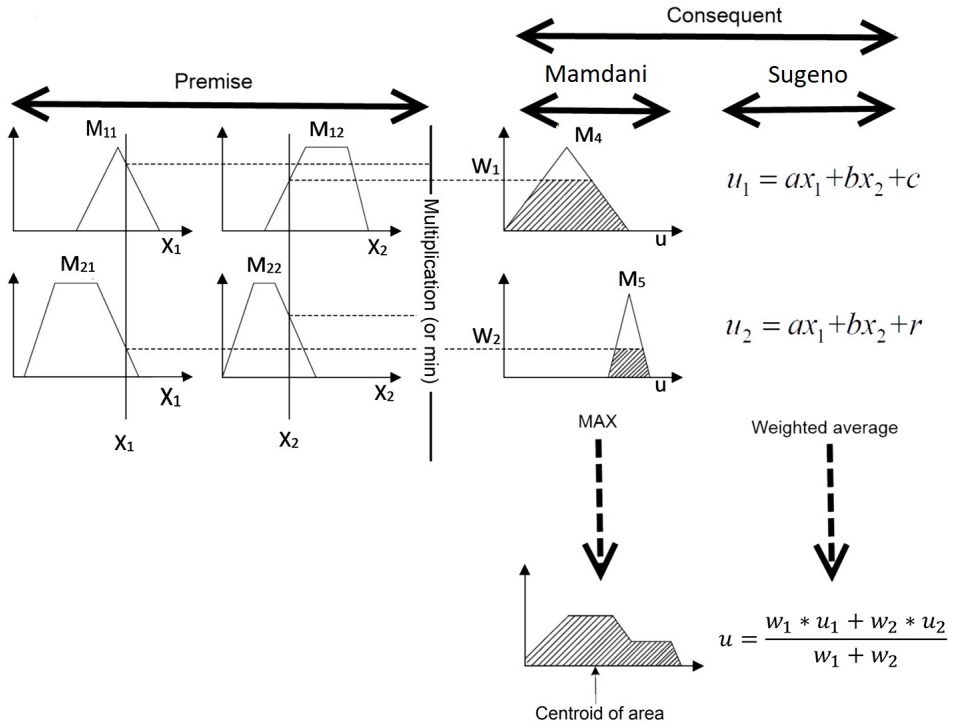

FIGURE 2.41: Diagram of Mamdani and Sugeno fuzzy inference systems.
Source: Cavallaro [125] (modified)

Wang and Mendel's method

This fuzzy rule-based space partitioning method was first proposed by Wang and Mendel [127]. The WM method consists of the following five steps:

In **step 1** the input and output spaces of the given numerical data are divided into $2N_{fr}+1$ fuzzy regions, where N_{fr} is a positive integer. N_{fr} and the length of the regions can differ among variables. Figure 2.42 shows an example for two input variables with $N_{fr}=2$ and $N_{fr}=3$ respectively, and $N_{fr}=2$ for the output space. All fuzzy membership functions are symmetric triangular fuzzy sets where the top vertex lies at the center of the region and the other two vertices lie at the centers of the two neighboring regions.

In **step 2** fuzzy IF-THEN rules are generated from the given data set according to the following actions: first, the degree of membership to each membership function of the input and output data pairs is calculated; second, the linguistic value corresponding to the regions with maximum degree is assigned to each data value; third, an AND type rule is generated for each input-output data.

In **step 3** a degree is assigned to each generated rule. Due to the large number of rules, which is equal to the amount of data, some rules may conflict. The proposed solution consists in selecting just the rule from the conflict group with the largest degree, thus, resolving the conflict and reducing the resulting number of rules.

In **step 4** a combined fuzzy rule base is created, which mixes the previously obtained rules

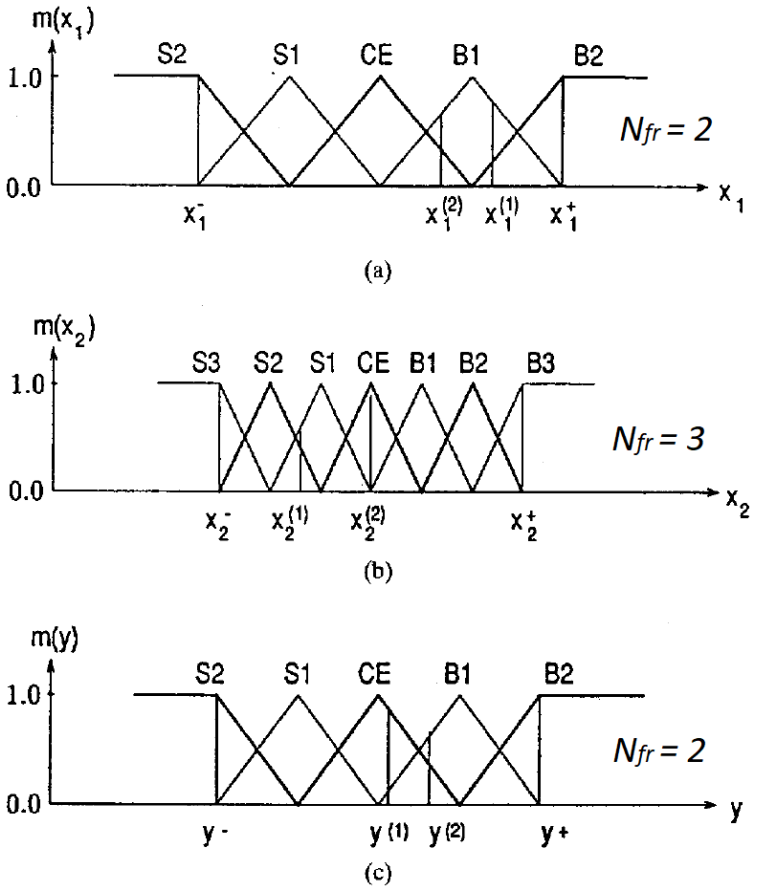

FIGURE 2.42: Fuzzy regions for input and output spaces and corresponding triangular membership functions.
Source: Wang & Mendel [127]

with those generated manually by expert staff. These rules have a degree that reflects the expert's conviction in the significance of the rule. If more than one rule from the combined fuzzy rule set has the same parameters, the rule with the largest degree is chosen.

In **step 5** the defuzzification is performed to determine the output value. The defuzzification of the centroid is carried out according to previously defined equation 2.27.

Dynamic evolving neural-fuzzy inference system

This fuzzy rule-based clustering method was proposed by Kasabov and Song [128] and it is composed of several stages. During the first stage of the DENFIS method, the input data is grouped into clusters, where the centers of these clusters are determined using the evolving clustering method (ECM), which is a distance-based connectionist clustering method. Distances are calculated according to general Euclidean distance defined in 2.29, where x and y represent two data vectors. From clusters, new parameters are extracted for the consequent training of the fuzzy rule-based model.

$$\|x-y\| = \sqrt{\frac{1}{k}\sum_{i=1}^{k}|x_i - y_i|^2} \tag{2.29}$$

The ECM algorithm is determined by a threshold value (*Dthr*). This parameter influences the amount of clusters that are created. When a new cluster is created, the first instance from the data stream is set as a cluster center, and the cluster radius (*Ru*) is initialized to zero. As more data is processed, some new clusters are created and others are updated by changing the positions of their centers and increasing their radiuses. When *Ru* reaches the *Dthr* value, it will not be updated anymore. All cluster centers are definitively obtained after evaluating the full data set. This process is illustrated in Figure 2.43.

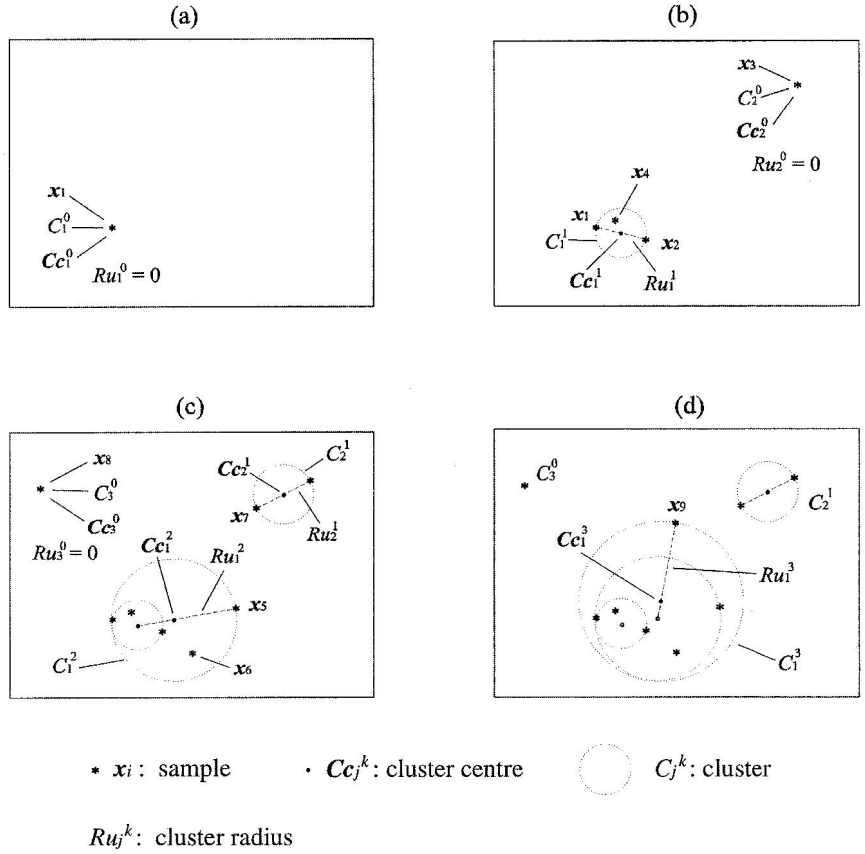

FIGURE 2.43: A brief clustering process using ECM.
Source: Kasabov & Song [128]

The values of the radiuses and centers of the resulting clusters are fixed to carry out the next stage, which consist of a Sugeno type fuzzy inference engine [131]. The fuzzy membership functions used at this stage are triangular type functions according to 2.30, where b is the value of the cluster center and d is a value in the range [1.2, 2], being $a = b - d \cdot Dthr$ and $c = b + d \cdot Dthr$.

$$R_{ij} = \text{Triangular}(x; a, b, c) = \begin{cases} 0 & \text{if } x \leq a \\ \dfrac{x-a}{b-a} & \text{if } a \leq x \leq b \\ \dfrac{c-x}{c-b} & \text{if } b \leq x \leq c \\ 0 & \text{if } c \leq x \end{cases} \tag{2.30}$$

First-order Sugeno type rules are employed, where linear functions (f) are created and updated by a linear least-squares estimator. Equation 2.31 shows an example of the structure of the implemented rule set, where R refers to the fuzzy set.

$$\begin{cases} \text{if } x_1 \text{ is } R_{11} \text{ and } x_2 \text{ is } R_{12} \text{ and } \ldots \text{ and } x_q \text{ is } R_{1q}, \text{ then } y \text{ is } f_1(x_1, x_2, \ldots, x_q) \\ \text{if } x_1 \text{ is } R_{21} \text{ and } x_2 \text{ is } R_{22} \text{ and } \ldots \text{ and } x_q \text{ is } R_{2q}, \text{ then } y \text{ is } f_2(x_1, x_2, \ldots, x_q) \\ \ldots \\ \text{if } x_1 \text{ is } R_{m1} \text{ and } x_2 \text{ is } R_{m2} \text{ and } \ldots \text{ and } x_q \text{ is } R_{mq}, \text{ then } y \text{ is } f_m(x_1, x_2, \ldots, x_q) \end{cases} \tag{2.31}$$

During prediction, the fuzzy rules that constitute the inference system vary according to the location of each sample in the input space. This phenomenon is illustrated in the example in Figure 2.44, where for two different samples, the fuzzy sets of the clusters closest to each sample are considered, along with their corresponding rules.

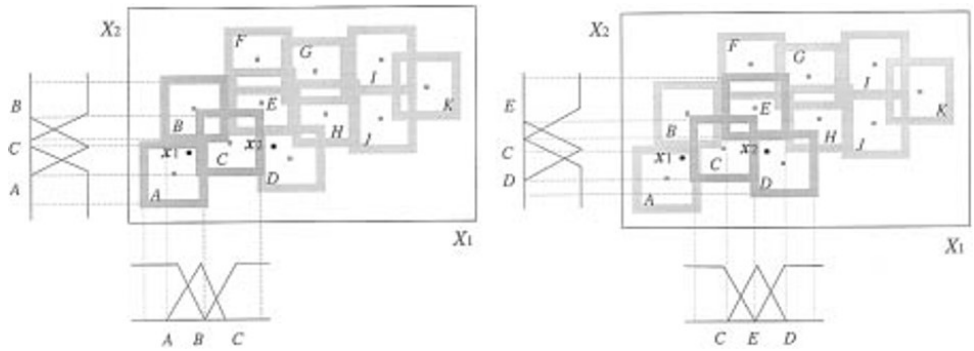

FIGURE 2.44: Two groups of fuzzy rules are formed to perform the inference of two input samples.
Source: Kasabov & Song [128]

Hybrid neural fuzzy inference system

This neuro-fuzzy inference method was proposed by Kim and Kasabov [129] and uses the Mamdani rule structure for learning. It consists of a two-phase framework, as illustrated in the schematic in Figure 2.45 extracted from [129]. First, fuzzy rules are generated in the knowledge acquisition module to find the initial structure of the neuro-fuzzy model. Second, backpropagation is used during parameter learning stage to tune the membership functions of the input-output linguistic variables.

Knowledge acquisition module

In the knowledge acquisition module, fuzzy rules are extracted by using the strategy proposed by Wang and Mendel previously seen in subsection 2.2.4 [127]. This is a one-step procedure that performs a fast generation of fuzzy rules from numerical input-output training data.

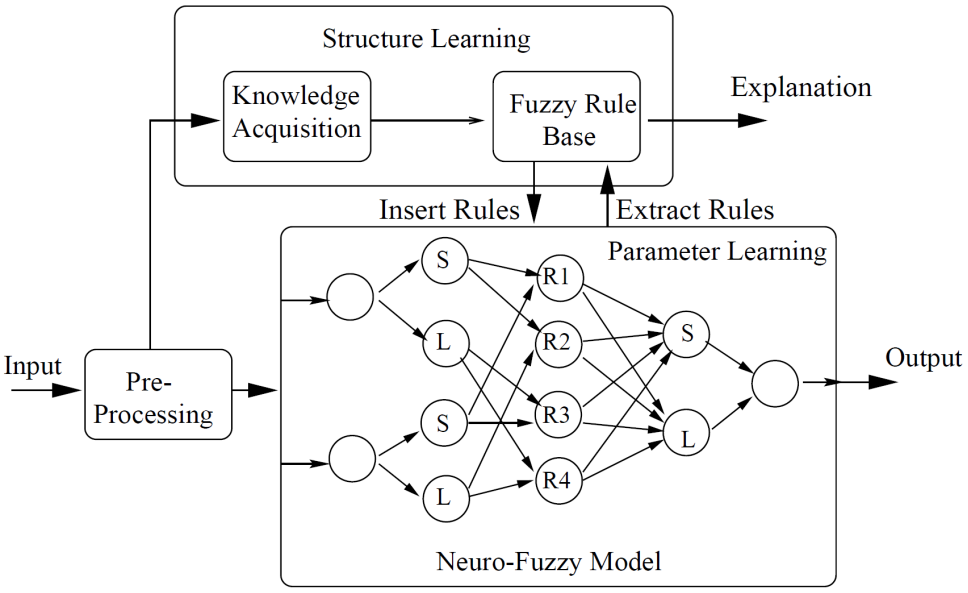

FIGURE 2.45: General diagram of the HyFIS model.
Source: Kim & Kasabov [129]

Parameter learning phase

Once the fuzzy rules are set, the entire network structure is established. In this stage, parametric tuning is performed, i.e. the tuning of the membership functions parameters and the tuning of the fuzzy rules weights. Among the different existing learning methods, in HyFIS algorithm the supervised learning backpropagation strategy is commonly used.

HyFIS architecture

The full model is divided into five layers as illustrated in the schematic in Figure 2.46 extracted from [129].

Layer 1: It consists of input nodes, which directly transmit input signals to the next layer.

Layer 2: This layer contains the membership functions, which represent the terms of the set of linguistic variables. All the membership functions consist on bell-shaped (Gaussian) functions as defined in equation 2.32, where σ refers to the standard deviation and μ represents the mean.

$$y_i^{(2)} = \text{Gaussian}(x;\mu,\sigma) = e^{-(x-\mu)^2/\sigma^2} \tag{2.32}$$

Layer 3: Each node in this layer represents the IF-part of a fuzzy rule, where every rule is implemented according to the logical operator AND. Hence, the operation is defined according to equation 2.33, where I_j is the set of indices of the layer 2 nodes connected to the j^{th} node in layer 3.

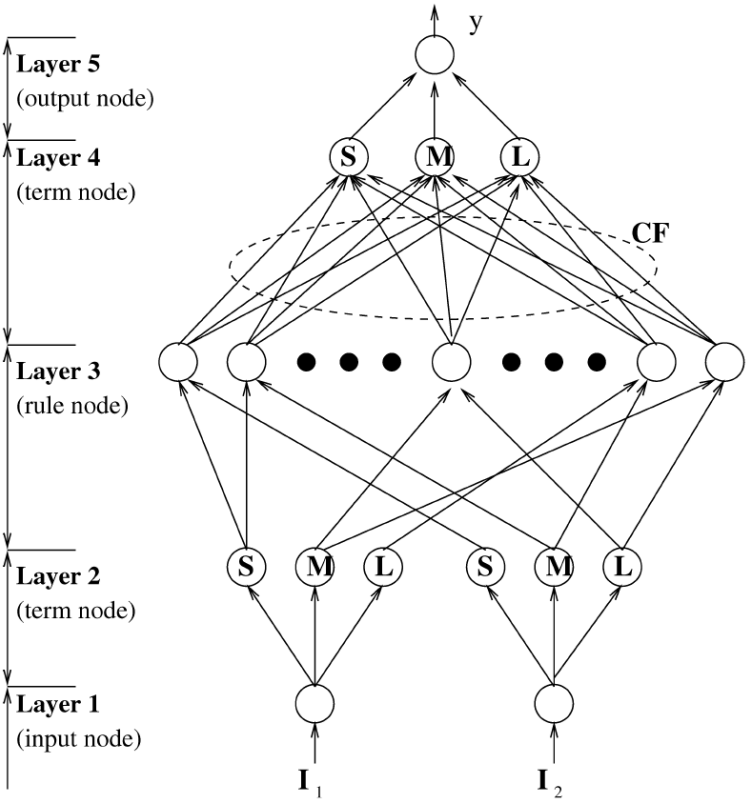

FIGURE 2.46: HyFIS layer structure.
Source: Kim & Kasabov [129]

$$y_j^{(3)} = \min_{i \in I_j}(y_i^{(2)}) \tag{2.33}$$

Layer 4: This layer contains the THEN-parts of the fuzzy rules. Each node of this layer integrates all the rules related to the same linguistic output variable by performing the logical operator OR according to equation 2.34, where I_k is the set of indices of the layer 3 nodes connected to the k^{th} node in layer 4.

$$y_k^{(4)} = \max_{j \in I_k}(y_j^{(3)} w_{kj}^2) \tag{2.34}$$

Layer 5: This is the output layer where defuzzification is performed. The centroid of the resulting two-dimensional area derived from the output membership functions is calculated according to equation 2.35, where I_l is the set of indices of the layer 4 nodes connected to the node l in layer 5. σ_{lk} and c_{lk} are the width and the centroid of the membership function of the k^{th} output linguistic variable in layer 4, respectively.

$$y_l^{(5)} = \frac{\sum_{k \in I_l} y_k^{(4)} \sigma_{lk} c_{lk}}{\sum_{k \in I_k} y_k^{(4)} \sigma_k} \tag{2.35}$$

Heuristics and gradient descent method

This heuristic fuzzy-rule based method was first proposed by Ishibuchi et al. [130]. The FS.HGD method consists of two stages: in the first stage, the heuristic method is employed for determining the initial consequent part of each fuzzy IF-THEN rule, and in the second stage, the learning method is implemented to tune these consequent parts. A simple fuzzy grid is used to perform the fuzzy partitioning of the input space, where all fuzzy membership functions are symmetric triangular fuzzy sets which intersect each other at the level of 0.5, as illustrated in Figure 2.47.

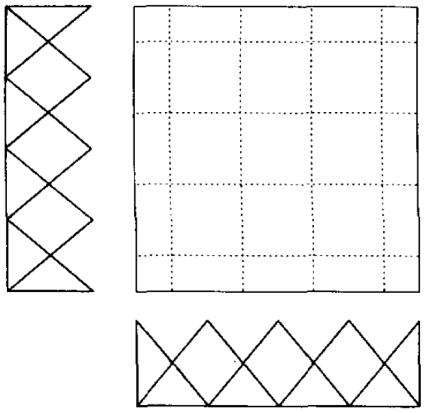

FIGURE 2.47: An example of fuzzy partition for a 2-dimensional input space and 5 fuzzy sets for each feature.
Source: Ishibuchi et al. [130]

For the modelling of a n-input and single output system, the IF-THEN rules have the format of equation 2.36, where $x_i^{(p)}$ is the i^{th} input variable of the input sample $x^{(p)}$, R is the fuzzy set, w_j is a real number, y is an output variable and N_r is the number of fuzzy IF-THEN rules.

$$\text{If } x_1^{(p)} \text{ is } R_{j1} \text{ and } x_2^{(p)} \text{ is } R_{j2} \text{ and } \ldots \text{ and } x_n^{(p)} \text{ is } R_{jn}, \text{ then } y \text{ is } w_j, \quad j = 1,2,\ldots,N_r. \tag{2.36}$$

The estimated output $o(x^{(p)})$ is calculated according to equation 2.37, where $\mu_j(x^{(p)})$ is the grade of the compatibility of $x^{(p)}$ with the j^{th} fuzzy IF-THEN rule.

$$o(x^{(p)}) = \sum_{j=1}^{N_r} \mu_j\left(x^{(p)}\right) \cdot w_j \tag{2.37}$$

The grade of the compatibility is defined according to equation 2.38.

$$\mu_j(x^{(p)}) = R_{1j}\left(x_1^{(p)}\right) \times R_{2j}\left(x_2^{(p)}\right) \times \cdots \times R_{nj}\left(x_n^{(p)}\right) \tag{2.38}$$

Heuristic method

In this stage, the antecedent part (IF-part) is generated using techniques of space partitioning. w_j is determined for each IF-THEN rule according to the heuristic method of equation 2.39, where the consequent part of each rule is determined by the average of $y^{(p)}$ weighted by the grade of the compatibility of the given training data set.

$$w_j^{\mathrm{HM}} = \frac{\sum_{p=1}^{m} \mu_j\left(x^{(p)}\right) \cdot y^{(p)}}{\sum_{p=1}^{m} \mu_j\left(x^{(p)}\right)}, \quad j = 1, 2, \ldots, N_r. \tag{2.39}$$

Learning method

The gradient descent method is used to tune the value of the consequent part where the total error is defined in equation 2.40.

$$E = \frac{1}{2} \sum_{p=1}^{m} \left(o\left(x^{(p)}\right) - y^{(p)}\right)^2 \tag{2.40}$$

The learning procedure consists on the following steps:

Step 1: The initial value of $w_j^{(init)}$, the learning rate and the maximum number of iterations are specified.

Step 2: For each input vector, w_j is adjusted according to the gradient descent method.

Step 3: Repeat step 2 until the maximum iteration number is reached.

2.2.5 Artificial neural networks

An artificial neural network (ANN) is an algorithm based on the behavior of the brain that performs a large number of small calculations as the data is propagated throughout it. It consists of a set of units, called artificial neurons, that emulate the behavior and morphology of real neurons as illustrated in Figure 2.48. Each neuron is connected with other neurons, where the value of the connection is modulated by a weight. These weights can increase or decrease the enervation of adjacent neurons. Furthermore, each neuron has a nonlinear activation function, which modifies the resulting value.

The first step toward ANNs began with McCulloch and Pitts [132], who modeled an ANN with electrical circuits. This idea was promoted with the backpropagation algorithm proposed by Werbos [133], which enabled multilayer network training, distributing the error term across the layers and modifying the weights at each node.

The basic training of an ANN consists of three iterative stages: a forward propagation stage, in which the outputs are obtained; a backpropagation stage, in which the error with respect to the reference value is used to calculate the gradients layer by layer; and an optimization stage, where weights and biases are updated. Figure 2.49 illustrates a standard

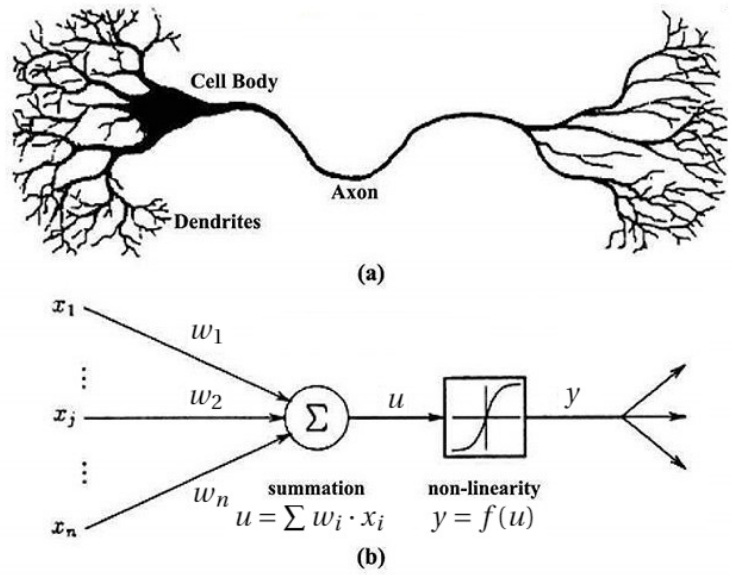

FIGURE 2.48: Real neuron (a) and artificial neuron (b) illustration where x_i represents an artificial neuron input, w_i the corresponding weight, f the activation function, and y the output value.

example of an ANN, consisting of layers of neurons such as an input layer, an output layer, and one or more hidden layers.

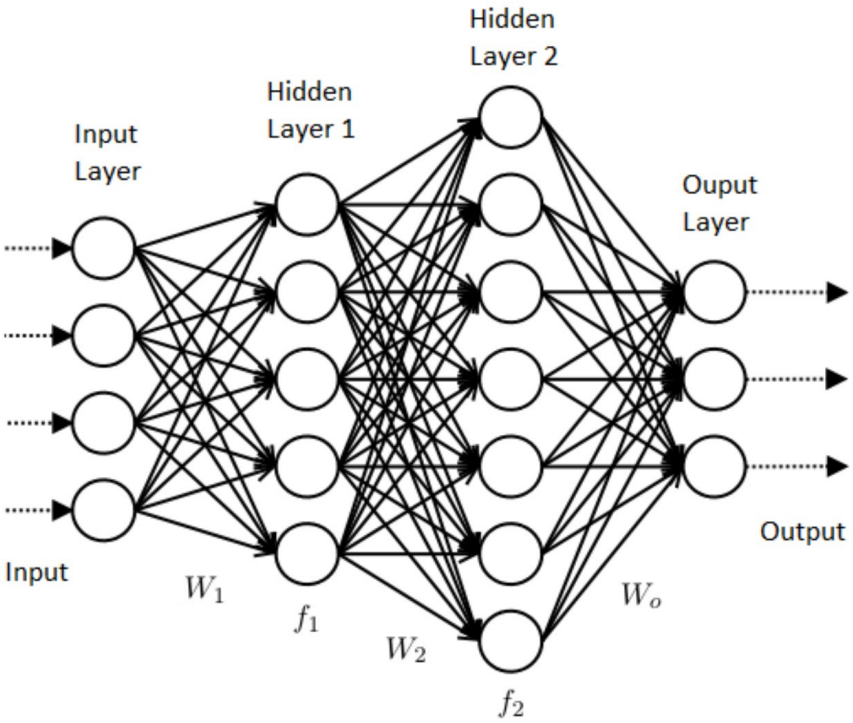

FIGURE 2.49: Standard ANN example.
Source: medium.com

Forward propagation

The process of passing the data through the ANN is known as forward propagation. For each neuron, input values (x_j) are multiplied with their corresponding weights (w_j). A weight represents the strength of its corresponding input value and determines how much influence the given input has on the output of the neuron. The resulting values are added together with a bias (b), resulting in equation 2.41, where n_x is the number of inputs to each neuron.

$$z = \sum_{j=1}^{n_x} x_j \cdot w_j + b \tag{2.41}$$

Activation functions are used to introduce nonlinearity into the output of the neurons. Without the nonlinearity the neuron is just a linear function. Sigmoid function (denoted by σ), also known as logistic function, is a standard among activation functions and is defined according to equation 2.42. The output of the network is known as the predicted value ($\hat{y}$).

$$\sigma(z) = \frac{1}{1+e^{-z}} \tag{2.42}$$

Backpropagation

This method for supervised learning is based on the calculation of the gradient of the loss function with respect to the weights. The average loss of the full data set is called the cost function (C). In equation 2.43 a cost function corresponding to the mean square error is presented, which is a standard in ANN training.

$$C = \frac{1}{n} \sum_{i=1}^{n} (y^{(i)} - \hat{y}^{(i)})^2 \tag{2.43}$$

In the following two steps, the calculation carried out in a single neuron is used to explain backpropagation. Gradients are used to know how the cost function changes in relation to weights and biases. The gradient of the cost function is calculated according to equation 2.44, where the chain rule is used to derive all the components between the final cost and the weights.

$$\frac{\partial C}{\partial w_j} = \frac{\partial C}{\partial \hat{y}} \times \frac{\partial \hat{y}}{\partial z} \times \frac{\partial z}{\partial w_j} \tag{2.44}$$

This results in the partial derivatives presented in equation 2.45 for a unique neuron, giving rise to equation 2.46.

$$\begin{cases} \dfrac{\partial C}{\partial \hat{y}} = \dfrac{2}{n}\sum_{i=1}^{n}(y^{(i)} - \hat{y}^{(i)}) \\ \dfrac{\partial \hat{y}}{\partial z} = \dfrac{\partial}{\partial z}\sigma(z) = \sigma(z) \times (1 - \sigma(z)) \\ \dfrac{\partial z}{\partial w_j} = \dfrac{\partial}{\partial w_j}(z) = x_j \end{cases} \tag{2.45}$$

$$\frac{\partial C}{\partial w_j} = \frac{2}{n}\left(\sum_{i=1}^{n}(y^{(i)} - \hat{y}^{(i)})\right) \times \sigma(z) \times (1 - \sigma(z)) \times x_j \tag{2.46}$$

The bias is considered to be a constant value, resulting in the gradient of equation 2.47.

$$\frac{\partial C}{\partial b} = \frac{2}{n}\left(\sum_{i=1}^{n}(y^{(i)} - \hat{y}^{(i)})\right) \times \sigma(z) \times (1 - \sigma(z)) \tag{2.47}$$

Optimization

Finally, optimization is carried out using the gradient descent method, which is a standard among the optimization algorithms. This algorithm changes the weights and biases, proportional to the negative of the backpropagation gradients according to equations 2.48 and 2.49, respectively. α corresponds to the value of the learning rate.

$$w_j = w_j - \left(\alpha \times \frac{\partial C}{\partial w}\right) \tag{2.48}$$

$$b = b - \left(\alpha \times \frac{\partial C}{\partial b}\right) \tag{2.49}$$

2.3 Data sets

This subsection describes the three data sets used throughout this thesis for the design and validation of the proposed algorithms. In the description of the first data set, the methodology used for the non-invasive collection of physiological records during the stress experiments conducted by Dr. Raquel Martinez at the University of the Basque Country (UPV/EHU) is described. The second data set corresponds to the MIT-BIH arrhythmia database, widely used in the validation of algorithms related to the electrocardiogram (ECG) processing. In this thesis, this data set is used to validate the proposed algorithm for the accurate detection of R-peaks in ECG signals. The third data set contains the oscillometric blood pressure (OBP) records acquired by the ECG clinics at Auckland City Hospital and Greenlane Clinical Centre in Auckland (New Zealand). These records were employed to develop and validate the proposed algorithm for the robust detection of foot points in OBP signals.

2.3.1 Stress and relaxation experiment

Physiological records have always been used in medicine for the diagnosis of both physical and psychological disorders. Many of the underlying physiological patterns are derived from the activity of the autonomic nervous system (ANS), which, in turn, is influenced by both external and internal factors of the organism itself. ANS activity is strongly reflected in signals such as the ECG, galvanic skin response (GSR) and breathing (RSP), which can be acquired non-invasively.

Throughout this thesis, the records extracted during the stress and relaxation experiment carried out in Martínez-Rodríquez [28] are used to develop most of the proposed algorithms. The experiment was carried out in a controlled laboratory environment. During the experiments, physiological signals closely related to the activity of the ANS, such as the previously mentioned ECG, GSR and RSP, were monitored. This experimental procedure was specifically designed to elicit emotional changes in the participants, resulting in a set of records related to relaxing and stressful situations.

Experiment design

The purpose of this experiment is to elicit states of stress and relaxation in order to collect physiological records reflecting the activation and deactivation of the ANS. To induce stressful responses in the participants, this experiment proposed the challenge of solving 3D wooden puzzles. Therefore, it requires participants to have spatial visualization and geometric measurement skills. During the experiment, four puzzles of different degrees of difficulty were used to obtain different degrees of stress responses. Figure 2.50 illustrates the different varieties of puzzles, where both the final solution and the phases for its resolution are also presented.

To evaluate the physiological changes during the activation stages of the ANS, it is necessary to compare these changes with a basal state of relaxation. Some experiments often utilize film clips and pictures to induce different physiological states [134]. In Sokhadze [135] it is reported that music reduces anxiety, thus it is commonly used to restore the basal psychological and physiological functioning. In this experiment, the visualization of videos with relaxing images and music is proposed to bring the subject to a basal state of relaxation before and after the realization of the puzzle.

Experimental stage

The experiment was carried out in a laboratory with the proper equipment to display the relaxing video on a screen and carry out the acquisition of the physiological records with the BIOPAC MP36/150 hardware. The experiment was conducted in pairs, so that the distractions caused among participants were minimal.

The experiment consisted of a three-phase challenge with an approximate duration of 14 minutes as depicted in Figure 2.51. In the first and third phases, the participant is taken to a basal state of relaxation by viewing a relaxing video. In the second phase, the participant

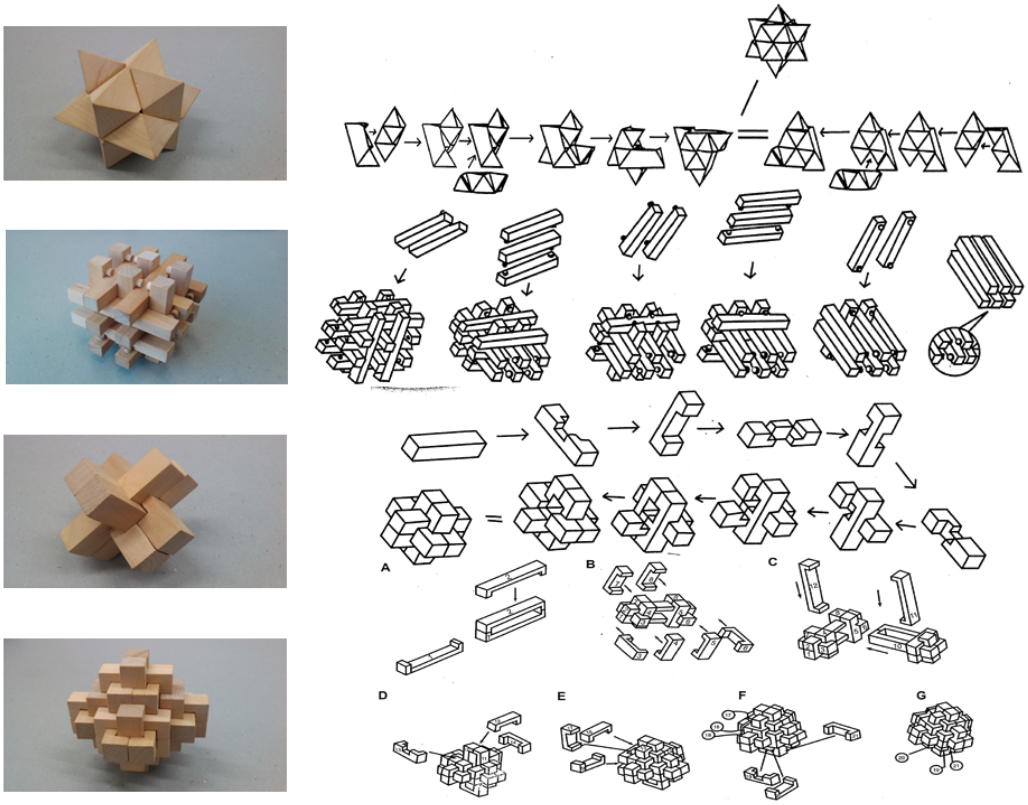

FIGURE 2.50: Final solution and phases of the 3D puzzles.

is induced into a state of stress by asking him/her to solve a three-dimensional puzzle. During the experiment all events that occurred were noted.

FIGURE 2.51: Phases and duration of the experimental stage for the acquisition of physiological records.

Experiment evaluation tools

The evaluation of the participants' response was carried out through three categories of emotional assessment: annotations collected during the experiment, a SAM questionnaire and a final interview.

Annotations

The annotations and marks were taken on the physiological records in real-time during the experimental stage. These marks indicate specific episodes such as the start of the experiment, the fall of an object (e.g., a puzzle piece), distractions and noises, among

others. These marks are intended to associate the different events occurred during the experiment with the time at which physiological responses are triggered.

SAM questionnaire

To address a dimensional measure of emotional states, Lang [136] proposed a nonverbal pictographic measure known as self-assessment manikin (SAM). The SAM is a picture-oriented instrument containing five images for each of the three affective dimensions that the participant rates: valence, arousal, and dominance. The three dimensions are evaluated in a range from 1 to 9 as shown in Figure 2.52.

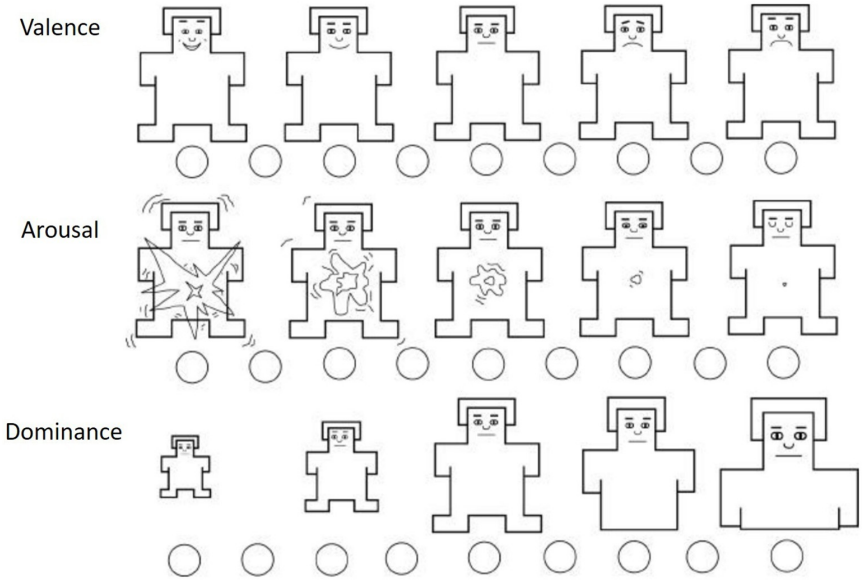

FIGURE 2.52: Example of a SAM questionnaire.

Valence represents the degree of happiness or sadness produced by emotional stimulation. Arousal refers to the level of alteration with which the subject responds to emotional stimulation. Finally, dominance indicates control over the situation.

Interview

Lastly, the participants were asked to participate in a brief interview in which they were asked how they felt during the different phases of the experiment.

Ethical regulations

To conduct experiments on humans, it is necessary to fulfill several ethical codes and legal regulations. The two pillars of the regulation in human experimentation are the Nuremberg Code (1947) [137] and the Declaration of Helsinki of the World Medical Association (1964) [138]. These documents summarize the ethical principles of human research. Both documents establish the obligation to preserve the confidentiality of the collected data and the existence of an informed consent signed by the participants. This experiment meets both conditions as explained below.

Data protection

The processing of personal data by any public or private entity entails obligations in Spain, both technical and organizational. This is included in the Royal Decree 1720/2010, where the Organic Law 15/1999 for the protection of personal data is approved [139]. The design and implementation of this experiment was reviewed and certified by the ethical committee of the UPV/EHU, more specifically, by the CEISH-UPV/EHU, BOPV 32 (M10_2016_189) [140].

Informed consent

The informed consent is a key point in human research as it seeks to protect the research subject from any improper interests. It is not a simple legal requirement or an administrative procedure, since it is a human right and must contain three elements: voluntariness, understanding and information. The consent form must be signed by both the researcher and the subject involved in the experiment. In this experiment, this aspect was considered by signing the informed consent of each participant before the experimental stage.

Data recording

To achieve a reliable data set of physiological records, during the experiment a standard medical device with its corresponding professional electrodes was used. The data was collected using both BIOPAC MP36/150 hardware (Biopac Systems Inc., USA) at a 1000 Hz sampling rate and AcqKnowledge 3.7.1 software. Considering the correlation between certain physiological signals and the activity of the ANS, the ECG, GSR and RSP were monitored using non-invasive sensors.

For ECG acquisition, Einthoven's triangle electrode configuration was used as explained in subsection 2.1.2. The electrodes were placed on the chest instead of the limbs, so that disturbances due to movements resulting from the performed tasks were not coupled. GSR was collected applying a low electrical potential between the two electrodes located in the distal phalanges of the non-dominant hand as indicated in subsection 2.1.2. Finally, a piezoelectric belt was used for RSP measurement as stated in subsection 2.1.2. Figure 2.53 shows the placement of the sensors used to collect these signals through the BIOPAC MP36/150 hardware.

Participants

In total, 166 participants (125 male and 41 female) between 19 and 45 years of age (mean = 22.88; standard deviation = 3.1) participated in the experiment in 2014. All subjects were volunteers of the engineering school at the UPV/EHU, with no exclusion criteria. All participants met the standards described in subsection 2.3.1.

For this thesis, a selection of the records that best met the criteria of the experiment was carried out, i.e., those that were not strongly influenced by factors external to the nature of the experiment. Finally, 42 records were selected to proceed with this thesis.

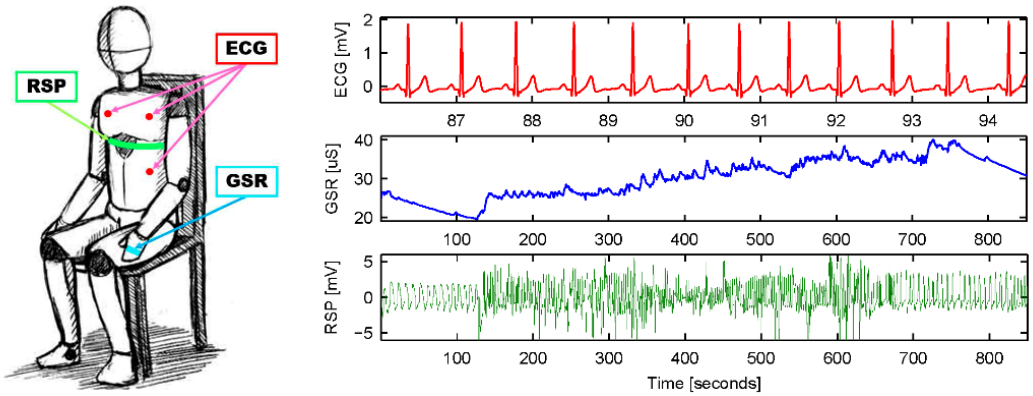

FIGURE 2.53: Sensor positioning scheme and collected ECG, GSR and RSP registers.

2.3.2 MIT-BIH arrhythmia database

The MIT-BIH arrhythmia database (MITADB) is the first standardized and publicly available data set for the evaluation of algorithms focused on ECG analysis [141]. In this thesis, the MITADB is used to evaluate the quality of the developed R-peak detection algorithm during ECG analysis, which is presented later in subsection 3.1.

The MITADB contains 48 half-hour two-channel ambulatory ECG recordings. These were obtained from 47 subjects studied by the BIH Arrhythmia Laboratory between 1975 and 1979. Twenty-three recordings were randomly selected from a data set of 4000 24-hour ambulatory ECG recordings collected from a mixed population of outpatients (about 40%) and inpatients (about 60%) at Beth Israel Hospital in Boston; the remaining twenty-five recordings were selected from the same data set to include less common but clinically significant arrhythmias [141].

The recordings were digitized at 360 Hz per channel with 11-bit resolution in a 10 mV range. Each record was annotated independently by two or more cardiologists; disagreements were resolved to digitize the reference annotations for each heartbeat included in the data set [141].

2.3.3 Oscillometric measurements

The OBP data used for the development of the foot point detection algorithm presented in subsection 3.2 was provided by the ECG clinics at Auckland City Hospital and Greenlane Clinical Centre, Auckland, New Zealand. The measurements were performed using the commercially available BP+ device (USCOM Limited, Sydney, Australia) in people who attended as part of usual care, with no other exclusion criteria. Ethics approval was granted by Auckland District Health Board Ethics Committee. The overall data set consists of 744 records from 569 patients aged between 15 and 93 years (mean (standard deviation) = 63 (16) years) where 59% were males and 41% females. Each record has a duration of 10 seconds and was acquired at 200 Hz. The labeling of the foot points was performed automatically by the BP+ device itself.

2.4 Implementation tools

This subsection introduces the software and hardware tools used during this thesis, both for the development and implementation of a functional hardware prototype containing the developed algorithms. The subsection is divided into two parts: on the one hand, the software tools used are explored in depth; on the other hand, the technical details of the hardware platforms used for the development of the prototype are presented.

2.4.1 Software

Python

Python is one of the most popular general-purpose programming languages nowadays. It was created in the late 1980s by Guido van Rossum at the Center for Mathematics and Informatics, in the Netherlands, as a successor to the ABC programming language, capable of handling exceptions and interacting with the Amoeba operating system [142].

Python is an interpreted programming language made up of high-level built in data structures, whose philosophy emphasizes the readability of its code. It is a multi-paradigm programming language, since it supports object orientation, imperative programming and, to a lesser extent, functional programming, which makes it a dynamic and multi platform language.

Its popularity has increased over time, becoming one of the most widely used languages in the field of research and artificial intelligence, and being one of the main programming languages in Google. It is an open source language, which means that the interpreter and the extensive modules and packages are available without charge for all major platforms, and is freely distributed.

Among the packages available, those shown below stand out in the accomplishment of this thesis:

Scikit-learn: This is an open source machine learning library that supports supervised, semi-supervised and unsupervised learning algorithms. Some of these algorithms are principal component analysis, label spreading and label propagation, among others. It also provides various tools for data preprocessing, model fitting, model selection and evaluation, and many other utilities.

NumPy: This is a fundamental package for scientific computing with Python. It contains powerful N-dimensional array objects, tools for integrating C/C++ and Fortran code, and useful linear algebra, Fourier transform and random number capabilities, among others.

Pandas: This NumPy extension is a high-level building block for practical, real world data analysis in Python. It provides data structures and operations to manipulate numeric tables and time series, thus being ideal for analyzing any type of complex information.

Matplotlib: This library is used to generate graphics from data contained in lists or arrays in the Python programming language. It supports NumPy and Pandas data structures. This tool extends to large number of third party packages, including several higher-level plotting interfaces (e.g., seaborn, HoloViews and ggplot) widely used in the scientific field.

Library *frbs*

Library ***frbs*** is an implementation in the CRAN (Comprehensive R Archive Network) repository of various learning algorithms consisting on fuzzy rule-based systems (FRBSs) for dealing with classification and regression tasks [126]. Some of these regression algorithms were previously explained in subsection 2.2.4. The ***frbs*** library includes the packages introduced below, which contains the processes needed to run the FRBSs:

The **sets** package includes the fundamental structures and operators of fuzzy sets (i.e, class intersection, union, negation and construction, among others). Additionally, it provides fuzzication, inference, and defuzzification mechanisms based on fuzzy rules and fuzzy variables [143].

The **fuzzyFDR** package uses discrete data to determine fuzzy decision rules for multiple testing of hypotheses.

The **fugeR** package implements learning in FRBSs through genetic algorithms.

The **e1071** package provides algorithms for fuzzy clustering and fuzzy k-means, which is an enhancement of the k-means clustering algorithm using fuzzy techniques [144].

gRPC framework

The gRPC framework is an open source and high performance remote procedure call framework developed at Google that can be run in any environment, since it generates cross-platform connections between client and server for different programming languages. It uses HTTP/2 and protocol buffers as interface description language and it can efficiently connect services in and across data centers. It has a pluggable support for authentication, bidirectional transmission, load balancing, tracing and health checking. Most use cases include distributed computing to connect devices, mobile applications and browsers to backend services. The languages and platforms among which gRPC communication can be carried out are listed in Table 2.7.

2.4.2 Hardware

In this subsection, the devices used for the final prototype of this thesis are presented. There exist several approaches that combine low-cost and wireless implementation [145, 146, 2, 147]. Considering price, size and popularity, Arduino and Raspberry Pi devices have proven to be suitable for a robust and low-cost prototyping [148, 149, 4]. While the Raspberry platform has considerable processing power, the Arduino board is capable of concurrently acquiring analog signals.

TABLE 2.7: Languages and platforms officially supported by the gRPC framework.

Language	Platform
C/C++	Linux, Mac, Windows 7+
C#	Linux, Mac, Windows 7+
Dart	Windows, Linux, Mac
Go	Windows, Linux, Mac
Java	Windows, Linux, Mac
Kotlin/JVM	Windows, Linux, Mac
Node.js	Windows, Linux, Mac
Objective-C	Mac OS X 10.11+, iOS 7.0+
PHP	Linux, Mac
Python	Windows, Linux, Mac
Ruby	Windows, Linux, Mac

Raspberry Pi

Raspberry Pi is a low-cost computer board developed in the United Kingdom by the Raspberry Pi foundation, with the aim of promoting the teaching of computer science in schools. It is a tiny motherboard made up of a processor, GPU, GPIOs and RAM. Figure 2.54 shows a diagram of the different types of inputs and outputs that most of the Raspberry models have, which can carry out UART (Universal Asynchronous Receiver/Transmitter), SPI (Serial Peripheral Interface) and I2C (Inter-Integrated Circuit) communications, among others.

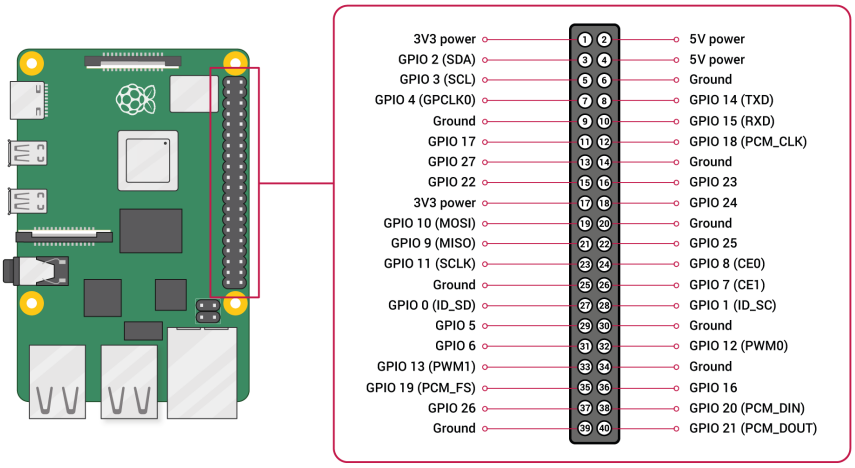

FIGURE 2.54: GPIO pin scheme for the Raspberry Pi model 3 B+ board.
Source: raspberrypi.org

It also has USB and video inputs/outputs to connect several devices, such as a monitor, a mouse and conventional USB keyboards. It can run different operating systems based on free software Linux, which integrate the Python programming environment [150]. Table 2.8 compares the technical specifications of two of the most widely used models, which differ mainly in power.

TABLE 2.8: Technical specifications of the Raspberry Pi 3 B+ and the Raspberry Pi 4 B boards.

	Raspberry Pi 3 B+	**Raspberry Pi 4 B**
Operating Voltage	5 V	5 V
SOC Type	BCM2837B0	BCM2711
Core Type	Cortex-A53 64-bit	Cortex-A72 64-bit
No. Of Cores	4	4
GPU	VideoCore IV	VideoCore VI
CPU Clock	1.4 GHz	1.5 GHz
RAM	1 GB DDR2	4 GB
No. GPIO	40	40
Length	85.6 mm	85.6 mm
Width	56.5 mm	56.5 mm
Weight	45 g	46 g

Arduino

Arduino is an open source development platform, which is based on free, flexible and easy to use hardware and software for developers. This platform allows creating different types of microcomputers from a single board, to which the community of developers can give different types of use. Arduino has an integrated development environment called Arduino IDE, consisting of a programming environment composed of a set of functions written in C/C++. It contains all the necessary elements to connect peripherals to the inputs and outputs of the microcontroller, as illustrated in the schematic in Figure 2.55.

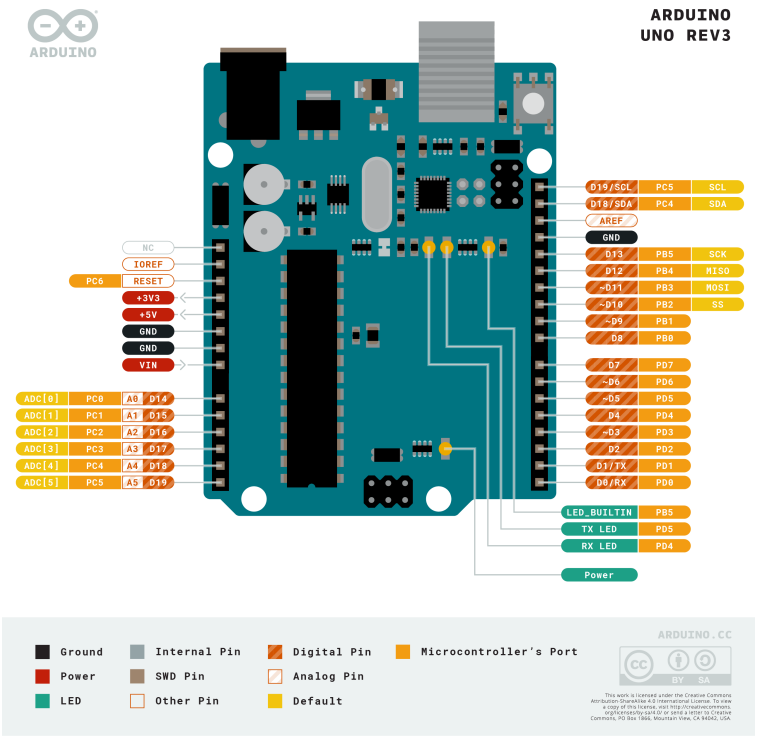

FIGURE 2.55: GPIO pin scheme for the Arduino UNO board.
Source: arduino.cc

Arduino is a project and not a specific model of board, which means that its basic design is shared by different types of boards. These boards may vary in shape, size and characteristics. Table 2.9 compares the technical specifications of two of the most widely used Arduino boards, which differ mainly in size.

TABLE 2.9: Technical specifications of the Arduino UNO and the Arduino Nano boards.

	Arduino UNO	**Arduino Nano**
Microcontroller	ATmega328P	ATmega328
Operating Voltage	5 V	5 V
Input Voltage	7-12 V	7-12 V
Digital I/O Pins	14	22
PWM Output	6	6
Analog Input Pins	6	8
DC Current per I/O Pin	20 mA	40 mA
DC Current for 3.3V Pin	50 mA	50 mA
Flash Memory	32 KB	32 KB
SRAM	2 KB	2 KB
EEPROM	1 KB	1 KB
Clock Speed	16 MHz	16 MHz
Length	68.6 mm	45 mm
Width	53.4 mm	18 mm
Weight	25 g	7 g

Bluetooth module

The HC-05 Bluetooth module is an easy to use Bluetooth serial port protocol module, designed for transparent wireless serial connection setup. It can be configured as both master and slave, and it also has many configuration parameters and interrogation capabilities. This module is often used to provide bluetooth communication to devices that do not have it, such as some versions of Arduino. The serial communication pins (Rx and Tx) operate at 3.3V as illustrated in Figure 2.56, thus sometimes it is necessary to use a bi-directional voltage converter to make it compatible with other devices. Table 2.10 shows the main technical specifications of this module.

TABLE 2.10: Technical specifications of the HC-05 Bluetooth module.

Radio chip	CSR BC417143
Operating voltage	3.6 V to 6 V
Operating current	50mA
Range	5-10 m
Frequency	2.4 GHz
Supported baud rate	9600, 19200, 38400, 57600, 115200, 230400, 460800
Protocol	IEEE 802.15.1
Profile	Bluetooth Serial Port
Transmission power	≤ 4 dBm
Length	27 mm
Width	12.7 mm

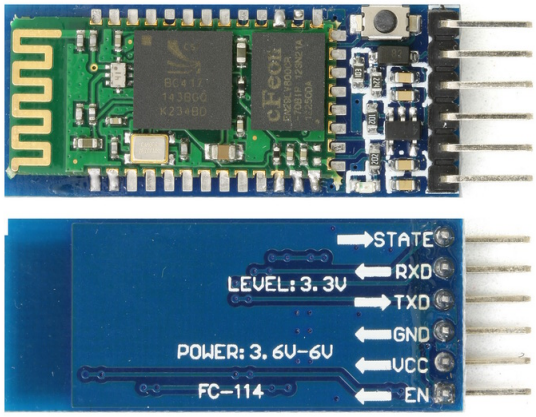

FIGURE 2.56: HC-05 Bluetooth module.

Bi-directional voltage level converter

The SparkFun bi-directional logic level converter (BOB-12009) is a small device that safely raises electrical signals from 3.3 V to 5 V and reduces them from 5V to 3.3V simultaneously. It also works with 1.8 V and 2.8 V devices. Each device has the capability to handle 4 pins of low voltage (LV1-4) and 4 pins of high voltage (HV1-4), which are divided in two inputs and two outputs for each type, as illustrated in Figure 2.57. To use the device, it is necessary to power the converter from the two voltage sources: high voltage to the "HV" pin, low voltage to the "LV" pin and system ground to the "GND" pin.

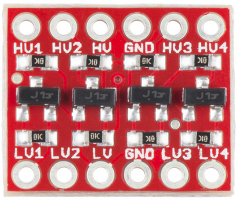

FIGURE 2.57: SparkFun bi-directional logic level converter (BOB-12009).

Galvanic skin response acquisition sensor

The Grove GSR (galvanic skin response) sensor is a small device equipped with two electrodes as illustrated in Figure 2.58. This device measures the galvanic response of the skin by means of the measurement of the electrical resistance between the two electrodes. The electrodes are intended to be placed on the hand, thus measuring the electrical resistance between two fingers, which is strongly influenced by the sweating of the hand. Table 2.11 shows the main technical specifications of the device.

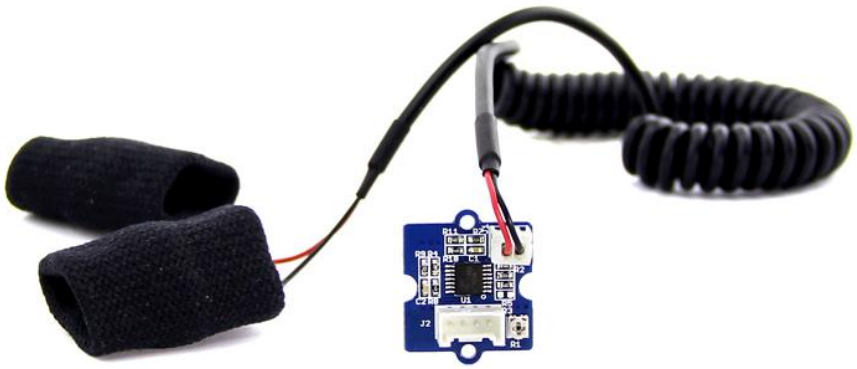

FIGURE 2.58: Grove GSR sensor v1.2.

TABLE 2.11: Technical specifications of the Grove GSR sensor v1.2.

Operating voltage	3.3 V to 5 V
Input Signal	Skin resistance
Output Signal	Voltage, analog reading
Length	24 mm
Width	20 mm
Height	9.8 mm
Weight	29 g

Electrocardiogram acquisition sensor

The heart rate monitor AD8232 illustrated in Figure 2.59 is a fully integrated signal conditioning device for single-lead electrocardiographic measurement applications. It is designed to extract, amplify, and filter small biopotential signals in noisy conditions, such as those conditions created by remote electrode placement or motion. The AD8232 is designed to amplify by 100 the acquired electrical potential to transform it into a digital signal by means of an analog-to-digital converter or an embedded microcontroller. A two or three electrode configuration can be chosen to carry out the acquisition. Table 2.12 shows the main technical specifications of the device.

FIGURE 2.59: Heart rate monitor AD8232.

2.5 Evaluation tools

In this subsection, the basic components of the most commonly used evaluation metrics are defined. These metrics summarize the performance of a prediction model according

TABLE 2.12: Technical specifications of the heart rate monitor AD8232.

Operating voltage	2.0 V to 3.5 V
Operating current	170 µA
Input voltage	Up to ±300 mV
Gain	100
Conector Jack	3.5mm
Length	36 mm
Width	28 mm

to the 2x2 confusion matrix shown in Table 2.13, which contains the four possible results: true positive (TP), true negative (TN), false positive (FP) and false negative (FN).

TABLE 2.13: Confusion matrix.

		True condition		
		Positive	Negative	Total
Predicted condition	Positive	TP	FP	$TP+FP$
	Negative	FN	TN	$FN+TN$
	Total	$TP+FN$	$FP+TN$	

The terminology positive or negative refers to the assignment to a positive or negative category, while true or false refers to the assignment as correct or incorrect. Thus, a true positive is when the model correctly predicts the positive class. Similarly, a true negative is when the model correctly predicts the negative class. Conversely, a false positive is when the model incorrectly predicts the positive class. And a false negative is when the model incorrectly predicts the negative class. This phenomenon is more intuitively reflected in Figure 2.60.

To achieve an objective validation and comparison of the results obtained according to the proposed methodologies throughout this thesis, evaluation metric based on the number of TP, TN, FP and FN are employed. This results in the performance metrics presented below:

Precision (*Pr*) or positive predictive value is the number of correct positive results divided by the number of all positive results, and is calculated according to equation 2.50.

$$Pr = \frac{TP}{TP+FP} \quad (\%) \tag{2.50}$$

Sensitivity (*Se*), also called recall, true positive rate or hit rate, is the number of correct positive results divided by the total number of samples that should have been identified as positive, and is calculated according to equation 2.51.

$$Se = \frac{TP}{TP+FN} \quad (\%) \tag{2.51}$$

Specificity (*Sp*), also called selectivity or true negative rate, measures the proportion of actual negatives that are correctly identified, and is calculated according to equation 2.52.

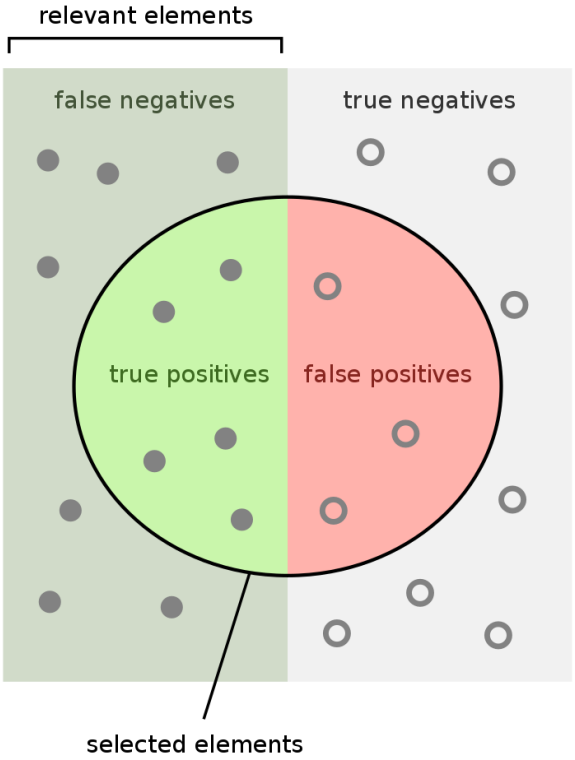

FIGURE 2.60: Graphic representation of true positives, true negatives, false positives and false negatives.
Source: Wikimedia (modified)

$$Sp = \frac{TN}{TN + FP} \quad (\%) \tag{2.52}$$

Accuracy (*Ac*) is the degree in which predictions are close to true values, and is calculated according to equation 2.53.

$$Ac = \frac{TP + TN}{TP + TN + FP + FN} \quad (\%) \tag{2.53}$$

F1 score (*F1*) is defined in this thesis as the harmonic mean of sensitivity and specificity, and is calculated according to equation 2.54.

$$F1 = 2 \cdot \frac{Se \cdot Sp}{Se + Sp} \quad (\%) \tag{2.54}$$

3 Heart period extraction: A new approach to ECG and OBP processing

Among the physiological signals used in this thesis, those related to the circulatory system require a more complex preprocessing to carry out the extraction of the heart period (HP), which is ultimately used for the extraction of cardiovascular parameters. This is mainly due to the fact that it is essential to identify the position of each heartbeat in order to extract the underlying HP signal. Each detection error can lead to a significant distortion in the resulting parameters.

Moreover, to design portable devices that perform continuous physiological recording, it is necessary to use the least invasive techniques. Among the non-invasively acquired signals, two of the most used in modern devices (e.g., smart watches and bracelets, heart rate monitors, etc.) to obtain the HP are the electrocardiogram (ECG) and the photoplethysmography (PPG). PPG is morphologically similar to the blood pressure (BP) signal, thus the algorithms employed to process them are similar in many cases. As previously explained in subsection 2.1.2, the R-peaks (in the ECG signals) and the foot points (in the PPG and BP signals) are the most commonly used references to extract the HP.

In this section, two different algorithms are presented, both with the same purpose: the calculation of the HP. On the one hand, this thesis presents an online robust R-peaks detection method applicable to noisy ECG signals using a novel iterative smart processing algorithm. On the other hand, a novel method for calculating foot points in BP signals is also proposed, which is suitable to be applied in PPG signals as well.

3.1 Online R-peaks detection in noisy electrocardiograms

For normal heart function, the ECG has the shape of the wave shown in Figure 3.1. The R-peak, located in the QRS complex, is the most characteristic waveform and it is usually employed as a reference for the ECG analysis [76]. Once the locations of the R-peaks are defined, the HP can be determined.

New technologies are increasingly leading to the acquisition of the ECG using three leads (Einthoven's triangle configuration) [38], two leads [151], or even just a single lead [152]. These configurations are vulnerable to artifacts such as baseline wander, electromyogram noise and power line interference, among others [153, 154, 155, 156, 157]. These artifacts

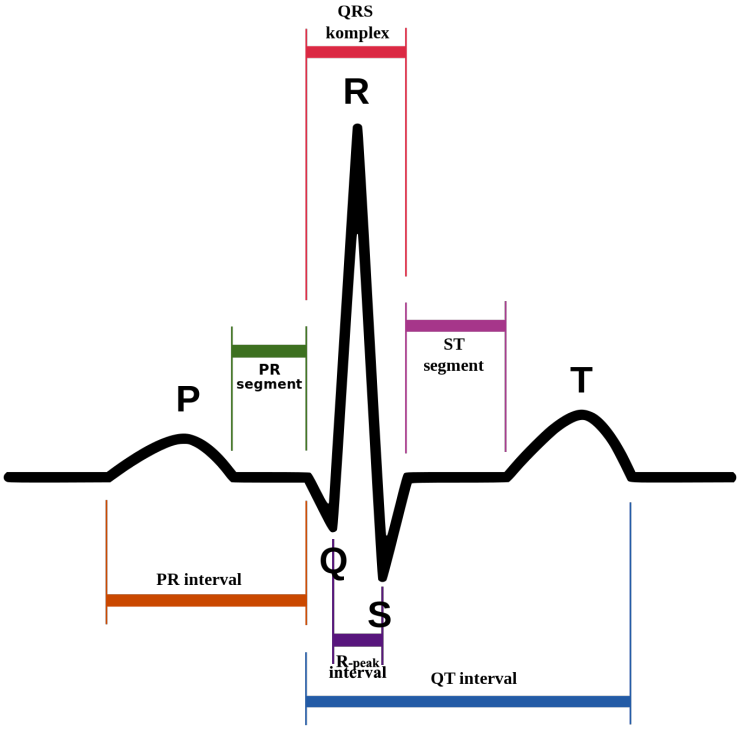

FIGURE 3.1: Intervals of the PQRST complex.

are shown in Figure 3.2, where graphs (a-d) correspond to ECG registers from the data set presented in subsection 2.3.1.

In this subsection, a robust R-peak detection algorithm is presented, where a short length sliding window (SW) is used for real-time ECG processing. Under these conditions, an error in the detection of R-peaks can generate an even greater error in the subsequent extraction of temporal, frequency and nonlinear parameters, which makes correct detection of R-peaks crucial. To achieve this, a novel iterative computing approach for ECG analysis is proposed in this thesis. In the scheme in Figure 3.3, the different steps of the developed algorithm are shown: in the first preprocessing step, artifacts are removed, followed by R-peaks detection by applying a computationally efficient analysis of the area over the QRS complex. Detected R-peaks are subsequently analyzed through a smart iterative algorithm, which is composed of three sequentially executed state machines (SMs). These SMs correct all detected false positives (FPs) or surplus R-peaks and false negatives (FNs) or undetected R-peaks, improving the final result. Furthermore, computational load and achieved results are discussed and compared with other methods in the literature at the end of this subsection.

The proposed algorithm was created and validated using two different data sets. The ECG signals recorded during the experiment presented in subsection 2.3.1 were used for preliminary development. By contrast, this proposal was tested on a large scale, processing the MIT-BIH arrhythmia database (MITADB) [151] presented in subsection 2.3.2, which is a gold standard in the validation of ECG processing algorithms.

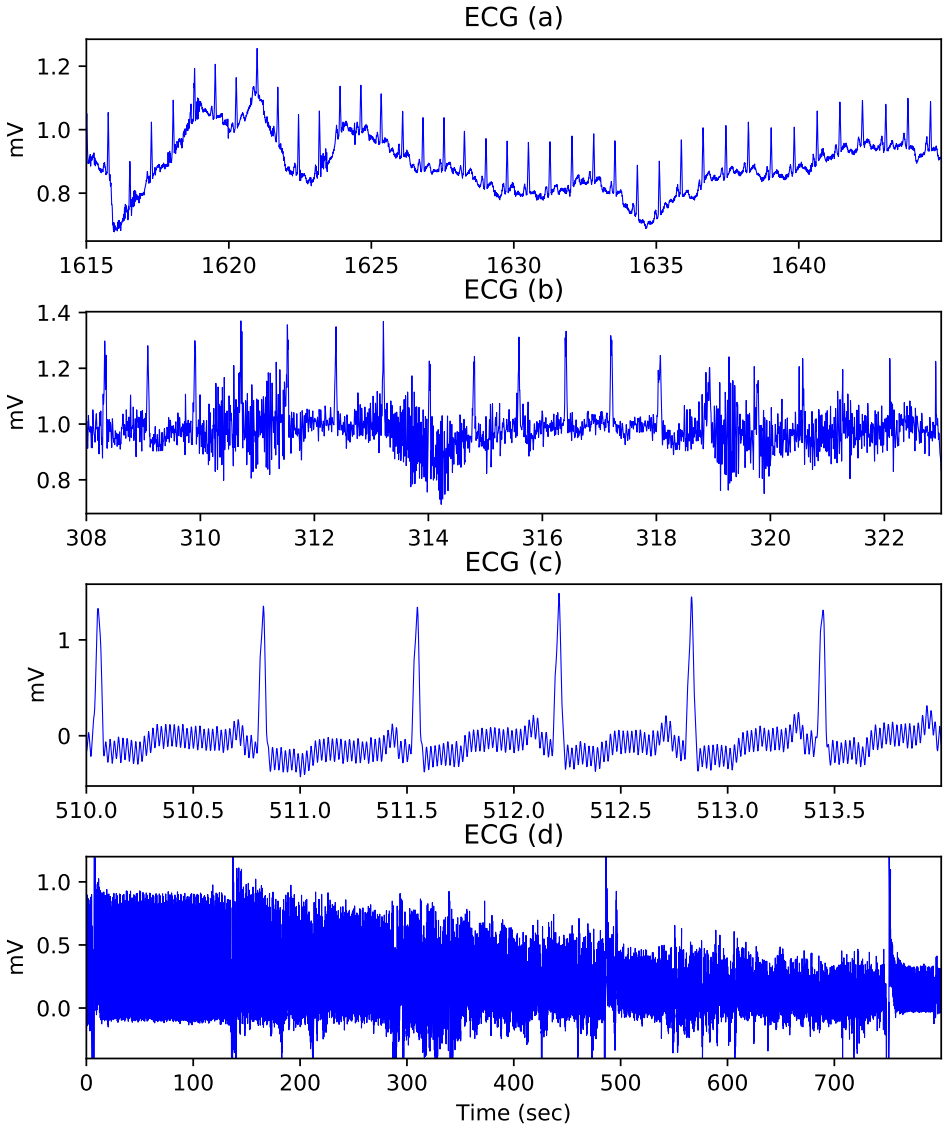

FIGURE 3.2: Artifacts present in an ECG signal acquired with Biopac MP36/150 in a daily situation: a) Baseline wander b) White noise c) Network 50Hz electromagnetic interference d) Loss of sensor conduction resulting in a loss of signal strength.

ECG analysis is divided into two main steps: a first artifact removal step and a second R-peak detection step. Among the proposed strategies, this method processes ECG by means of a short length SW. Specifically, a 20-second SW is used, since it contains enough information for robust real-time parameter extraction [7, 38].

3.1.1 Preprocessing: ECG cleaning

This solution proposes temporal-domain methods to perform, in two stages, the removal of artifacts that affect the ECG. Due to the distortions generated in the R-peaks positions when modifying the spectrum and the high computational load, frequency-domain methods were discarded [79]. Among the aforementioned artifacts, first, baseline wander is

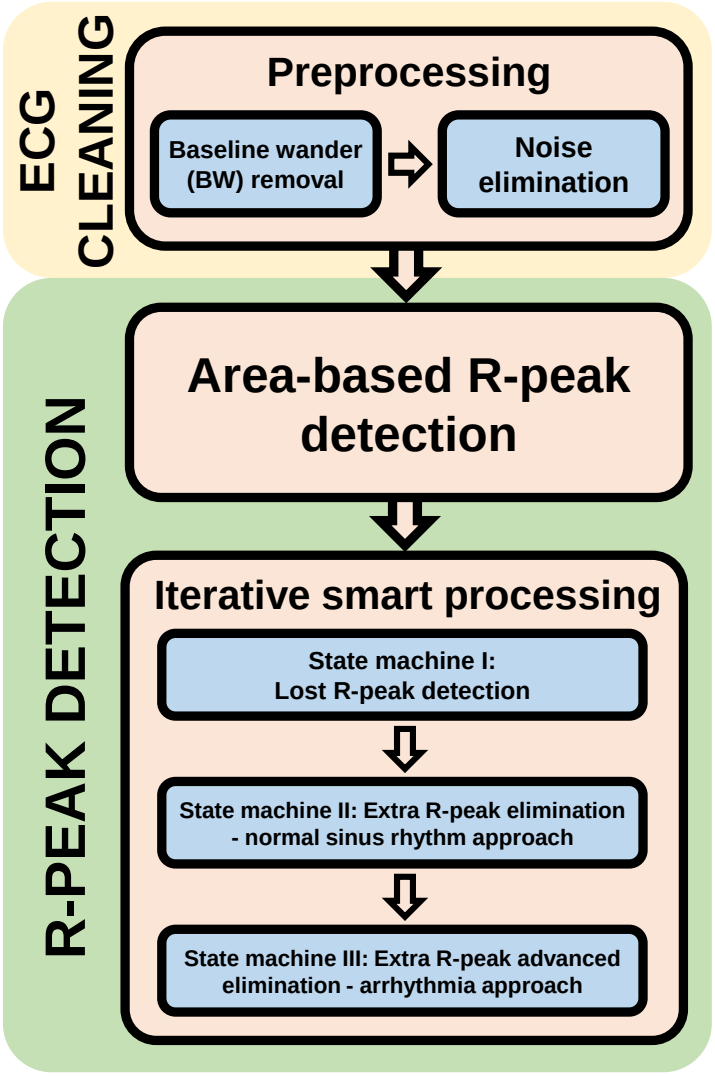

FIGURE 3.3: Scheme of the proposed R-peak detection method.

eliminated. Second, the artifacts due to electromyogram noise and power line interference are removed as illustrated in the example in Figure 3.4.

ECG baseline wander removal

The interaction between the electrodes and the skin can generate a low-frequency artifact commonly called baseline wander (BW) [156, 154, 94]. Several techniques are proposed in the literature for the elimination of BW such as wavelet filters, adaptive filters and high pass filters, among others [156, 157, 155, 158].

In this step, a computationally efficient cubic interpolation of the stepped moving median filtering is proposed for BW removal. The high amplitude and short-duration of the R-peaks make them ideal to be filtered using a moving median filter [156, 155, 94, 82, 158]. However, the computational load required to calculate the median value for each sample can be quite high.

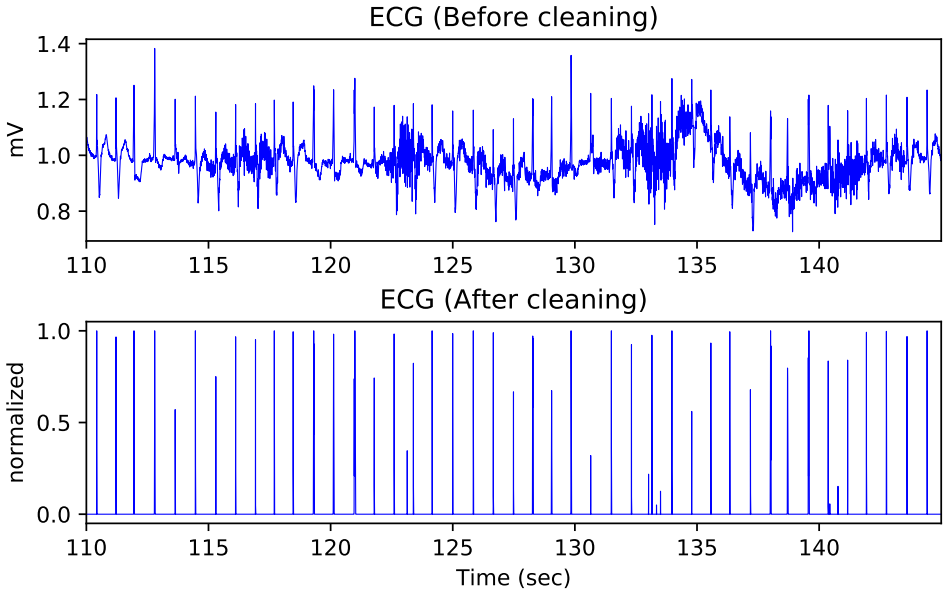

FIGURE 3.4: MITADB ECG signal frame (record 104) before and after preprocessing. The resulting signal consists of the normalized R-peaks in the range [0, 1].

The proposed approach is based on the union of the stepped median points (p_i) by performing the cubic interpolation according to equations 3.1 and 3.2 respectively, where S_x^i is the ECG frame defined by the width of the median filter in the i^{th} processing step.

$$p_i(x) = \text{median}_{t \in S_x^i}\{ECG_t\} \tag{3.1}$$

$$\begin{aligned} BW_i^{i+1} = &\Big(-\frac{1}{2}p_{i-1} + \frac{3}{2}p_i - \frac{3}{2}p_{i+1} + \frac{1}{2}p_{i+2}\Big)x^3 + \Big(p_{i-1} - \\ &\frac{5}{2}p_i + 2p_{i+1} - \frac{1}{2}p_{i+2}\Big)x^2 + \Big(-\frac{1}{2}p_{i-1} + \frac{1}{2}p_{i+1}\Big)x + p_i \end{aligned} \tag{3.2}$$

To maintain R-peaks intact, the width of the median filter must be greater than twice the width of the R-peak. However, it should be as small as possible, as the computational load increases proportionally to the width of the median filter. Considering that the width of a normal R-peak has an average value of around 60 milliseconds [159], in this development a 150-millisecond median filter is proposed. Moreover, to set up the width of the step, the overlap of the median filter window was considered, thus establishing half the width of the median filter. Figure 3.5 illustrates the ECG signal before and after the BW removal (ECG′), performed according to equation 3.3.

$$ECG' = ECG - BW \tag{3.3}$$

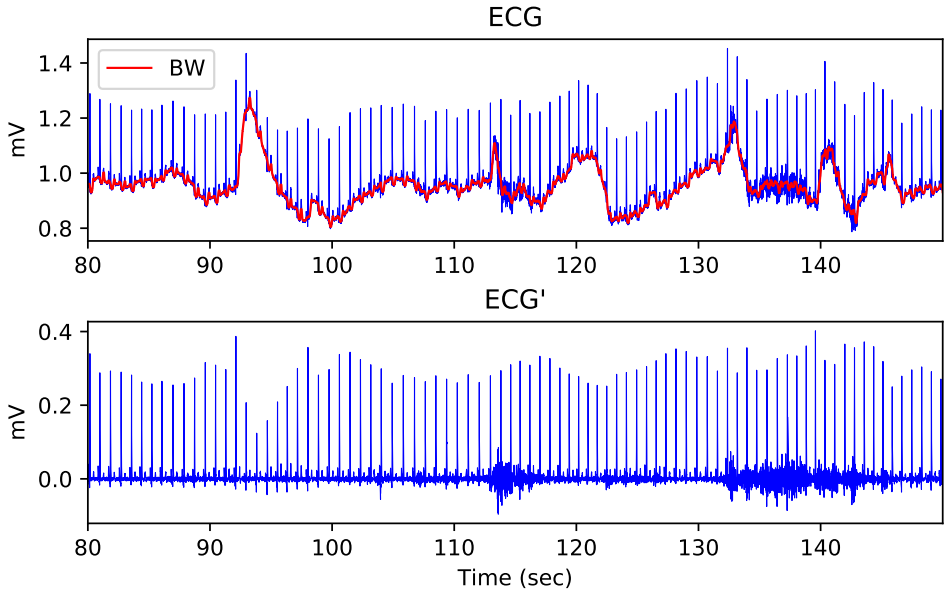

FIGURE 3.5: ECG signal before (top graph) and after (bottom graph) the BW removal.

Noise elimination

Electromyogram noise and power line interference also generate harmful artifacts that must be removed. In this thesis, a novel solution based on the processing of signal and noise intensity values is proposed in order to calculate a dynamic cutting line (CL: black line in Figure 3.6) according to equation 3.6. The ECG is further processed (ECG″) according to equation 3.7, where the signal is cut keeping R-peaks and eliminating the noise below the CL. The necessary parameters to calculate the CL are explained below:

- Signal Intensity (SI): It consist of the maximum values of the ECG according to equation 3.4 (green line in Figure 3.6), where the largest R-peak amplitudes are considered to generate the SI line. A SW (width: 1 second, step: 0.5 second) is used to loop through the signal and obtain the maximum values.

$$SI_i(x) = \max_{t \in S_x^i} \{ECG'_t\} \tag{3.4}$$

- Noise Intensity (NI): It consists of the standard deviation of the ECG according to equation 3.5 (pink line in Figure 3.6), where the value of the resulting standard deviation is multiplied by 2 so that 95% of the noise is below the NI line. A SW (width: 1 second, step: 0.5 second) is used to loop through the signal and obtain the standard deviation values.

$$NI_i = 2 * \sqrt{\frac{1}{fs-1} \sum_{j=i-fs/2}^{i+fs/2} \left(ECG'_j - \overline{ECG'}\right)^2} \tag{3.5}$$

- Aggressiveness level (α): This parameter is used to calibrate the aggressiveness level in the elimination of noise during the cut, where the CL is calculated according to equation 3.6. Best empirical results were obtained with an α value equal to 5 for the whole data set. This value should be set according to the quality of the signal acquired by the device in which the proposed solution is implemented, with 1 the most aggressive value and 10 the least aggressive.

$$CL_i = NI_i + (SI_i - NI_i) \cdot \frac{10 - \alpha}{9} \qquad \{\alpha \in \mathbb{R} \mid 1 \leq \alpha \leq 10\} \tag{3.6}$$

$$ECG''_i = \begin{cases} ECG'_i - CL_i & \text{if } ECG'_i > CL_i \\ 0 & \text{if } ECG'_i \leq CL_i \end{cases} \tag{3.7}$$

Finally, a normalization is carried out (ECG$'''$ in the top graph in Figure 3.6) according to equation 3.8, to keep the signal in the range [0, 1].

$$ECG'''_i = \frac{ECG''_i}{SI_i - NI_i} \tag{3.8}$$

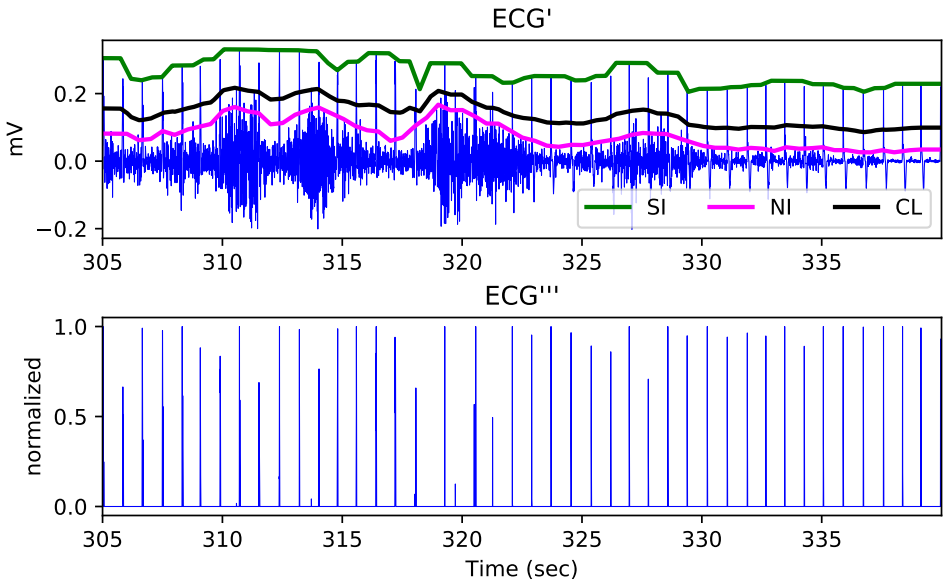

FIGURE 3.6: ECG signal affected by electromagnetic interference (top graph) and the resulting artifact-free ECG after removing noise below the CL (bottom graph).

3.1.2 R-peak detection

Two phases are differentiated throughout the R-peak detection step. First, a general detection of R-peaks is performed based on the analysis of the area over the QRS complexes [152]. Second, erroneous detections are corrected through a new algorithm consisting

of three SMs, where previously detected R-peaks are evaluated using a set of conditions based on expert knowledge.

Area-based R-peak detection

Considering the fact that R-peaks are typically narrow and have a large amplitude as previously shown in Figure 3.1, in the area-based R-peak detection method the neighbors (N) are defined for each local maximum in ECG''', which correspond to half the value of the duration of the QRS complex (W). Furthermore, M is defined as the amplitude of the local maximum [152]. The area-based R-peak detection consists of calculating, according to equation 3.9, the area over the QRS complex. The resulting area corresponds to the blue area represented in Figure 3.7.

Essentially, for high, narrow peaks such as R-peaks, the area over the curve is high. The remaining peaks corresponding to the PQRST complex do not have this morphology, so the value of the resulting area is small. According to the literature, a QRS complex has a duration of 100 ms, which was considered in this solution for the implementation of equation 3.9 [76, 152, 159, 160, 161].

$$area = \frac{1}{2 \cdot N} \sum_{i=-N \cdot fs}^{N \cdot fs} \left(M - ECG_i''' \right) \tag{3.9}$$

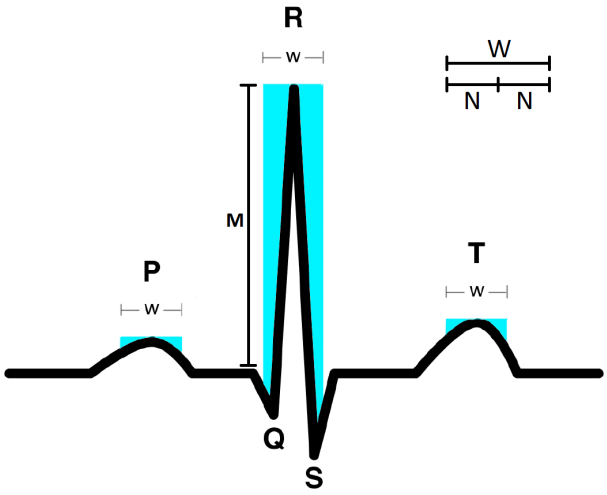

FIGURE 3.7: Areas (blue shading) over the PQRST local maxima.
Source: Liao et al. [152] (modified)

To know which area values correspond to R-peaks and which do not, this solution proposes the definition of a cut-off value. This value was configured according to an analysis performed on all areas of the data set presented in subsection 2.3.1. A total of 321449 areas were detected, of which 313078 were R-peaks. The result of this analysis is represented graphically in Figure 3.8, where the logarithmic scale is used to improve visualization. The highest accuracy was achieved with a cut-off value of 0.55 (black line), which corresponds to the minimum number of FPs and FNs.

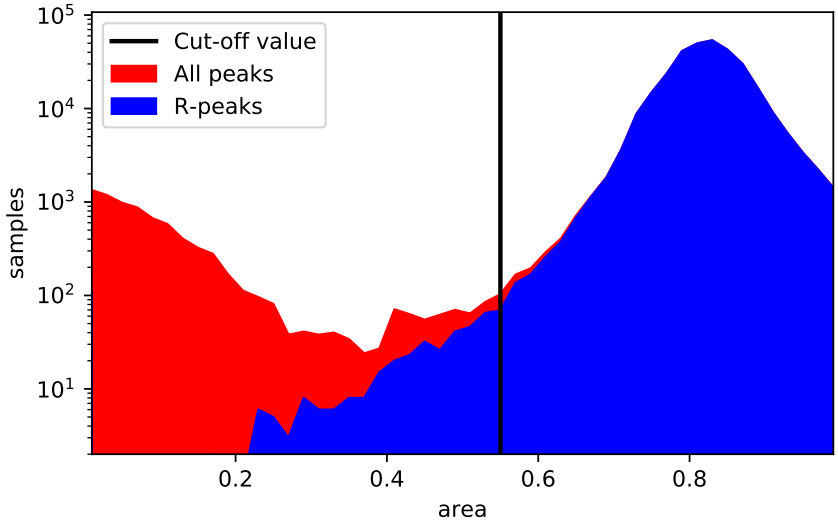

FIGURE 3.8: Area value distribution of all peaks (red) versus area value distribution of R-peaks (blue).

Iterative smart processing method

Some pathologies, such as the premature ventricular contraction (PVC) illustrated in Figure 3.9, can cause erroneous R-peak detections due to their morphologies. This may result in an area different from that of the R-peaks, leading to the appearance of FNs. Something similar happens when very noisy sections are removed from ECG during the filtering step. In this case, the amplitude of some R-peaks is reduced as illustrated in Figure 3.10, where the value of some areas does not overcome the cut-off value.

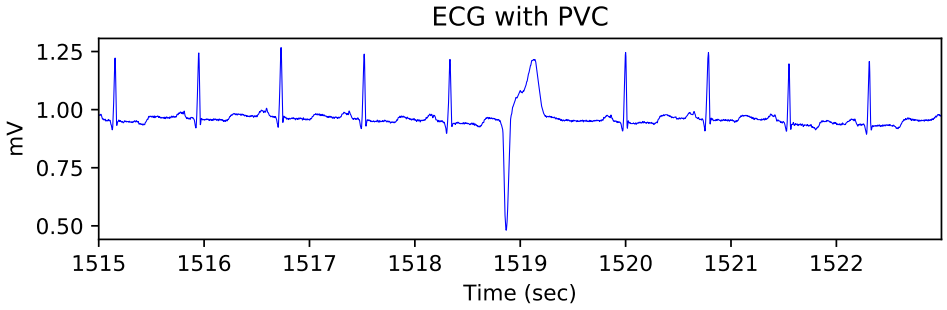

FIGURE 3.9: A premature ventricular contraction in a signal from the MITADB.

To improve and strengthen the detection of R-peaks in ECG signals strongly affected by artifacts, three sequentially executed SMs are proposed. These SMs are designed to perform a selective detection and elimination of FP and FN based on a set of predefined conditions. They perform a set of conditional operations that associate the distances between the detected R-peaks to perform a smart optimization. The constants used to define these

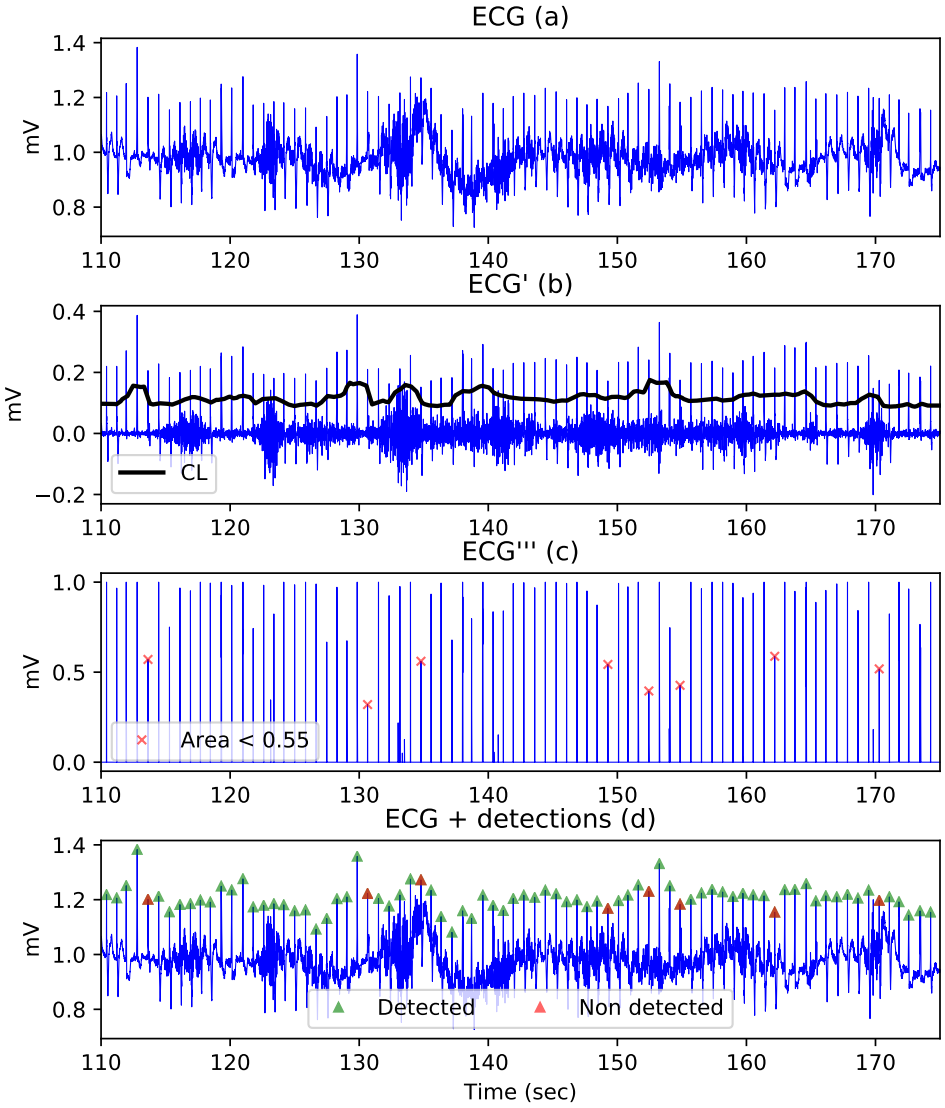

FIGURE 3.10: Particular case of non-detected R-peaks that do not overcome the cut-off value: a) Real ECG signal frame, b) ECG with BW filtered (ECG'), c) Cut and normalized ECG (ECG'''), d) Non-detected peaks in red.

conditions were extracted empirically from the observation of patterns related to the appearance of FPs and FNs. First, the detection of undetected R-peaks is performed. Second, the surplus R-peaks are eliminated according to conditions based on normal HP sinus rhythm. Third, the remaining FPs are removed considering variations in HP due to possible arrhythmias.

To calculate HP, the detected R-peaks are used according to equation 2.6, previously introduced in subsection 2.1.2, where *rpeaks* is an N_H length array composed of the timestamps of the detected R-peaks.

In addition, minimum HP (HP_{min}), maximum HP (HP_{max}) and median HP ($median(HP)$) are used to normalize the conditions of the SMs for different registers.

SM I - Lost R-peak detection

To effectively remove surplus FPs, first, it is necessary to have enough information by detecting all R-peaks that have not been previously detected. This first SM was created to analyze the distances between the detected R-peaks iteratively looking for abnormal events that indicate the lack of undetected R-peaks. This process is illustrated in the scheme in Figure 3.11 and depends on the condition represented in equation 3.10, which considers the cases in which an FN occurs.

$$\begin{aligned} &Condition_1 = \\ &(HP_i > \max(HP)) \cap (HP_i > 1.7 \cdot \text{median}(HP)) \cap \\ &(1.3 \cdot HP_{i-1} < HP_i) \cup (HP_i > 1.3 \cdot HP_{i+1}) \cap \\ &(HP_i > 1.5 \cdot HP_{i+1}) \cap (HP_i > 1.5 \cdot HP_{i-1}) \cap \\ &(1.3 \cdot HP_{i-1} < HP_i) \cup (1.3 \cdot HP_{i-2} < HP_i) \cap \\ &(1.3 \cdot HP_{i+1} < HP_i) \cup (1.3 \cdot HP_{i+2} < HP_i) \end{aligned} \tag{3.10}$$

The activation of condition 1 refers to the fact that the algorithm detects an FN, leading to the search for the missing R-peak between the two consecutive R-peaks where it is supposed to be. During this process, the cut-off value is reduced to 0.4, which provides a greater margin for detecting missing R-peaks that might have been overlooked during the first search. However, if several peaks are detected with an area over the QRS complex greater than 0.4, the largest one is taken. If none is detected, the maximum value will be considered as the missing R-peak.

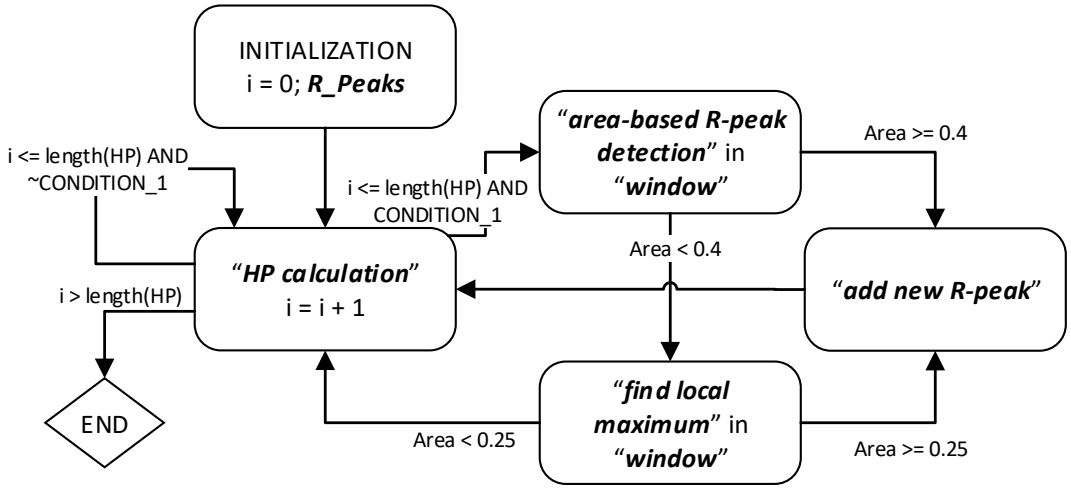

FIGURE 3.11: First SM for missing R-peak detection. "***area-based R-peak detection***" is the processing carried out in section 3.1.2. "***window***" is the signal frame that goes from $rpeaks_i$ to $rpeaks_{i+1}$. "***find local maximum***" looks for the maximum value in "***window***". "***add new R-peak***" is a function that adds the new R-Peak to the set of detected R-peaks.

SM II - Extra R-peak elimination: a normal sinus rhythm approach

In the second SM, it is assumed that the HP morphology corresponds to a normal sinus rhythm in order to perform a search for FPs from the R-peaks obtained from the previous SM. To attain this, condition 2.1 and 2.2 were defined according to equations 3.11 and 3.12, respectively. These are based on the fact that each HP is related to contiguous HPs, so certain distances between contiguous R-peaks must be maintained.

$$\begin{aligned} Condition_{2.1} = (HP_i < \min(HP)) \cup \\ (HP_i < 0.6 \cdot \text{median}(HP)) \cup (W_t < 2.5 \cdot \text{median}(HP)) \end{aligned} \tag{3.11}$$

$$\begin{aligned} Condition_{2.2} = (HP_i < \min(HP)) \cup \\ (HP_i < 0.6 \cdot \text{median}(HP)) \cup (W_t \geq 2.5 \cdot \text{median}(HP)) \end{aligned} \tag{3.12}$$

Both conditions depend on "***window***" (W_t), which consists of a dynamically generated series of R-peaks, corresponding to consecutive HPs that meet the conditions $HP_i < HP_{min}$ and $HP_i < 0.6 * median(HP)$. These conditions were deduced empirically from the observation of patterns related to the appearance of FPs.

On the one hand, the activation of condition 2.1 means that the R-peak related to the current index "i" is an FP. On the other hand, activation of condition 2.2 means that at least one R-peak is considered an FP, which results in a selective R-peak elimination. The full process is illustrated in the scheme in Figure 3.12.

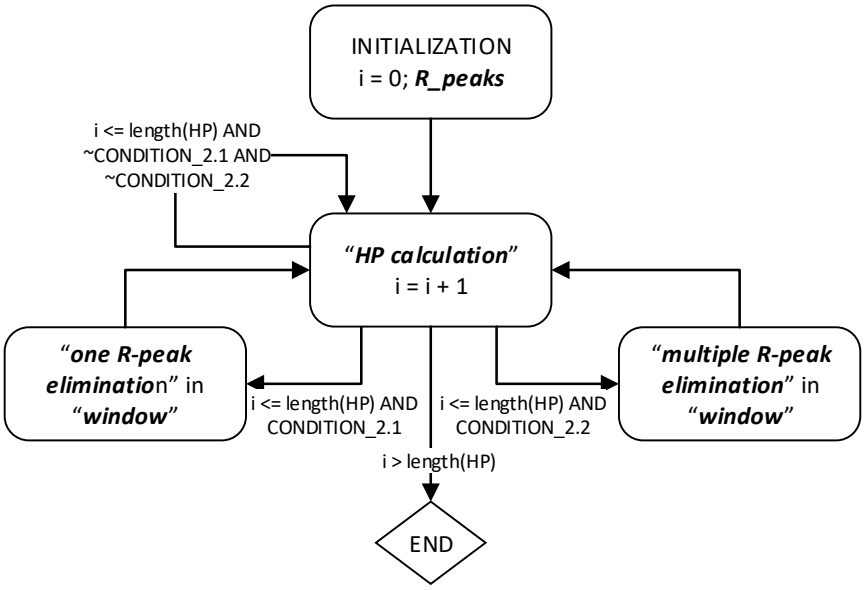

FIGURE 3.12: Second SM for surplus R-peak elimination. "***window***" is the signal frame where consecutive surplus R-peaks have been detected. "***one R-peak elimination***" removes one R-peak from "***window***" when condition 2.1 is met. "***multiple R-peak elimination***" removes at least one R-peak from "***window***" when condition 2.2 is met.

SM III - Extra R-peak advanced elimination: an arrhythmia approach

Since the second SM only considers normal sinus rhythm situations, arrhythmia situations could be problematic. The third SM performs a more sophisticated process focused on FP elimination by considering HP variations during arrhythmia events. Each HP is analysed in a broader context, considering a wider range of distances between contiguous R-peaks according to conditions 3.1-3.5, which are defined in 3.13, 3.14, 3.15, 3.16 and 3.17, respectively. Since these conditions make the algorithm very sensitive to an excess of FP, it was necessary to first perform a raw FP elimination in the second SM.

$$\begin{gathered} Condition_{3.1} = \\ (1.2 \cdot (HP_1 + HP_2) > HP_3 > (HP_1 + HP_2)/1.2) \cup \\ (1.2 \cdot (HP_1 + HP_2) > HP_4 > (HP_1 + HP_2)/1.2) \cup \\ (HP_3 > \min(HP)) \cup (HP_4 > \min(HP)) \end{gathered} \tag{3.13}$$

$$\begin{gathered} Condition_{3.2} = \\ (1.2 \cdot (HP_{i+1} + HP_{i+2}) > HP_i > (HP_{i+1} + HP_{i+2})/1.2) \cup \\ (1.2 \cdot (HP_{i+1} + HP_{i+2}) > HP_{i+3} > (HP_{i+1} + HP_{i+2})/1.2) \cup \\ (HP_i > \min(HP)) \cup (HP_{i+3} > \min(HP)) \end{gathered} \tag{3.14}$$

$$\begin{gathered} Condition_{3.3} = \\ (1.2 \cdot (HP_{N-1} + HP_N) > HP_{N-2} > (HP_{N-1} + HP_N)/1.2) \cup \\ (1.2 \cdot (HP_{N-1} + HP_N) > HP_{N-3} > (HP_{N-1} + HP_N)/1.2) \cup \\ (HP_{N-2} > \min(HP)) \cup (HP_{N-3} > \min(HP)) \end{gathered} \tag{3.15}$$

$$\begin{gathered} Condition_{3.4} = \\ (1.2 \cdot (HP_{i+1} + HP_{i+2}) > HP_{i+2} > (HP_{i+1} + HP_{i+2})/1.2) \cup \\ (1.2 \cdot (HP_{i+1} + HP_{i+2}) > HP_{i+3} > (HP_{i+1} + HP_{i+2})/1.2) \cup \\ (1.1 \cdot HP_{i+3} > HP_{i+2} > HP_{i+3}/1.1) \cup \\ (1.1 \cdot HP_{i+2} > HP_{i+3} > HP_{i+2}/1.1) \cup \\ (HP_{i+2} > \min(HP)) \cup (HP_{i+3} > \min(HP)) \cup \\ (HP_i + HP_{i+1} > \min(HP)) \cup (HP_i + HP_{i+1} < \max(HP)) \end{gathered} \tag{3.16}$$

$$\begin{gathered} Condition_{3.5} = \\ (1.2 \cdot (HP_{i+2} + HP_{i+3}) > HP_i > (HP_{i+2} + HP_{i+3})/1.2) \cup \\ (1.2 \cdot (HP_{i+2} + HP_{i+3}) > HP_{i+1} > (HP_{i+2} + HP_{i+3})/1.2) \cup \\ (HP_i > \min(HP)) \cup (HP_{i+1} > \min(HP)) \end{gathered} \tag{3.17}$$

Moreover, several irregularities due to arrhythmia events are considered in these conditions as a result of the displacement of the R-peaks in relation to their expected position in normal sinus rhythm circumstances. The fulfilment of any of these five conditions during the analysis of an R-peak implies that the peak is an FP and, thus, must be eliminated. The full process is illustrated in the scheme in Figure 3.13.

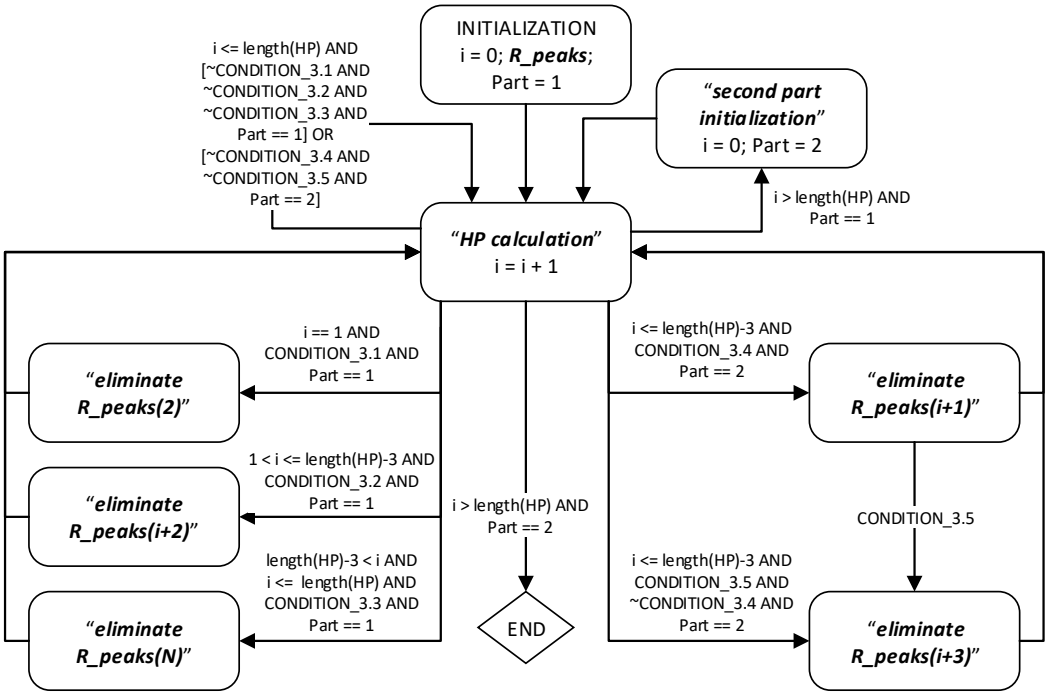

FIGURE 3.13: Third SM for an advanced surplus R-peak elimination. "***second part initialization***" initializes the parameters for the execution of the conditions of the second part of the SM. "***eliminate rpeaks(x)***" eliminates R-peaks in position ***x***.

As a result of applying the proposed iterative smart processing method, Figure 3.14 illustrates the detection of the resulting R-peaks after processing the initially detected peaks previously shown in Figure 3.10 through the three SMs.

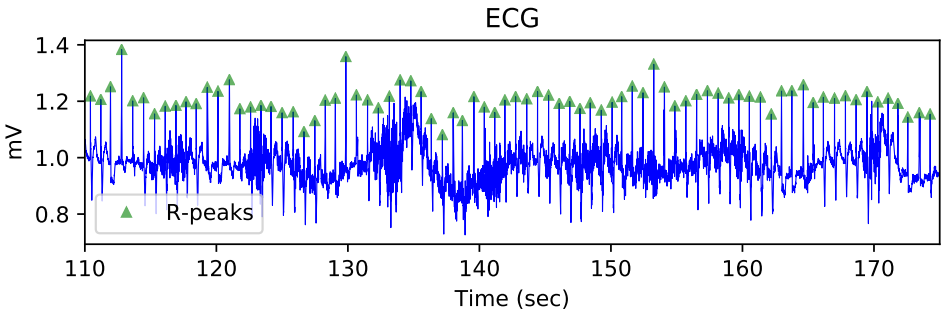

FIGURE 3.14: Resulting R-peaks detection after running the iterative smart processing method.

3.1.3 Results and discussion on R-peak detection

To validate and compare the proposed R-peak detection algorithm, MITADB was used [151], which is a gold standard in the validation of algorithms related to ECG processing. In Table 3.1 results obtained are presented according to precision (*Pr*) and sensitivity (*Se*) measures, corresponding to previously defined equations 2.50 and 2.51, respectively. For this purpose, the number of TPs, FPs and FNs were obtained.

TABLE 3.1: Performance of the proposed algorithm in the MITADB.

Tape No.	#annotations	TP	FP	FN	Se(%)	Pr(%)
100	2273	2273	0	0	100.00	100.00
101	1865	1864	3	1	99.95	99.84
102	2186	2185	2	1	99.95	99.91
103	2084	2084	0	0	100.00	100.00
104	2228	2227	3	1	99.96	99.87
105	2559	2557	9	2	99.92	99.65
106	1978	1970	0	8	99.60	100.00
107	2099	2093	3	6	99.71	99.86
108	1755	1753	73	2	99.89	96.00
109	2521	2519	0	2	99.92	100.00
111	2124	2124	0	0	100.00	100.00
112	2539	2539	0	0	100.00	100.00
113	1795	1795	0	0	100.00	100.00
114	1875	1874	183	1	99.95	91.10
115	1953	1953	0	0	100.00	100.00
116	2393	2390	1	3	99.87	99.96
117	1533	1532	0	1	99.93	100.00
118	2275	2275	0	0	100.00	100.00
119	1958	1953	0	5	99.74	100.00
121	1863	1862	0	1	99.95	100.00
122	2476	2476	0	0	100.00	100.00
123	1516	1515	0	1	99.93	100.00
124	1614	1613	0	1	99.94	100.00
200	2587	2585	8	2	99.92	99.69
201	1806	1783	1	23	98.73	99.94
202	2124	2122	1	2	99.91	99.95
203	2557	2496	24	61	97.61	99.05
205	2627	2622	0	5	99.81	100.00
207	1803	1794	89	9	99.50	95.27
208	2424	2348	4	76	96.86	99.83
209	3004	3003	0	1	99.97	100.00
210	2531	2514	1	17	99.33	99.96

Continued on next page

Table 3.1 – *Continued from previous page*

Tape No.	#annotations	TP	FP	FN	Se(%)	Pr(%)
212	2748	2748	0	0	100.00	100.00
213	3212	3206	0	6	99.81	100.00
214	2216	2209	1	7	99.68	99.95
215	3304	3295	1	9	99.73	99.97
217	2207	2206	1	1	99.95	99.95
219	2115	2109	0	6	99.72	100.00
220	2036	2034	0	2	99.90	100.00
221	2405	2401	0	4	99.83	100.00
222	2414	2403	0	11	99.54	100.00
223	2458	2436	0	22	99.10	100.00
228	2042	2040	9	2	99.90	99.56
230	2254	2253	0	1	99.96	100.00
231	1886	1885	2	1	99.95	99.89
232	1136	1043	12	93	91.81	98.86
233	2472	2385	0	87	96.48	100.00
234	2751	2750	0	1	99.96	100.00
Total	**106581**	**106096**	**431**	**485**	**99.54**	**99.60**

The overall results are quite promising considering the high success during the R-peak detection and the low number of FP, which correspond to a *Se* and *Pr* values of 99.54% and 99.60%, respectively.

It was found that the non-detection of some of the R-peaks is due to their large width, as occurs in PVC. In these cases, the area over the QRS complex has a small value, which means that it is not identified as an R-peak during the area-based R-peak detection stage. Some of the processed records present this phenomenon, i.e., records 114, 207 and 208, among others.

Moreover, there were difficulties in processing record 207 due to the left bundle branch block events along with first-degree atrioventricular block, in addition to the multiform PVCs. In record 114, the large amount of PVCs led to erroneous detections during the area-based R-peak detection. The amount of undetected R-peaks in register 208 is also remarkable, mainly due to uniform PVCs and ventricular and normal beat fusions. Several R-peaks were not detected during the processing of the SMs in register 232, mainly due to the ineffectiveness of distance-based conditions on sections affected by long intervals between consecutive R-peaks (up to 6 seconds). Finally, record 208 contains several multiform PVCs, along with first-degree atrioventricular blocks, which resulted in a considerable amount of FPs.

In Table 3.2, the proposed algorithm is compared with other works in the literature according to the *Pr* and *Se* obtained in the records from the MITADB. As proposed by Kooler et al.

[79], the computational load is considered in the comparison, and it is represented as low, medium and high according to the complexity of the techniques used for the detection of R-peaks and the generation of signal features.

TABLE 3.2: Performance comparison in the MITADB (first channel).

Method	#peaks	TP	FP	FN	Se(%)	Pr(%)	Load [79]
Pan and Tompkins [84]	109809	109208	507	601	99.45	99.54	High
Hamilton and Tompkins [85]	109267	108927	248	340	99.69	99.77	Medium
Saxena et al. [90]	103763	103664	102	99	99.90	99.90	Medium
Martinez et al. [91]	109428	109208	153	220	99.80	99.86	High
Ghaffari et al. [92]	109428	109327	129	101	99.91	99.88	High
Choouakri et al. [93]	109488	108043	3068	1445	98.68	97.24	High
Zhang et al. [162]	109510	109297	204	213	99.81	99.81	Medium
Christov [99]	110050	109548	215	502	99.54	99.80	Medium
Chen et al. [100]	110050	109615	239	435	99.60	99.78	Medium
Afonso et al. [88]	90909	90535	406	374	99.59	99.55	Low
Bahoura et al. [95]	109809	109635	135	174	99.84	99.88	Medium
Li et al. [96]	104182	104070	65	112	99.89	99.94	High
Proposed method	**106581**	**106096**	**431**	**485**	**99.54**	**99.60**	**Low**

High *Pr* and *Se* values were achieved in all works compared in Table 3.2. However, there are greater differences in computational load, which is particularly important in real-time processes with tight restrictions. In addition, computational load is also related to energy expenditure, which is critical in portable devices focused on long-term ECG acquisition such as medical devices or smart watches and wristbands. The proposed algorithm was tested on low-cost portable devices such as the Raspberry Pi boards, leading to effective, real-time detection of the R-peak in real-world conditions.

Moreover, the proposed algorithm was validated on the MITADB, demonstrating that it is capable of detecting accurately R-peaks in signals strongly affected by both artifacts and disturbances due to cardiovascular diseases. This robustness is fundamental in the follow-up of patients suffering from these cardiovascular diseases.

3.2 Pulse wave foot point detection

In this subsection, a novel oscillometric foot point (FPO) detection algorithm is presented. The FPO is defined as the point of minimum amplitude of the oscillometric BP (OBP) valley as illustrated in Figure 3.15, and is located between the rear front of the current wave and the forefront of the subsequent wave.

The OBP data set presented in subsection 2.3.3, which was provided by the ECG clinics at Auckland City Hospital and Greenlane Clinical Centre, Auckland, New Zealand, was used for the development and validation of the proposed FPO detection algorithm. OBP measurements were performed using the commercially available BP+ device (USCOM Limited, Sydney, Australia). The FPOs automatically detected by the BP+ were subsequently

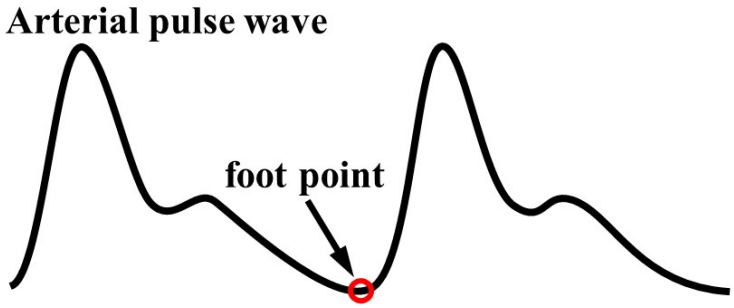

FIGURE 3.15: Graphical representation of the FPO.

corrected manually due to erroneous detections caused by several types of signal artifacts. Some of those artifacts (e.g., noise and baseline wander) are presented in Figure 3.16, where the displayed signals correspond to real OBP records from the data set.

In Kazanavicius et al. [104] some of the most used algorithms in the detection of FPOs are introduced, i.e., the tangent intersection foot-to-foot method, the OBP foot polynomial approximation method, the second derivative maximum method and the bottom straight-line and forefront tangent intersection method, among others. It is proven that in these methods accuracy decreases the lower the signal-to-noise ratio is. This fact is particularly concerning considering that FPO detection errors during short duration OBP frames processing generate deviations in the values of the parameters extracted from them.

To perform a robust FPO detection, a method based on several steps is proposed. These steps are illustrated in the schematic in Figure 3.17, where an accurate FPO detection is accomplished through two newly developed techniques: the moving interpolation difference method for BW removal and an improved second derivative maximum method for local minimum detection. These methods are later used to extract OBP parameters to train an artificial neural network (ANN) model for FPO detection.

3.2.1 OBP baseline wander elimination

Existing methods have shown good performance for FPO detection in relatively artifact-free signals. However, they are less efficient at processing registers that are strongly affected by artifacts such as BW and noise [104]. While noise generates minor distortions that do not critically affect the signal morphology, BW can completely displace the local minima of the valleys in OBP signals, resulting in false FPO locations, as illustrated in the example in Figure 3.18.

Looking closer, two trends are distinguished in OBP signals. The first due to short-term variations, corresponding to changes in the OBP signal mainly induced by heartbeats (red lines in Figure 3.19). The second due to long-term variations, which are caused by the BW (green lines in Figure 3.19).

This phenomenon led to the study of techniques focused on short- and long-term analysis of temporal signals. One such technique is to use the difference between two averages

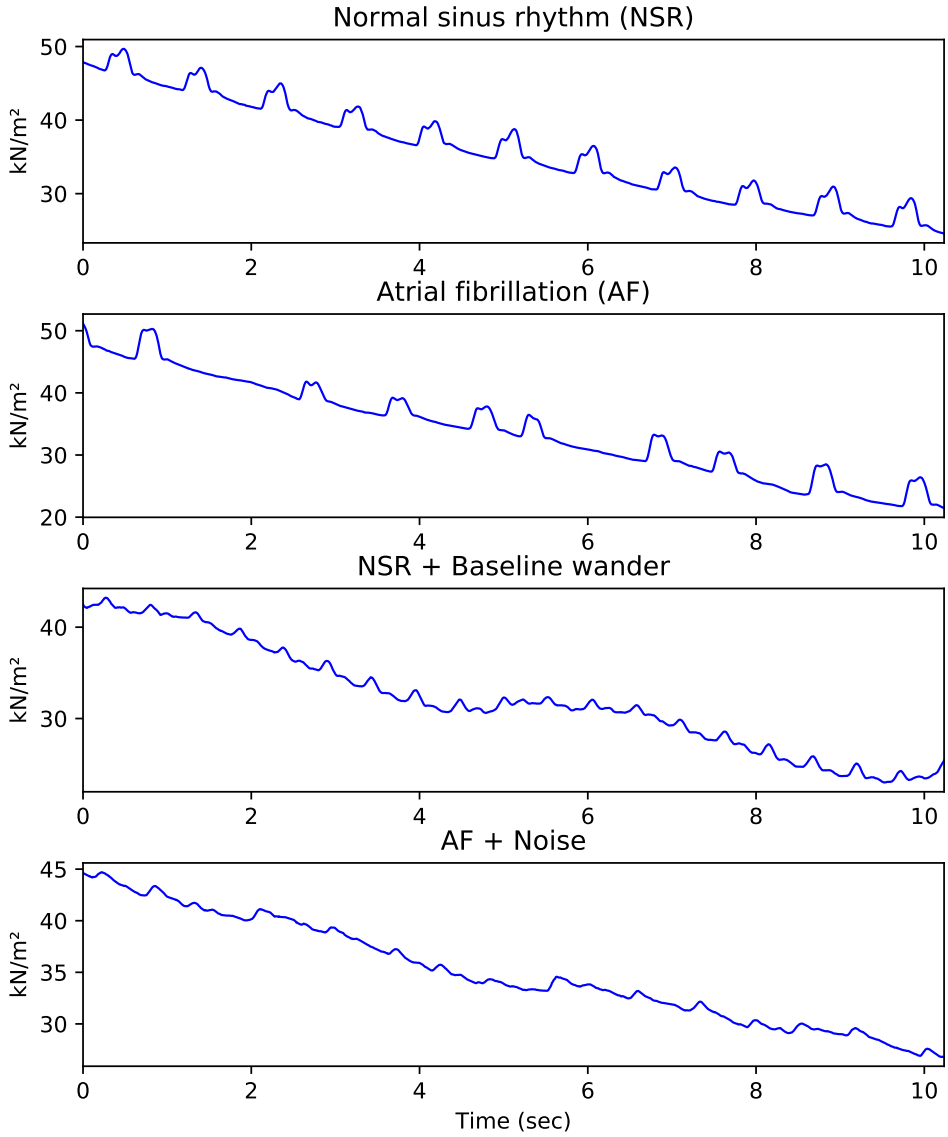

FIGURE 3.16: OBP records corresponding to normal sinus rhythm and atrial fibrillation in the upper graphs, affected by different artifacts in the lower graphs.

calculated from short- and long-term SWs to detect relevant trend changes. This method is known as the moving average convergence-divergence method [163].

In this development, the moving average convergence-divergence method was adapted, replacing the averages with slopes values, thus filtering some of the noises and removing the BW. These slopes are calculated by interpolating the OBP signal by using the long SW (LSW) and short SW (SSW) data at each point. This slope calculation results in two parameters that represent the long-term (LTV) and short-term variations (STV), corresponding to equations 3.18 and 3.19, respectively, where N_L and N_S are the lengths of LSW and SSW.

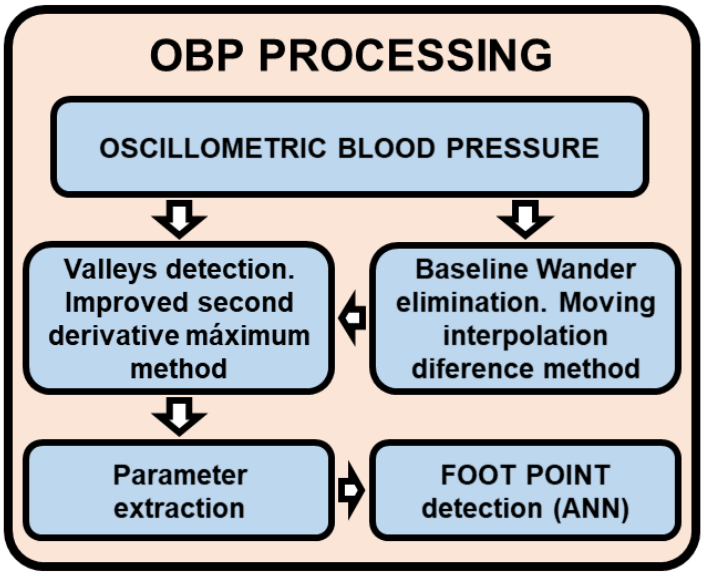

FIGURE 3.17: Scheme of the proposed FPO detection methodology.

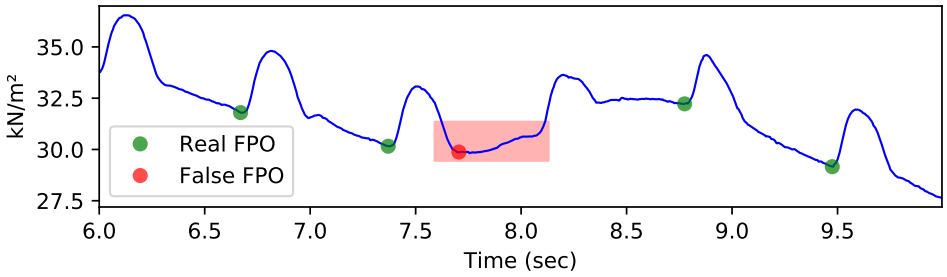

FIGURE 3.18: An example of the effect of BW on the generation of valleys that do not correspond to a real FPO.

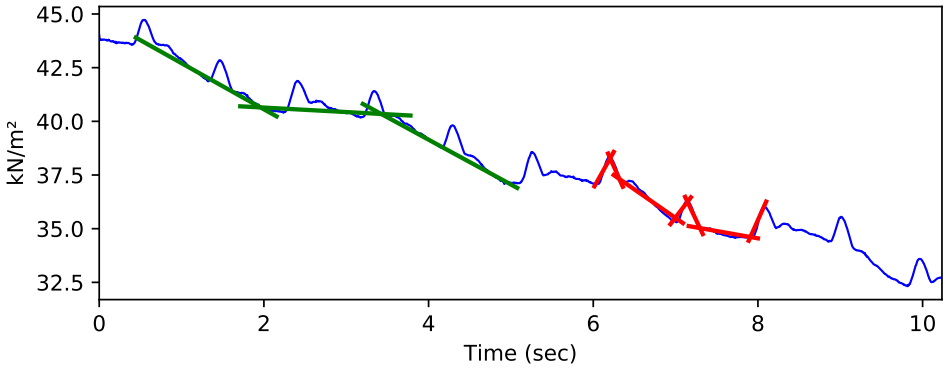

FIGURE 3.19: Short and long-term variations in a standard OBP signal.

$$LTV_i = \frac{\sum_{j=i}^{N_L}\left(LSW_{xj}^{(i)} - \overline{LSW_x^{(i)}}\right)\cdot\left(LSW_{yj}^{(i)} - \overline{LSW_y^{(i)}}\right)}{\sum_{j=i}^{N_L}\left(LSW_{xj}^{(i)} - \overline{LSW_x^{(i)}}\right)^2} \tag{3.18}$$

where $LSW^{(i)} = (LSW_x^{(i)}, LSW_y^{(i)})$.

$$STV_i = \frac{\sum_{j=i}^{N_S}\left(SSW_{xj}^{(i)} - \overline{SSW_x^{(i)}}\right)\cdot\left(SSW_{yj}^{(i)} - \overline{SSW_y^{(i)}}\right)}{\sum_{j=i}^{N_S}\left(SSW_{xj}^{(i)} - \overline{SSW_x^{(i)}}\right)^2} \tag{3.19}$$

where $SSW^{(i)} = (SSW_x^{(i)}, SSW_y^{(i)})$.

The moving interpolation difference (MID) is calculated by extracting the difference of the LTV and STV according to equation 3.20. The MID line is a byproduct of the OBP signal that is not affected by the long-term variation (i.e., the BW) since it is computed on the basis of slope measurements, which are equivalent to first derivatives. The MID line represents the information contained in the OBP signal, free of BW. The disturbances due to noise are also filtered out as a result of the interpolation performed along the signal. In addition, the MID has a characteristic morphology that makes the FPOs identifiable as illustrated in the third graph in Figure 3.20. The OBP signal and its corresponding LTVs and STVs are also represented in the first and second graphs, respectively.

$$MID_i = STV_i - LTV_i \tag{3.20}$$

The aforementioned characteristic morphology is clearly reflected in the amplified graphs in Figure 3.21, where the long and short trends are perfectly visible as well as the corresponding MID line.

Figure 3.22 shows several MID line examples corresponding to the OBP signals affected by BW and noise previously shown in Figure 3.16. It can be observed how the MID line retains the information of every heartbeat in its morphology but free of contamination with BW and noise.

3.2.2 Valleys detection

According the second derivative maximum method (SDMM) presented by Kazanavicius et al. [104], the FPO location corresponds to the maximum value of the OBP signal acceleration, i.e., the maximum value of the second derivative of the OBP signal, as illustrated in Figure 3.23.

In practice, small changes in the OBP variations can generate additional local maxima in the second derivative, resulting in surplus FP detections. Hence, in this development, an improved SDMM was implemented together with the MID line to determine which of the second derivative maxima correspond to potential FPOs.

In the modified version of the SDMM implemented in this solution, the first derivative ($D1$) was calculated by computing the slope of the OBP signal. The second derivative ($D2$) was then calculated by computing the slope of $D1$, as defined in equations 3.21 and 3.22,

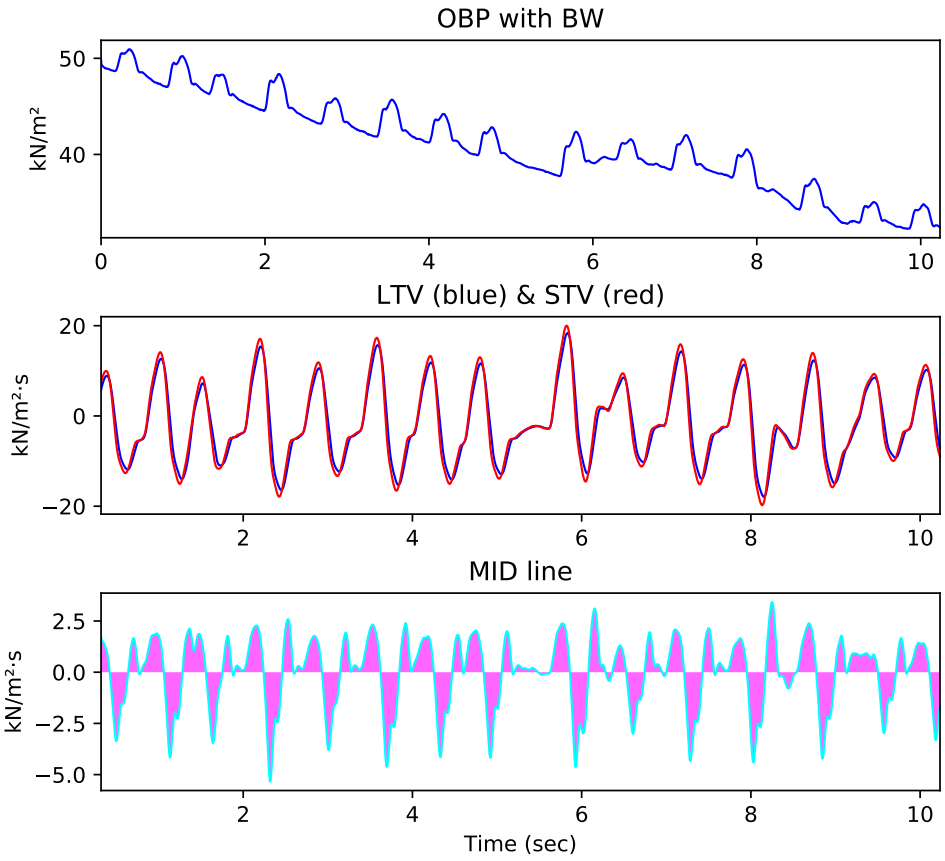

FIGURE 3.20: Top graph: OBP signal. Central graph: Long- and short-term variations in the OBP. Bottom graph: MID of the two trends (light blue line).

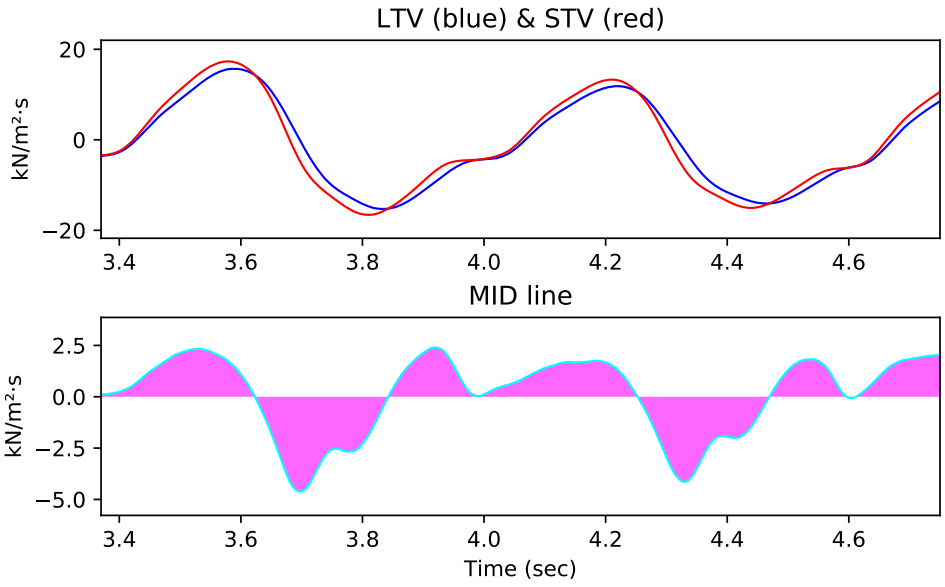

FIGURE 3.21: Top graph: Long- and short-term trends zoomed. Bottom graph: MID of the two trends (light blue line).

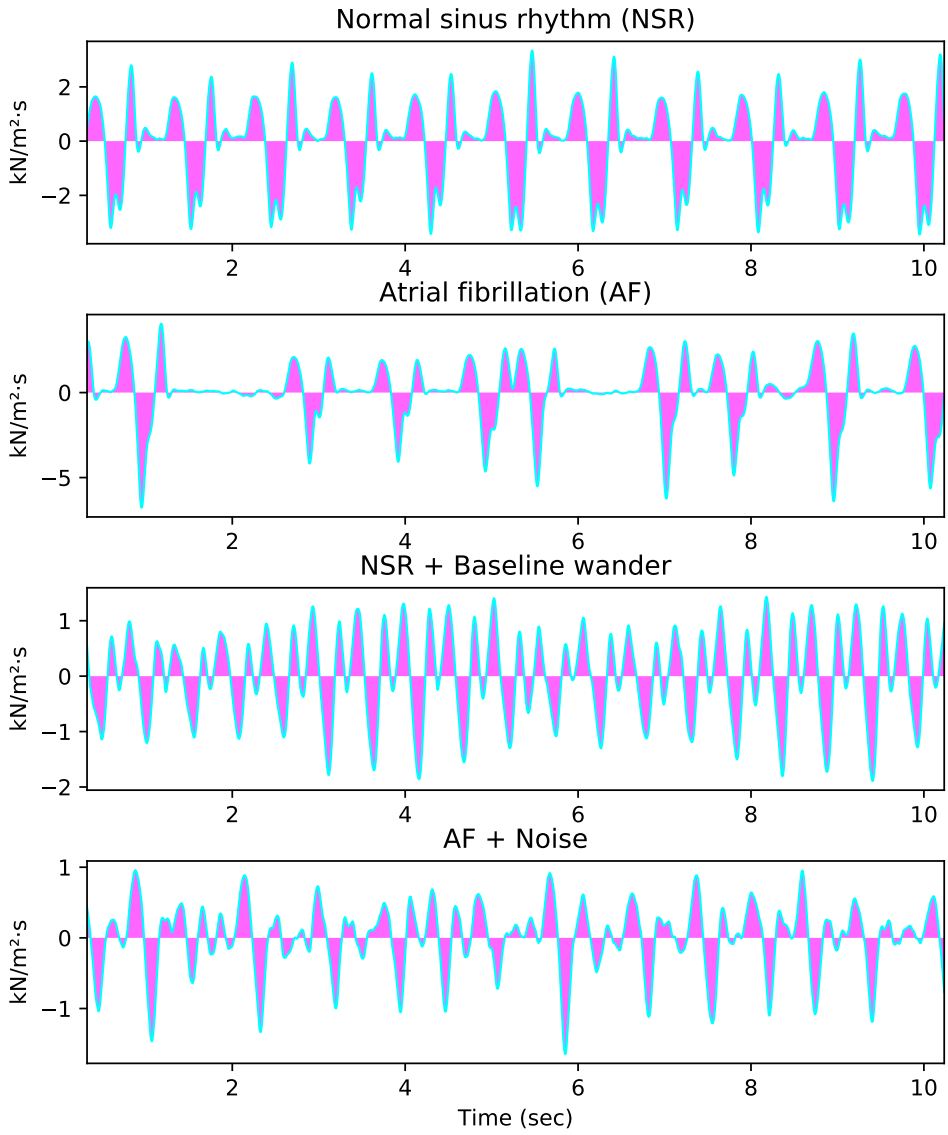

FIGURE 3.22: Set of MID lines corresponding to different APW signals from the data set.

respectively. To avoid distortions caused by noise, the window (w) length (N_D) was set to 100 milliseconds.

$$D1_i = \frac{\sum_{j=i}^{N_D}\left(OBP(w^{(i)})_{xj} - \overline{OBP(w^{(i)})_x}\right)\cdot\left(OBP(w^{(i)})_{yj} - \overline{OBP(w^{(i)})_y}\right)}{\sum_{j=i}^{N_D}\left(OBP(w^{(i)})_{xj} - \overline{OBP(w^{(i)})_x}\right)^2} \tag{3.21}$$

where $OBP(w^{(i)}) = (OBP(w^{(i)})_x, OBP(w^{(i)})_y)$.

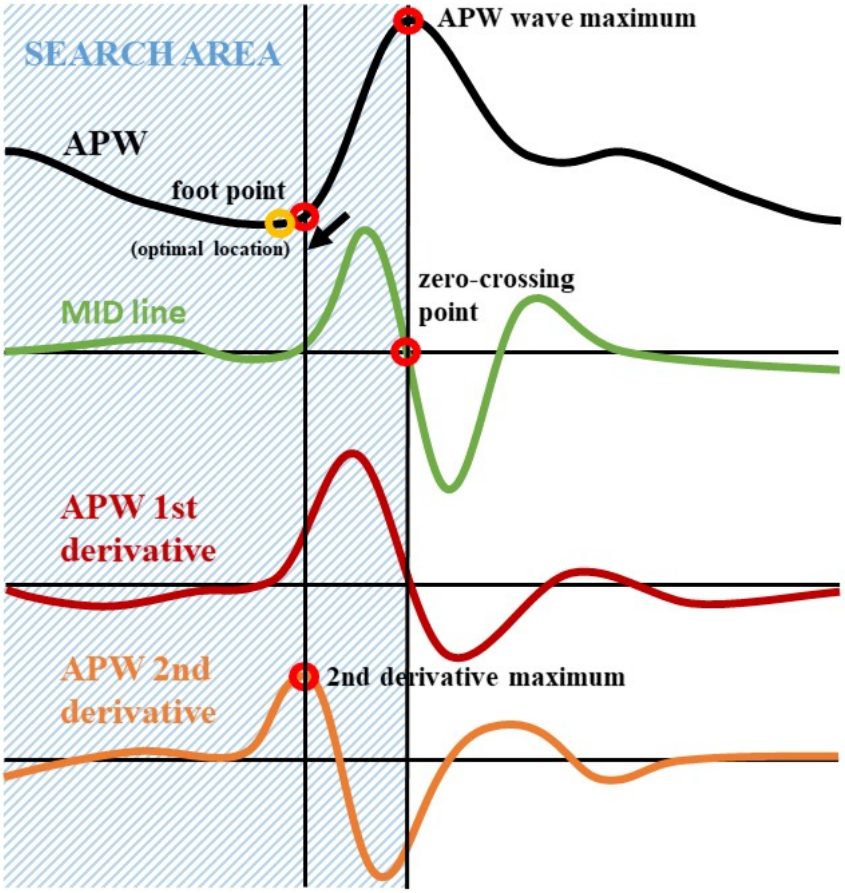

FIGURE 3.23: The OBP signal (black), the MID of the signal (green), the first derivative of the signal (red) and the second derivative of the signal (orange).

$$D2_i = \frac{\sum_{j=i}^{N_D}\left(D1\left(w^{(i)}\right)_{xj} - \overline{D1\left(w^{(i)}\right)_x}\right)\cdot\left(D1\left(w^{(i)}\right)_{yj} - \overline{D1\left(w^{(i)}\right)_y}\right)}{\sum_{j=i}^{N_D}\left(D1\left(w^{(i)}\right)_{xj} - \overline{D1\left(w^{(i)}\right)_x}\right)^2} \tag{3.22}$$

where $D1\left(w^{(i)}\right) = \left(D1\left(w^{(i)}\right)_x, D1\left(w^{(i)}\right)_y\right)$.

When a heartbeat occurs, the local maximum of the OBP signal coincides with the zero-crossing point (ZCP) of the MID line. The ZCP is located where the MID line crosses zero from the positive to the negative hemisphere. Accordingly, an FPO search area can be defined to the left of the ZCP, as illustrated in Figure 3.23. Inside that area, the maximum of the second derivative of the OBP signal that is closest to the ZCP is established as the location of the current FPO.

The FPOs detected using the SDMM are not entirely accurate due to signal noise. Considering that the FPO is the point with the minimum amplitude between the rear front of the current wave and the forefront of the subsequent wave, the SDMM was adapted to

descend the slope of the OBP signal from the location of the $D2$ maximum until the optimal local minimum is reached. This results in an accurate detection of possible FPOs associated with the ZCPs of MID waves with a specific morphology.

3.2.3 OBP parameter extraction

In this stage, a method for extracting MID waveform parameters is presented. These parameters are then used to perform a classification of the MID waveform in order to discriminate real FPOs from artifacts.

First, characteristic points of the MID waves are located. Each MID wave has an associated ZCP. However, zero crossings occur not only in the presence of a heartbeat, but also with the appearance of artifacts. Therefore, it is necessary to differentiate which MID waveforms correspond to real heartbeats and which do not. For that purpose, the MID waveform minimum (MI), maximum (MA) and ZCP locations were detected, as represented in the bottom graph in Figure 3.24.

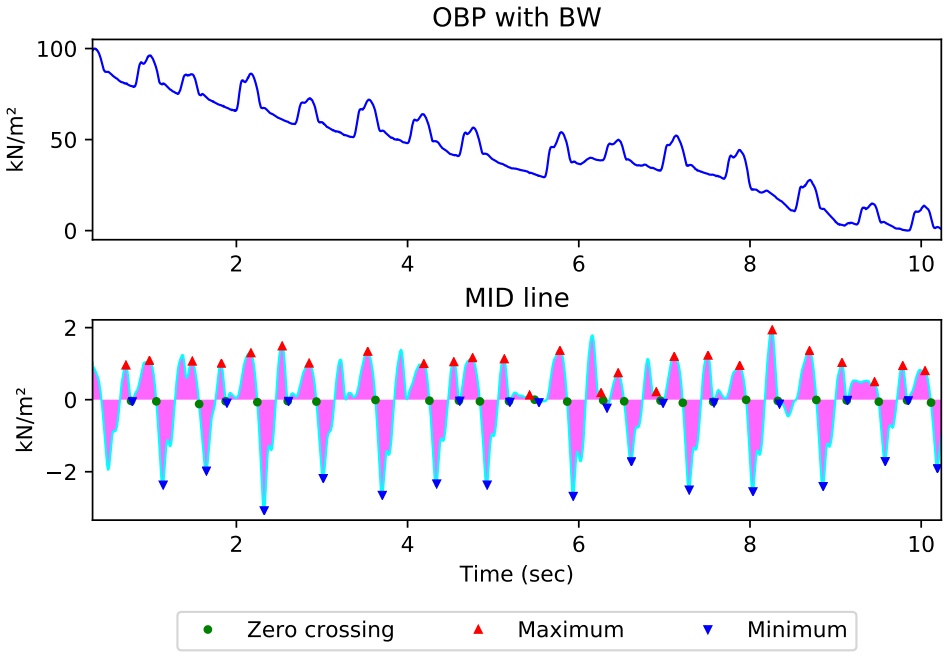

FIGURE 3.24: OBP signal (top graph) and characteristic points of the MID line (bottom graph).

From the MA, MI and ZCP, a total of five representative parameters of the MID waveform were extracted: the ratio of the difference in the MI and ZCP positions to the difference in the ZCP and MA positions 3.23, the MI value divided by the MA value 3.24, the difference between the MA and MI positions 3.25, the difference between the MA and MI values 3.26 and the product of the previous two parameters 3.27. Below are the equations for calculating these parameters, where the subscripts “y” and “x” refer to the positions of the points on the magnitude and time axes, respectively.

$$P_1 = \frac{MI_x - ZCP_x}{ZCP_x - MA_x} \tag{3.23}$$

$$P_2 = \frac{MI_y}{MA_y} \tag{3.24}$$

$$P_3 = MA_x - MI_x \tag{3.25}$$

$$P_4 = MA_y - MI_y \tag{3.26}$$

$$P_5 = P_1 \cdot P_2 \tag{3.27}$$

The significance of these five parameters lies in their ability to define the morphology of each MID wave associated with a valley. Thus, it is possible to classify each valley as corresponding to a real or false FPO (artifact) considering the morphology of the MID line. To represent these parameters in relation to their correspondence to real and false FPOs, a principal component analysis (PCA) visualization is employed in Figure 3.25. The axes correspond to the first and second principal components, which retain most of the information.

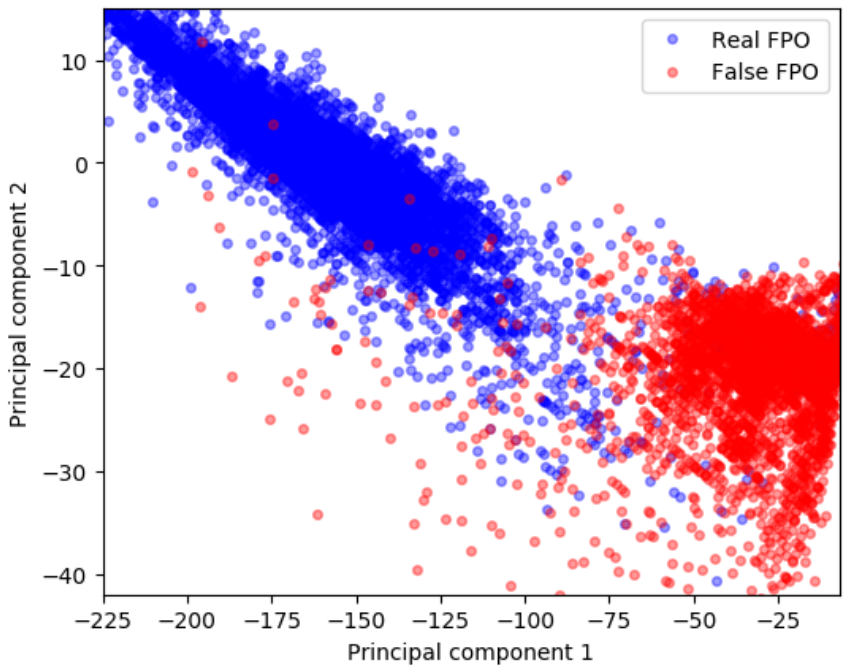

FIGURE 3.25: Two-dimensional PCA representation of the parameters extracted from MID waveforms corresponding to real and false FPOs.

3.2.4 ANN for FPO detection

Due to the reduced number and the static nature of the parameters derived from MID waveforms, a fully connected ANN is proposed to classify the valleys into real and false FPOs [164].

To optimize the ANN model that relates the five input parameters extracted from the MID waveform to the real and false FPO output labels, both the N_S and N_L and the ANN configuration hyperparameters were mapped to find the combination yielding the best results. Since the morphology of the MID line determines the values of the input parameters of the ANN, and, in turn, strongly depends on the N_S and N_L, it is necessary to identify the optimal values for these two hyperparameters.

To optimize the ANN configuration for each combination of N_S and N_L values, the ANN hyperparameters were optimized based on an exhaustive search of the optimal number of neurons in each hidden layer (HL). The number of HLs ranged from 1 to 2, and the number of neurons in each HL ranged from 1 to 10, where the number of neurons in the second HL was limited to no more than the number of neurons in the first HL. In the output layer, a single node with a sigmoid activation function was used that yielded an output value of 1 for real FPOs and 0 for false FPOs. The binary cross-entropy loss function was employed to train the network along with the Adam optimization algorithm.

Furthermore, to ensure that N_L would always be greater than N_S, a parameter alpha (α) was defined, thus, N_S was calculated relative to N_L according to equation 3.28. Hence, a mapping was defined to range N_L from 0.25 to 0.8 seconds and α from 1.05 to 4 units. Algorithm 1 illustrates the method used to generate the mapping.

$$N_S = \frac{N_L}{\alpha} \;\forall\; (\alpha \in \mathbb{R} \mid 1.05 \leq \alpha \leq 4) \tag{3.28}$$

Algorithm 1 Parameter mapping for FPO detection optimization.

for ($LWL = 0.25$; $LWL \leq 0.8$; $LWL = LWL + 0.05$) **do**
  for ($\alpha = 1.05$; $\alpha \leq 4$; $\alpha = \alpha + 0.05$) **do**
    for ($HL_1 = 1$; $HL_1 \leq 10$; $HL_1 = HL_1 + 1$) **do**
      for ($HL_2 = 1$; $HL_2 \leq HL_1$; $HL_2 = HL_2 + 1$) **do**
        $\text{params}^{(LWL,\,\alpha)} \leftarrow$ **ApwParamExt** (APWsignals, [LWL, α])
        $\text{ann}^{(LWL,\alpha)}_{(HL_1,\,HL_2)} \leftarrow$ **AnnTraining** ($\text{params}^{(LWL,\alpha)}$, [$HL_1$, HL_2])
      end for
    end for
  end for
end for

3.2.5 Results and discussion on foot point detection

The performance was measured according to specificity (*Sp*), *Se* and F1 score (*F1*), corresponding to equations 2.52, 2.51 and 2.54, respectively. These were obtained based on the

number of TP, FP and FN. The data set described in subsection 2.3.3 was used for validation.

The ANN model was evaluated based on the arithmetic mean of the *F1* in 20-fold cross-validation (CV) sets for each mapped hyperparameter configuration. The best hyperparameter configuration achieved a mean *F1* of 99.18% (99.17% *Se* and 99.21% *Sp*), represented by a blue cross in Figure 3.26. This representation illustrates the results obtained for each combination of N_L and α values. The best results are colored in red while the worst ones are colored in blue. The optimized hyperparameter values are as follows:

- LSW length: 0.45 seconds
- Alpha: 1.4
- Number of neurons in each HL:
  - First HL: 8 neurons
  - Second HL: 5 neurons

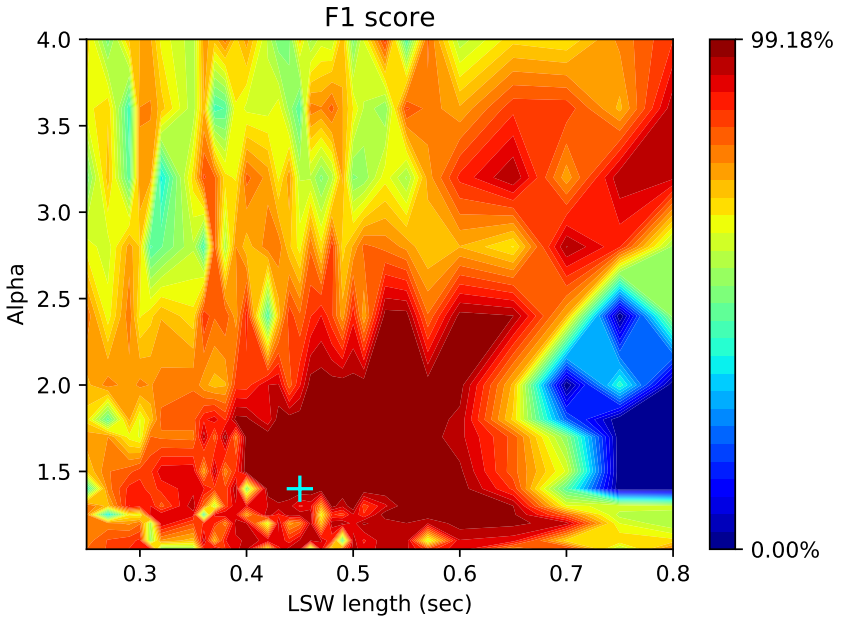

FIGURE 3.26: Average value of the *F1* for FPO detection in 20-fold CV for each combination of values of the alpha parameter and the LSW length (N_L).

For the optimized hyperparameter values N_L=0.45 and α=1.4, the performance of the ANN for each HL configuration is illustrated in Figure 3.27. The blue cross indicates the ANN configuration that achieves the highest *F1*, corresponding to 8 neurons in the first HL and 5 neurons in the second HL, as indicated above.

In contrast to the results obtained in this development, the commercial BP+ device achieves an *F1* of 97.7%. By comparison, the proposed model achieves an *F1* of 99.18%, an improvement of 1.48 percentage points. This improvement is crucial, considering that failure in

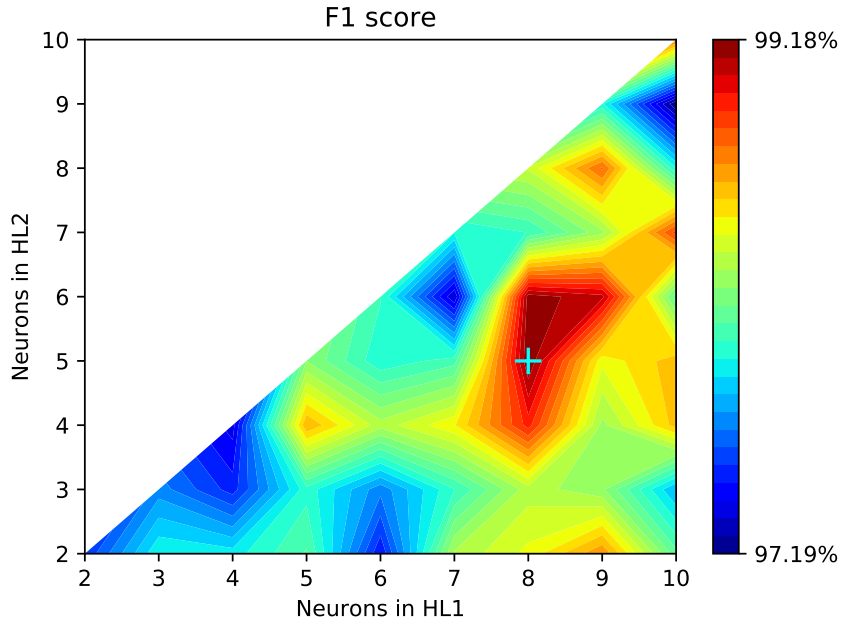

FIGURE 3.27: Average value of the *F1* for FPO detection in 20-fold CV for each combination of the numbers of neurons in the first and second HLs.

the detection of a single FPO in a small context OBP signal can generate an even greater error in the subsequent extraction of parameters due to the resulting HP morphology.

4 Physiological signal processing: Parameter extraction, analysis, normalization and labeling

This section presents a novel methodology for the parameter extraction, analysis, normalization and labeling of physiological records, which was optimized for the identification of stress and relaxation states. The 42 registers collected during the experimental stage carried out in subsection 2.3.1 are used for this development. Each register consists of a set of physiological signals, i.e., galvanic skin response (GSR), breathing (RSP) and heart period (HP), where HP is calculated from the electrocardiographic signal applying the R-peak detection algorithm proposed in the previous subsection 3.1. Figure 4.1 illustrates these signals, which correspond to one of the records in the dataset. These physiological signals are subsequently processed to obtain information related to the activity of the autonomic nervous system (ANS) contained in the physiological parameters, as physiological parameters have proven to be useful for estimating states of stress and relaxation [19, 20, 28, 165, 166].

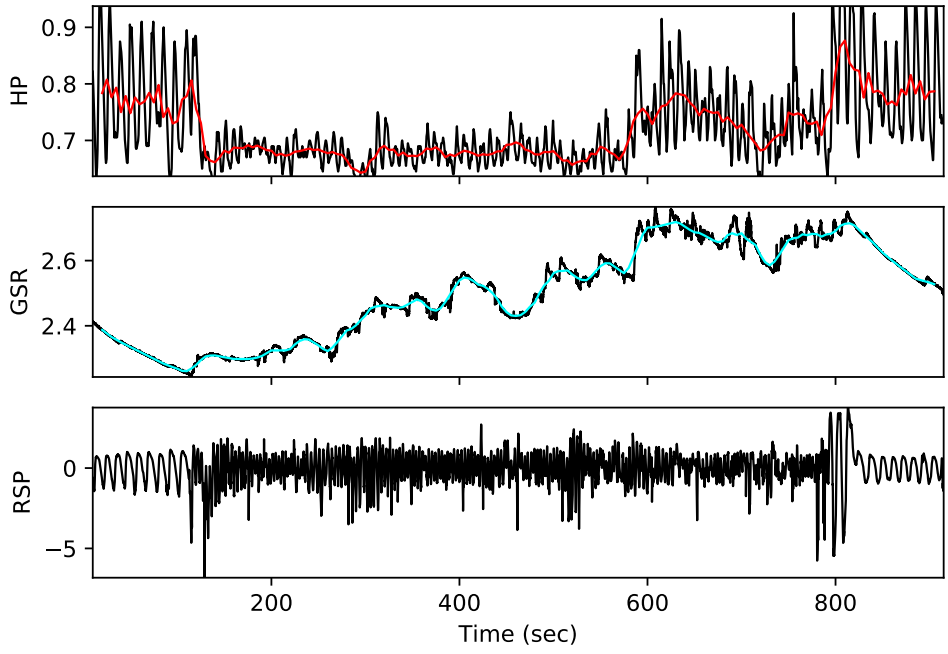

FIGURE 4.1: Physiological records corresponding to HP, GSR and RSP.

Physiological differences among people result in considerable deviations in the parameters extracted during states of stress and relaxation. Therefore, the implementation of a generic algorithm to process parameters extracted from different people is a challenging task. In this section, a novel methodology is proposed for the selection of the best normalization technique for each extracted parameter. This methodology focuses on both obtaining the greatest differentiation between states of stress and relaxation and equalizing the ranges of parameter values for different people.

This thesis proposes continuous labeling of the registers in the range [0, 1], where 0 represents the maximum relaxation value and 1 the maximum stress value, in terms relative to the experiment from which the analysed signals were extracted. Based on the assumption that it is not possible to objectively assign a representative continuous value of stress and relaxation level to each record manually, two partial and binary labelings are proposed to capture stress and relaxation regions, where stress was denoted with the label "1" and relaxation with the label "0", respectively. The first partial labeling (type 1 labeling) was conducted by the author of this thesis. The second partial labeling (type 2 labeling) was performed by experts in the interpretation of physiological signals. The labeling of the signals was subsequently completed through the implementation of a semi-supervised learning algorithm, using type 1 and type 2 labelings for training and validation, respectively. This is called pseudo-labeling, which consists of turning a partial labeling into a complete labeling as illustrated in the diagram in Figure 4.2.

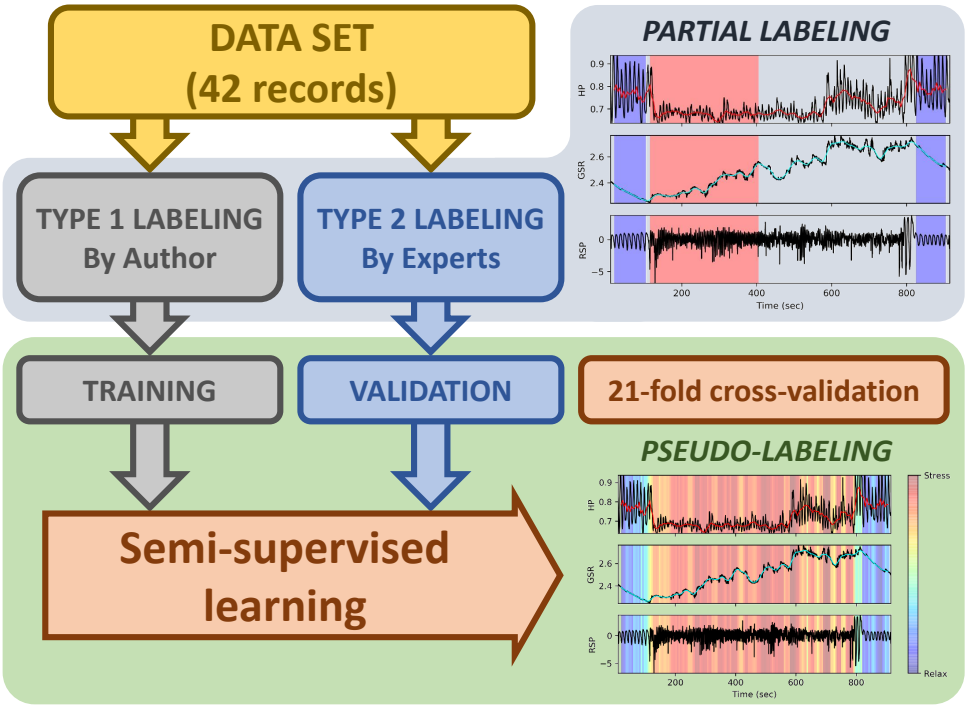

FIGURE 4.2: Diagram representing the labeling process carried out in this thesis.

To strengthen the reliability of the methodology, 21-fold cross-validation was used. Of the 42 available records, 30 (72%) were used for development and 12 (28%) in the validation

stage. In addition, each of the stages was performed in duplicate, both with normalized and unnormalized parameters, to verify the improvement in the results implicit in the proposed normalization methodology. Figure 4.3 illustrates the strategy used for the 21-fold cross-validation, where each column corresponds to each of the 42 records and each row to each of the 21 folds. The records used for training are displayed in green and those used for validation are displayed in yellow.

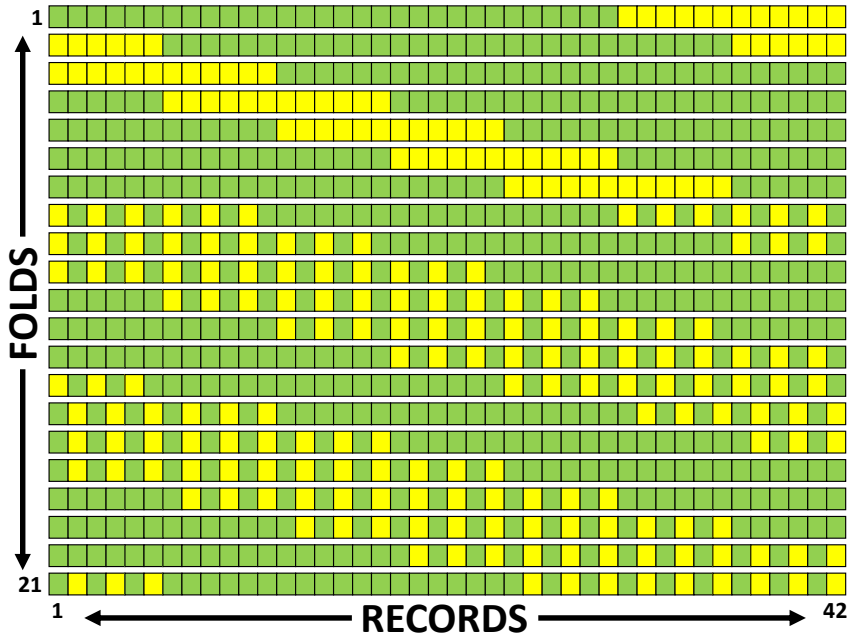

FIGURE 4.3: A 21-fold cross-validation strategy where training records are displayed in green and those used for validation are displayed in yellow.

The proposed development is based on the use of the principal components (PCs), extracted through the application of principal component analysis (PCA). For each of the 21-fold, the PCA model was trained using the parameters of the training set. The trained PCA model was subsequently used to obtain the PCs of both the training set and the validation set. As mentioned above, PCs were processed using a semi-supervised learning algorithm to perform a pseudo-labeling. During this process, type 1 partial labels were used as initial labels for the training of the semi-supervised learning algorithm. In contrast, type 2 partial labels were used to validate the performance of the resulting pseudo-labeling. Figure 4.4 shows an outline of the methodology proposed in this section.

4.1 Parameter extraction

The extraction of the physiological parameters is performed by analyzing the signals in a 20-second sliding window, with 15-second overlap, which means a 5-second step as illustrated in Figure 4.5. This configuration allows to process enough information from the signal in order to extract reliable physiological parameters [28]. Furthermore, it is suitable for real-time implementation, as demonstrated later in section 6.

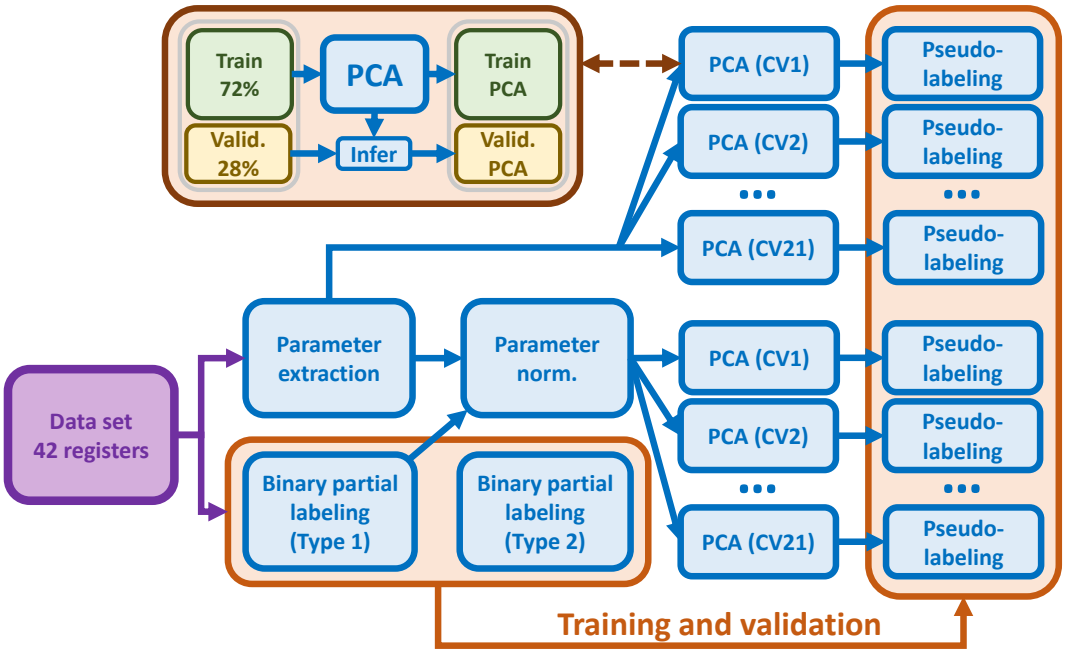

FIGURE 4.4: Flow chart of the proposed methodology for the normalization and labeling of the extracted parameters.

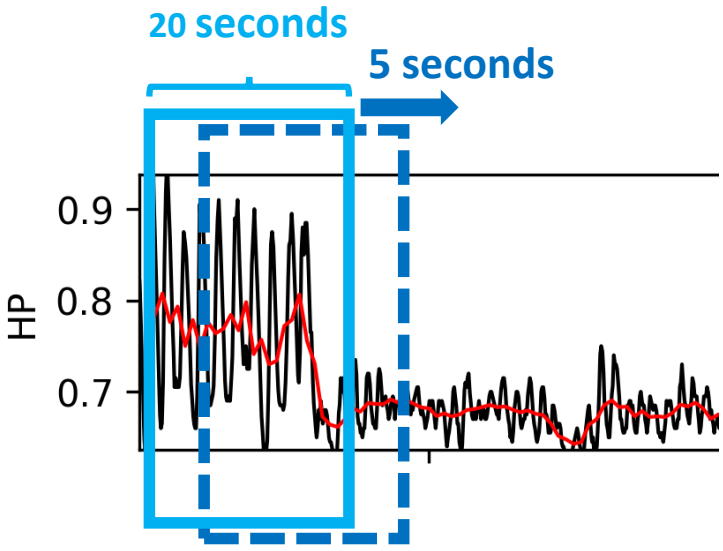

FIGURE 4.5: Proposed methodology for the processing of physiological signals using a 20-second sliding window, with a step of 5 seconds.

A total of 29 parameters are extracted in this study, of which 19 correspond to HP, 3 to GSR, 5 to RSP and 2 to both HP and RSP. These are presented below along with their corresponding equations. They are all closely related to changes in the physiological state, which makes them good indicators of the activity of the ANS [19]. At the end of this subsection, Figure 4.10 illustrates the total of parameters extracted for a given register in the data set. Finally, as a result of the study carried out on these parameters in subsequent stages, the most representative in terms of stress and relaxation states will be selected from the 29 extracted parameters. For this purpose, indicators related to the capacity of

each parameter to differentiate between these two states will be considered.

4.1.1 Heart period

This subsection delves into the parameters derived from the HP that are commonly used in the interpretation of the psychophysiological state in people. Some of them have already been introduced in subsection 2.1.2. These parameters are classified on temporal-domain, frequency-domain and nonlinear. The parameters of the HP used in this development are introduced below, together with their corresponding equations, where N_H is the number of detected heartbeats (R-peaks or FPOs, depending on from which signal the HP is extracted) and t_i the temporal location of the i^{th} heartbeat.

Temporal-domain parameters were selected based on their capacity of identifying irregularities in the HP and the possibility of being processed in a sliding window of reduced context. Thus, geometric features, which require a context of several minutes to extract reliable parameters, were discarded. Selected parameters are listed in Table 4.1, where HP_a and HP_b represent the a^{th} and b^{th} percentiles of HPs, respectively.

TABLE 4.1: HP temporal-domain features.

Feature	Calculation
Mean HP	$MHP = \frac{1}{N_H-1} \cdot \sum_{i=1}^{N_H-1} HP_i$
Variation of the HP	$VHP = \frac{(N_H-1)\cdot \sum_{i=1}^{N_H-1}(t_{i+1}\cdot HP_i) - \left(\sum_{i=1}^{N_H-1} t_{i+1}\right)\cdot\left(\sum_{i=1}^{N_H-1} HP_i\right)}{(N_H-1)\cdot \sum_{i=1}^{N_H-1} t_{i+1}^2 - \left(\sum_{i=1}^{N_H-1} t_{i+1}\right)^2}$
Irregularity index	$IRRX(a,b) = \frac{\sigma(HP)}{\overline{HP}} \;\forall\; (HP_a < HP < HP_b)$
Number of successive HPs that differ by more than 50ms	$NN50 = \sum_{i=1}^{N_H-2} (HP_i - HP_{i-1}) > 0.05$
Percentage of NN50	$PNN50 = \frac{NN50}{N_H-2} \cdot 100$
Root mean square of the HP	$RMS = \sqrt{\frac{1}{N_H-1} \cdot \sum_{i=1}^{N_H-1} HP_i^2}$
Root mean square of successive HP differences	$RMSSD = \sqrt{\frac{1}{N_H-2} \cdot \sum_{i=1}^{N_H-2} (HP_i - HP_{i-1})^2}$
Standard deviation of the HP	$SDNN = \sqrt{\frac{1}{N_H-1} \cdot \sum_{i=1}^{N_H-1} (HP_i - \overline{HP})^2}$
Standard deviation of successive HP differences	$SDSD = \sqrt{\frac{1}{N_H-2} \cdot \sum_{i=1}^{N_H-2} \left((HP_i - HP_{i-1}) - \frac{\sum_{j=1}^{N_H-2} HP_j - HP_{j-1}}{N_H-2} \right)^2}$
Standard error of the HP mean	$SENN = \frac{1}{N_H-1} \cdot \sqrt{\sum_{i=1}^{N_H-1} (HP_i - \overline{HP})^2}$

From HP *frequency-domain* parameters, four main frequency bands are distinguished, i.e.: high frequency (HPHF, 0.15 – 0.4Hz), low frequency (HPLF, 0.04 – 0.15Hz), very low frequency (HPVLF, 0.0033 – 0.04Hz), and ultralow frequency (HPULF, <0.0033Hz) [107]. Due to the variability of the beats periodicity throughout the signal, it is necessary to interpolate and resample the HP using equal intervals [167, 168, 109, 169]. Considering the maximum frequency analyzed (0.4 Hz in the HF band), a sampling frequency of 4 Hz was used, thus avoiding aliasing [168, 169, 170]. Cross correlation was applied to assess the degree of similarity between the interpolated HP signal and the frequencies in the range (0, 0.5] Hz with a resolution of 0.0001 Hz.

From *nonlinear* parameters, the standard deviations of the Poincaré plot (POSD1 and POSD2) are widely used to detect irregularities in HP [108]. POSD1 is more related to fast HP variability, while POSD2 represents the long-term HP variability according to equations 4.1 and 4.2, respectively. The ratio between POSD1 and POSD2 (POSD12) is also frequently employed according to equation 4.3.

$$POSD1 = \sqrt{\frac{1}{2} \cdot SDSD^2} \tag{4.1}$$

$$POSD2 = \sqrt{2 \cdot SDNN^2 - \frac{1}{2} \cdot SDSD^2} \tag{4.2}$$

$$POSD12 = \frac{POSD1}{POSD2} \tag{4.3}$$

The dispersion of points around diagonal line in Poincaré plot (DIS) and the mean stepping increment of inter-beat intervals (STEP) are also used according to equations 4.4 and 4.5, respectively. These parameters have proven to be effective in detecting irregularities in the HP [171].

$$DIS = \frac{\sqrt{\frac{1}{2(N_H-2)} \sum_{i=1}^{N_H-2} (HP_i - HP_{i+1})^2 - \left(\frac{1}{(N_H-2)\sqrt{2}} \sum_{i=1}^{N_H-2} |HP_i - HP_{i+1}| \right)^2}}{\frac{1}{2(N_H-2)} \left(-HP_1 - HP_{N_H-1} + 2 \sum_{i=1}^{N_H-2} HP_i \right)} \tag{4.4}$$

$$STEP = \frac{\frac{1}{N_H-3} \sum_{i=1}^{N_H-3} \sqrt{(HP_i - HP_{i+1})^2 + (HP_{i+1} - HP_{i+2})^2}}{\frac{1}{N_H-1} \sum_{i=1}^{N_H-1} HP_i} \tag{4.5}$$

4.1.2 Galvanic skin response

Parameters derived from the GSR are considered to be among the most representative of the activity of the ANS. In fact, GSR is directly related to the sympathetic nervous system (SNS) activity. Therefore, the parameters extracted from GSR have a great interest in the

detection of the activation and deactivation of the SNS. This information was extracted using a 20-second context in a sliding window, which contains enough information to obtain representative parameters of the physiological state related to stress and relaxation.

In each sliding window, the mean value of the GSR (MGSR) was calculated as a representative value of the signal level according to equation 4.6, where N_G refers to the number of GSR samples in each sliding window and t_i is the temporal location of the i^{th} sample.

$$MGSR = \frac{1}{N_G} \cdot \sum_{i=1}^{N_G} GSR_i \tag{4.6}$$

The activity of the sweat glands increases when the sympathetic branch of the ANS is activated and decreases when it is deactivated. This makes the variation of the GSR (VGSR) a significant parameter of the activity of the SNS, as illustrated in Figure 4.6 [19, 20, 11]. To quantify VGSR, a linear regression is performed where the slope is obtained according to equation 4.7.

$$VGSR = \frac{N_G \cdot \sum_{i=1}^{N_G} (t_i \cdot GSR_i) - \left(\sum_{i=1}^{N_G} t_i\right) \cdot \left(\sum_{i=1}^{N_G} GSR_i\right)}{N_G \cdot \sum_{i=1}^{N_G} t_i^2 - \left(\sum_{i=1}^{N_G} t_i\right)^2} \tag{4.7}$$

In the same way, the value of the GSR is more chaotic during stressful periods due to skin conductance response and more stable during relaxation [8, 172]. This fact led to the application of the differential area between the GSR signal and its first-order interpolation (AGSR), which is represented in light blue in Figure 4.6. AGSR is calculated conforming to equation 4.9, where the linear interpolation *offset* is calculated according to equation 4.8.

$$offset = \frac{\sum_{i=1}^{N_G} GSR_i - VGSR \cdot \sum_{i=1}^{N_G} t_i}{N_G} \tag{4.8}$$

$$AGSR = \frac{\sum_{i=1}^{N_G} |GSR_i - (VGSR \cdot t_i + offset)|}{N_G} \tag{4.9}$$

4.1.3 Breathing

In the study of RSP, it was observed that during states of relaxation (corresponding to the areas colored in blue in the top graph in Figure 4.7) RSP is similar to a sinusoidal waveform containing a dominant harmonic. In contrast, during states of stress (corresponding to the

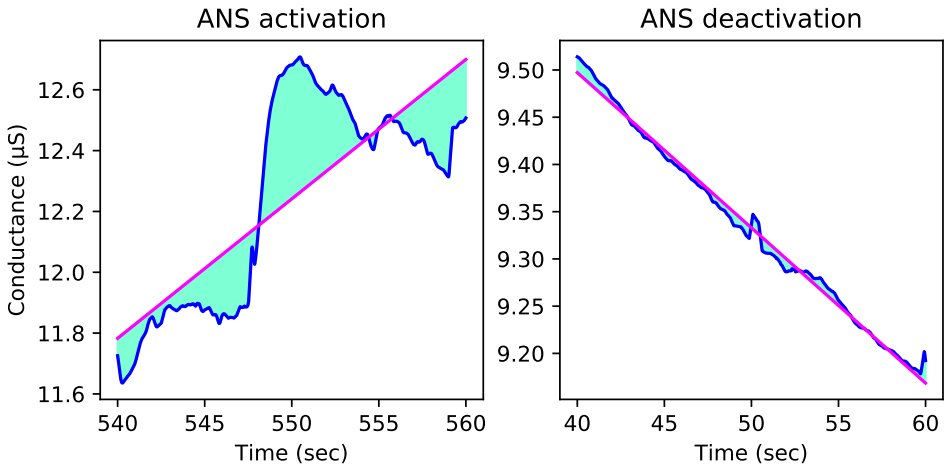

FIGURE 4.6: GSR signal (dark blue) and its first-order interpolation (pink line) in a 20-second window. Light blue color represents the area between both.

area colored in red in the top graph in Figure 4.7) RSP becomes more chaotic, thus increasing the number of harmonics. This phenomenon is illustrated in the frequency correlation in the bottom graph in Figure 4.7, and was considered in order to extract frequency-domain parameters from RSP that capture those alterations related to states of stress and relaxation.

As in HP frequency-domain parameter extraction, the same cross correlation method was employed to assess the degree of similarity between the RSP signal and the frequencies in the range (0, 0.5] Hz with a resolution of 0.0001 Hz. Therefore, it was necessary to downsample the signal from 1000 Hz to 4 Hz so that the computational load would not be excessive. Four main parameters were extracted from frequency correlation, i.e.: high frequency band (RSPHF, 0.15 – 0.4Hz), low frequency band (RSPLF, 0.04 – 0.15Hz), very low frequency band (RSPVLF, 0.0033 – 0.04Hz), and ultralow frequency band (RSPULF, <0.0033Hz).

During relaxation, the RSP has a sinusoidal shape, while the opposite occurs during a stressful situation, where RSP becomes more frequent and inharmonious [172]. Figure 4.8 illustrates this phenomenon, where the standard deviation of the frequencies (SDRSP) is calculated according to equation 4.10, which reflects the frequency dispersion. N_f represents the number of frequencies processed during cross correlation (CC).

$$SDRSP = \sqrt{\frac{1}{N_f} \cdot \sum_{i=1}^{N_f} (CC_i - \overline{CC})^2} \tag{4.10}$$

Due to the similarity of SDRSP with the RMS of HP presented in Table 4.1, it was noted that the combination of both parameters results in a more reliable representation of relaxation and stress. This phenomenon can be observed by performing the product between SDRSP and RMS (HSCR) according to equation 4.11. Figure 4.9 shows an example of RMS

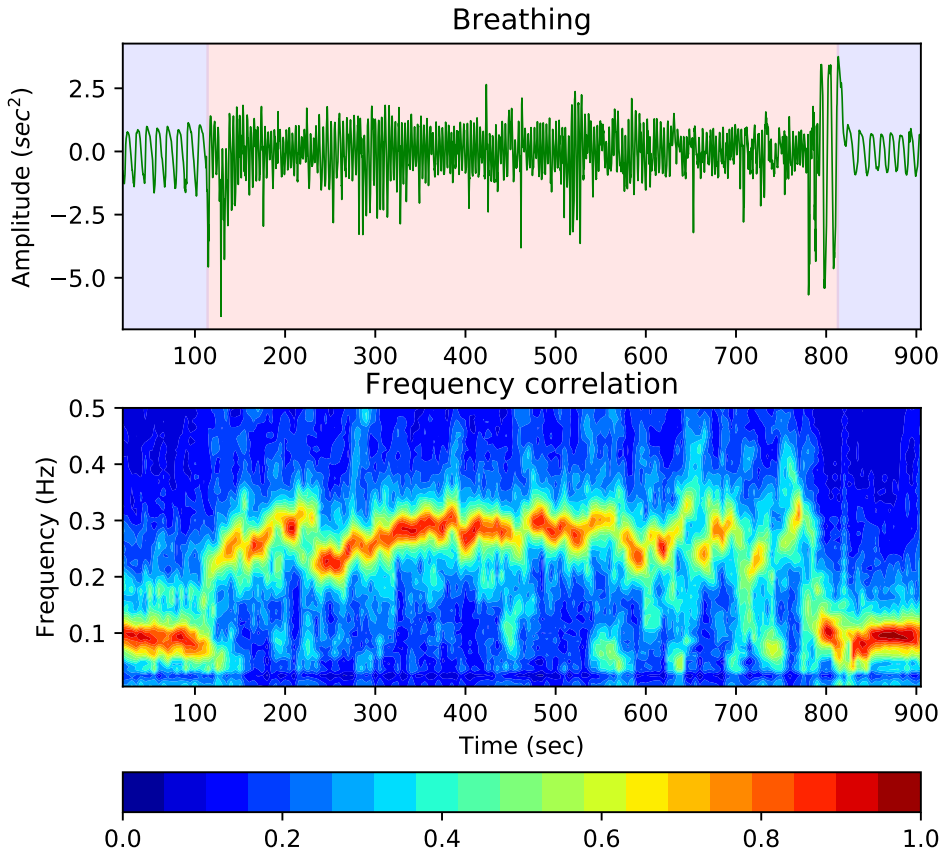

FIGURE 4.7: RSP signal (top graph) and the corresponding frequency correlation (bottom graph).

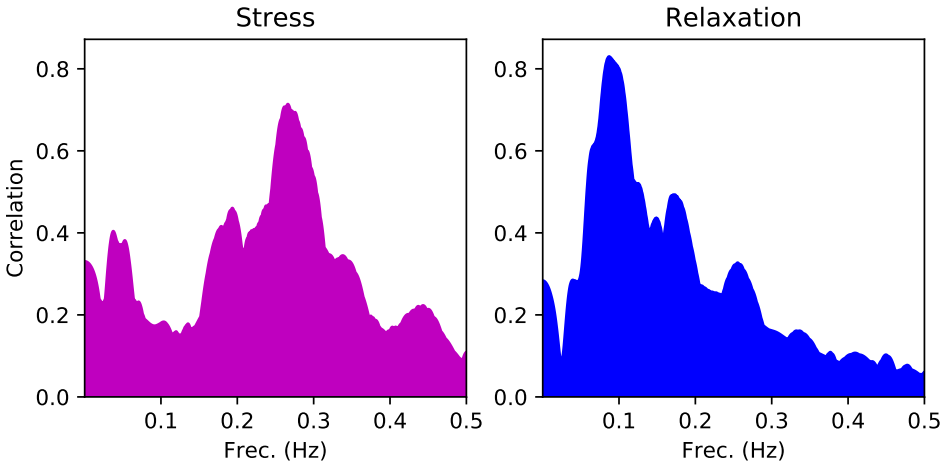

FIGURE 4.8: RSP frequency correlations during stress and relaxation.

and SDRSP during relaxation and stress, and the resulting HSCR. For the calculation of the HSCR, SDRSP and RMS are scaled between 0 and 1 to avoid the imposition of the morphology of the parameter with magnitudes closer to 0 over the morphology of the other parameter when performing the product of both. The resulting HSCR is finally rescaled according to the product of the minimum and maximum values of the original SDRSP and

RMS.

$$HSCR = SDRSP \cdot RMS \tag{4.11}$$

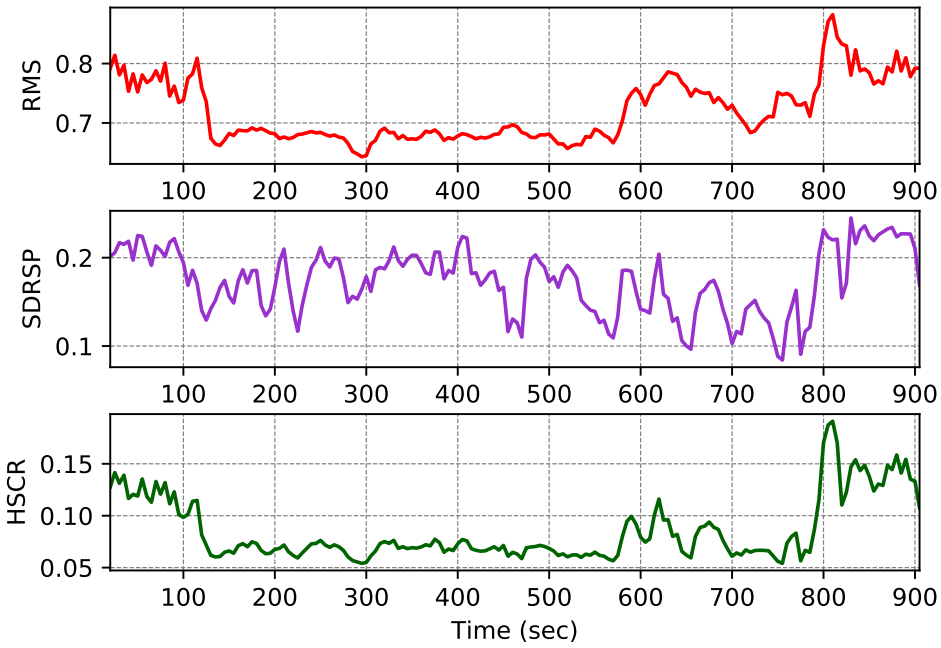

FIGURE 4.9: RMS (top graph), SDRSP (central graph) and the resulting HSCR (bottom graph).

During respiratory sinus arrhythmia, cardiac coherence (CACO) is frequently employed as an index of the contribution of the parasympathetic nervous system to cardiac regulation [173, 19, 174]. This phenomenon takes place during relaxation, when the acceleration and deceleration of the HP is coordinated with the respiratory rate and the correlation between the frequencies of the RSP and the HP is high. In this study, the CACO was calculated by measuring the difference between the frequency correlations of the RSP and the HP according to equation 4.12, where CC_{RSP} and CC_{HP} refer to the frequency correlation of the RSP and HP, respectively.

$$CACO = \frac{1}{N_f} \cdot \sum_{i=1}^{N_f} |CC_{RSPi} - CC_{HPi}| \tag{4.12}$$

Figure 4.10 illustrates all the physiological parameters that were extracted up to this point, which will be used in the following steps.

4.2 Binary partial labeling

Parallel to the parameter extraction, in this stage a partial labeling of each record was performed. Considering the complexity of the physiological signals and the several factors

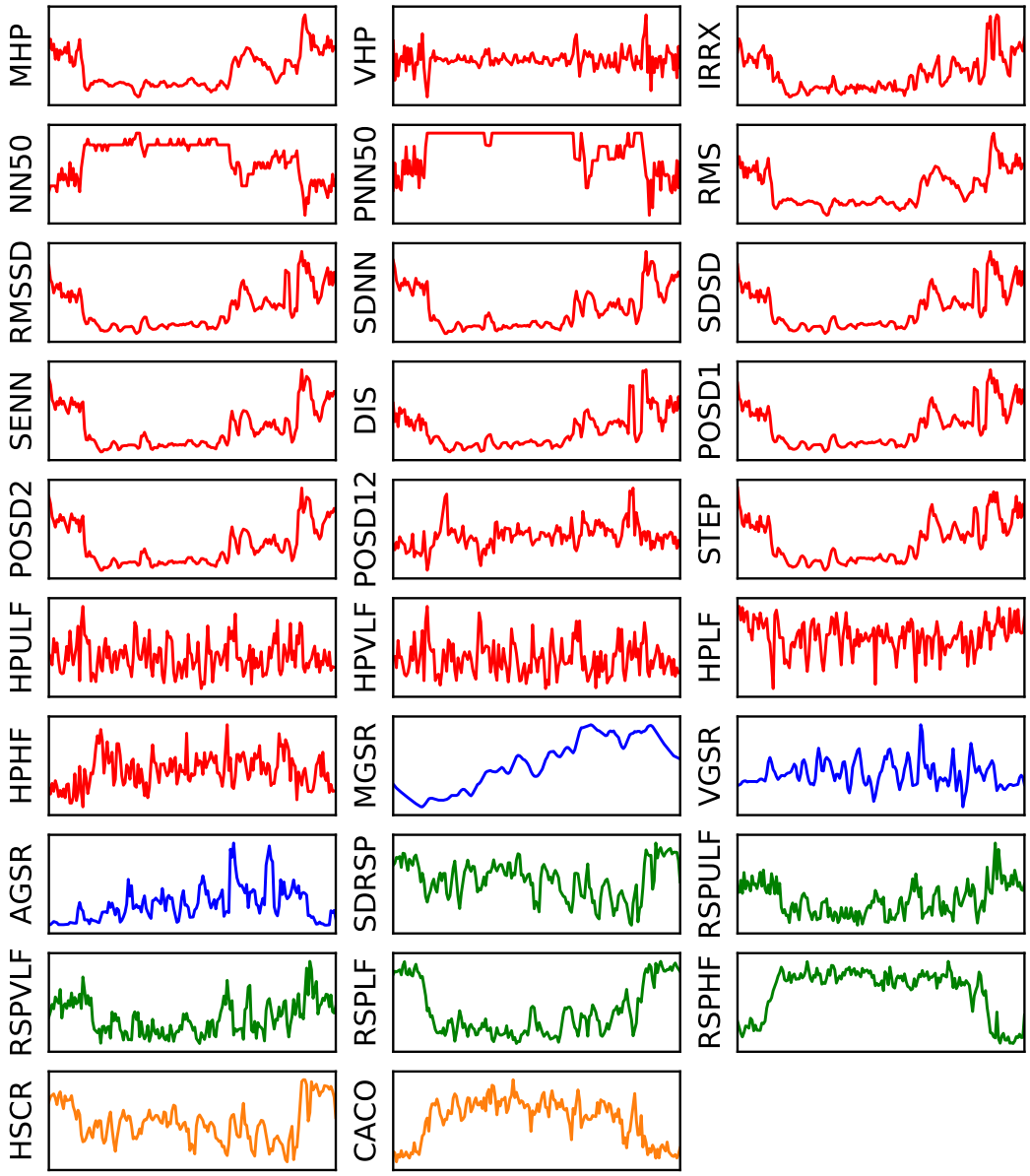

FIGURE 4.10: Parameters extracted from GSR, RSP and HP signals.

that affect them, it was assumed that it is not possible to objectively assign a representative value of stress and relaxation level to each analyzed window. For this reason, a particular methodology is proposed in this thesis, where human knowledge is used to label the areas clearly belonging to states of stress and relaxation by means of a binary labeling of "1" and "0", respectively. This labeling is illustrated in Figure 4.11, where the blue and red areas represent states of relaxation and stress.

In total, two different labeling sets were generated: the first, known as type 1 labeling, was proposed by the author of this thesis, and is based on the nature of the experiment carried out for the acquisition of the physiological records, which was introduced in subsection 2.3.1. During the experiment two phases of relaxation are distinguished, at the beginning and at the end, along with an intermediate phase of stress. These phases were used as

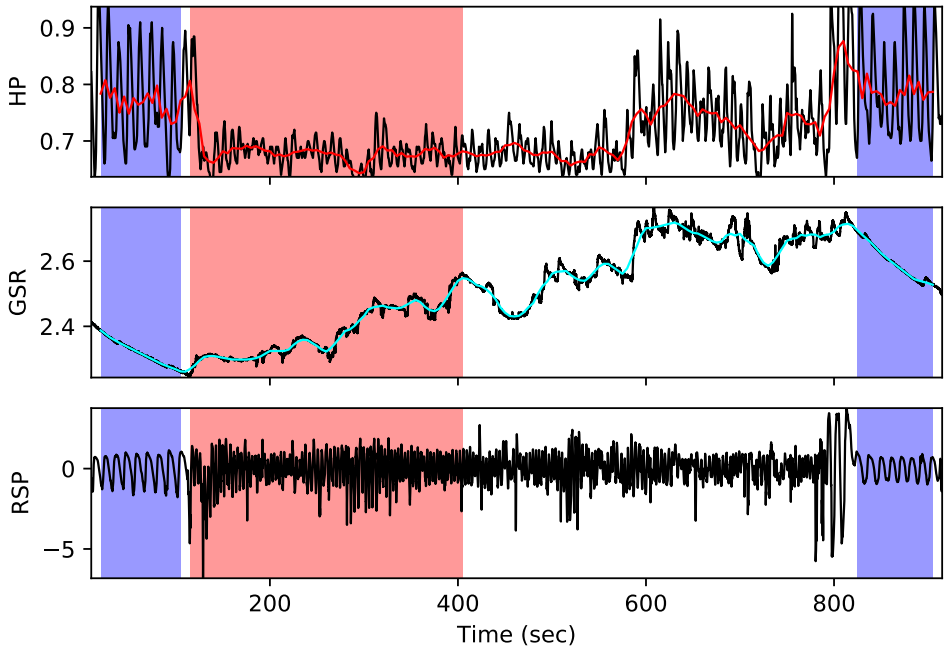

FIGURE 4.11: Example of a binary labeling where the blue areas correspond to the record segments labeled as relaxation and the red area to the segment labeled as stress.

a reference to perform type 1 labeling. The second labeling, known as type 2 labeling, was carried out by personnel with expert knowledge in the interpretation of physiological signals, and was performed blinded to the nature of the experiment to avoid being affected by the interpretations derived from it.

The two labeling types were used for different purposes, type 1 labeling for the development and training of the proposed algorithms and models, and type 2 labeling for their validation. More specifically, type 1 labeling was used to select from extracted parameters, those that best differentiate both stages of stress and relaxation, and also to determine the best normalization strategy, as developed in the following subsection. It was also used as initial labeling to train a semi-supervised model for each register in order to perform the pseudo-labeling. Besides, type 2 labeling is used to validate the pseudo-labeling derived from the study of normalized and unnormalized parameters at the end of this section. It is also used later in section 5 to validate the trained stress and relaxation prediction models.

4.3 Parameter normalization

Due to the existing physiological differences among individuals, this stage focuses on the importance of normalizing physiological parameters. When the parameters extracted from different participants are compared, significant variations are observed. The distribution of the parameter values that represent stressful situations for some individuals are mixed with the relaxation values of other individuals and vice versa. This phenomenon is

reflected in the example in Figure 4.12, where the mean HP corresponding to 42 individuals (from the stress and relaxation experiment presented in subsection 2.3.1) and collected during the same phases of stress and relaxation are mixed.

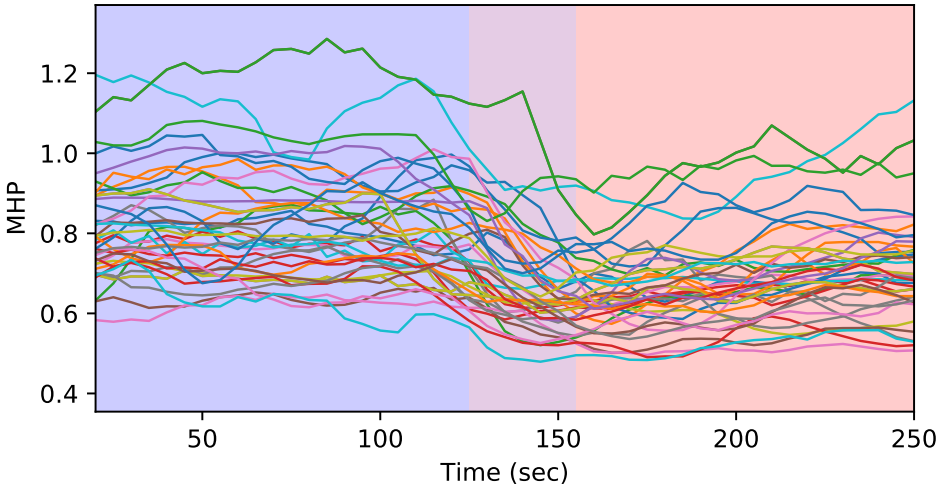

FIGURE 4.12: HP records from different individuals during the same period of the stress and relaxation experiment. The figure displays the physiological change (purple area) from a relaxing state (blue area) to a stressful state (red area).

The same phenomenon is observed in the remaining parameters to a greater or lesser extent. Figure 4.13 shows the parameters extracted from the 42 records of the data set plotted at the same time, where it is difficult to discern the stress and relaxation phases only by considering the magnitude values.

This phenomenon is further illustrated in Figure 4.14, in which the distribution of each parameter is represented based on its belonging to states of stress and relaxation according to the type 1 partial labels.

Considering the need for a parameter normalization methodology in order to standardize parameter ranges among participants, in this solution various normalization methods, in addition to those that already exist, are proposed, together with a methodology to assess their effectiveness in this specific context.

Two normalization classes are differentiated depending on the nature of the parameters: The first class corresponds to those parameters that only have positive values before normalization and the zero-crossing has no relevant meaning. The second class are those parameters that have positive and negative values and the zero-crossing represents a relevant state change, therefore, the zero value must be fixed. To this last class belong, for example, VGSR and VHP, which represent the variations in the GSR and HP, respectively.

Among the first class normalization methods, the gold standards z-score and max-min normalization stand out, corresponding to equations 4.13 and 4.14, respectively. A modified version of the max-min method that scales the values in the range [-1 1] was also

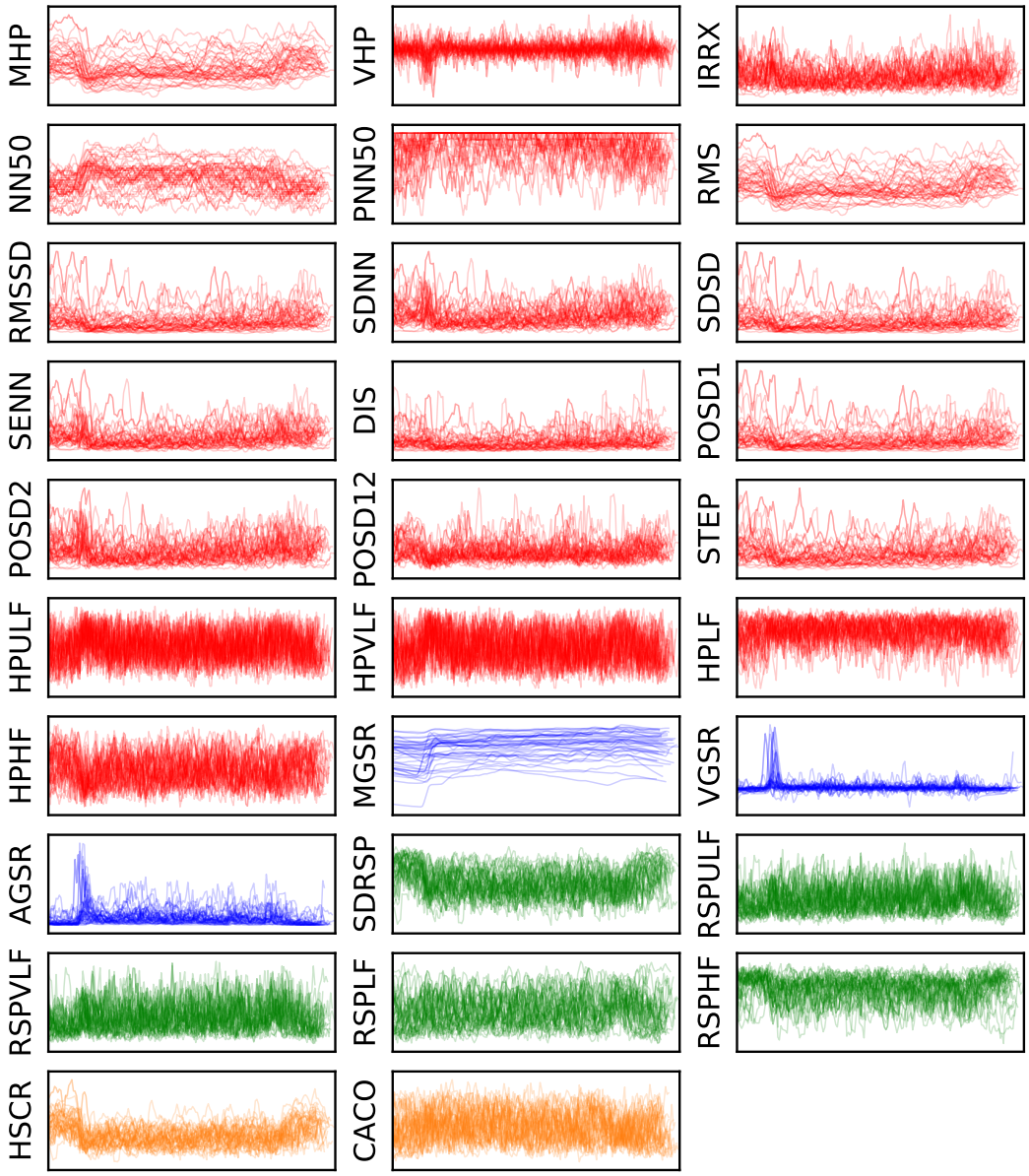

FIGURE 4.13: Parameters extracted from all the participants displayed at the same time without normalization.

implemented in this thesis according to equation 4.15. The fourth method proposed corresponds to equation 4.16, where the minimum value is adjusted to zero while the rest of the signal is scaled based on the median value.

$$x' = \frac{x - \mu}{\sigma} \tag{4.13}$$

$$x' = \frac{x - x_{min}}{x_{max} - x_{min}} \tag{4.14}$$

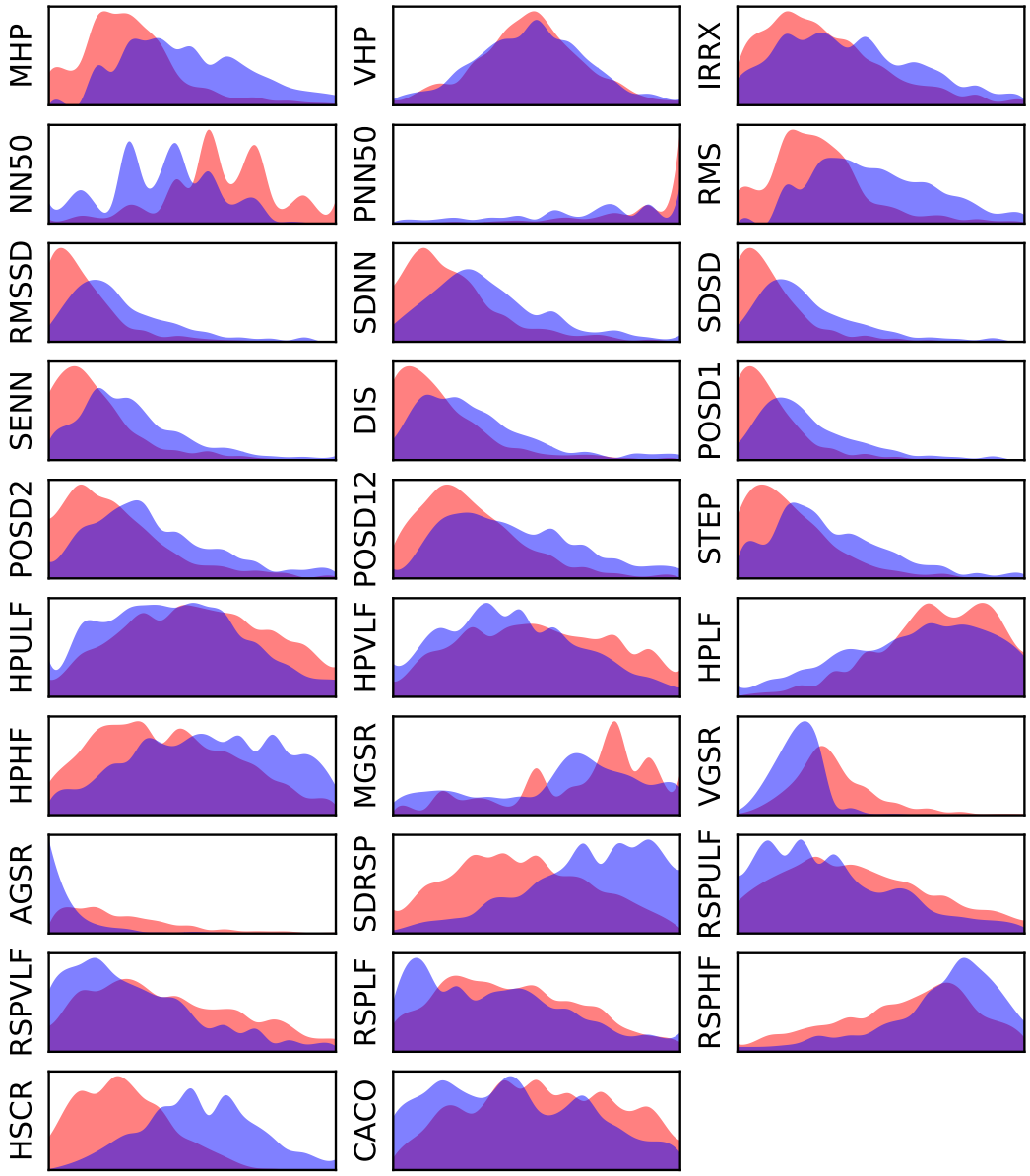

FIGURE 4.14: Histogram of the values corresponding to states of stress (red) and relaxation (blue) for each parameter.

$$x' = 2 * \frac{x - x_{min}}{x_{max} - x_{min}} - 1 \tag{4.15}$$

$$x' = \frac{x - x_{min}}{(x - x_{min})_{median}} \tag{4.16}$$

On the other hand, three methods are proposed to carry out the second class of normalization. The first method is related to z-score, but the subtraction of the average value is excluded to keep the zero in the same position according to equation 4.17. The second is another modified version of the max-min method, where the values are only divided by the maximum absolute value to keep zero in the same position according to equation

4.18. The third and last is a nonlinear normalization method that analyzes positive and negative values separately, dividing them by the maximum absolute value for each of the signs to scale the signal in the range [-1, 1] according to equation 4.19.

$$x' = \frac{x}{\sigma} \tag{4.17}$$

$$x' = \frac{x}{|x|_{max}} \tag{4.18}$$

$$\begin{cases} x'[x>0] = \dfrac{x[x>0]}{x[x>0]_{max}} \\ x'[x<0] = \dfrac{x[x<0]}{|x[x<0]|_{max}} \end{cases} \tag{4.19}$$

To assess which of these normalization methods is the most appropriate for each parameter, the loss function shown in 4.20 is proposed. This function is based on two principles reflected in its dividend and divisor. The first principle, reflected in the dividend, states that the standard deviation of the parameter values of all participants together during the relaxation (σ_{relax}) and stress (σ_{stress}) stages has to be small. Therefore, the product between the standard deviation of the normalized values of the parameters in the stress and relaxation intervals must be as small as possible. The second principle, reflected in the divisor, states that the difference between the mean value of the normalized parameters in the relaxation intervals (μ_{relax}) and in the stress intervals (μ_{stress}) must be as large as possible. This principle is reflected in Figure 4.15.

$$norm_{loss} = \frac{\sigma_{relax} * \sigma_{stress}}{\mu_{relax} - \mu_{stress}} \tag{4.20}$$

Table 4.2 shows the losses obtained for each of the parameters according to the different classes of normalization applied. The lower the value, the better the normalization method adjusts to the proposed problem. Values in bold represent the method with the lowest loss for each of the parameters.

According to the results observed in Table 4.2, the max-min 4.14 and modified max-min 4.18 normalizations achieved the lowest losses for each of the parameter normalization classes defined in this thesis. Figure 4.16 shows the parameters of all individuals plotted at the same time after normalization.

In Figure 4.17 the distribution of each normalized parameter is represented based on its belonging to states of stress and relaxation according to the type 1 partial labels. These normalized parameters are better distributed than the previously shown unnormalized parameters in Figure 4.14.

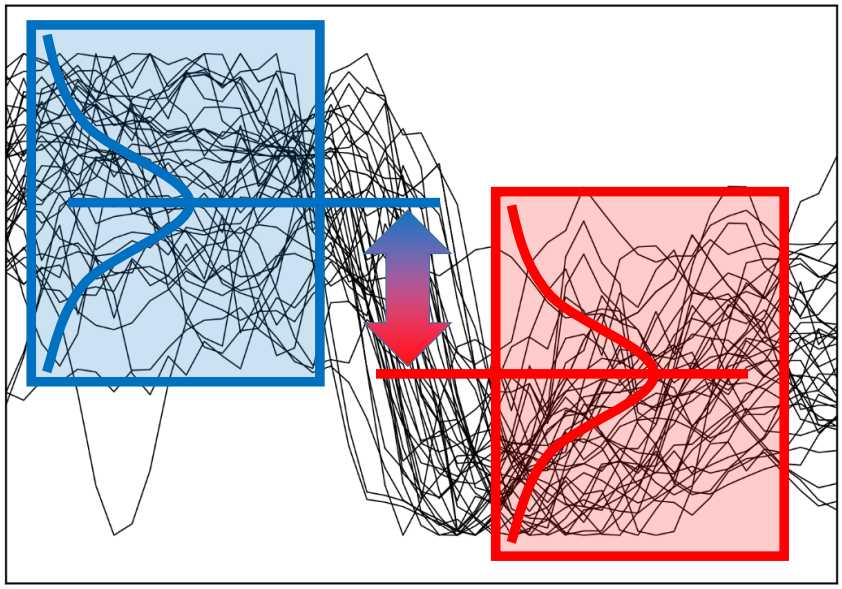

FIGURE 4.15: Blue and red boxes correspond to the relaxation and stress stages respectively, from which the standard deviations and the mean values of relaxation and stressful states are extracted.

4.4 Distribution analysis and parameter selection

With the parameters optimally normalized, it is necessary to select the most appropriate according to their ability to differentiate between states of relaxation and stress. For this purpose, the histograms of each of the normalized parameters plotted in Figure 4.17 according to their belonging to states of relaxation and stress were considered. Furthermore, in Figure 4.18 the probabilities for each normalized parameter to belong to a state of relaxation or stress are graphically represented, in the range [-1, 1], where 1 represents the maximum belonging to stress, -1 the maximum belonging to relaxation and 0 the same belonging to both states. This representation makes it easier to identify those parameters that are most influenced by changes resulting from stress and relaxation. To calculate the probabilities, data from Figure 4.17 were processed according to equation 4.21, where $stress_i$ and $relaxation_i$ refer to the distribution of each parameter ($param$) for a parameter value i.

$$P(param)_i = \frac{stress_i - relax_i}{stress_i + relax_i} \tag{4.21}$$

In addition to the graphical representations of the parameter distribution and probabilities, the losses from Table 4.2 were also used to carry out the parameter selection. These are good indicators of the quality of the parameters, since a lower loss value represents a greater potential to carry out the differentiation between stress and relaxation states. These losses are illustrated in Figure 4.19, in which the best normalization loss obtained for each parameter is graphically represented.

TABLE 4.2: Loss of normalization methods.

	$Norm_0$	$Norm_1$	$Norm_2$	$Norm_3$	$Norm_4$	$Norm_5$	$Norm_8$
AGSR	-	0.2396	**0.0561**	0.1122	-	-	0.2592
CACO	-	1.3077	**0.2760**	0.5521	-	-	0.6956
DIS	-	0.5460	**0.1346**	0.2693	-	-	0.5181
HPHF	-	0.7108	**0.1668**	0.3336	-	-	0.3456
HPLF	-	1.5048	**0.2950**	0.5900	-	-	0.4726
HPULF	-	1.1522	**0.2733**	0.5466	-	-	0.5501
HPVLF	-	1.0227	**0.2583**	0.5165	-	-	0.5040
HSCR	-	0.2053	**0.0490**	0.0979	-	-	0.1218
IRRX	-	1.2257	**0.2410**	0.4819	-	-	0.7686
MGSR	-	0.6350	**0.1762**	0.3524	-	-	0.3162
MHP	-	0.1203	**0.0299**	0.0598	-	-	0.1168
NN50	-	2.2381	**0.8409**	0.8409	-	-	0.8409
PNN50	-	-	-	-	-	-	-
POSD1	-	0.2738	**0.0682**	0.1363	-	-	0.2544
POSD12	-	0.5248	**0.1102**	0.2204	-	-	0.2817
POSD2	-	0.6874	**0.1417**	0.2835	-	-	0.5367
RMS	-	0.1196	**0.0297**	0.0594	-	-	0.1163
RMSSD	-	0.2754	**0.0682**	0.1365	-	-	0.2557
RSPHF	-	0.7960	**0.1843**	0.3685	-	-	0.2616
RSPLF	-	2.0636	**0.6847**	1.3693	-	-	2.1185
RSPULF	-	1.3787	**0.3037**	0.6073	-	-	0.9166
RSPVLF	-	1.1525	**0.2377**	0.4753	-	-	0.8584
SDNN	-	0.5705	**0.1241**	0.2482	-	-	0.4587
SDRSP	-	0.3864	**0.0937**	0.1875	-	-	0.1775
SDSD	-	0.2738	**0.0682**	0.1363	-	-	0.2544
SENN	-	0.4494	**0.0969**	0.1937	-	-	0.3799
STEP	-	0.3682	**0.0835**	0.1670	-	-	0.2737
VGSR	0.3139	-	-	-	**0.0727**	0.1322	-
VHP	3.0637	-	-	-	**0.9134**	1.0607	-

Considering the distribution, probabilities and normalization loss obtained for each parameter according to type 1 partial labels, the parameters selected to continue with the next phases of the development are the following: MHP, RMS, RMSSD, SDSD, DIS, POSD1, STEP, VGSR, AGSR, SDRSP and HSCR. These parameters present the lowest losses in Table 4.2 and a solid distribution in Figures 4.17 and 4.18.

4.5 Correlation and principal component analysis

An important factor to consider is the correlation that exists among different parameters. The use of strongly correlated parameters can lead to redundant information that negatively affects the result of the used algorithms, which can provide more weight to the redundant information than to the rest of the information. Figure 4.20 shows the correlation between the different parameters, where the positive and negative correlation is represented with the same color since they have the same redundant effect.

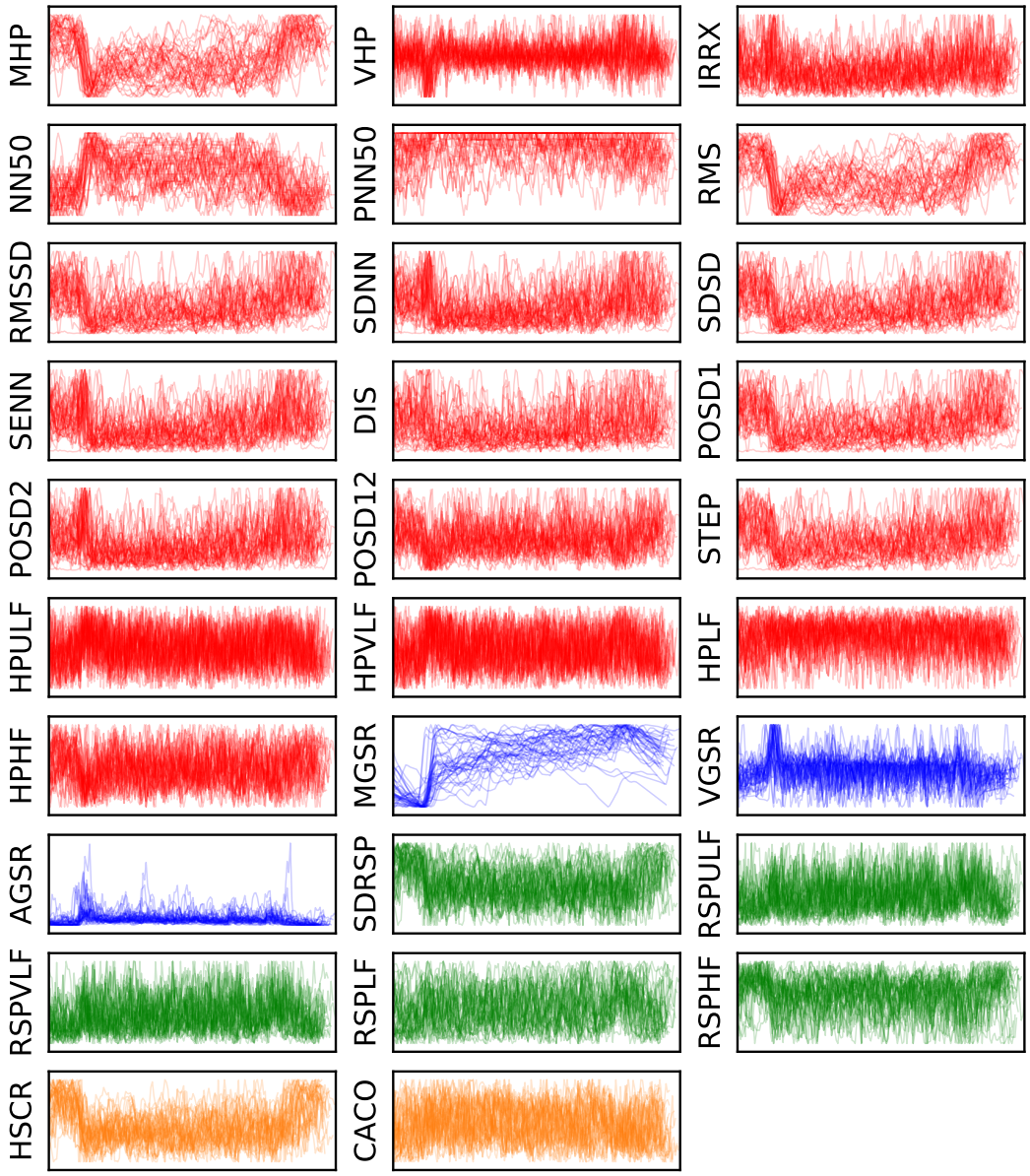

FIGURE 4.16: Parameters extracted from all participants displayed at the same time after normalization.

This solution proposes the use of PCA to eliminate redundancy with the minimum loss of useful information and achieve an orthogonalised set of PCs. Figure 4.21 shows the percentage of original information retained according to the loss of cumulative variance for each number of PCs. A maximum loss of cumulative variance of 1% was set, which is a gold standard in PCA.

The minimum number of PCs that complies with the 1% loss is 5. These PCs, which are an orthogonalised and reduced version of the original parameters, are shown to the right of Figure 4.22, and will be used from this point for further processing.

In Figure 4.23, the first three PCs are illustrated in a three-dimensional graph, showing the clear difference that exists between the values representative of relaxation (blue) and

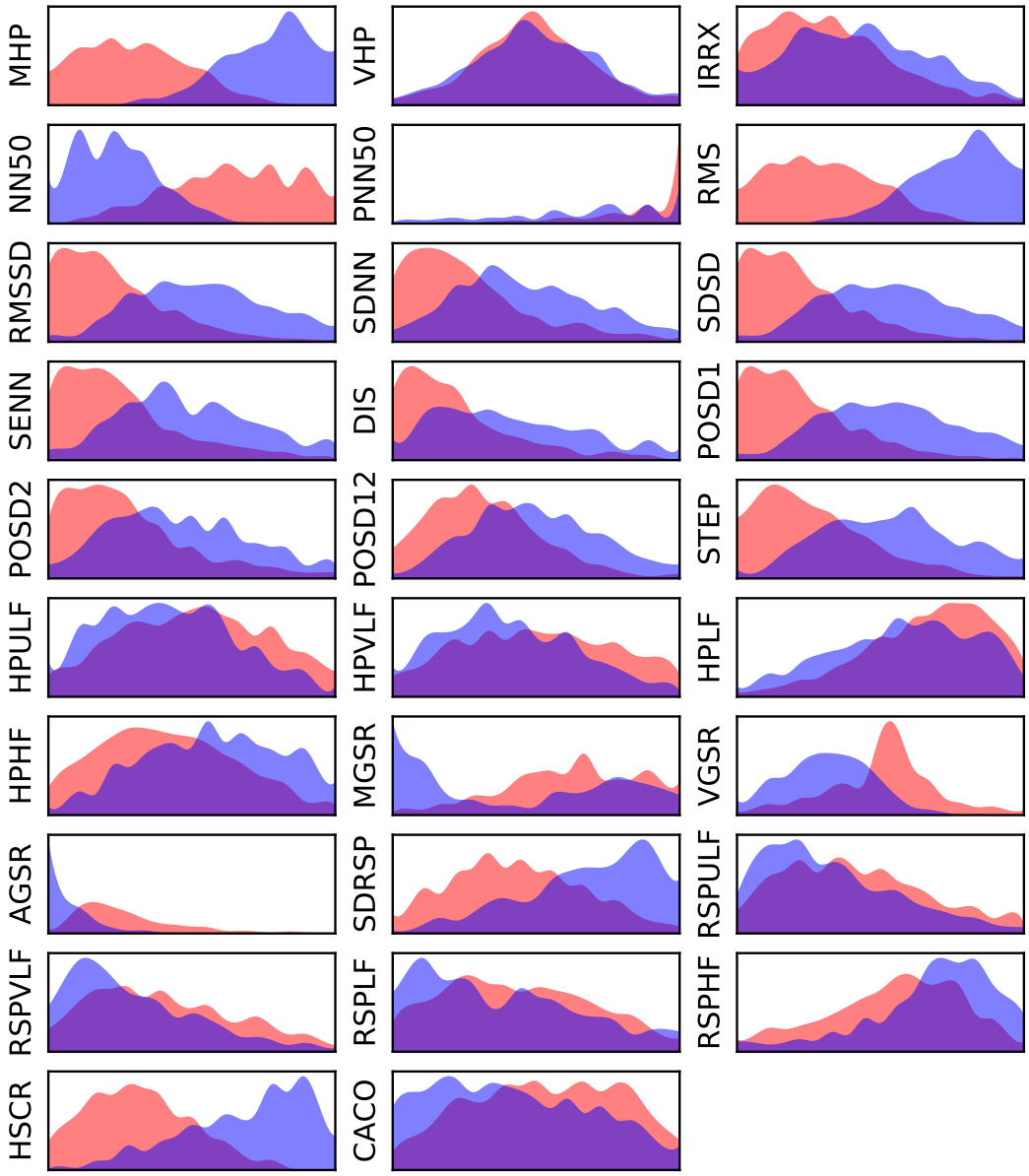

FIGURE 4.17: Histogram of the values corresponding to states of stress (red) and relaxation (blue) for each normalized parameter.

stress (red). The signal used in this representation is the same as in Figure 4.22, as well as the values labeled on it.

4.6 Continuous pseudo-labeling

To complete the previously performed partial labeling, this subsection proposes the implementation of a semi-supervised learning methodology to extract a continuous level of relaxation and stress in the range [0, 1], with 0 being the maximum measured relaxation and 1 the maximum stress value. To do this, the label spreading method was used, which, unlike the label propagation method, allows the labels initially set to be adjusted during the process, thus correcting any errors made during partial labeling.

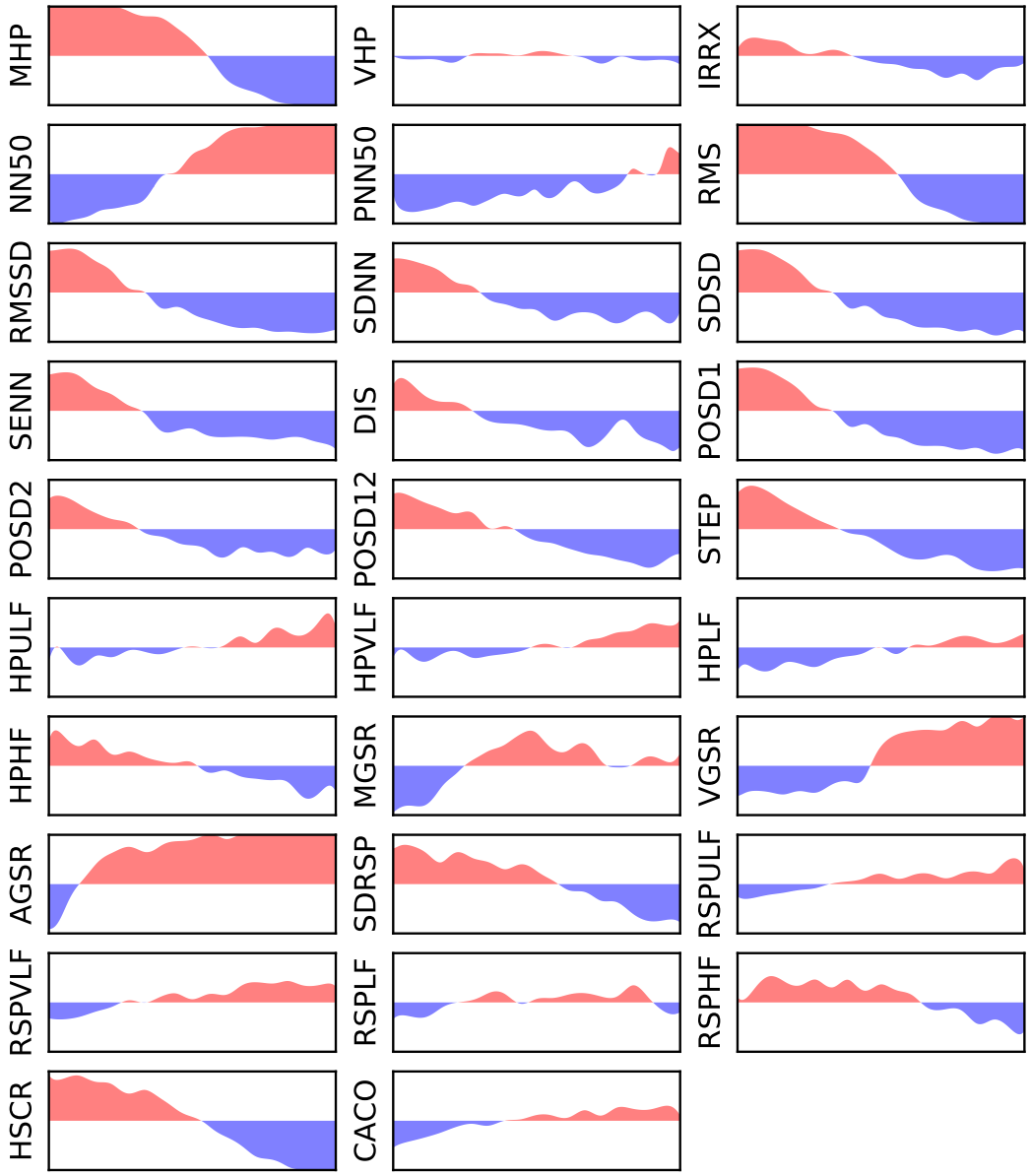

FIGURE 4.18: Graphic representation of the probability for each normalized parameter to belong to a state of stress (red) or relaxation (blue).

The label spreading algorithm provides two outputs. The first output is the complete labeling of the signal. The second output is the possibility of each analyzed window to belong to each of the labels. These possibilities are defined in a continuous range [0, 1]. In this particular case only two labels are used, so the possibilities associated with each of the labels are inversely proportional to each other. Therefore, it is sufficient to use one of the possibilities as a continuous signal representative of the level of relaxation and stress at each moment. This results in the labeling illustrated in Figure 4.24, where the blue bands represent a higher level of relaxation and the red bands a higher level of stress.

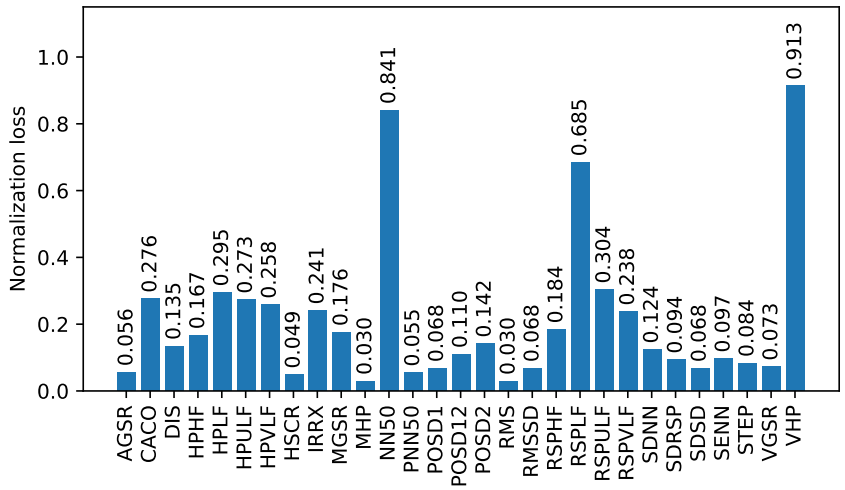

FIGURE 4.19: Graphical representation of the best normalization loss obtained for each physiological parameter.

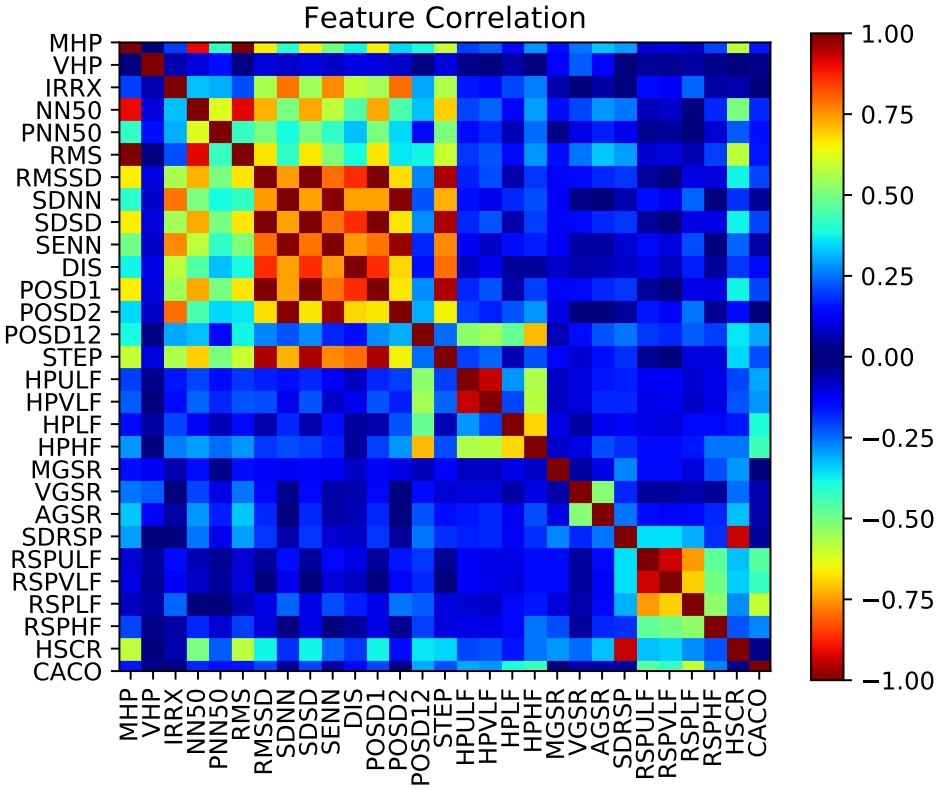

FIGURE 4.20: Parameter correlation.

4.7 Results and discussion on pseudo-labeling

To evaluate the proposed method, the entire methodology, from PCA to pseudo-labeling, was validated using 21-fold cross-validation on both normalized and unnormalized parameters. Figures 4.25, 4.26, 4.27 and 4.28 show a representation of the first two PCs as a function of the labels obtained after performing the continuous pseudo-labeling. Figures

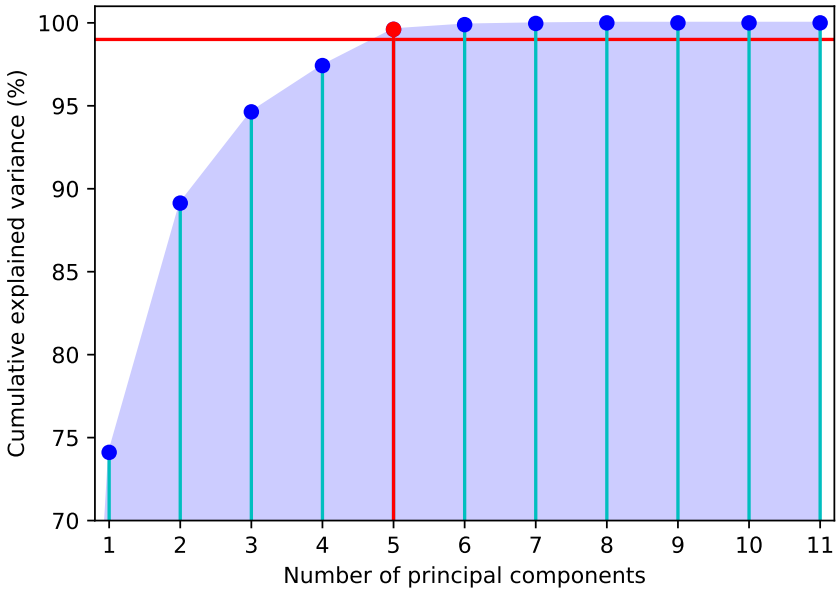

FIGURE 4.21: Cumulative percentage of variance depending on the number of PCs.

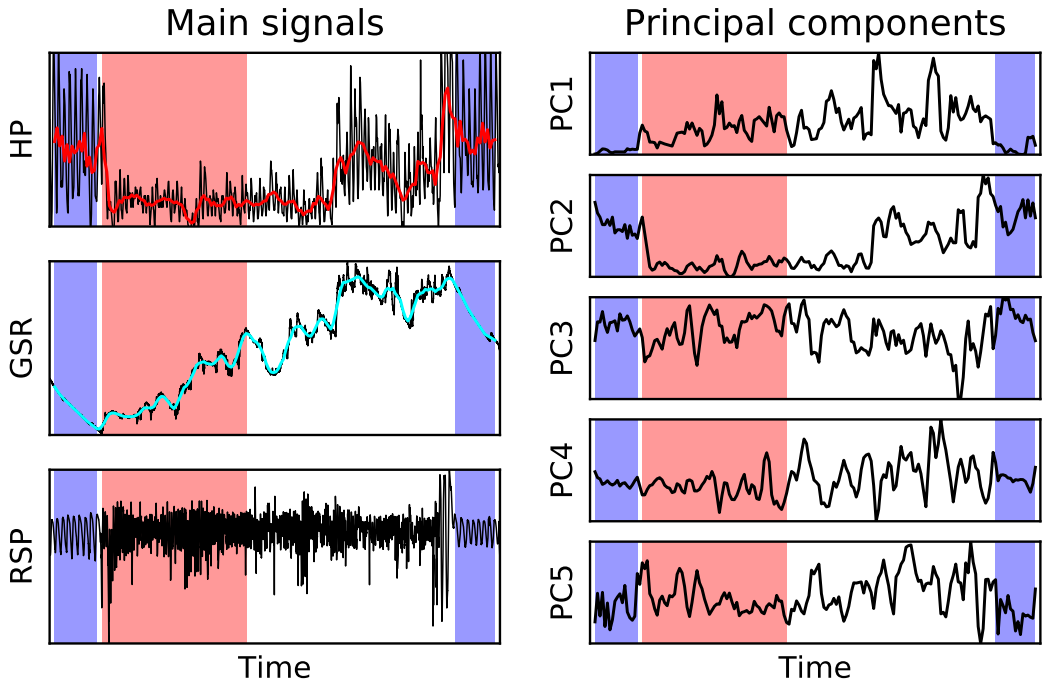

FIGURE 4.22: Main physiological signals in the graphs on the left and PCs in the graphs on the right.

4.25 and 4.26 correspond to the training and validation sets of the unnormalized parameters respectively, while Figures 4.27 and 4.28 correspond to the training and validation sets of the normalized parameters. These figures show the improvement resulting from the parameter normalization, which results in a more uniform distribution compared to the continuous labeling obtained from unnormalized parameters.

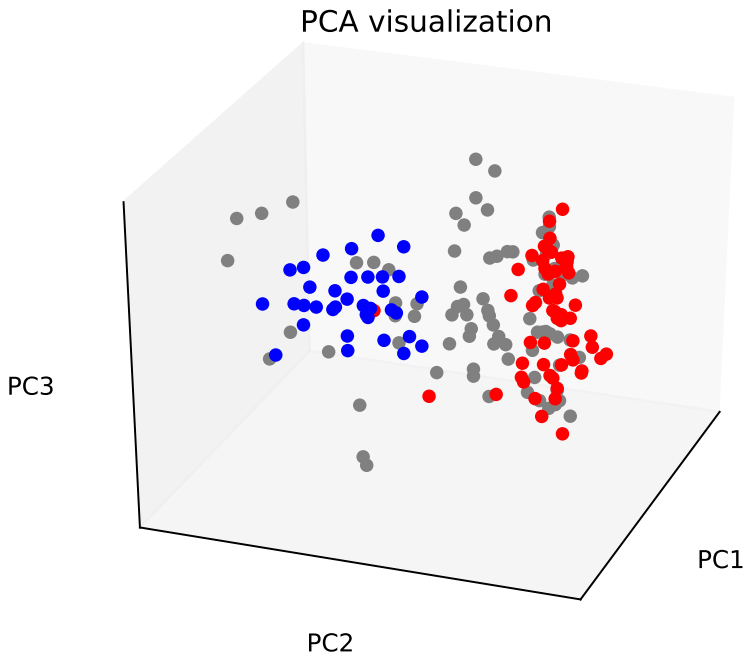

FIGURE 4.23: Three-dimensional representation of the PCs with the relaxation values colored in blue and the stress values colored in red. The grey dots correspond to the unlabeled values.

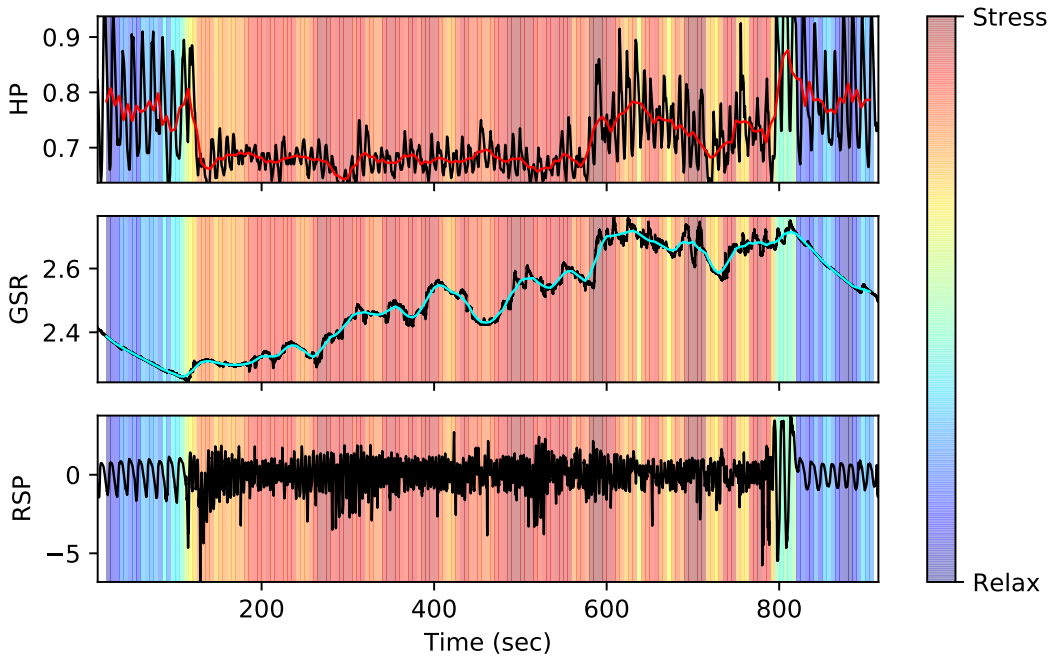

FIGURE 4.24: Pseudo-labeling of the signal in a continuous range [0, 1].

To achieve an objective assessment of the stress and relaxation level estimations (ranging between 0 and 1) compared to binary type 2 labeling, error metrics were defined as follows: a true positive (TP) corresponds to a real state of stress in which the obtained relaxation-stress level is > 0.5, a true negative (TN) corresponds to a real state of relaxation

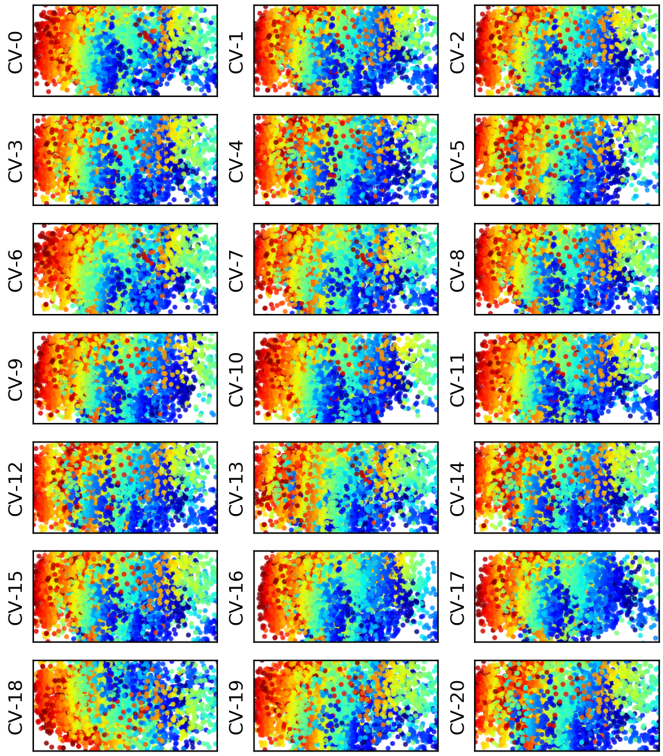

FIGURE 4.25: Labeling of the 21-fold training sets without normalization.

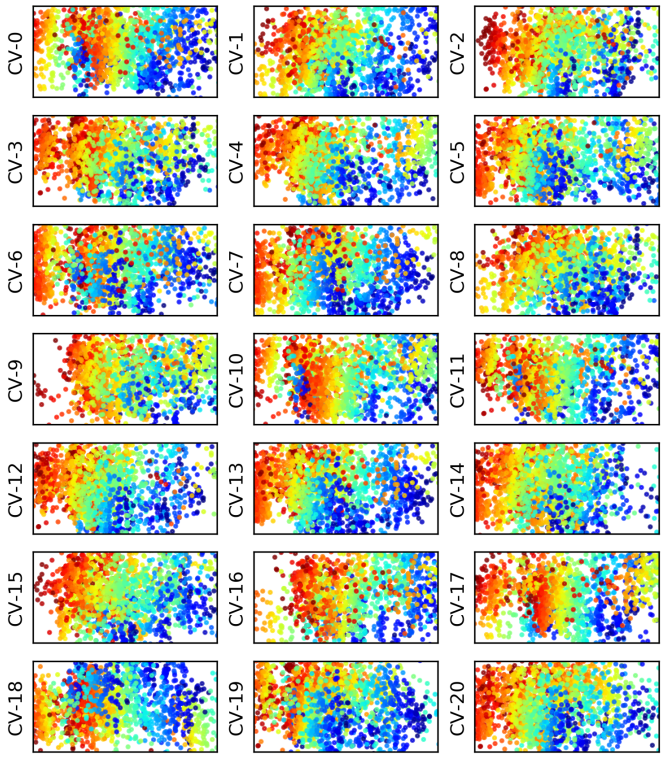

FIGURE 4.26: Labeling of the 21-fold validation sets without normalization.

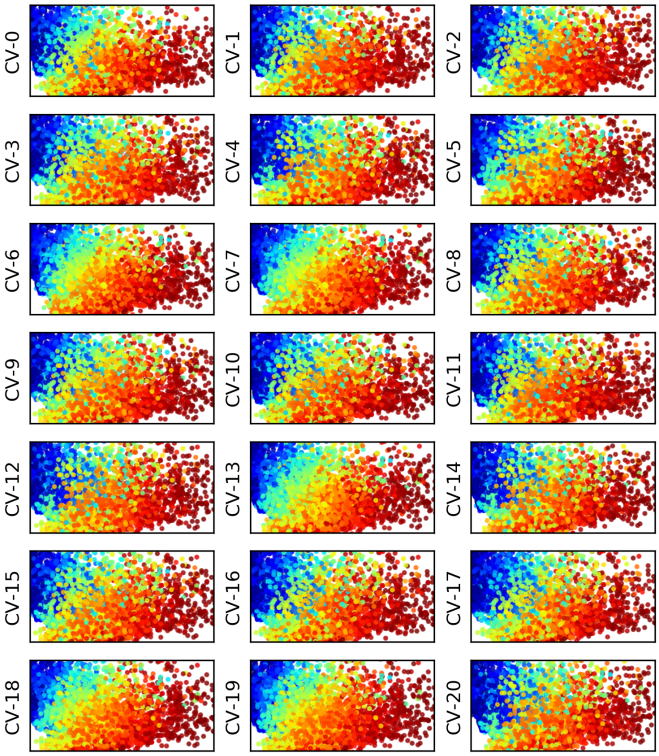

FIGURE 4.27: Labeling of the 21-fold normalized training sets.

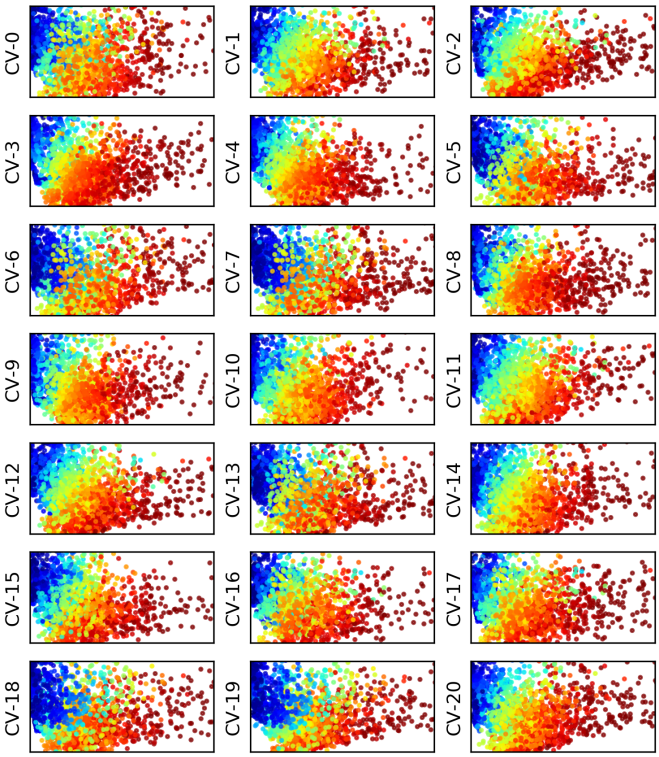

FIGURE 4.28: Labeling of the 21-fold normalized validation sets.

in which the obtained relaxation-stress level is ≤ 0.5, a false positive (FP) corresponds to a

real state of relaxation in which the obtained relaxation-stress level is > 0.5 and a false negative (FN) corresponds to a real state of stress in which the obtained relaxation-stress level is ≤ 0.5. These metrics were used to calculate the sensitivity (*Se*), specificity (*Sp*), accuracy (*Ac*) and F1 score (*F1*), according to equations 2.51, 2.52, 2.53 and 2.54, respectively. The resulting scores, for both normalized and unnormalized parameters, are shown in Table 4.3, which are also graphically represented in Figure 4.29.

TABLE 4.3: Results obtained during pseudo-labeling cross-validation for normalized and unnormalized parameters derived from HP, GSR and RSP.

Class	TP	TN	FP	FN	Se (%)	Sp (%)	Ac (%)	F1 (%)
Unnorm.	7890	23457	1155	1371	85.20	95.31	92.55	89.97
Norm.	9114	24444	168	147	98.41	99.32	99.07	98.86

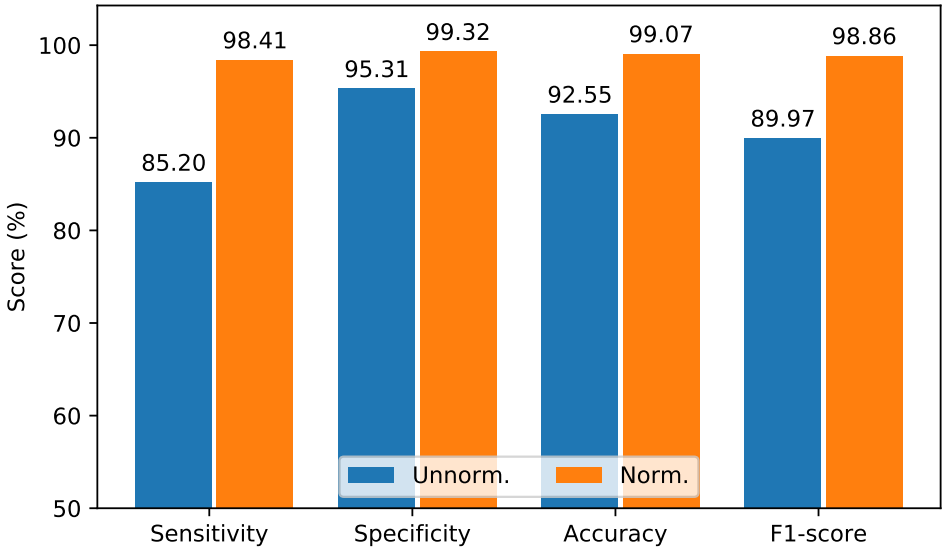

FIGURE 4.29: Graphical representation of the results obtained during pseudo-labeling cross-validation for normalized and unnormalized parameters derived from HP, GSR and RSP.

As expected from the distribution analysis and parameter selection stage by observing the labels dispersion with normalized and unnormalized parameters, the quality of the results obtained from the normalized parameters is considerably better than using the unnormalized parameters. To further investigate the results obtained with the normalized parameters, the whole process was repeated for different combinations of physiological signals, leading to the results presented in Table 4.4 and graphically represented in Figure 4.30.

According to the results obtained in Table 4.4, the combined implementation of GSR and HP stands out, achieving slightly better results by adding RSP to the processing. The GSR shows a higher *Sp* than *Se*, emphasizing the ability of this signal to reflect relaxation states. GSR is directly related to sympathetic activation, so non-activation becomes much more noticeable, resulting in TNs. Definitely, the labeling achieved shows a high accuracy rate,

TABLE 4.4: Results obtained during pseudo-labeling cross-validation according to the combination of the normalized parameters of different signals.

Signals	TP	TN	FP	FN	Se (%)	Sp (%)	Ac (%)	F1 (%)
HP	8043	19925	4687	1218	86.85	80.96	82.54	83.80
GSR	7665	24528	84	1596	82.77	99.66	95.04	90.43
RSP	7917	19236	5376	1344	85.49	78.16	80.16	81.66
HP, GSR	9030	24465	147	231	97.51	99.40	98.88	98.45
HP, RSP	8421	20622	3990	840	90.93	83.79	85.74	87.21
GSR, RSP	8400	24360	252	861	90.70	98.98	96.71	94.66
HP, GSR, RSP	9114	24444	168	147	98.41	99.32	99.07	98.86

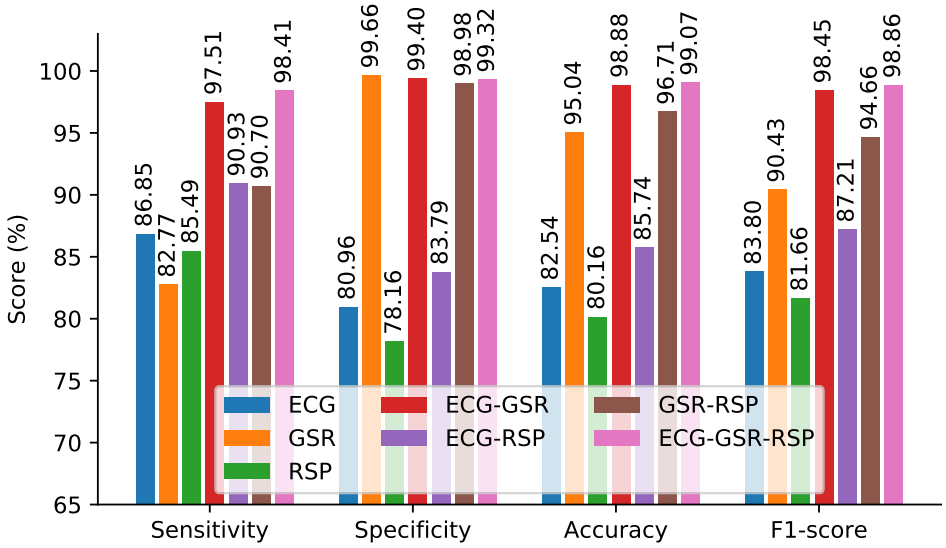

FIGURE 4.30: Graphical representation of the results obtained during pseudo-labeling cross-validation according to the combination of the normalized parameters of different signals.

which is considered adequate to carry out the training of a generalized model for the prediction of the level of relaxation and stress in the next section.

5 ANS activity prediction: Design and comparison of intelligent models

In this section, a methodology for evaluating existing supervised and unsupervised learning techniques in relation to their ability to predict the level of relaxation and stress in people is proposed by using the labels and principal components (PCs) calculated in the previous section. For this purpose, the capacity of each method to predict the level of stress and relaxation was evaluated considering the sensitivity (*Se*), specificity (*Sp*), accuracy (*Ac*) and F1 score (*F1*) as objective indicators of their performance. In addition, an evaluation of the training and inference times was performed, which are critical regarding the required development time and their implementation in real-time applications.

Two main approaches were considered for the selection of these methods. The first approach is based on the use of fuzzy logic for the implementation of an unsupervised algorithm whose kernel consists of a set of rules derived from expert knowledge. The second approach is the application of different supervised learning methods based on fuzzy rules. These were trained on the pseudo-labels estimated from type 1 labels in the previous section, which have proven to be robust as they obtained a high *F1* during the evaluation stage against type 2 labels. Fuzzy rule-based supervised learning systems have been particularly interesting in the development of this thesis, since it is possible to extract knowledge from human physiology through the rules and fuzzy sets inferred during the training stage. The evaluated fuzzy rule-based supervised learning methods were the Wang and Mendel's method (WM), the dynamic evolving neural-fuzzy inference system (DENFIS), the hybrid neural fuzzy inference system (HyFIS) and the heuristics and gradient descent method (FS.HGD). In addition, artificial neural networks (ANNs) were also evaluated.

Achieved results were validated using the type 2 labels from the previous section in 21-fold cross-validation (CV) according to the CV strategy previously depicted in Figure 4.3. Type 2 labels were generated by personnel with expert knowledge in the interpretation of physiological signals. Of the 42 available records, 30 (72%) were used for training and 12 (28%) in the validation stage. Moreover, training and validation processes were carried out in duplicate, both using the PCs derived from the normalized and unnormalized parameters. In the design of the fuzzy algorithm, only normalized parameters were used since it is impractical to define the membership functions from unnormalized parameters. Figure 5.1 shows an outline of the methodology followed in this section.

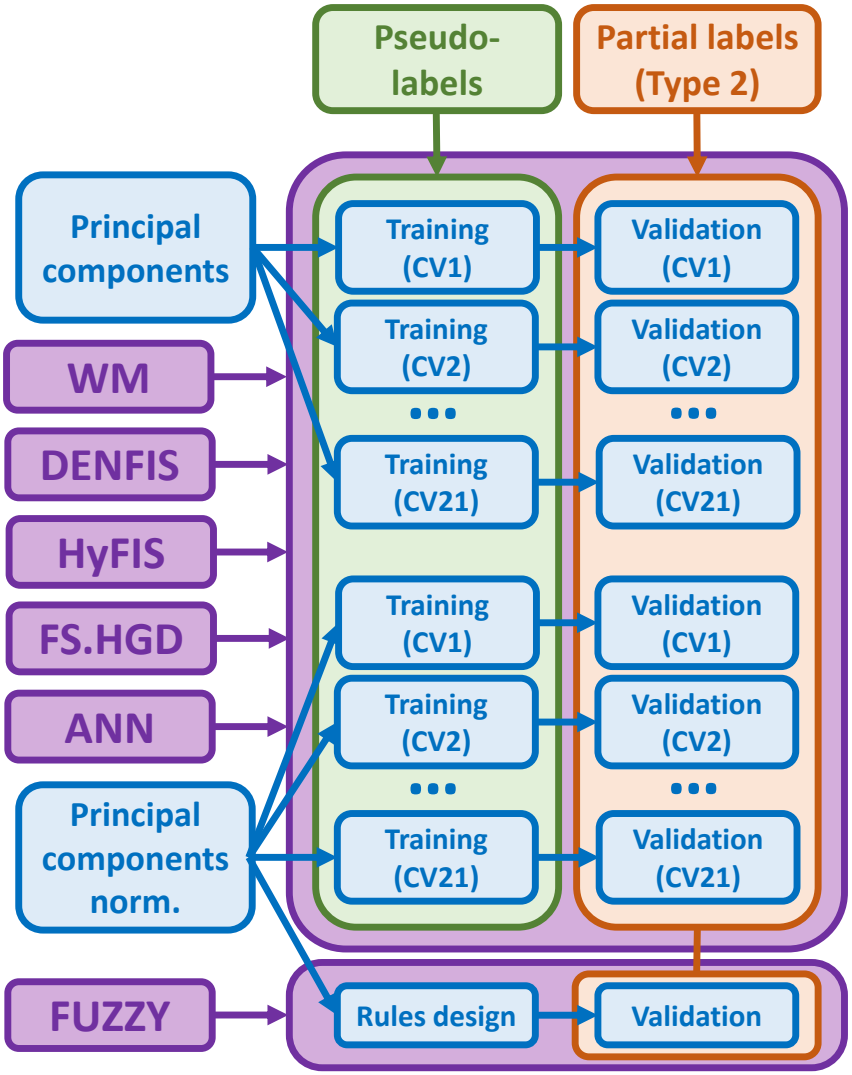

FIGURE 5.1: Flowchart of the proposed methodology for training and validation of the models.

Below, the fuzzy logic model implemented in this thesis is presented, followed by the different configurations employed in the supervised learning models. Finally, the results achieved are presented and discussed.

5.1 Design of the unsupervised fuzzy logic model

Considering the fact that the records are not originally labeled, in this subsection an unsupervised Mamdani fuzzy logic model is presented for the estimation of the level of relaxation and stress through rules based on expert knowledge.

To estimate the physiological state of the individual using a fuzzy logic model, five parameters representative of the state and variation of the heart period (HP), galvanic skin response (GSR) and breathing (RSP) signals defined in section 4 were selected. These are: the mean HP (MHP), which represents the average HP at each moment; the variation of

the HP (VHP), which indicates strong changes in the HP; the product between the standard deviation of the RSP frequencies and root mean square of the HP (HSCR), which represents the alteration in both the frequency dispersion of the RSP and variations in the HP through the root mean square; the variation in the galvanic skin response (VGSR), which emphasizes the strong changes in the stability of the GSR; and the differential area between the GSR signal and its first-order interpolation (AGSR), which reliably represents the non-activation of the sympathetic nervous system (SNS) in the GSR. Figure 5.2 shows an outline of the implemented fuzzy model.

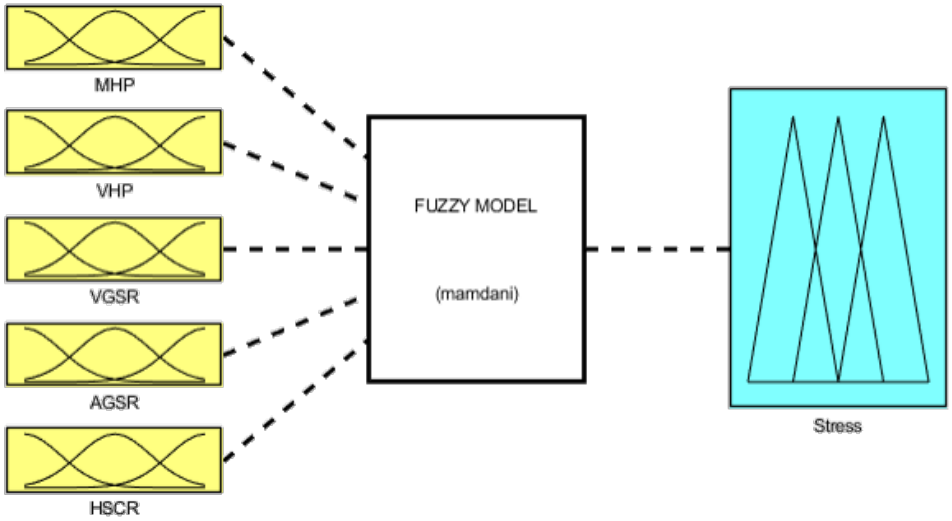

FIGURE 5.2: Diagram of the proposed fuzzy model.

The output of the model was ranged from 0 to 1, where 0 represents the maximum relaxation level and 1 represents the maximum stress level. Table 5.1 shows the configuration that was employed to set up the membership function (MF) for each input and output, where PIMF, TRAPMF, SMF and ZMF refer to the Pi-shaped MF, trapezoidal MF, S-shaped MF and Z-shaped MF, respectively. Expert knowledge was applied via well-defined rules extracted from the literature [175, 19, 20, 11, 172, 173]. This approach facilitated the construction of the set of rules shown in Table 5.2.

Figure 5.3 shows the total weight of each parameter in the set of rules. MHP and HSCR are the parameters with the greatest weight because both are derived from the cardiovascular response. Therefore, they are strongly correlated with both parasympathetic and sympathetic branches of the autonomic nervous system (ANS). Otherwise, the parameters derived from GSR are closely related to sympathetic activity. For this reason, they are suitable for measuring only the activity of the SNS, but not that of the parasympathetic nervous system [19].

5.2 Configuration of the supervised learning models

The training of the supervised learning models was performed using the five PCs and the labels obtained during the pseudo-labeling in the previous section as inputs and outputs

TABLE 5.1: Expert knowledge-based rules.

Type	Name	Range	MF name	MF type	MF parameters
Input 1	MHP	[0 1]	Low	SMF	[0.5 1]
			Medium	PIMF	[0 0.5 0.5 1]
			High	ZMF	[0 0.5]
Input 2	VHP	[-2 2]	Low	SMF	[0 1.5]
			Medium	PIMF	[-1.5 0 0 1.5]
			High	ZMF	[-1.5 0]
Input 3	VGSR	[-2 2.5]	Low	ZMF	[-2 0]
			Medium	PIMF	[-2 0 0 2.5]
			High	SMF	[0 2.5]
Input 4	AGSR	[0 1]	Low	ZMF	[0 1]
			High	SMF	[0 1]
Input 5	HSCR	[0 1]	Low	SMF	[0.5 1]
			Medium	PIMF	[0 0.5 0.5 1]
			High	ZMF	[0 0.5]
Output	Stress	[0 1]	Low	TRAPMF	[-0.5 -0.25 0.25 0.5]
			Medium	TRAPMF	[0 0.25 0.75 1]
			High	TRAPMF	[0.5 0.75 1.25 1.5]

TABLE 5.2: Implemented membership function parameters.

MHP	VHP	VGSR	AGSR	HSCR	Weight	Connection	Stress
High	-	-	-	-	0.3	OR	High
Medium	-	-	-	-	0.3	OR	Medium
Low	-	-	-	Low	0.3	OR	Low
High	-	-	-	High	0.4	AND	High
Medium	-	-	-	Medium	0.5	AND	Medium
Low	-	-	-	Low	0.6	AND	Low
High	-	-	High	High	0.7	AND	High
Low	-	Low	Low	Low	0.8	AND	Low
High	High	High	High	High	1	AND	High
Medium	Medium	Medium	-	Medium	1	AND	Medium
Low	Low	Low	Low	Low	1	AND	Low
-	-	Low	Low	-	0.5	AND	Low
-	Low	Low	-	-	0.1	OR	Low
-	High	High	-	-	0.1	OR	High
-	Low	Low	-	-	0.2	AND	Low
-	High	High	-	-	0.2	AND	High
High	-	-	-	Low	0.2	AND	Medium
-	-	-	-	High	0.1	OR	High
-	-	-	-	Medium	0.2	OR	Medium
-	Medium	Medium	-	-	0.1	OR	Medium
-	Medium	Medium	-	-	0.2	AND	Medium

of the models, respectively. As mentioned previously, the supervised learning algorithms validated in this proposal are: WM, DENFIS, HyFIS, FS.HGD and ANN. These algorithms contain several hyperparameters that must be tuned to obtain optimal results. Next, the

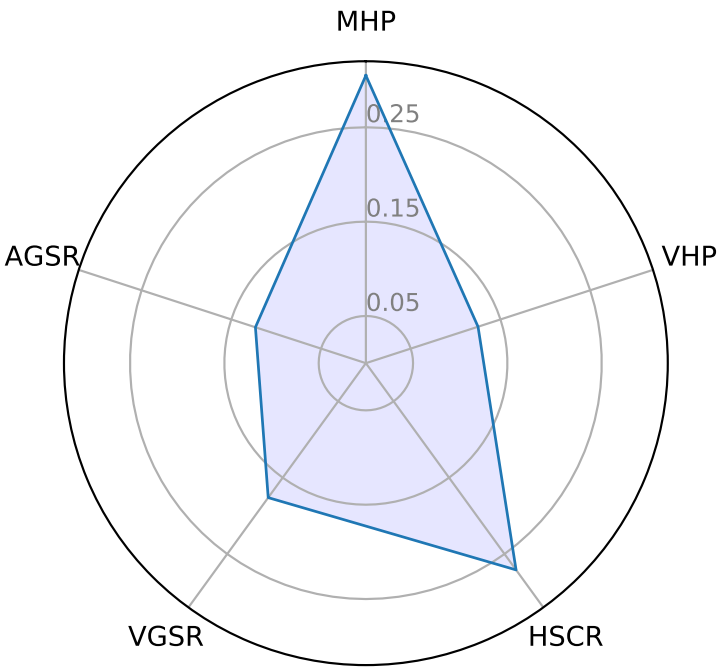

FIGURE 5.3: Total weight of each parameter in the set of rules.

main hyperparameters of the fuzzy rule-based systems (FRBSs) and the configuration used to train the ANN are presented.

5.2.1 Fuzzy rule-based systems

For a reliable implementation of the FRBSs, a validated framework is needed to carry out both training and inference of the models. For the training and validation of the fuzzy rule-based supervised learning models, the widely used "*frbs*" package developed in R was selected, which is available in the CRAN (comprehensive R archive network) repository [126]. This package contains all the FRBSs implemented in this solution and provides simple and effective tools for their deployment. To perform the integration of this package with the code developed up to this point, an implementation in Python of the "*frbs*" package is proposed in this thesis, which allows the execution of the R commands of the "*frbs*" package through functions developed in Python. This contribution provides the opportunity to train the different models using the Python programming language, which was used throughout this thesis, thus connecting the different sections of the current development. In addition, the proposed abstraction allows the implementation of FRBS algorithms that were not previously developed in Python.

The models contained in the "*frbs*" package can be customized by modifying their hyperparameters in order to find the combination that best fits each particular problem. To better understand the model tuning carried out throughout this section, a scheme of each of the hyperparameters corresponding to each of the FRBSs implemented in this solution are shown below, along with their possible values:

- **WM**
  - *num.labels*: a positive integer to determine the number of labels (linguistic terms).
  - *type.mf*: the type of the membership function.
    1. TRIANGLE refers to triangular shape MF.
    2. TRAPEZOID refers to trapezoid shape MF.
    3. GAUSSIAN refers to gaussian shape MF.
    4. SIGMOID refers to sigmoid MF.
    5. BELL refers to generalized bell MF.
  - *type.tnorm*: the type of conjunction operator (t-norm).
    1. MIN means standard type (minimum).
    2. HAMACHER means Hamacher product.
    3. YAGER means Yager class (with tao = 1).
    4. PRODUCT means product.
    5. BOUNDED mean bounded product.
  - *type.snorm*: the type of disjunction operator (s-norm).
    1. MAX means standard type (maximum).
    2. HAMACHER means Hamacher sum.
    3. YAGER means Yager class (with tao = 1).
    4. SUM means sum.
    5. BOUNDED mean bounded sum.
  - *type.defuz*: the type of the defuzzification method.
    1. WAM refers to the weighted average method.
    2. FIRST.MAX refers to the first maxima.
    3. LAST.MAX refers to the last maxima.
    4. MEAN.MAX refers to the mean maxima.
    5. COG refers to the modified center of gravity.
- **DENFIS**
  - *Dthr*: threshold value for the evolving clustering method, ranged between 0 and 1.

  - *d*: width of the triangular membership function.
  - *max.iter*: a positive integer to determine the maximum number of iterations.
  - *step.size*: the step size of the gradient descent method, a real number between 0 and 1.

- **HyFIS**
  - *num.labels*: a positive integer to determine the number of labels (linguistic terms).
  - *max.iter*: a positive integer to determine the maximum number of iterations.
  - *step.size*: the step size of the gradient descent method, a real number between 0 and 1.

- **FS.HGD**
  - *num.labels*: a positive integer to determine the number of labels (linguistic terms).
  - *max.iter*: a positive integer to determine the maximum number of iterations.
  - *step.size*: the step size of the gradient descent method, a real number between 0 and 1.
  - *alpha.heuristic*: a positive real number representing a heuristic value. The default value is 1.

5.2.2 Customized ANN

The design of the ANN was performed using the Tensorflow tool. A fully connected neural network architecture was implemented as illustrated in Figure 5.4, for which a customized design of a loss function is proposed in this thesis according to the desired stress and relaxation prediction values. The model was trained on labels in the range [-1, 1] using a hyperbolic tangent-based loss function directly on the output neuron. Note that in this section the hyperbolic tangent does not refer to the activation function of the output neuron, but to the function on which the loss function designed for this proposal is based, as explained below. This loss function evaluates the linear output of the output neuron defined as $z_{\text{out}} = \sum_{j=1}^{n_x} x_j \cdot w_j^{\text{out}} + b^{\text{out}}$, where w_j^{out} and b^{out} are the weights and bias of the output neuron, respectively. Once the network is trained, the inference is performed by adding a sigmoid activation function to the output neuron in order to range the output from 0 (maximum relaxation level) to 1 (maximum stress level) and to smooth out possible outliers.

Although the sigmoid function has similar properties to the hyperbolic tangent in the machine learning field, the hyperbolic tangent facilitates the convergence of the algorithm as its derivatives are larger than the derivatives of the sigmoid function, so the loss function minimizes faster. The fact that the hyperbolic tangent range is between -1 and 1 instead

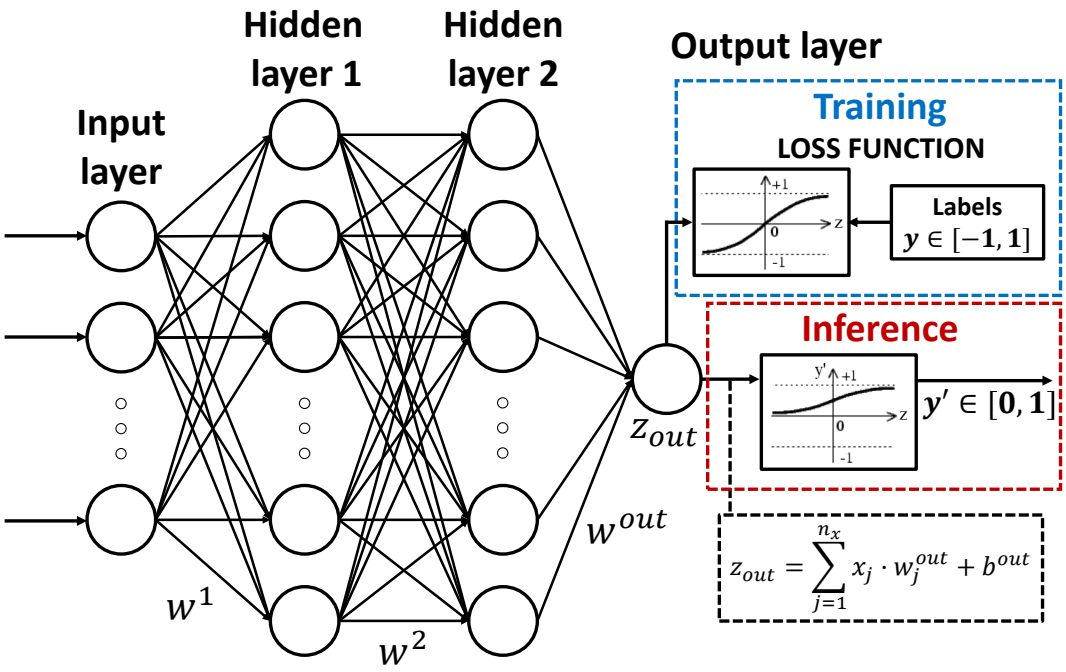

FIGURE 5.4: Diagram of the implemented ANN structure.

of 0 and 1 makes this function more convenient for training ANNs. This intuition is illustrated in Figure 5.5, where the ratio between the hyperbolic tangent and sigmoid functions corresponds to equation 5.1. As a result, the values of the derivatives are larger for the hyperbolic tangent function according to equation 5.2.

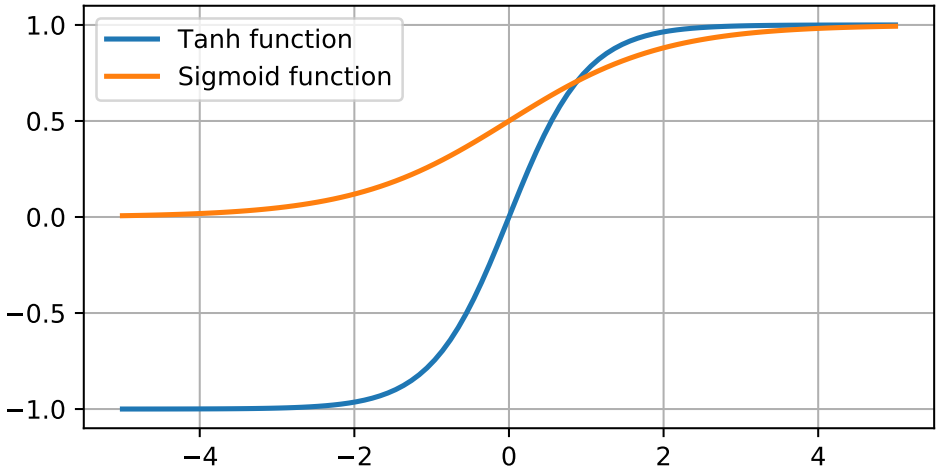

FIGURE 5.5: Illustration of the hyperbolic tangent and sigmoid functions.

$$\tanh(x) = 2\sigma(2x) - 1 \tag{5.1}$$

$$\left|\frac{\partial \tanh(x)}{\partial x}\right| > \left|\frac{\partial \sigma(x)}{\partial x}\right| \tag{5.2}$$

To calculate the loss, the linear value of the output neuron without activation function (z_{out}) was used, as explained above. Considering that the objective is the prediction of a continuous output z_{out} of relaxation and stress in the range [-1, 1] during the training stage (do not mistake with the range [0, 1] used for inference through the sigmoid activation function), both deviations of the predictions from the target value (y) and predictions with a value greater than 1 and less than -1 were penalized according to equations 5.3 and 5.4, respectively. As a result, z_{out} remains in an interval around -1 and 1 where the continuous prediction level of relaxation and stress are smoothed to prevent overfitting, thus the prediction does not get stuck in extreme values. Figure 5.6 illustrates a mapping of the proposed loss function according to equation 5.5, where not only incorrect predictions are penalized, but extreme values as well.

$$loss_1 = |y - \tanh(z_{\text{out}})| \tag{5.3}$$

$$loss_2 = \left(2 \cdot \tanh\left(\frac{z_{\text{out}}}{2}\right) - \tanh(z_{\text{out}})\right)^2 \tag{5.4}$$

$$loss_T = loss_1 + loss_2 \tag{5.5}$$

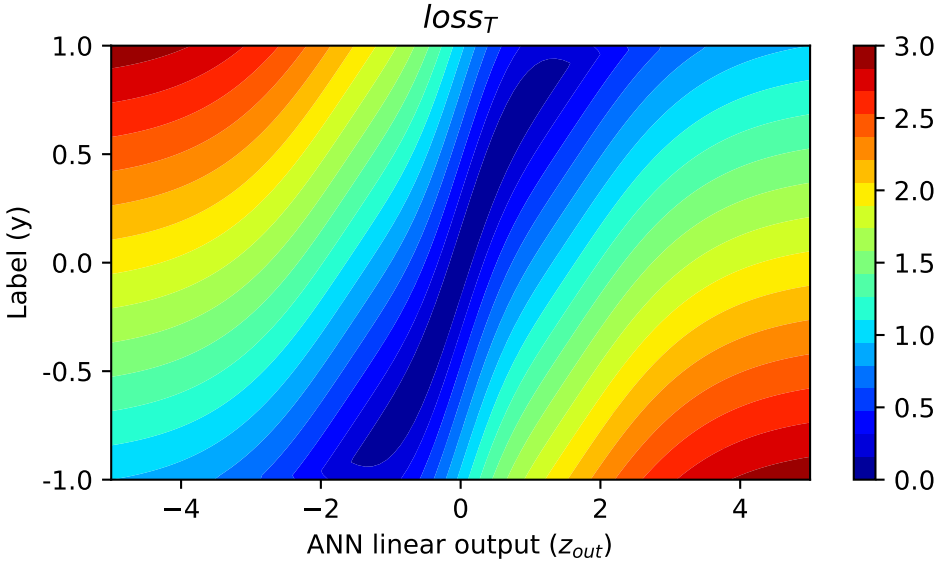

FIGURE 5.6: Total loss ($loss_T$) according to the output of the ANN and the reference label.

To find the optimal ANN configuration, the number of neurons that constitute the network were mapped. For this purpose, two hidden layers (HL1 and HL2) were defined, where the number of neurons in each hidden layer were mapped from 1 to 10. Once the ANN is trained, the model is exported by adding a sigmoid activation function to the linear output z_{out} of the output neuron as previously mentioned. This results in an output value

in the range [0, 1] where 0 represents the maximum relaxation level and 1 the maximum stress level.

5.3 Results and discussion on model performance

This subsection contains the results obtained from the training and validation of the implemented algorithms, as well as a discussion about the presented results. The proposed supervised and unsupervised algorithms were validated using the type 2 labels from the previous section. Due to the binary format of the labels (1 and 0 for representing the real states of stress and relaxation respectively), the evaluation was carried out according to the following metrics: a true positive (TP) corresponds to a real state of stress in which the obtained relaxation-stress level is > 0.5, a true negative (TN) corresponds to a real state of relaxation in which the obtained relaxation-stress level is ≤ 0.5, a false positive (FP) corresponds to a real state of relaxation in which the obtained relaxation-stress level is > 0.5 and a false negative (FN) corresponds to a real state of stress in which the obtained relaxation-stress level is ≤ 0.5. These were used to calculate the *Se*, *Sp*, *Ac* and *F1*, according to equations 2.51, 2.52, 2.53 and 2.54, respectively.

5.3.1 Fuzzy logic model results

Cross-validation was not required for the evaluation of the fuzzy model. Due to the fact that the rules for inference are constructed manually, the standard fuzzy model does not require further training, so the validation was carried out on all 42 records as shown in the results of Table 5.3. The normalized parameters were used, since unnormalized parameters make it impossible to define effective fuzzy sets manually.

Analyzing Table 5.3, a significant *F1* (94.19%) is achieved, where the *Sp* (96.16%) is higher than the *Se* (92.29%). This fact suggests that the algorithm is more robust in the detection of relaxation states. These results support the idea of the difficulty of detecting stress states due to the different levels of activation for different individuals in a variety of situations.

Some records of Table 5.3, such as 2, 9, 10, 16 and 24, are below the average. In a further analysis, it was found that the normalization drastically altered the values due to outliers, shifting the normalized values away from the corresponding MFs and leading to an increase in FP and FN.

5.3.2 Supervised learning models results

To achieve the best solution for each supervised learning model, the corresponding hyperparameters were tuned by mapping their possible values. To validate each of the resulting configurations, 21-fold cross-validation was applied, from which the average *F1* was considered to select the best hyperparameters for each model.

For the WM model, the following hyperparameters were mapped according to the list of values associated with each of them: num.labels [2, 3, 5, 7], type.mf [1, 2, 3, 4, 5],

TABLE 5.3: Results obtained after comparing the estimation of the level of relaxation and stress of the fuzzy algorithm against type 2 labels.

Tape No.	TP	TN	FP	FN	Se (%)	Sp (%)	Ac (%)	F1 (%)
1	7	14	0	0	100.00	100.00	100.00	100.00
2	9	41	7	0	100.00	85.42	87.72	92.13
3	10	39	2	0	100.00	95.12	96.08	97.50
4	5	17	0	0	100.00	100.00	100.00	100.00
5	11	6	0	0	100.00	100.00	100.00	100.00
6	7	28	0	0	100.00	100.00	100.00	100.00
7	15	43	0	1	93.75	100.00	98.31	96.77
8	14	46	0	1	93.33	100.00	98.36	96.55
9	10	55	5	1	90.91	91.67	91.55	91.29
10	17	10	6	3	85.00	62.50	75.00	72.03
11	13	37	0	0	100.00	100.00	100.00	100.00
12	3	12	0	0	100.00	100.00	100.00	100.00
13	6	24	0	0	100.00	100.00	100.00	100.00
14	9	15	0	1	90.00	100.00	96.00	94.74
15	20	18	0	4	83.33	100.00	90.48	90.91
16	7	35	6	1	87.50	85.37	85.71	86.42
17	20	68	9	0	100.00	88.31	90.72	93.79
18	10	20	0	1	90.91	100.00	96.77	95.24
19	20	31	0	4	83.33	100.00	92.73	90.91
20	7	15	0	2	77.78	100.00	91.67	87.50
21	4	33	0	1	80.00	100.00	97.37	88.89
22	9	30	3	0	100.00	90.91	92.86	95.24
23	8	33	0	1	88.89	100.00	97.62	94.12
24	3	4	0	5	37.50	100.00	58.33	54.55
25	4	32	0	0	100.00	100.00	100.00	100.00
26	6	35	0	1	85.71	100.00	97.62	92.31
27	9	32	0	0	100.00	100.00	100.00	100.00
28	3	33	0	1	75.00	100.00	97.30	85.71
29	5	7	0	0	100.00	100.00	100.00	100.00
30	7	36	3	0	100.00	92.31	93.48	96.00
31	6	25	1	1	85.71	96.15	93.94	90.63
32	7	23	1	1	87.50	95.83	93.75	91.48
33	22	33	0	1	95.65	100.00	98.21	97.78
34	31	43	2	0	100.00	95.56	97.37	97.73
35	12	37	0	0	100.00	100.00	100.00	100.00
36	0	16	0	0	-	100.00	100.00	-
37	15	15	0	0	100.00	100.00	100.00	100.00
38	6	18	0	1	85.71	100.00	96.00	92.31
39	6	14	0	0	100.00	100.00	100.00	100.00
40	0	26	0	0	-	100.00	100.00	-
41	15	7	0	1	93.75	100.00	95.65	96.77
42	9	21	0	1	90.00	100.00	96.77	94.74
Total	**407**	**1127**	**45**	**34**	**92.29**	**96.16**	**95.10**	**94.19**

type.tnorm [1, 4, 5], type.snorm [1, 4, 5] and type.defuz [1, 5]. Figure 5.7 illustrates the mapping of the most significant hyperparameters (num.labels and type.mf) according to

their influence on *F1* variation. The configuration with the highest *F1* corresponds to the following hyperparameters:

- num.labels: 7
- type.mf: 3 (GAUSSIAN)
- type.tnorm: 4 (PRODUCT)
- type.snorm: 5 (BOUNDED)
- type.defuz: 1 (WAM)

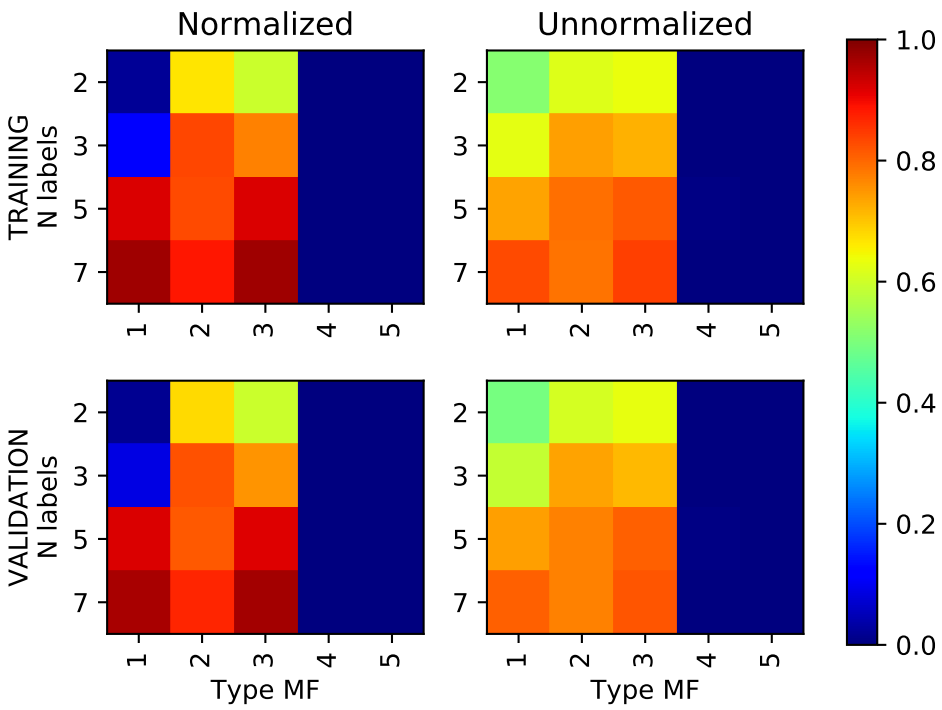

FIGURE 5.7: WM hyperparameters mapping during training (top plots) and validation (bottom plots) using the normalized and unnormalized PC sets.

For the DENFIS model, the following hyperparameters were mapped according to the list of values associated with each of them: Dthr [0.2, 0.15, 0.12, 0.1], d [1, 1.5, 2, 2.5], max.iter [300] and step.size [0.01]. Figure 5.8 illustrates the mapping of the Dthr and d according to the achieved *F1*. The configuration with the highest *F1* corresponds to the following hyperparameters:

- Dthr: 0.1
- d: 2.5
- max.iter: 300
- step.size: 0.01

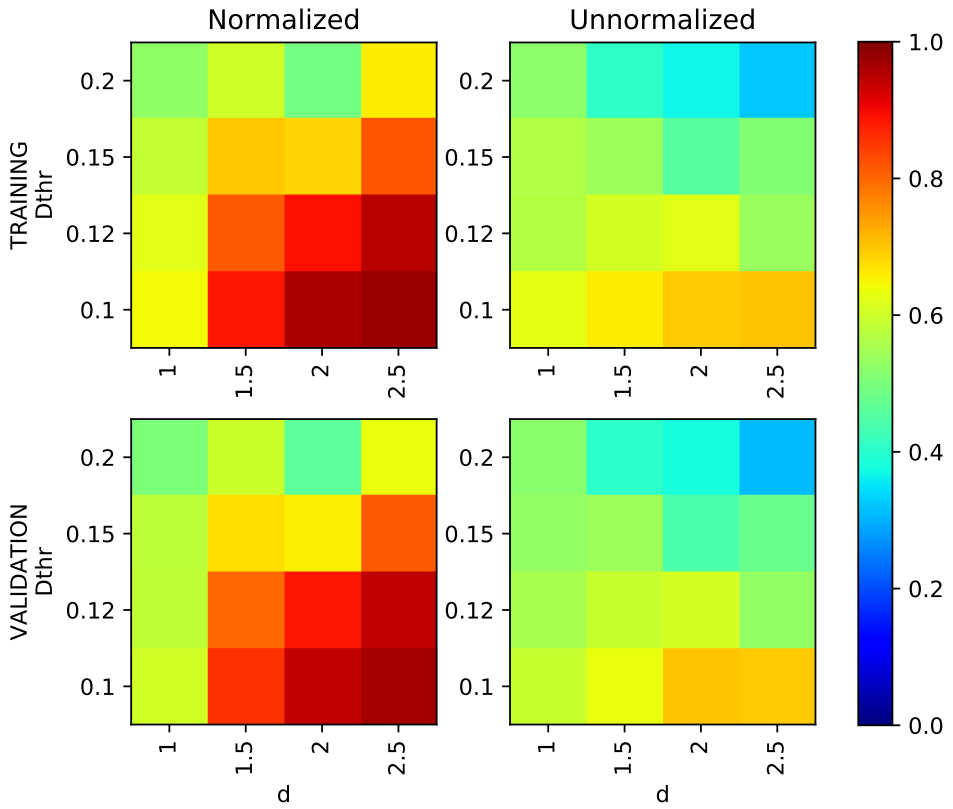

FIGURE 5.8: DENFIS hyperparameters mapping during training (top plots) and validation (bottom plots) using the normalized and unnormalized PC sets.

For the HyFIS model, the following hyperparameters were mapped according to the list of values associated with each of them: num.labels [2, 3, 5, 7], max.iter [5, 10, 20, 30] and step.size [0.01]. Figure 5.9 illustrates the mapping of the num.labels and max.iter according to the achieved *F1*. The configuration with the highest *F1* corresponds to the following hyperparameters:

- num.labels: 7
- max.iter: 30
- step.size: 0.01

For the FS.HGD model, the following hyperparameters were mapped according to the list of values associated with each of them: num.labels [2, 3, 5, 7], max.iter [5, 10, 20, 30], step.size [0.01] and alpha.heuristic [1]. Figure 5.10 illustrates the mapping of the num.labels and max.iter according to the achieved *F1*. The configuration with the highest *F1* corresponds to the following hyperparameters:

- num.labels: 2
- max.iter: 30
- step.size: 0.01

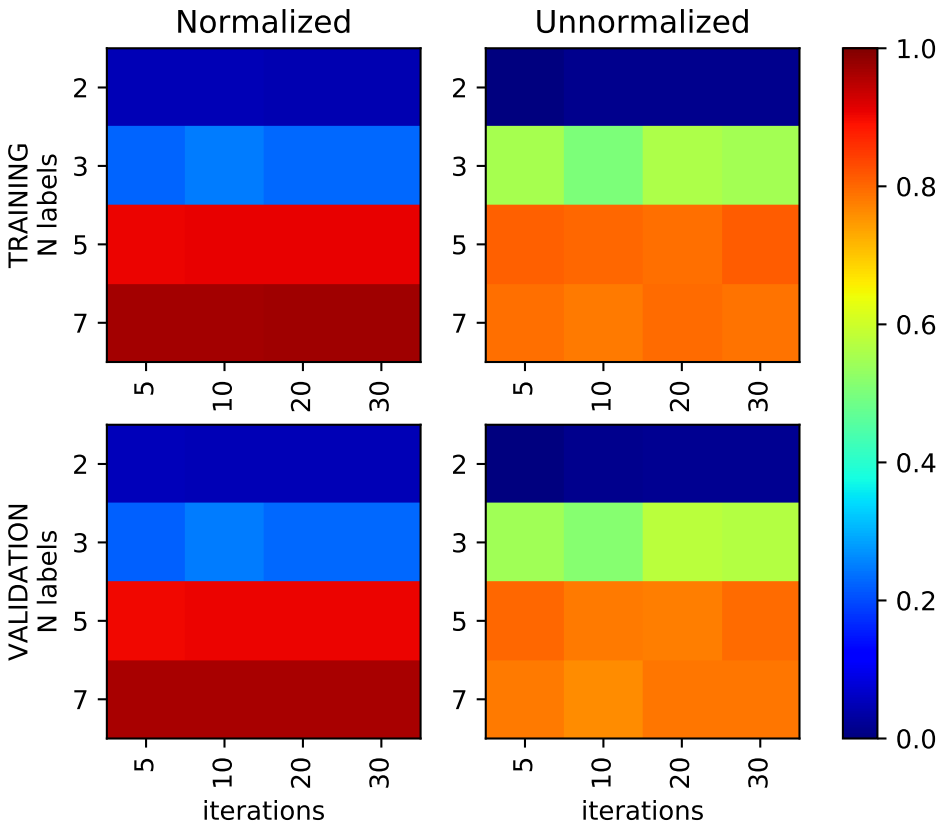

FIGURE 5.9: HyFIS hyperparameters mapping during training (top plots) and validation (bottom plots) using the normalized and unnormalized PC sets.

- alpha.heuristic: 1

For the ANN model, the following hyperparameters were mapped according to the list of values associated with each hidden layer: HL1 [1, 2, 3, 4, 5, 6, 7, 8, 9, 10] and HL2 [1, 2, 3, 4, 5, 6, 7, 8, 9, 10]. Figure 5.11 illustrates the mapping of both hyperparameters according to the achieved *F1*. The configuration with the highest *F1* corresponds to the following hyperparameters:

- HL1: 4 neurons
- HL2: 5 neurons

The scores obtained during the training and validation of each model resulted in a remarkable improvement in the quality of the predictions when using the normalized PCs as input parameters instead of unnormalized ones. Table 5.4 shows the results obtained in the training and validation steps for each of the models with the optimized hyperparameters using the normalized and unnormalized PCs. In Figure 5.12 the *F1* is shown for the normalized PCs, where it is evident that the best results were obtained by the ANN and FS.HGD models, being the *F1* of the FS.HGD slightly higher. However, the ANN model achieved the most stable (equal) results according to the *Se* and *Sp* values, which is an important factor to consider.

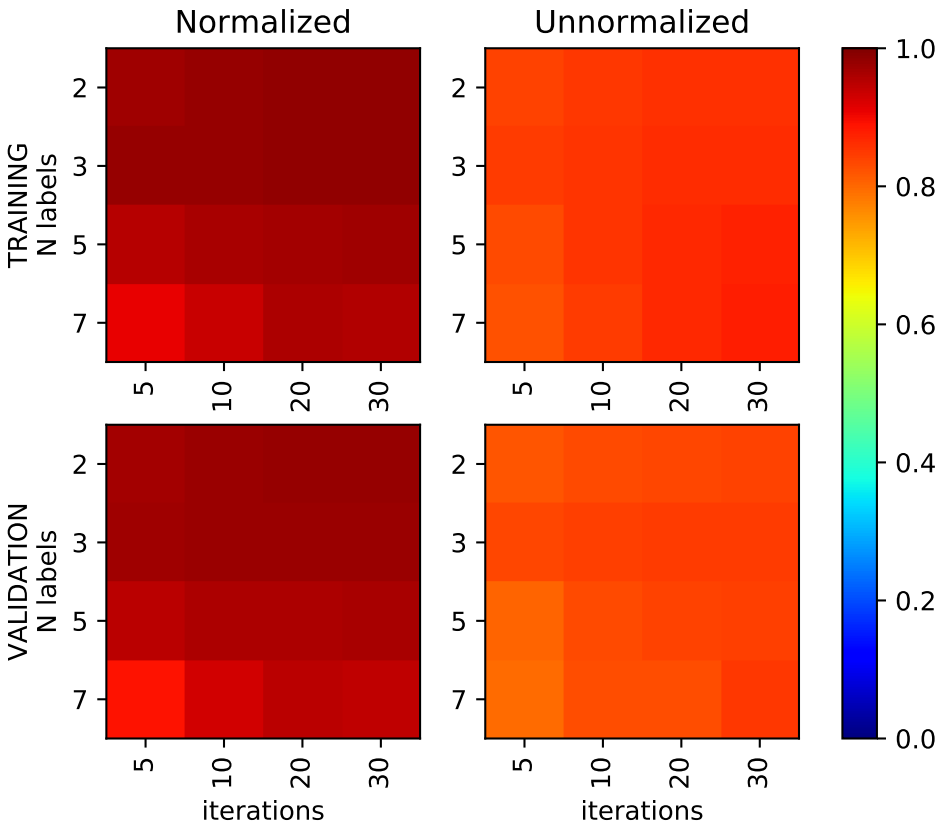

FIGURE 5.10: FS.HGD hyperparameters mapping during training (top plots) and validation (bottom plots) using the normalized and unnormalized PC sets.

TABLE 5.4: Results obtained for the different methods during training and validation in the cross-validation sets with normalized and unnormalized PCs.

		Training				**Validation**			
	Method	**Se** (%)	**Sp** (%)	**Ac** (%)	**F1** (%)	**Se** (%)	**Sp** (%)	**Ac** (%)	**F1** (%)
Norm.	ANN	98.03	98.03	98.03	98.03	97.93	97.92	97.91	97.91
	DENFIS	97.59	97.19	97.30	97.39	96.86	96.62	96.69	96.73
	HYFIS	97.87	95.95	96.48	96.89	97.88	94.95	95.78	96.38
	WM	97.61	96.62	96.90	97.11	97.46	95.59	96.09	96.51
	FS.HGD	97.75	99.02	98.68	98.38	97.02	99.02	98.48	97.99
Unnorm.	ANN	92.69	86.56	88.24	89.44	90.85	83.23	85.27	86.57
	DENFIS	94.34	58.51	68.27	70.18	93.44	57.49	67.35	69.34
	HYFIS	78.02	84.14	82.51	78.86	77.37	82.81	81.17	78.37
	WM	84.35	84.23	84.27	84.25	82.57	82.19	82.20	81.96
	FS.HGD	85.72	87.19	86.87	85.93	83.41	87.17	85.88	83.68

The training and inference times for each model are shown in Table 5.5. This information is particularly interesting for the implementation of the algorithm in a functional device, since it represents the required development time and the resources that the model can consume when implemented. Figure 5.13 shows on a logarithmic scale the training and inference times associated with each model, where the ANN presents the second lowest

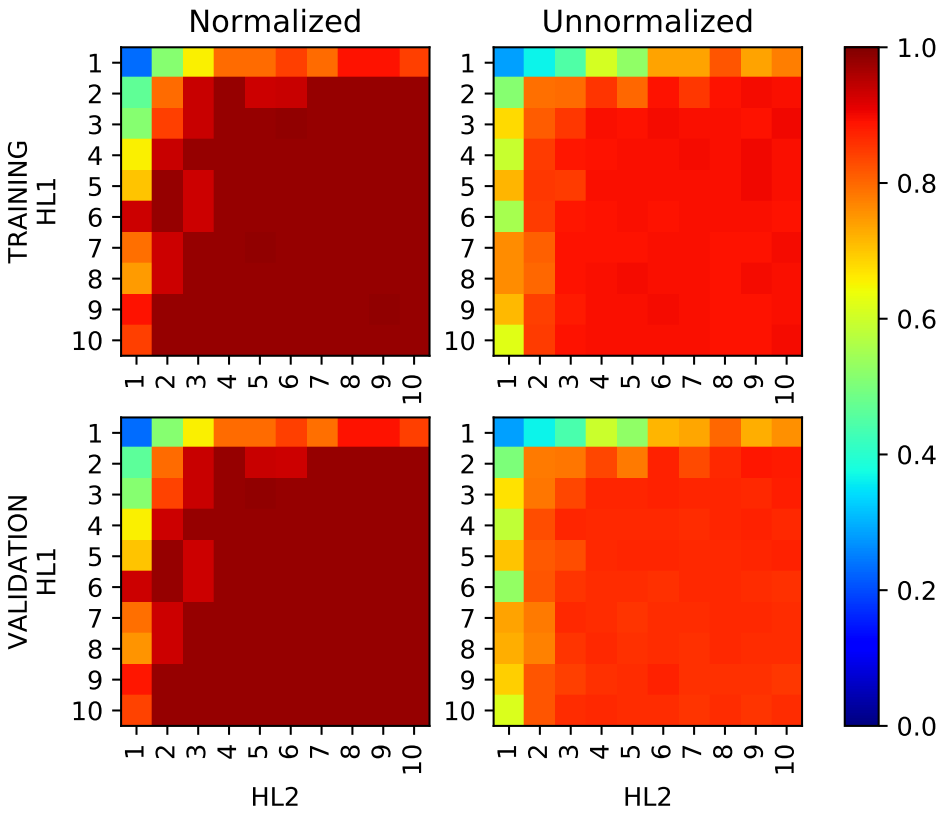

FIGURE 5.11: ANN hyperparameters mapping during training (top plots) and validation (bottom plots) using the normalized and unnormalized PC sets.

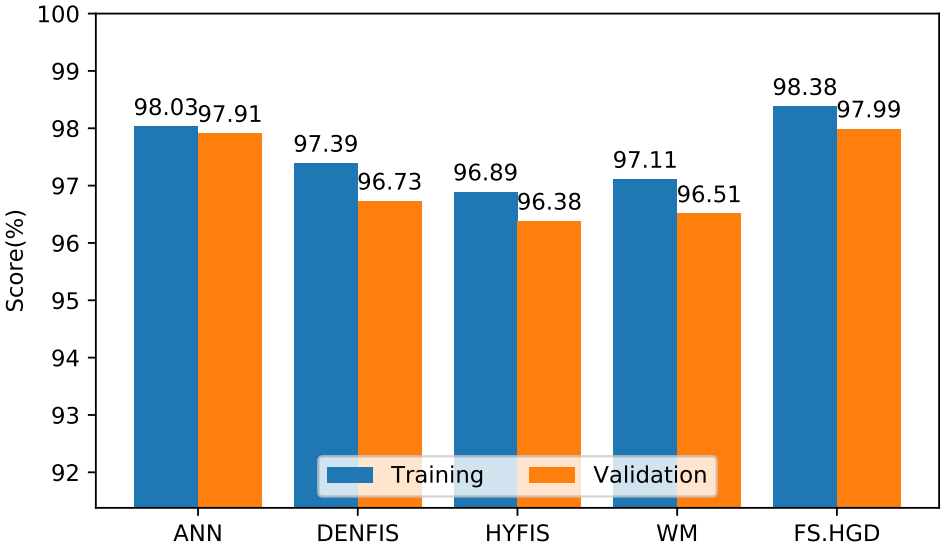

FIGURE 5.12: *F1*s obtained during the training and validation stages using the normalized data set.

training time, only surpassed by the WM model, and the lowest inference time by far.

These results highlight the improvement implicit in the normalization of physiological

TABLE 5.5: Average training and inference times of the different methods.

	Training	Inference
ANN	0:00:03.078720	0:00:00.000216
DENFIS	0:24:59.378496	0:00:00.095633
HYFIS	1:40:59.445965	0:00:08.172145
WM	0:00:00.661490	0:00:09.702216
FS.HGD	0:05:46.763769	0:00:00.177498

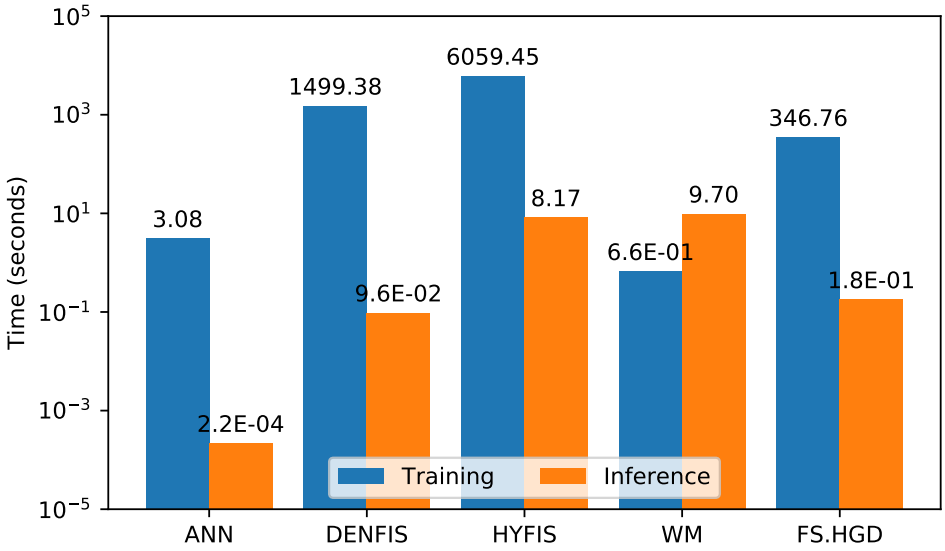

FIGURE 5.13: Logarithmic representation of the training and inference times associated with each model.

parameters conducted in the previous section. For the normalized parameters, *F1* has a score above 96% in all cases, while for unnormalized parameters *F1* is under 87%. The best *F1* was achieved with the FS.HGD method, closely followed by the ANN, which achieved a more stable (equal) *Se* and *Sp*. In addition, the ANN provides promising training and inference times, where the inference time makes the ANN suitable for implementation in real-time systems.

Extended ANN results

Considering both the scores obtained during validation and the training and inference times of each of the models, the ANN presents the most attractive results to be implemented in later stages of this thesis. Going deeper into ANN results, Figures 5.14, 5.15, 5.16 and 5.17 show the first two PCs as a function of the predictions obtained during cross-validation. Figures 5.14 and 5.15 correspond to the predictions during training and validation respectively of the unnormalized PCs, while Figures 5.16 and 5.17 correspond to the predictions during training and validation respectively of the normalized PCs. These last two figures show a more uniform distribution in the results obtained from the normalized PCs, while for the unnormalized PCs the distribution is more chaotic.

As can be deduced from the distribution of the ANN predictions, the results obtained from

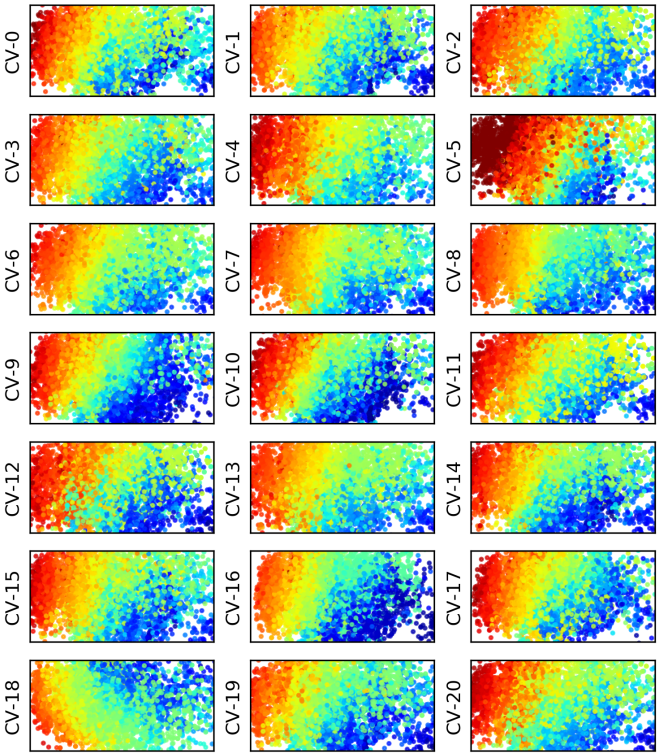

FIGURE 5.14: Predictions of the 21-fold training sets without normalization.

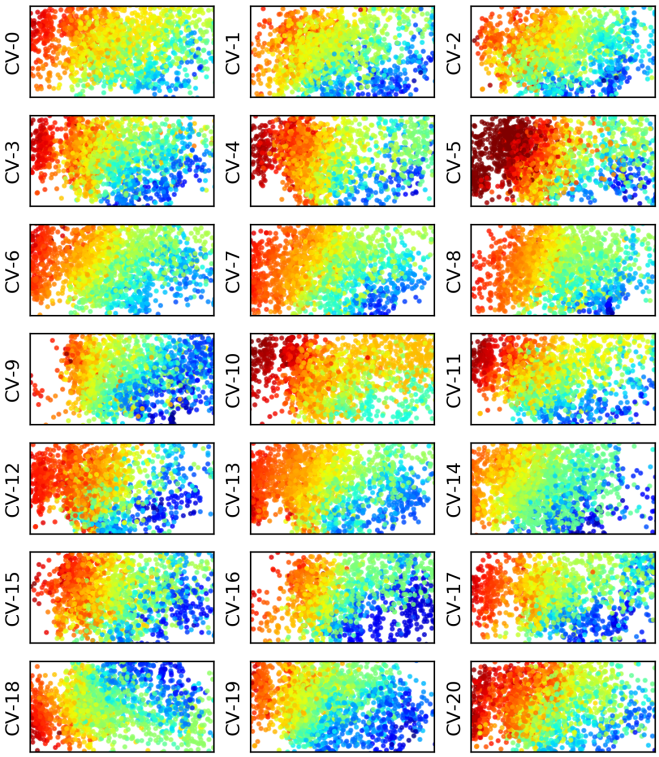

FIGURE 5.15: Predictions of the 21-fold validation sets without normalization.

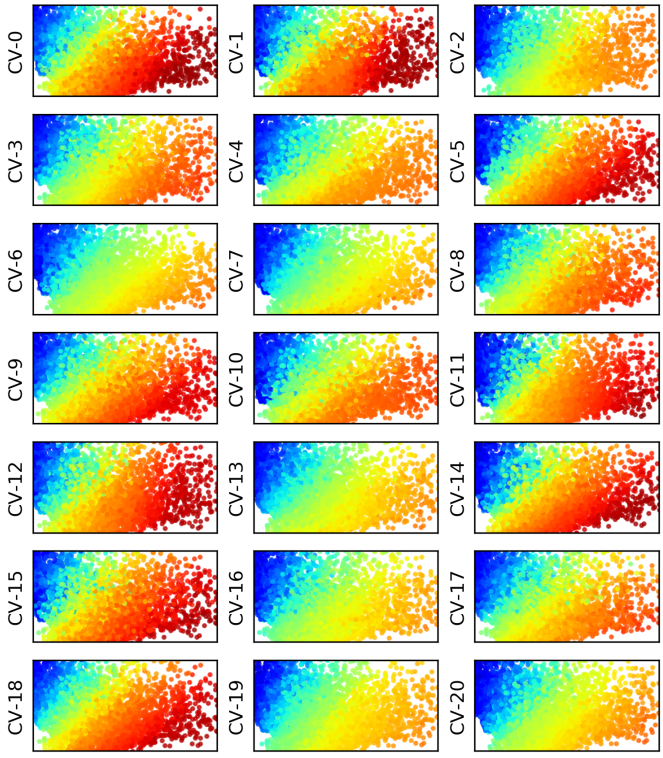

FIGURE 5.16: Predictions of the 21-fold normalized training sets.

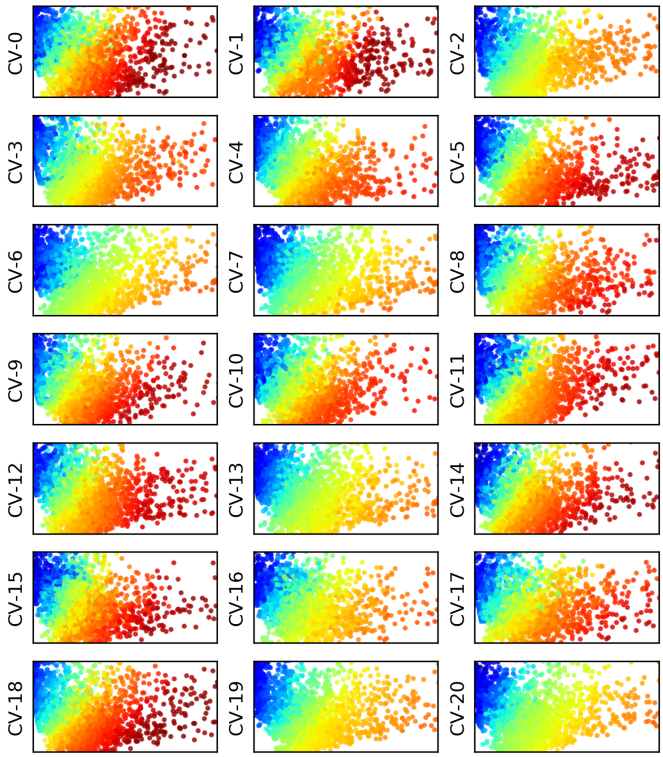

FIGURE 5.17: Predictions of the 21-fold normalized validation sets.

the normalized PCs are considerably better than those from the unnormalized ones. To

further explore the results obtained with the normalized PCs, the whole process was repeated for different combinations of physiological signals with their respective parameters, leading to the results presented in Table 5.6 and graphically illustrated in Figure 5.18.

TABLE 5.6: Results obtained for different combinations of parameters during ANN training in the cross-validation sets.

	Training				**Validation**			
Signals	**Se** (%)	**Sp** (%)	**Ac** (%)	**F1** (%)	**Se** (%)	**Sp** (%)	**Ac** (%)	**F1** (%)
HP	88.34	84.17	85.32	86.19	88.37	82.94	84.24	85.39
GSR	84.43	99.55	95.40	91.33	84.21	99.56	95.28	91.05
RSP	87.82	77.94	80.61	82.53	87.95	78.58	80.93	82.76
HP, GSR	98.21	98.57	98.48	98.39	98.02	98.30	98.25	98.15
HP, RSP	92.02	85.94	87.60	88.86	92.23	85.14	86.94	88.36
GSR, RSP	92.87	99.27	97.51	95.96	92.35	99.30	97.34	95.66
HP, GSR, RSP	98.03	98.03	98.03	98.03	97.93	97.92	97.91	97.91

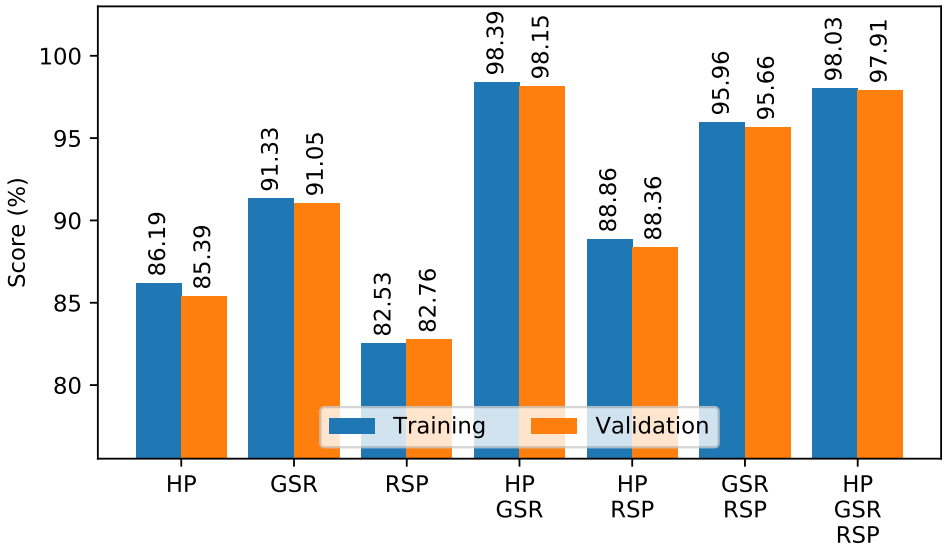

FIGURE 5.18: Graphical representation of the average *F1* obtained for different combinations of parameters during ANN training in the cross-validation sets.

Analyzing these results, the best scores are achieved by combining the HP and the GSR with an *Se* of 98.02% and an *Sp* of 98.30%, followed by the combination of the HP, GSR and RSP. However, this conclusion does not make RSP an insignificant signal, since looking at the results in more detail, the combination of RSP with any of the other signals improves the results obtained by these other signals individually. Furthermore, the RSP itself can achieve an *F1* over 82%. The results obtained with the GSR signal are also remarkable, exceeding the 90% of the *F1* with an *Sp* higher than the *Se*. This fact suggests that GSR may be suitable for implementation in a specific algorithm for detecting relaxation states, since *Sp* is directly related to TNs. The HP itself also achieves an *F1* over 85%, although its combination with the GSR provides the best results for a robust prediction of the ANS activity in relation to the level of relaxation and stress.

6 Hardware implementation

In the last decade, several works have attempted to implement in hardware platforms algorithms for the detection of events related to the autonomic nervous system (ANS) in order to be used in both general and clinical contexts. These works were conducted by analyzing physiological signals in short length sliding windows or intervals, thus performing the processing in real-time. Among the existing proposals, Minguillon et al. [1] presented a portable real-time stress detection device that consists of multiple biosignal sensors (i.e., galvanic skin response (GSR), electrocardiogram (ECG), electromyogram (EMG) and electroencephalogram (EEG)), a laptop, an Arduino e-Health board and the RaBio w8 system to collect and process the physiological signals. They achieved 86% accuracy (*Ac*) by analysing collected physiological signals in a 2-second sliding window. Han et al. [176] performed stress detection from breathing and ECG records acquired by a wearable device at 1-minute intervals, achieving 94% *Ac*. However, these records were processed offline once the acquisition process was finished. Salai et al. [32] achieved 74.6% *Ac* by integrating a stress detection algorithm in a low-cost portable device and analyzing 560 RR intervals extracted from ECG registers. Gjoreski et al. [3] used a wrist device to perform stress detection with 70% sensitivity processing parameters extracted from skin temperature (ST), photoplethysmography (PPG), acceleration (ACC) and GSR registers. They utilized 20-minute intervals and 2-minute intervals for context-based stress detection and short-term-based stress detection, respectively. Golgouneh and Tarvirdizadeh [7] achieved 81% *Ac* by processing PPG and GSR registers at 20-second intervals in an online stress detection algorithm implemented in a portable device.

In this section, a low-cost IoT-based prototype for the acquisition, transmission and processing of physiological records is proposed. The results obtained in the previous section were crucial in the selection of the signals and physiological parameters for the current hardware development. Thus, due to the results obtained and the availability of low-cost measurement devices, the ECG and GSR were selected to predict the level of activity of the ANS in terms of stress and relaxation.

The proposed development consists of three main components illustrated in the scheme in Figure 6.1: First, the acquisition device collects the ECG and GSR data and sends this data wirelessly (or by cable, both options are available) to the server, which stores and processes the received signals. Then, the server sends the processed data to the client, who will receive information about the acquired records as well as the extracted physiological parameters and the estimated stress and relaxation level.

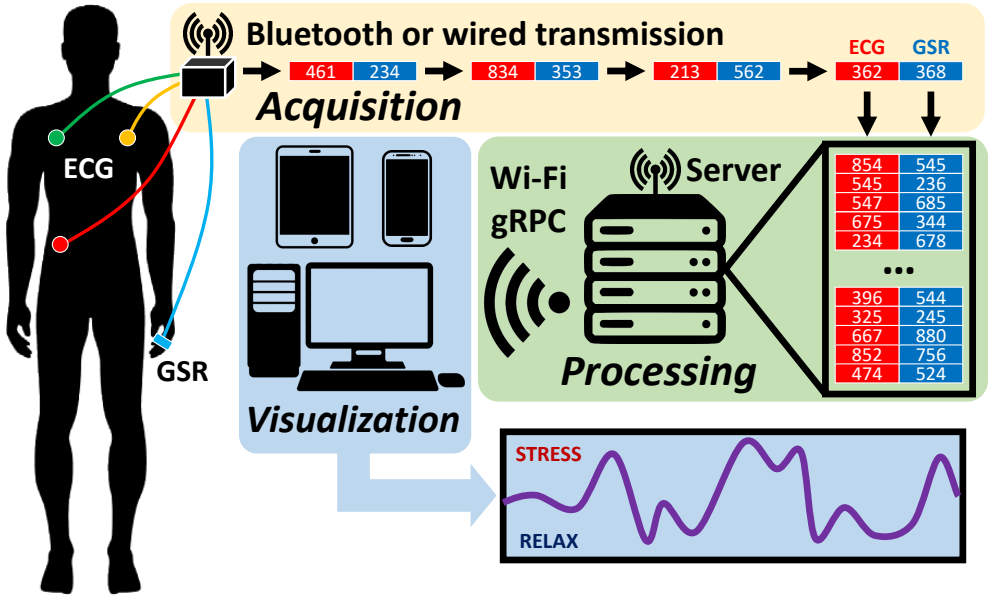

FIGURE 6.1: Schematic representation of the different stages that constitute the proposed methodology for the hardware implementation.

6.1 Physiological data acquisition

The acquisition device is a critical point in the development of the proposed prototype, since it is in direct contact with the subject. Therefore, it must be as less invasive as possible and it must acquire physiological signals without coupling excessive noise. For the hardware construction, the cost of the components was considered, since an excessive cost would not be suitable for general purpose use.

The prototype consists on a set of components installed on a small-sized printed circuit board (PCB) that provides the device with inputs, to carry out the acquisition of physiological signals, and Bluetooth connection, for wireless data transmission, but this solution also considers the possibility of doing so by cable. The proposed design consists of an Arduino Nano board (ArdN) for concurrent acquisition of physiological records, a Bluetooth module (HC-05) for sending the data packages to the server, a bi-directional converter (BOB-12009) to adjust the voltage levels between these two components, an AD8232 device for ECG acquisition using the three lead Einthoven's triangle configuration and a GSR sensor (Grove v1.2) for skin conductance acquisition, which is intended to be located in the distal phalanges of the non-dominant hand. Figure 6.2 shows the proposed layout for connecting all components.

The digital outputs D2 and D3 of the ArdN are used as alternative TX and RX connections, respectively. Thus, a serial channel was created to connect to the Bluetooth device via the bi-directional voltage converter. The bi-directional converter is used to bridge the 5V digital ports of the ArdN to the 3.3V digital ports of the HC-05.

The PCB used for the implementation of the circuit was modularly assembled as shown in

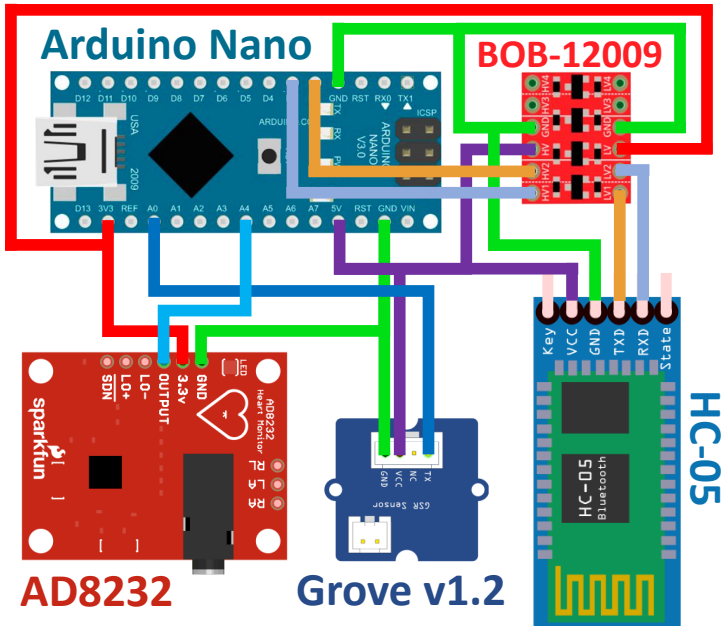

FIGURE 6.2: Layout of the prototype for the acquisition and Bluetooth transmission of the GSR and ECG data.

the pictures in Figure 6.3. Thus, if any component breaks down, it is easy to replace it without purchasing all the components again. The PCB dimensions are 5x7cm as illustrated in Figure 6.4, where all the components are shown connected.

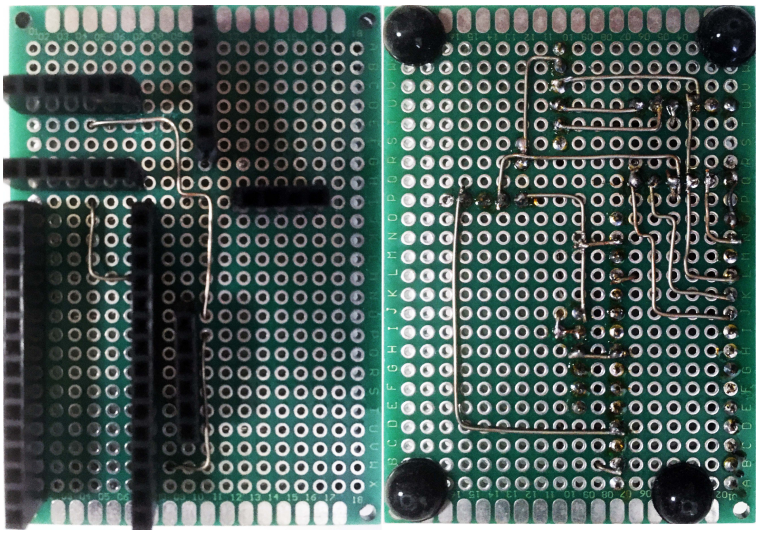

FIGURE 6.3: PCB board with the connectors soldered. The left figure shows the upper section of the board and the right figure shows the lower section.

The sensors used for ECG and GSR acquisition are also replaceable. For ECG, the leads are connected directly to a jack connector. The GSR sensor includes a coiled wire that provides the required elasticity to prevent restricting the movement of the arm. Figure 6.5 shows all components attached and operating together, where the power source is a portable battery connected to the ArdN through a USB cable. The ArdN, in turn, powers

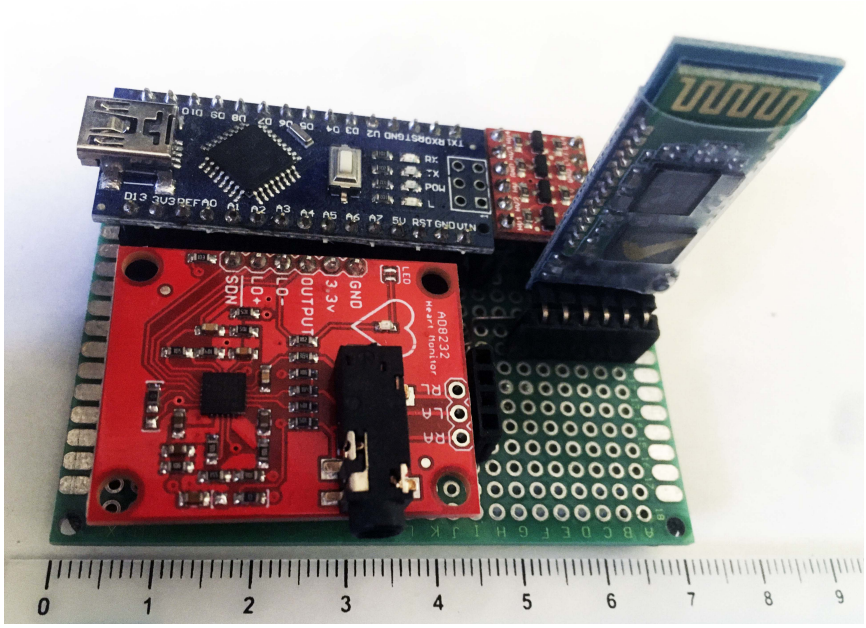

FIGURE 6.4: PCB board of the acquisition device with all the components connected.

the remaining components with its 3.3 and 5V outputs.

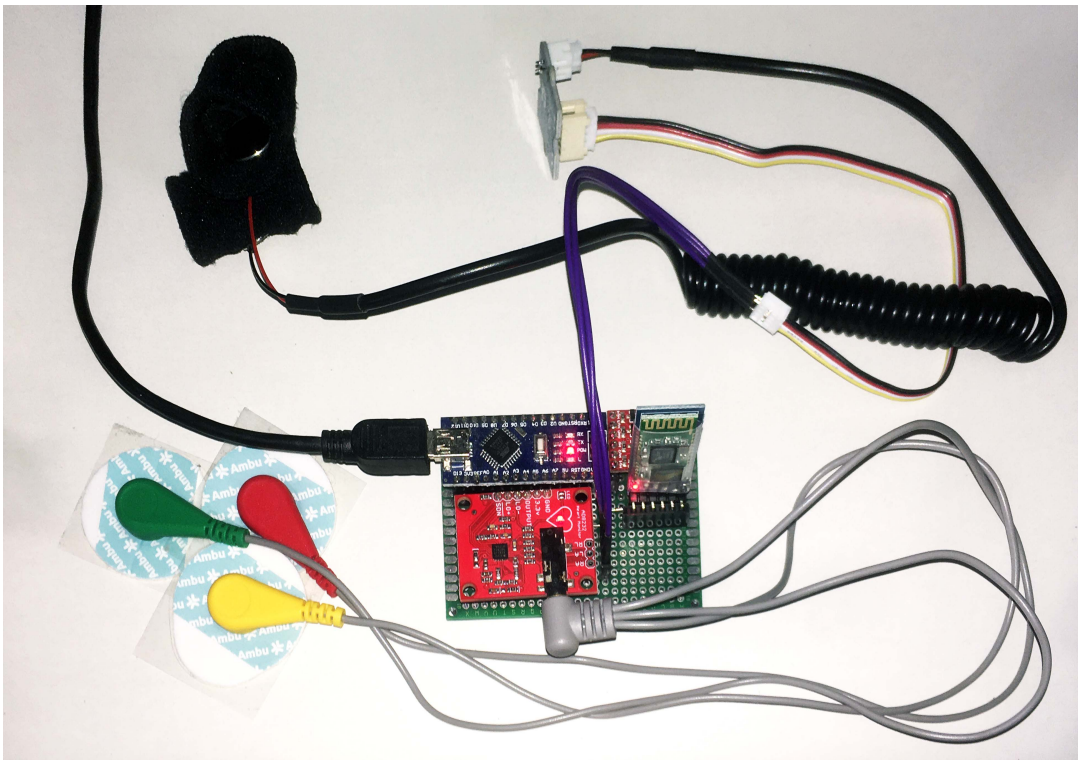

FIGURE 6.5: Acquisition prototype with ECG and GSR sensors connected and running.

6.1.1 Acquisition algorithm

Algorithm 2, implemented in the ArdN, performs the acquisition and sending of physiological samples at a specific sampling frequency (F_S). More specifically, the analog inputs A0 and A4 of the ArdN board are used to carry out the acquisition of the GSR and ECG, respectively.

Algorithm 2 Algorithm for acquisition and sending of physiological samples.

1: $tic \leftarrow time$
2: **while** True **do**
3: $\quad tic \leftarrow tic + 1/F_S$
4: $\quad$ **wait**$(tic - time)$
5: $\quad GSR \leftarrow analogRead(A0)$
6: $\quad ECG \leftarrow analogRead(A4)$
7: $\quad$ **writeBT**(ECG, GSR)
8: **end while**

It is crucial to set an appropriate F_S, high enough so that important details of the ECG and GSR signals are not lost, but low enough so that the computational load is not excessive. According to the literature, QRS complexes can be detected effectively at 200 Hz in ECG signals [177]. For GSR, 32 Hz provides sufficient information to carry out parameter extraction [178]. Considering that the ECG has the highest resolution requirements, an F_S = 200 Hz was established to perform the acquisition. Figure 6.6 shows a real example of the ECG and GSR signals collected using the developed acquisition prototype.

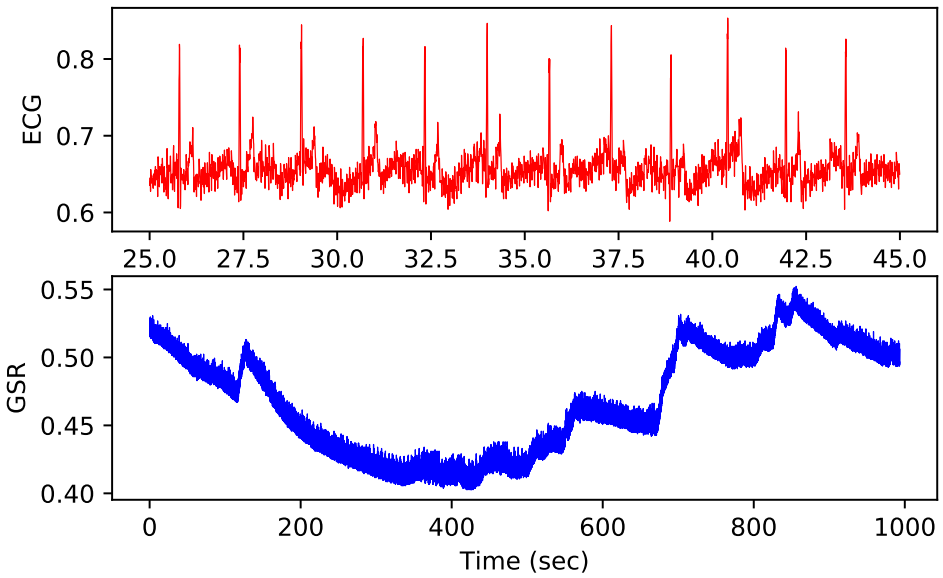

FIGURE 6.6: Display of ECG and GSR records acquired through the developed acquisition prototype.

6.2 Server processing

Several platforms were tested during the development of the server, i.e., Raspberry Pi 3 (RPi3) and 4 (RPi4) and a regular desktop PC. Although for the final implementation, the RPi3 was used, which despite having the lowest performance, it is enough to adequately implement the proposed solution. It is also the device with the lowest price and the smallest in size and energy consumption.

For this solution, the Raspbian Stretch Lite operating system was used, which eliminates the interface by focusing performance on physiological data processing and wireless connection of the device, both to the client via Wi-Fi, and to the acquisition prototype via Bluetooth. Moreover, the Python programming language was used for the code implementation. This programming language is fully integrated in all Raspbian operating systems and it provides a comprehensive set of tools to implement the different processes.

As presented in section 4, a 20-second sliding window was used to carry out the processing of the physiological signals. The sliding window is updated every 5 seconds by discarding the oldest data and stacking new data according to a FIFO protocol. Subsequently, parameter extraction, normalization and principal component analysis (PCA) are performed from the physiological registers stored in the sliding window, followed by the artificial neural network (ANN) processing, which generates an estimation of the relaxation and stress level. This process is represented in Figure 6.7.

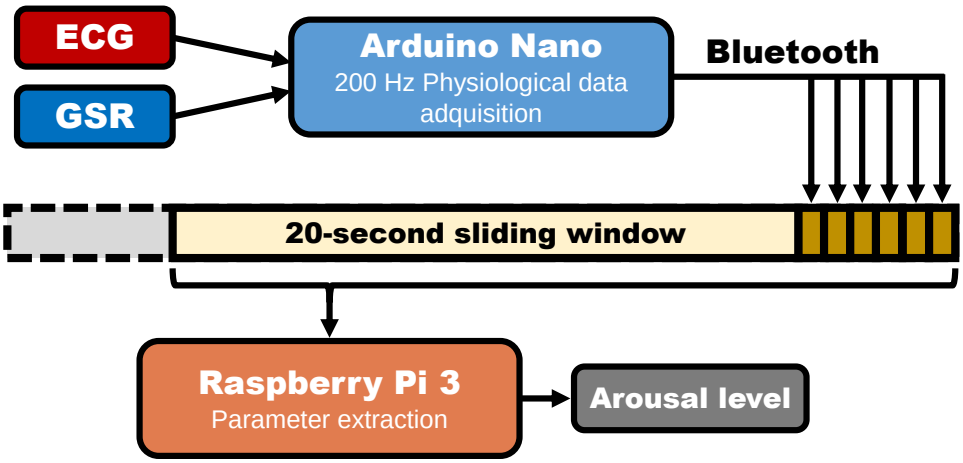

FIGURE 6.7: Schematic representation of the acquisition, 20-second sliding window generation and relaxation and stress level estimation.

6.2.1 Processing algorithm

The server programming consists of two main concurrent tasks, which are responsible of storing the ECG and GSR signals in sliding windows and processing the stored data at each step, respectively.

Algorithm 3 represents the first of the concurrent tasks, which acquires the data received from the Bluetooth channel and appends it to the sliding windows of the ECG (ECG_{SW})

and GSR (GSR_{SW}). When the sliding windows reach the length of 20 seconds, this data is copied into the buffers that send the data to the next concurrent task. Meanwhile, the initial samples of the sliding windows are removed to leave space for the new incoming data.

Algorithm 3 Bluetooth buffer reading and sliding window generation thread.

```
1: ECG_SW ← []
2: GSR_SW ← []
3: step ← 5 * F_S
4: window ← 20 * F_S
5: while True do
6:     ECG, GSR ← readBT
7:     ECG_SW append ECG
8:     GSR_SW append GSR
9:     if cont >= window then
10:        writeECGbuffer(ECG_SW)
11:        writeGSRbuffer(GSR_SW)
12:        ECG_SW ← ECG_SW[1 : (window − step)]
13:        GSR_SW ← GSR_SW[1 : (window − step)]
14:    end if
15: end while
```

During the execution of the second concurrent task, the data is read from the buffers that contain each of the windows for analysis, as presented in Algorithm 4. The 20-second ECG and GSR windows are processed for parameter extraction, which are, in turn, normalized and reduced through PCA. Finally, the resulting features are processed through an ANN and the obtained relaxation and stress level estimation is sent together with the extracted parameters to the client via gRPC.

Algorithm 4 Thread for parameter extraction, normalization, PCA and arousal level estimation.

```
1: while True do
2:     ECG_SW ← readECGbuffer
3:     GSR_SW ← readGSRbuffer
4:     params ← parameters(ECG_SW, GSR_SW)
5:     norm ← normalization(params)
6:     pca ← PCA(norm)
7:     arousal ← ANN(pca)
8:     writeResults(arousal, params)
9: end while
```

6.3 Client authentication and security

The implementation of the client was conducted through the gRCP communication protocol. This mechanism makes it possible to send data between clients and servers, programmed in a wide variety of languages. Thus, it is possible to link the server to any application or web service developed for any device. Hence, the front-end development can

be customized for any platform.

In this thesis, the client was developed using the Python programming language for testing purposes and to verify the correct performance of the system implementation in real-time conditions. As gRPC is designed to work with a variety of authentication mechanisms, there is the possibility of integrating the SSL/TLS protocol to encrypt all the data exchanged between the client and the server. Optional mechanisms that provide certificates for mutual authentication are also available for clients.

gRPC also provides an authentication method through credentials attached to the package metadata. It is possible to send in the metadata of the first package a verification token from the client, which must be the same as the one in the server in order to make the connection possible and secure. Both the authentication method and SSL/TLS encryption can be used together to make the system even more secure.

6.4 Results and considerations

To provide a real perspective for medical and commercial use, the algorithm must be within established performance ranges. On the one hand, to perform real-time data acquisition and transmission at 200 Hz, the ArdN must execute each sampling and data transfer cycle in less than $1/200Hz = 5ms$. On the other hand, since the sliding window step was set to 5 seconds, this value is also the maximum time available to process the current window until the next window is ready. Table 6.1 presents the average times (in milliseconds) measured for each of the tasks executed in different devices. The standard deviation was considered to evaluate the deviation during normal operation due to the simultaneous execution of other processes in the operating system. The maximum and minimum run times were also considered as a reference for the best and worst case scenarios, respectively.

During the acquisition performed by the ArdN and the processing executed on the server hosted on the RPi3 and other devices, the worst case scenarios (maximum measured times) do not reach the established limits. This fact leaves a significant safety margin and ensures a robust real-time execution of the proposed system. In Figure 6.8 the average times obtained from each of the devices tested as a server are graphically represented in logarithmic scale.

An additional factor that must be considered is the total price. This fact has a direct influence on the demand, thus it is important to maintain a low-cost in order to make the device accessible to the public and medical centres. Table 6.2 shows a detailed overview of the cost of each of the components at the date of purchase. The battery was excluded from the total cost as the prototype has not yet a proven power source. However, the cost is under 100 euros, which is a promising starting point that brings a real perspective for implementation in an approved device.

TABLE 6.1: Comparison of time results extracted from each task during real-time execution of different devices on a single CPU/Micro.

Device	CPU/Micro	Process	Mean (ms)	Std (ms)	Max (ms)	Min (ms)
ArdN	**ATmega328 16MHz**	Acquisition	0.692	0.013	0.784	0.672
RPi3	**ARM Cortex-A53 1.20GHz**	Window	0.438	0.780	101.112	0.199
		Parameters	189.784	66.173	1663.007	160.307
		Normalization	10.821	0.411	11.721	10.074
		PCA	0.077	0.032	0.356	0.064
		ANN	2.774	6.969	134.475	1.700
		Total	**203.894**	**74.366**	**1910.671**	**172.344**
RPi4	**ARM Cortex-A72 1.50GHz**	Window	0.247	0.370	12.764	0.090
		Parameters	118.024	32.937	731.848	84.968
		Normalization	4.662	0.138	5.057	4.018
		PCA	0.042	0.015	0.238	0.038
		ANN	1.389	1.991	27.710	1.004
		Total	**124.364**	**35.452**	**777.617**	**90.118**
PC	**i7-4790K 4.00GHz**	Window	0.112	0.109	5.283	0.020
		Parameters	16.744	4.558	113.206	10.684
		Normalization	0.845	0.050	1.218	0.792
		PCA	0.010	0.001	0.024	0.009
		ANN	0.344	0.460	6.482	0.282
		Total	**18.054**	**5.178**	**126.213**	**11.786**

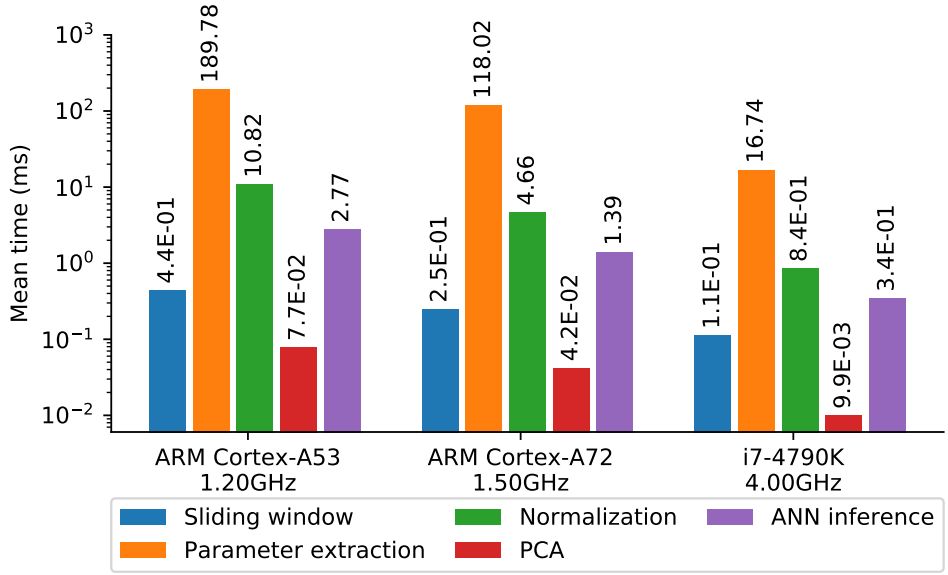

FIGURE 6.8: Comparison of the average time extracted from each task during real-time execution of different devices on a single CPU.

Table 6.3 compares the performance of the proposed algorithm in predicting states of stress and relaxation together with the implementation in a hardware device with other well-known works. It also includes information on whether the solution proposed by each author is integrated into a hardware device (HW) or not, if the device is portable (P) or not and if the execution is carried out in real-time (RT) or not. Other interesting parameters

TABLE 6.2: Price of each of the components that conform the proposed hardware implementation and total price.

Product name	Price (€)
Arduino Micro (A000053)	18.00
SparkFun Logic Level Converter Bi-Directional (BOB-12009)	2.66
Bluetooth Module HC-05	2.32
Heart Monitor (AD8232)	4.30
Grove GSR Sensor V1.2	15.60
ELEGOO Double Sided PCB	0.70
Raspberry Pi 3 Model B	37.44
Total	**81.02**

as the population size (n), acquired physiological signals, size of the sliding window/step (W/S) and price of the device are also collected. The price of the proposed prototype corresponds to that shown in Table 6.2, since the remaining devices were only employed in the experimental stage and in the preliminary development stage, such as BIOPAC MP36, which was used for the acquisition and generation of the data set during the development of the proposed system.

The achieved performance and the low-cost of the components employed in this proposal makes it possible to transform the proposed system into a commercial application. Thus, the developed algorithms could be successfully implemented in an embedded device that fulfils the stability and safety requirements of a real medical device.

TABLE 6.3: Comparison of stress and relaxation estimation performance represented by sensitivity *Se* and specificity (*Sp*), respectively.

Reference	Se (%)	Sp (%)	Signals	n	HW	P	RT	W/S	Price (€)
Sharawi et al. [179]	60-78	-	ST, GSR	35	Yes	No	Yes	-/-	Not available
Gjoreski et al. [3]	70	-	PPG, ST, GSR, ACC	5	Yes	Yes	Yes	2-20/- min	+1000
Salai et al. [32]	75	74.2	ECG	5	Yes	Yes	No	560/20 HP	+115
Kulic and Croft [180]	76	-	ECG, EMG, GSR	8	No	No	No	-/-	No device
Guang-yuan and Min [181]	75-85	-	ECG, EMG, GSR, RSP	1	No	No	No	-/-	No device
Golgouneh and Tarvirdizadeh [7]	81	-	PPG, GSR	16	Yes	Yes	Yes	20/1 sec	+80
Minguillon et al. [1]	86	-	ECG, EMG, EEG, GSR	10	Yes	Yes	Yes	2/2 sec	Not available
Wagner et al. [182]	79.5-96.6	-	ECG, EMG, GSR, RSP	1	No	No	No	2/- min	No device
Cai and Lin [183]	85-96	-	BVP, ST, GSR, RSP	-	Yes	No	No	-/-	Not available
Han et al. [176]	94	94	ECG, RSP	39	No	No	No	1/1 min	No device
Healey and Picard [166]	97.4	-	ECG, EMG, GSR, RSP	24	No	No	Yes	5/- min	No device
Proposed	**98.02**	**98.3**	**ECG, GSR**	**42**	Yes	Yes	Yes	20/5 sec	81.02

7 Conclusions

The main objective of this thesis was the automatic and real-time estimation of the level of stress and relaxation in a continuous operation through the analysis of non-invasively acquired physiological measures. Since stress and relaxation are closely related to the activity of the autonomic nervous system, it is essential to study the physiological patterns related to such activity. For this reason, the development of novel algorithms based on intelligent computing techniques was proposed, focused on the real-time processing of physiological parameters for pattern extraction. Finally, the implementation of the final solution in a low-cost hardware device with portability capabilities was also proposed.

Thus, this thesis was structured in four main sections, in which an advanced processing of the physiological data, a novel analysis and labeling of the extracted parameters, a complete comparison of the performance of various intelligent algorithms, and a robust hardware implementation of the final solution were carried out. This solution focused principally on the processing of the heart period, galvanic skin response and breathing, since they can be non-invasively acquired from a wide range of devices and are directly related to the activity of the autonomic nervous system.

The first section was focused on the development of algorithms for reliable extraction of the heart period. As reflected in the state of the art, the period between heartbeats can be obtained from several biosignals. However, these signals are frequently affected by artifacts that result in erroneous measurements of the heart period, distorting the estimation of the autonomic nervous system activity. To improve the extraction of the heart period, two novel proposals were presented in this thesis: one for the processing of the electrocardiogram and another for the oscillometric blood pressure signal processing.

The algorithm developed for the extraction of the heart period from the electrocardiographic signals is focused on the robust detection of R-peaks. This thesis proposes an original and computationally efficient method for online and robust detection of R-Peaks divided in three main stages: First, a complete elimination of artifacts is performed based on a noise and signal intensity approach during the preprocessing stage. Second, a preliminary R-peaks detection methodology is applied for the identification of R-peaks through an efficient area over the QRS complex measurement. Finally, the detected R-peaks are subsequently processed iteratively by means of three innovative state machines that fix the errors committed during the first detection by adding and removing the missing and exceeding R-peaks, respectively. For each state machine, a set of conditions that assesses the reliability of the HP at every instant was developed. Moreover, the algorithm was

designed to carry out the processing of the electrocardiogram using a 20-second sliding window, thus being implementable in real-time applications. Very promising results were achieved, reaching a sensitivity of 99.54% and a precision of 99.60% in R-peak detection. Additionally, the algorithm entails a reduced computational cost, suitable for its implementation in a low performance platform. The results obtained acquire relevance considering that a small error during the R-peaks detection in short duration windows can lead to major changes in the parameters obtained from the resulting heart period. This development was published in the prestigious Applied Mathematics and Computation journal (JCR: 3.472 - Q1) under the title "*Online robust R-peaks detection in noisy electrocardiograms using a novel iterative smart processing algorithm*."

The algorithm proposed for the extraction of the heart period in oscillometric blood pressure signals combines advanced processing methods and artificial neural networks to carry out an accurate estimation of the foot points location. New processing techniques such as the moving interpolation difference method and improved second derivative maximum method were developed in order to achieve a robust elimination of the baseline wander and a reliable detection of any existing valley in the oscillometric blood pressure signal. These valleys are subsequently classified into real and false foot points according to five characteristic parameters extracted from the morphology of the moving interpolation difference line. Classification was carried out using a specialized artificial neural network, which combines at the input the five extracted parameters to determine at the output whether the valley corresponds to a real foot point or not. 10-second oscillometric blood pressure registers were used, achieving a sensitivity of 99.17% and a specificity of 99.21% in foot point detection. Considering the similarity between the morphology of the oscillometric blood pressure registers and the photoplethysmographic signals, this algorithm is potentially applicable on the latter type as well. Similarly to the algorithm for electrocardiogram processing, the possibility of processing the oscillometric blood pressure signal in short length windows makes this algorithm implementable in real-time execution systems. This development led to a publication in the well-known Computer Methods and Programs in Biomedicine journal (JCR: 3.632 - Q1) under the title "*Diagnosis of atrial fibrillation based on arterial pulse wave foot point detection using artificial neural networks*."

In the second section, novel methodologies were proposed for the normalization and labeling of physiological parameters extracted from the heart period, galvanic skin response and breathing. This section proposes a partial binary labeling (0/1) of the registers intervals clearly identified as stress and relaxation states, followed by an innovative normalization and an original pseudo-labeling of all the registers. To address the challenge of providing a set of normalized parameters not affected by interpersonal discrepancies, a novel approach was developed by automatically selecting the normalization methodology that best suits each parameter. For this purpose, existing normalization methods and those proposed in this thesis were evaluated by means of a customized loss function. This loss function was designed to discriminate between states of stress and relaxation, being

the methods with the smallest loss the most suitable to carry out the normalization. Moreover, the most representative parameters of stress and relaxation states were selected by a comprehensive distribution analysis. Redundancy was subsequently eliminated through principal component analysis. The resulting principal components were consistently implemented together with the partial labels in a semi-supervised learning algorithm, thus resulting in a continuous pseudo-labeling of the entire signals. The results obtained were verified against a second validation label set conducted by experts in physiological signal analysis, reaching 98.41% sensitivity and 99.32% specificity.

In the third section, the principal components and the pseudo-labels obtained in the previous section are used to compare the stress and relaxation prediction capability of different intelligent algorithms based on supervised and unsupervised learning methods. Studied techniques include fuzzy logic, several fuzzy rule-based supervised learning systems (i.e., Wang and Mendel's method, dynamic evolving neural-fuzzy inference system, hybrid neural fuzzy inference system and heuristics and gradient descent method) and artificial neural networks. Each technique was validated using an original methodology based on the mapping of the possible values for each hyperparameter through 21-fold cross-validation. The results obtained led to a sensitivity of 97.93% and a specificity of 97.92% for artificial neural networks, which present the most stable results and the smallest training and inference times. Furthermore, the evaluation of the artificial neuronal networks was also carried out along with all the different combinations of the three studied physiological signals (i.e., heart period, galvanic skin response and breathing), concluding that the heart period and the galvanic skin response together obtain the best results in the estimation of the level of stress and relaxation, corresponding to a sensitivity of 98.02% and a specificity of 98.30%. A further relevant conclusion is that breathing contributes to improve the results that the heart period and the galvanic skin response achieve separately.

The fourth and last main section describes the hardware implementation of the algorithms developed and validated throughout this thesis. For this purpose, a portable, real-time acquisition platform was designed, combining in an original manner a variety of easily affordable, low-cost electronic components. Moreover, the algorithms were implemented on a low-cost and low-performance server, such as the Raspberry Pi platform. The server receives the physiological signals recorded by the acquisition platform wirelessly (Bluetooth). Meanwhile, the extracted parameters are processed by an artificial neural network, resulting in a continuous measurement of the level of stress and relaxation. The results obtained are subsequently sent to the client via Internet (wire or Wi-Fi) using the gRPC protocol, which enables the implementation of encryption and authentication procedures. The concurrency of the system was validated by subjecting both the acquisition platform and the server to real-time performance tests and obtaining the temporal results supporting their correct execution.

Both the implementation of the fuzzy logic model for the continuous estimation of stress and relaxation levels in the third section and the integration of the algorithm in a low-cost platform resulted in a publication in the well-known IEEE Access journal (JCR: 3.745 - Q1)

under the title "*A low-cost, portable solution for stress and relaxation estimation based on a real-time fuzzy algorithm*."

Therefore, the culmination of this thesis is the design of four well-defined modules that describe the methodologies established to carry out the complete development of algorithms for the continuous, real-time and automatic estimation of stress and relaxation level by processing parameters extracted from non-invasively acquired physiological signals. The full development was finally implemented on a low-cost portable hardware platform. During the process, techniques from the field of computational intelligence were employed, including supervised, semi-supervised and unsupervised learning algorithms. In addition, new methodologies were provided both for the processing of physiological signals and for the normalization, analysis and labeling of the parameters extracted from them. An original use of semi-supervised learning algorithms was also performed to carry out a novel pseudo-labeling, thus converting binary and partial labels into continuous and complete labels. A further contribution is the customized loss function for the training of the artificial neural network, which was specifically developed for the estimation of stress and relaxation levels. Finally, a great effort was placed on the hardware implementation, where different types of devices were combined to create an integrated system capable of acquiring physiological signals in real-time and executing the developed algorithms concurrently.

All the algorithms were developed in Python programming language. This language was used both during the development stage and in the implementation of the final code in the production server. Thus, a complete development from the first phases of study to the hardware implementation was carried out using a single programming language.

It should be noted that physiological differences between individuals still represent a challenge in terms of physiological data normalizacion. This factor has a direct impact on the design of generic algorithms capable of processing physiological parameters across different individuals simultaneously. Each person is unique, and this is reflected in the physiological reactions of each person to the same kind of events, both in the manner and in the intensity of the reaction. This thesis addressed this challenge in an original and effective, but not perfect way, as some signals may diverge slightly from others due to their morphology during the normalization stage. This phenomenon can lead to the appearance of false positives and false negatives during the stress and relaxation level estimation. Labeling of physiological registers constituted another major challenge, requiring each signal to be studied individually, both to carry out the partial labeling manually and to subsequently achieve the continuous labeling through pseudo-labeling techniques. Although the proposed pseudo-labeling method has proven to be effective, outlier data can potentially affect the value of the new obtained labels, altering the ranges and leading to differences between individuals.

Further research is proposed on the development of new methodologies for the normalization and labeling of physiological signals. This study represents a strong and validated

starting point for the construction of more advanced methodologies that will provide even more robust results in the processing of physiological patterns. The development of a more sophisticated hardware implementation is also proposed for further consideration. Since this thesis presents a functional prototype that carries out both the acquisition and the processing stages under strict and validated operating conditions, the creation of a commercial device would take this development to the next stage. This would provide an opportunity to design a wearable sensor solution in conjunction with a more embedded and miniaturized hardware. Furthermore, the implementation of the algorithms in production-oriented languages should improve the efficiency and reliability of the system, such as C++ for the acquisition stage and JavaScript for the server execution. Finally, the validation of the foot point detection algorithm in plethysmographic signals is proposed, which has already been validated in oscillometric blood pressure signals, whose morphology is very similar to plethysmographic ones.

Bibliography

[1] Jesus Minguillon et al. “Portable System for Real-Time Detection of Stress Level”. In: *Sensors* 18.8 (Aug. 2018), p. 2504. DOI: 10.3390/s18082504.

[2] E. Monton et al. “Body area network for wireless patient monitoring”. In: *IET Communications* 2.2 (Feb. 2008), pp. 215–222. ISSN: 1751-8628. DOI: 10.1049/iet-com:20070046.

[3] Martin Gjoreski et al. “Monitoring stress with a wrist device using context”. In: *Journal of Biomedical Informatics* 73 (Sept. 2017), pp. 159–170. DOI: 10.1016/j.jbi.2017.08.006.

[4] Chrystinne Oliveira Fernandes et al. “Enabling a Smart and Distributed Communication Infrastructure in Healthcare”. In: *Innovation in Medicine and Healthcare 2015*. Springer, 2016, pp. 435–446.

[5] Hans Selye. *Stress in health and disease*. Butterworth-Heinemann, 2013.

[6] Carmen Blanco et al. “The use of relaxation techniques in a psychology clinic practice”. In: *Anales de Psicología* 30.2 (May 2014). DOI: 10.6018/analesps.30.2.158451.

[7] Alireza Golgouneh and Bahram Tarvirdizadeh. “Fabrication of a portable device for stress monitoring using wearable sensors and soft computing algorithms”. In: *Neural Computing and Applications* (June 2019). ISSN: 1433-3058. DOI: 10.1007/s00521-019-04278-7.

[8] Raquel Martinez et al. “A Self-Paced Relaxation Response Detection System Based on Galvanic Skin Response Analysis”. In: *IEEE Access* 7 (2019), pp. 43730–43741. DOI: 10.1109/access.2019.2908445.

[9] J.J.G.a de Vries, S.C.a Pauws, and M.b Biehl. “Insightful stress detection from physiology modalities using Learning Vector Quantization”. English. In: *Neurocomputing* 151.P2 (2015), pp. 873–882. ISSN: 09252312. DOI: 10.1016/j.neucom.2014.10.008.

[10] F. Mokhayeri, M. Akbarzadeh-T, and S. Toosizadeh. “Mental stress detection using physiological signals based on soft computing techniques”. In: *2011 18th Iranian Conference of Biomedical Engineering (ICBME)*. Dec. 2011, pp. 232–237. DOI: 10.1109/ICBME.2011.6168563.

[11] G. Fink. *Stress: Concepts, Cognition, Emotion, and Behavior: Handbook of Stress*. English. cited By 0. Elsevier, 2016, pp. 1–487. ISBN: 9780128009512.

[12] *Safer and Healthier Work for All - Modernisation of the EU Occupational Safety and Health Legislation and Policy*. Jan. 2017.

[13] Frank P. Grad. “The Preamble of the Constitution of the World Health Organization”. In: *Bulletin of the World Health Organization* 80.12 (2002), pp. 981–984.

[14] C. R. Snyder and Shane J. Lopez. *Handbook of Positive Psychology*. Oxford University Press, Dec. 2001. ISBN: 0195135334.

[15] Martin E. P. Seligman and Mihaly Csikszentmihalyi. “Positive Psychology: An Introduction”. In: *Flow and the Foundations of Positive Psychology: The Collected Works of Mihaly Csikszentmihalyi*. Dordrecht: Springer Netherlands, 2014, pp. 279–298. ISBN: 978-94-017-9088-8. DOI: 10.1007/978-94-017-9088-8_18.

[16] Martin E. P. Seligman. *Flourish: A Visionary New Understanding of Happiness and Well-being*. Atria Books, 2011.

[17] Pagnini Francesco et al. “The efficacy of relaxation training in treating anxiety.” In: *International Journal of Behavioral Consultation and Therapy* 5.3-4 (2010), pp. 264–269. DOI: 10.1037/h0100887.

[18] Sean E. Stevens et al. “Are Complex Psychotherapies More Effective than Biofeedback, Progressive Muscle Relaxation, or Both? A Meta-Analysis”. In: *Psychological Reports* 100.1 (Feb. 2007), pp. 303–324. DOI: 10.2466/pr0.100.1.303-324.

[19] John T Cacioppo, Louis G Tassinary, and Gary Berntson. *Handbook of psychophysiology*. Cambridge University Press, 2007.

[20] S.D. Kreibig. “Autonomic nervous system activity in emotion: A review”. In: *Biological Psychology* 84.3 (2010), pp. 394–421. DOI: 10.1016/j.biopsycho.2010.03.010.

[21] H. Selye. “The general adaptation syndrome and the diseases of adaptation”. English. In: *The Journal of clinical endocrinology and metabolism* 6 (1946), pp. 117–230. ISSN: 0021972X.

[22] G. Fink. “Stress: Definition and History”. In: *Encyclopedia of Neuroscience*. Elsevier, 2009, pp. 549–555. DOI: 10.1016/b978-008045046-9.00076-0.

[23] Walter B. Cannon. *The Wisdom Of The Body*. W. W. Norton and Company, Inc., 1963. ISBN: 0393002055.

[24] Walter B. Cannon. *Bodily changes in pain, hunger, fear and rage: An account of recent researches into the function of emotional excitement*. D Appleton & Company, 1915. DOI: 10.1037/10013-000.

[25] Herbert Benson and Miriam Z. Klipper. *The Relaxation Response*. HarperCollins e-books, 2009.

[26] Walter B. Cannon. “Organization for physiological homeostasis”. In: *Physiological Reviews* 9.3 (July 1929), pp. 399–431. DOI: 10.1152/physrev.1929.9.3.399.

[27] Michael Lewis, Jeannette M Haviland-Jones, and Lisa Feldman Barrett. *Handbook of emotions*. Guilford Press, 2008.

[28] Raquel Martínez Rodríguez. “Diseño de un sistema de detección y clasificación de cambios emocionales basado en el análisis de señales fisiológicas no intrusivas”. PhD thesis. University of the Basque Country (UPV/EHU), 2016.

[29] Alberto de Santos Sierra et al. “A Stress-Detection System Based on Physiological Signals and Fuzzy Logic”. In: *IEEE Transactions on Industrial Electronics* 58.10 (Oct. 2011), pp. 4857–4865. DOI: 10.1109/tie.2010.2103538.

[30] Rosalind W. Picard. *Affective computing*. Vol. 252. MIT press Cambridge, 1997. ISBN: 0262661152.

[31] C.S. Pattichis et al. “Wireless telemedicine systems: an overview”. In: *IEEE Antennas and Propagation Magazine* 44.2 (Apr. 2002), pp. 143–153. DOI: 10.1109/map.2002.1003651.

[32] Mario Salai, István Vassányi, and István Kósa. “Stress Detection Using Low Cost Heart Rate Sensors”. In: *Journal of Healthcare Engineering* 2016 (2016), pp. 1–13. DOI: 10.1155/2016/5136705.

[33] Jonathan Lazar, Jinjuan Heidi Feng, and Harry Hochheiser. “Measuring the human”. In: *Research Methods in Human Computer Interaction*. Elsevier, 2017, pp. 369–409. DOI: 10.1016/b978-0-12-805390-4.00013-3.

[34] D. Arney et al. “Biomedical devices and systems security”. In: *2011 Annual International Conference of the IEEE Engineering in Medicine and Biology Society*. IEEE, Aug. 2011. DOI: 10.1109/iembs.2011.6090663.

[35] Unai Zalabarria, Eloy Irigoyen, and Andrew Lowe. “Diagnosis of atrial fibrillation based on arterial pulse wave foot point detection using artificial neural networks”. In: *Computer Methods and Programs in Biomedicine* 197 (Dec. 2020), p. 105681. DOI: 10.1016/j.cmpb.2020.105681.

[36] Unai Zalabarria et al. “A Low-Cost, Portable Solution for Stress and Relaxation Estimation Based on a Real-Time Fuzzy Algorithm”. In: *IEEE Access* 8 (2020), pp. 74118–74128. DOI: 10.1109/access.2020.2988348.

[37] Unai Zalabarria et al. “Online robust R-peaks detection in noisy electrocardiograms using a novel iterative smart processing algorithm”. In: *Applied Mathematics and Computation* 369 (Mar. 2020), p. 124839. DOI: 10.1016/j.amc.2019.124839.

[38] A. Salazar-Ramirez et al. “An enhanced fuzzy algorithm based on advanced signal processing for identification of stress”. In: *Neurocomputing* 271 (2018), pp. 48–57. ISSN: 0925-2312. DOI: 10.1016/j.neucom.2016.08.153.

[39] Unai Zalabarria et al. “Acquisition and Fuzzy Processing of Physiological Signals to Obtain Human Stress Level Using Low Cost Portable Hardware”. In: *International Joint Conference SOCO’17-CISIS’17-ICEUTE’17 León, Spain, September 6–8, 2017, Proceeding*. Springer International Publishing, Aug. 2017, pp. 68–78. DOI: 10.1007/978-3-319-67180-2_7.

[40] Unai Zalabarria et al. “Detection of Stress Level and Phases by Advanced Physiological Signal Processing Based on Fuzzy Logic”. In: *International Joint Conference SOCO’16-CISIS’16-ICEUTE’16*. Springer International Publishing, Oct. 2016, pp. 301–312. DOI: 10.1007/978-3-319-47364-2_29.

[41] Unai Zalabarria et al. “Adquisición y procesamiento difuso de señales fisiológicas para la obtención del nivel de estrés utilizando hardware portable de bajo coste”. In: *XIII Simposio CEA de Control Inteligente*. 2017, pp. 52–57.

[42] Unai Zalabarria et al. “Detección del nivel y fases de estrés mediante procesamiento avanzado de señales fisiológicas basado en lógica difusa”. In: *XII Simposio CEA de Control Inteligente*. 2016, pp. 31–36.

[43] Unai Zalabarria et al. “Procesamiento robusto para el análisis avanzado de señales electrocardiográficas afectadas por perturbaciones”. In: *Actas de las XXXVI Jornadas de Automática*. 2015, pp. 807–814.

[44] Norman S. Greenfield. *Handbook of Psychophysiology*. Holt, Rinehart and Winston, 1972. ISBN: 0030866561.

[45] R. M. Rose. “Introduction and overview of our model”. In: *Paper presented at the National Center for Complementary and Alternative Medicine meeting on Integrating Mechanisms Linking Mind, Brain, and Periphery: Applications in Asthma and Atherosclerosis* (July 2005).

[46] Dorland. *Dorland’s Illustrated Medical Dictionary*. Saunders, 2011. ISBN: 1416062572.

[47] W. Jänig. “Autonomic Nervous System”. In: *Human Physiology*. Springer Berlin Heidelberg, 1989, pp. 333–370. DOI: 10.1007/978-3-642-73831-9_16.

[48] Uwe Ernsberger and Hermann Rohrer. “Sympathetic tales: subdivisons of the autonomic nervous system and the impact of developmental studies”. In: *Neural Development* 13.1 (Sept. 2018). DOI: 10.1186/s13064-018-0117-6.

[49] L.K.a b McCorry. “Physiology of the autonomic nervous system”. English. In: *American Journal of Pharmaceutical Education* 71.4 (2007). ISSN: 00029459.

[50] Ian Gibbins. “Functional organization of autonomic neural pathways”. In: *Organogenesis* 9.3 (July 2013), pp. 169–175. DOI: 10.4161/org.25126.

[51] Stephen Palmer and Windy Dryden. *Counselling for Stress Problems*. SAGE Publications Ltd, 1995. DOI: 10.4135/9781446222263.

[52] Blasina De Camargo. “Stress, General Adaptation Syndrome or General Alarm Reaction”. In: *Revista Médico Científica* 17.2 (2010), pp. 78–86.

[53] H. Selye. “Stress and disease”. English. In: *Science* 122.3171 (1955), pp. 625–631. ISSN: 00368075.

[54] Hans Selye. *The stress of life*. 1956.

[55] P.G. Nixon. “The human function curve - a paradigm for our times”. In: 1982.

[56] Francesco Pagnini et al. “A brief literature review about relaxation therapy and anxiety”. In: *Body, Movement and Dance in Psychotherapy* 8.2 (May 2013), pp. 71–81. DOI: 10.1080/17432979.2012.750248.

[57] Edmund Jacobson. *Progressive Relaxation*. University of Chicago Press, 1938. ISBN: 0226390586.

[58] D. C. Fowles. “Psychophysiology: Systems, Processes and Applications”. In: ed. by Michael G.H. Coles, Emanuel Donchin, and Stephen W. Porges. The Guilford Press, 1986. Chap. The eccrine system and electrodermal activity, pp. 51–96. ISBN: 0898626404.

[59] A. N. Ishchenko and P. P. Shev’ev. “Automated complex for multiparameter analysis of the galvanic skin response signal”. In: *Biomedical Engineering* 23.3 (May 1989), pp. 113–117. DOI: 10.1007/bf00562429.

[60] Robert. Edelberg. “Electrical Activity of the Skin: Its Measurement and Uses in Psychophysiology”. In: 1972.

[61] Yawen Hu et al. “Neural control of sweat secretion: A review”. In: *The British journal of dermatology* 178 (July 2017). DOI: 10.1111/bjd.15808.

[62] Chester W. Darrow. “Neural mechanisms controlling the palmar galvanic skin reflex and palmar sweating”. In: *Archives of Neurology & Psychiatry* 37.3 (Mar. 1937), p. 641. DOI: 10.1001/archneurpsyc.1937.02260150171011.

[63] J. Tarchanoff. “Galvanic phenomena in the human skin during stimulation of the sensory organs and during various forms of mental activity”. In: *Pflugers Archive fur die Gesamte Physiologie des Menschen und der Tiere* 46 (1890), pp. 46–55.

[64] Wolfram Boucsein. *Electrodermal Activity*. Springer, 2012. ISBN: 9781461411260.

[65] David T. Lykken and Peter H. Venables. “DIRECT MEASUREMENT OF SKIN CONDUCTANCE: A PROPOSAL FOR STANDARDIZATION”. In: *Psychophysiology* 8.5 (Sept. 1971), pp. 656–672. DOI: 10.1111/j.1469-8986.1971.tb00501.x.

[66] J. P. D. Serrano et al. “Portable Stress Level Detector based on Galvanic Skin Response, Heart Rate, and Body Temperature”. In: *2018 IEEE 10th International Conference on Humanoid, Nanotechnology, Information Technology,Communication and Control, Environment and Management (HNICEM)*. Nov. 2018, pp. 1–5. DOI: 10.1109/HNICEM.2018.8666352.

[67] P. H. Venables and M. J. Christie. “Techniques in Psychophysiology”. In: ed. by I. Martin and P.H. Venables. Chichester UK: Wiley, 1980. Chap. Electrodermal activity, pp. 3–67.

[68] D. T. Lykken et al. “Correcting psychophysiological measures for individual differences in range.” In: *Psychological Bulletin* 66.6 (1966), pp. 481–484. DOI: 10.1037/h0023922.

[69] Branislava Medić. “The role of autonomic control in cardiovascular system: Summary of basic principles”. In: *Medicinski podmladak* 67.1 (2016), pp. 14–18. DOI: 10.5937/medpodm1601014m.

[70] F. Bohm and J. Pernow. “The importance of endothelin-1 for vascular dysfunction in cardiovascular disease”. In: *Cardiovascular Research* 76.1 (Oct. 2007), pp. 8–18. DOI: 10.1016/j.cardiores.2007.06.004.

[71] Bernard J. Gersh. *Mayo Clinic Heart Book, Revised Edition: The Ultimate Guide to Heart Health*. William Morrow, 2000. ISBN: 9780688176426.

[72] Jill Jin. “Screening for Cardiovascular Disease Risk With ECG”. In: *JAMA* 319.22 (June 2018), pp. 2346–2346. ISSN: 0098-7484. DOI: 10.1001/jama.2018.7311. eprint: https://jamanetwork.com/journals/jama/articlepdf/2684609/jama_jin_2018_pg_180018.pdf.

[73] A. Lowe, T. H. Oh, and R. Stewart. “Screening for Atrial Fibrillation During Automatic Blood Pressure Measurements”. In: *IEEE Journal of Translational Engineering in Health and Medicine* 6 (2018), pp. 1–7. ISSN: 2168-2372. DOI: 10.1109/JTEHM.2018.2869609.

[74] S. M. Zakharov. “Estimation of arterial pressure from pletismography data”. In: *Issues of radio electronics* 10 (Oct. 2019), pp. 70–76. DOI: 10.21778/2218-5453-2019-10-70-76.

[75] Francisco G. Cosío et al. “The Electrocardiogram”. In: *The ESC Textbook of Cardiovascular Medicine*. Oxford University Press, Jan. 2009, pp. 29–82. DOI: 10.1093/med/9780199566990.003.002.

[76] John Hampton. *The ECG made easy*. Edinburgh New York: Churchill Livingstone/Elsevier, 2013. ISBN: 978-0-7020-4641-4.

[77] Malcolm S. Thaler. *The Only Ekg Book You'll Ever Need (4th Edition)*. LWW, 2002. ISBN: 0781741769.

[78] Richard E. Klabunde. *Cardiovascular Physiology Concepts*. LWW, 2011. ISBN: 9781451113846.

[79] B. U. Kohler, C. Hennig, and R. Orglmeister. “The principles of software QRS detection”. In: *IEEE Engineering in Medicine and Biology Magazine* 21.1 (Jan. 2002), pp. 42–57. ISSN: 0739-5175. DOI: 10.1109/51.993193.

[80] R. Silipo and C. Marchesi. “Artificial neural networks for automatic ECG analysis”. In: *IEEE Transactions on Signal Processing* 46.5 (May 1998), pp. 1417–1425. ISSN: 1053-587X. DOI: 10.1109/78.668803.

[81] S.S. Mehta and N.S. Lingayat. “SVM-based algorithm for recognition of QRS complexes in electrocardiogram”. In: *IRBM* 29.5 (Nov. 2008), pp. 310–317. DOI: 10.1016/j.rbmret.2008.03.006.

[82] P. Valluraiah and B. Biswal. “ECG signal analysis using Hilbert transform”. In: *2015 IEEE Power, Communication and Information Technology Conference (PCITC)*. Oct. 2015, pp. 465–469. DOI: 10.1109/PCITC.2015.7438211.

[83] R. Poli, S. Cagnoni, and G. Valli. “Genetic design of optimum linear and nonlinear QRS detectors”. In: *IEEE Transactions on Biomedical Engineering* 42.11 (Nov. 1995), pp. 1137–1141. ISSN: 0018-9294. DOI: 10.1109/10.469381.

[84] J. Pan and W. J. Tompkins. “A Real-Time QRS Detection Algorithm”. In: *IEEE Transactions on Biomedical Engineering* BME-32.3 (Mar. 1985), pp. 230–236. ISSN: 0018-9294. DOI: 10.1109/TBME.1985.325532.

[85] P. S. Hamilton and W. J. Tompkins. “Quantitative Investigation of QRS Detection Rules Using the MIT/BIH Arrhythmia Database”. In: *IEEE Transactions on Biomedical Engineering* BME-33.12 (Dec. 1986), pp. 1157–1165. ISSN: 0018-9294. DOI: 10.1109/TBME.1986.325695.

[86] Mourad Adnane, Zhongwei Jiang, and Samjin Choi. “Development of QRS detection algorithm designed for wearable cardiorespiratory system”. In: *Computer Methods and Programs in Biomedicine* 93.1 (Jan. 2009), pp. 20–31. DOI: 10.1016/j.cmpb.2008.07.010.

[87] R. K. Bal and A. Kumar. “Improved QRS detector using hybrid MAMEMI filter”. In: *2016 IEEE International Conference on Recent Trends in Electronics, Information Communication Technology (RTEICT)*. May 2016, pp. 1351–1355. DOI: 10.1109/RTEICT.2016.7808051.

[88] V. X. Afonso et al. “ECG beat detection using filter banks”. In: *IEEE Transactions on Biomedical Engineering* 46.2 (Feb. 1999), pp. 192–202. ISSN: 0018-9294. DOI: 10.1109/10.740882.

[89] S.S. Mehta et al. “K-means algorithm for the detection and delineation of QRS-complexes in Electrocardiogram”. In: *IRBM* 31.1 (Feb. 2010), pp. 48–54. DOI: 10.1016/j.irbm.2009.10.001.

[90] S. C. Saxena, V. Kumar, and S. T. Hamde. “Feature extraction from ECG signals using wavelet transforms for disease diagnostics”. In: *International Journal of Systems Science* 33.13 (Jan. 2002), pp. 1073–1085. DOI: 10.1080/00207720210167159.

[91] J. P. Martinez et al. “A wavelet-based ECG delineator: evaluation on standard databases”. In: *IEEE Transactions on Biomedical Engineering* 51.4 (Apr. 2004), pp. 570–581. ISSN: 0018-9294. DOI: 10.1109/TBME.2003.821031.

[92] A. Ghaffari et al. “A robust wavelet-based multi-lead electrocardiogram delineation algorithm”. In: *Medical Engineering & Physics* 31.10 (Dec. 2009), pp. 1219–1227. DOI: 10.1016/j.medengphy.2009.07.017.

[93] S.A. Chouakri, F. Bereksi-Reguig, and A. Taleb-Ahmed. “QRS complex detection based on multi wavelet packet decomposition”. In: *Applied Mathematics and Computation* 217.23 (Aug. 2011), pp. 9508–9525. DOI: 10.1016/j.amc.2011.03.001.

[94] P Sasikala and RSD Wahidabanu. “Robust R Peak and QRS detection in Electrocardiogram using Wavelet Transform”. In: *International Journal of Advanced Computer Science and Applications-IJACSA* 1.6 (2010), pp. 48–53.

[95] M. Bahoura, M. Hassani, and M. Hubin. “DSP implementation of wavelet transform for real time ECG wave forms detection and heart rate analysis”. In: *Computer Methods and Programs in Biomedicine* 52.1 (Jan. 1997), pp. 35–44. DOI: 10.1016/s0169-2607(97)01780-x.

[96] Cuiwei Li, Chongxun Zheng, and Changfeng Tai. “Detection of ECG characteristic points using wavelet transforms”. In: *IEEE Transactions on Biomedical Engineering* 42.1 (Jan. 1995), pp. 21–28. ISSN: 0018-9294. DOI: 10.1109/10.362922.

[97] Yun-Chi Yeh and Wen-June Wang. “QRS complexes detection for ECG signal: The Difference Operation Method”. In: *Computer Methods and Programs in Biomedicine* 91.3 (Sept. 2008), pp. 245–254. DOI: 10.1016/j.cmpb.2008.04.006.

[98] L. She et al. “An Adaptive Threshold Algorithm Combining Shifting Window Difference and Forward-Backward Difference in Real-Time R-Wave Detection”. In: *2009 2nd International Congress on Image and Signal Processing*. Oct. 2009, pp. 1–4. DOI: 10.1109/CISP.2009.5304666.

[99] Ivaylo I Christov. “Real time electrocardiogram QRS detection using combined adaptive threshold”. In: *BioMedical Engineering OnLine* 3.1 (2004), p. 28. DOI: 10.1186/1475-925x-3-28.

[100] Szi-Wen Chen, Hsiao-Chen Chen, and Hsiao-Lung Chan. “A real-time QRS detection method based on moving-averaging incorporating with wavelet denoising”. In: *Computer Methods and Programs in Biomedicine* 82.3 (June 2006), pp. 187–195. DOI: 10.1016/j.cmpb.2005.11.012.

[101] William Marston. “Superficial surgery and perforator interruption in the treatment of venous leg ulcers”. In: *Venous Ulcers*. Elsevier, 2007, pp. 149–172. DOI: 10.1016/b978-012373565-2.50016-6.

[102] G.E. Burch. “Digital Plethysmography: Introducing a Method for Recording Simultaneously the Time Course of the Rate of Blood Flow into and out of the Finger Tip”. In: *Journal of the American Medical Association* 156.7 (Oct. 1954), p. 749. DOI: 10.1001/jama.1954.02950070077027.

[103] Mathilde C. Hemon and Justin P. Phillips. “Comparison of foot finding methods for deriving instantaneous pulse rates from photoplethysmographic signals”. In: *Journal of Clinical Monitoring and Computing* 30.2 (Apr. 2015), pp. 157–168. DOI: 10.1007/s10877-015-9695-6.

[104] Egidijus Kazanavicius et al. “Mathematical methods for determining the foot point of the arterial pulse wave and evaluation of proposed methods”. In: *Information Technology and Control* 34.1 (2005), pp. 29–36.

[105] Gary G. Berntson, John T. Cacioppo, and Karen S. Quigley. “The metrics of cardiac chronotropism: Biometric perspectives”. In: *Psychophysiology* 32.2 (Mar. 1995), pp. 162–171. DOI: 10.1111/j.1469-8986.1995.tb03308.x.

[106] Julian F. Thayer and Richard D. Lane. “Claude Bernard and the heart–brain connection: Further elaboration of a model of neurovisceral integration”. In: *Neuroscience & Biobehavioral Reviews* 33.2 (Feb. 2009), pp. 81–88. DOI: 10.1016/j.neubiorev.2008.08.004.

[107] Mirja A. Peltola. “Role of editing of R–R intervals in the analysis of heart rate variability”. In: *Frontiers in Physiology* 3 (2012). DOI: 10.3389/fphys.2012.00148.

[108] U. Rajendra Acharya et al. “Heart rate variability: a review”. In: *Medical & Biological Engineering & Computing* 44.12 (Nov. 2006), pp. 1031–1051. DOI: 10.1007/s11517-006-0119-0.

[109] M. Malik et al. “Heart rate variability. standards of measurement, physiological interpretation, and clinical use”. English. In: *European Heart Journal* 17.3 (1996), pp. 354–381. ISSN: 0195668X.

[110] Elaine Nicpon Marieb and Katja Hoehn. *Human anatomy & physiology*. Pearson education, 2007.

[111] “Your lungs and exercise”. In: *Breathe* 12.1 (Mar. 2016), pp. 97–100. DOI: 10.1183/20734735.elf121.

[112] John G. Widdicombe. “The Autonomic Nervous System and Breathing”. In: *Archives of Internal Medicine* 126.2 (Aug. 1970), p. 311. DOI: 10.1001/archinte.1970.00310080117020.

[113] Gary G. Berntson, John T. Cacioppo, and Karen S. Quigley. “Respiratory sinus arrhythmia: Autonomic origins, physiological mechanisms, and psychophysiological implications”. In: *Psychophysiology* 30.2 (Mar. 1993), pp. 183–196. DOI: 10.1111/j.1469-8986.1993.tb01731.x.

[114] J. N. Han et al. “Influence of awareness of the recording of breathing on respiratory pattern in healthy humans”. In: *European Respiratory Journal* 10.1 (Jan. 1997), pp. 161–166. DOI: 10.1183/09031936.97.10010161.

[115] Paolo Bifulco et al. “Monitoring of respiration, seismocardiogram and heart sounds by a PVDF piezo film sensor”. In: 2014.

[116] Robert Reris and J. Paul Brooks. “Principal Component Analysis and Optimization: A Tutorial”. In: *Operations Research and Computing: Algorithms and Software for Analytics*. INFORMS, Jan. 2015, pp. 212–225. DOI: 10.1287/ics.2015.0016.

[117] Rakesh Pimplikar et al. “Learning to Propagate Rare Labels”. In: *Proceedings of the 23rd ACM International Conference on Conference on Information and Knowledge Management - CIKM '14*. ACM Press, 2014. DOI: 10.1145/2661829.2661982.

[118] Usha Nandini Raghavan, Réka Albert, and Soundar Kumara. “Near linear time algorithm to detect community structures in large-scale networks”. In: *Physical Review E* 76.3 (Sept. 2007). DOI: 10.1103/physreve.76.036106.

[119] Xiaojin Zhu and Zoubin Ghahramani. “Learning from Labeled and Unlabeled Data with Label Propagation”. In: (July 2003).

[120] Dengyong Zhou et al. “Learning with Local and Global Consistency”. In: *Advances in Neural Information Processing Systems 16* 16 (Mar. 2004).

[121] L.A. Zadeh. “Fuzzy sets”. In: *Information and Control* 8.3 (June 1965), pp. 338–353. DOI: 10.1016/s0019-9958(65)90241-x.

[122] E.H. Mamdani and S. Assilian. “An experiment in linguistic synthesis with a fuzzy logic controller”. In: *International Journal of Man-Machine Studies* 7.1 (Jan. 1975), pp. 1–13. DOI: 10.1016/s0020-7373(75)80002-2.

[123] Michio Sugeno. *Industrial Applications of Fuzzy Control*. USA: Elsevier Science Inc., 1985. ISBN: 0444878297.

[124] Àngela Nebot and Francisco Mugica. “Small-Particle Pollution Modeling Using Fuzzy Approaches”. In: *Advances in Intelligent Systems and Computing*. Springer International Publishing, 2014, pp. 239–252. DOI: 10.1007/978-3-319-03581-9_17. URL: https://doi.org/10.1007/978-3-319-03581-9_17.

[125] Fausto Cavallaro. “A Takagi-Sugeno Fuzzy Inference System for Developing a Sustainability Index of Biomass”. In: *Sustainability* 7.9 (Sept. 2015), pp. 12359–12371. DOI: 10.3390/su70912359.

[126] Lala Septem Riza et al. “frbs: Fuzzy Rule-Based Systems for Classification and Regression in R”. In: *Journal of Statistical Software* 65.6 (2015). DOI: 10.18637/jss.v065.i06.

[127] L. -X. Wang and J. M. Mendel. “Generating fuzzy rules by learning from examples”. In: *IEEE Transactions on Systems, Man, and Cybernetics* 22.6 (Nov. 1992), pp. 1414–1427. ISSN: 2168-2909. DOI: 10.1109/21.199466.

[128] N. K. Kasabov and Qun Song. “DENFIS: dynamic evolving neural-fuzzy inference system and its application for time-series prediction”. In: *IEEE Transactions on Fuzzy Systems* 10.2 (Apr. 2002), pp. 144–154. ISSN: 1063-6706. DOI: 10.1109/91.995117.

[129] J. Kim and N. Kasabov. "HyFIS: adaptive neuro-fuzzy inference systems and their application to nonlinear dynamical systems". In: *Neural Networks* 12.9 (Nov. 1999), pp. 1301–1319. DOI: 10.1016/s0893-6080(99)00067-2.

[130] Hisao Ishibuchi et al. "Empirical study on learning in fuzzy systems by rice taste analysis". In: *Fuzzy Sets and Systems* 64.2 (June 1994), pp. 129–144. DOI: 10.1016/0165-0114(94)90329-8.

[131] T. Takagi and M. Sugeno. "Fuzzy identification of systems and its applications to modeling and control". In: *IEEE Transactions on Systems, Man, and Cybernetics* SMC-15.1 (Jan. 1985), pp. 116–132. ISSN: 2168-2909. DOI: 10.1109/TSMC.1985.6313399.

[132] Warren S. McCulloch and Walter Pitts. "A logical calculus of the ideas immanent in nervous activity". In: *The Bulletin of Mathematical Biophysics* 5.4 (Dec. 1943), pp. 115–133. DOI: 10.1007/bf02478259.

[133] P.J. Werbos. *Beyond Regression: New Tools for Prediction and Analysis in the Behavioral Sciences*. Harvard University, 1975.

[134] J.J. Gross and R.W. Levenson. "Emotion Elicitation using Films". English. In: *Cognition and Emotion* 9.1 (1995), pp. 87–108. ISSN: 02699931. DOI: 10.1080/02699939508408966.

[135] Estate M. Sokhadze. "Effects of Music on the Recovery of Autonomic and Electrocortical Activity After Stress Induced by Aversive Visual Stimuli". In: *Applied Psychophysiology and Biofeedback* 32.1 (Feb. 2007), pp. 31–50. DOI: 10.1007/s10484-007-9033-y.

[136] P. J. Lang. "Behavioral treatment and bio-behavioral assessment: Computer applications". In: *Technology in mental health care delivery systems*. Ed. by J. B. Sidowski, J. H. Johnson, and T. A. Williams. Norwood, NJ: Ablex, 1980, pp. 119–137.

[137] "The Nuremberg Code (1947)". In: *BMJ* 313.7070 (Dec. 1996), pp. 1448–1448. DOI: 10.1136/bmj.313.7070.1448.

[138] "World Medical Association Declaration of Helsinki". In: *JAMA* 310.20 (Nov. 2013), p. 2191. DOI: 10.1001/jama.2013.281053.

[139] *Ley Orgánica 15/1999, de 13 de diciembre, de Protección de Datos de Carácter Personal*. Dec. 1999.

[140] Aitzol Ezeiza et al. "Ethical issues on the design of assistive technology for people with mental disabilities". In: *International Conference on Ethics and Human Values in Engineering* (Mar. 2008), pp. 75–84.

[141] George B Moody and Roger G Mark. *MIT-BIH Arrhythmia Database*. 1992. DOI: 10.13026/C2F305.

[142] Mark Lutz. *Programming Python*. USA: O'Reilly & Associates, Inc., 1996. ISBN: 1565921976.

[143] David Meyer and Kurt Hornik. "Generalized and Customizable Sets in R". In: *Journal of Statistical Software* 31.2 (2009). DOI: 10.18637/jss.v031.i02.

[144] David Meyer et al. "Misc Functions of the Department of Statistics, ProbabilityTheory Group (Formerly: E1071), TU Wien". In: 2015.

[145] M. U. H. A. Rasyid, F. A. Saputra, and A. Christian. "Implementation of blood glucose levels monitoring system based on Wireless Body Area Network". In: *Proc.*

IEEE Int. Conf. Consumer Electronics-Taiwan (ICCE-TW). May 2016, pp. 1–2. DOI: 10.1109/ICCE-TW.2016.7521005.

[146] Y Ungson, MA Reyna, and ME Bravo-Zanoguera. "Development of an ambulatory ECG system based on Arduino and mobile telephony for wireless transmission". In: *Health Care Exchanges (PAHCE), 2014 Pan American*. IEEE. 2014, pp. 1–5.

[147] E. Jovanov et al. "Stress monitoring using a distributed wireless intelligent sensor system". In: *IEEE Engineering in Medicine and Biology Magazine* 22.3 (May 2003), pp. 49–55. ISSN: 0739-5175. DOI: 10.1109/MEMB.2003.1213626.

[148] Fahim Slauddin and Tarif Riyad Rahman. "A Fuzzy based low-cost monitoring module built with raspberry pi-python-java architecture". In: *International Conference on Smart Sensors and Application (ICSSA)*. 2015.

[149] L. J. V. Escobar and S. A. Salinas. "e-Health prototype system for cardiac telemonitoring". In: *Proc. 38th Annual Int. Conf. of the IEEE Engineering in Medicine and Biology Society (EMBC)*. Aug. 2016, pp. 4399–4402. DOI: 10.1109/EMBC.2016.7591702.

[150] Tim Cox. *Raspberry Pi Cookbook for Python Programmers*. Packt Publishing Ltd, 2014.

[151] A. L. Goldberger et al. "PhysioBank, PhysioToolkit, and PhysioNet: Components of a New Research Resource for Complex Physiologic Signals". In: *Circulation* 101.23 (June 2000). Circulation Electronic Pages: http://circ.ahajournals.org/content/101/23/e215.full PMID:1085218; doi: 10.1161/01.CIR.101.23.e215, e215–e220.

[152] Yangdong Liao, Ru-Xin Na, and D. Rayside. "Accurate ECG R-peak detection for telemedicine". In: *2014 IEEE Canada International Humanitarian Technology Conference - (IHTC)*. June 2014, pp. 1–5. DOI: 10.1109/IHTC.2014.7147524.

[153] G. Han, B. Lin, and Z. Xu. "Electrocardiogram signal denoising based on empirical mode decomposition technique: An overview". English. In: *Journal of Instrumentation* 12.3 (2017). ISSN: 17480221. DOI: 10.1088/1748-0221/12/03/P03010.

[154] M. Shahbakhti et al. "A New Strategy for ECG Baseline Wander Elimination Using Empirical Mode Decomposition". English. In: *Fluctuation and Noise Letters* 15.2 (2016). ISSN: 02194775. DOI: 10.1142/S0219477516500176.

[155] Ankit Jayant, Tripti Singh, and Manpreet Kaur. "Different Techniques to Remove Baseline Wander from ECG Signal". In: *International Journal of Emerging Research in Management &Technology* 2.6 (June 2013), pp. 16–19. ISSN: 2278-9359.

[156] V. R. Lele and K. S. Holkar. "Removal of Baseline Wander from ECG Signal". In: *Special Issue of International Journal of Electronics, Communication & Soft Computing Science & Engineering*. 2013, pp. 60–65.

[157] Ravindra Pratap Narwaria, Seema Verma, and P. K. Singhal. "Removal of Baseline Wander and Power Line Interference from ECG Signal - A Survey Approach". In: *International Journal of Electronics Engineering* 3 (2011), pp. 107–111.

[158] Francisco Perdigón Romero et al. "Baseline wander removal methods for ECG signals: A comparative study". In: *Electrical Engineering and Systems Science at Cornell University* (2018).

[159] Henry Blackburn. “Classification of the electrocardiogram for population studies: Minnesota code”. In: *Journal of Electrocardiology* 2.3 (1969), pp. 305–310. ISSN: 0022-0736. DOI: https://doi.org/10.1016/S0022-0736(69)80120-2.

[160] Mohammad Shenasa. *The ECG handbook of contemporary challenges*. Minneapolis: CardioText, 2015. ISBN: 978-1-935395-88-1.

[161] A. Aurobinda, B. P. Mohanty, and M. N. Mohanty. “R-peak detection of ECG using adaptive thresholding”. In: *2016 International Conference on Communication and Signal Processing (ICCSP)*. Apr. 2016, pp. 284–287. DOI: 10.1109/ICCSP.2016.7754140.

[162] Huaxiang Zhang and Jing Lu. “Semi-supervised fuzzy clustering: A kernel-based approach”. In: *Knowledge-Based Systems* 22.6 (2009), pp. 477–481. ISSN: 0950-7051. DOI: https://doi.org/10.1016/j.knosys.2009.06.009.

[163] John J. Murphy. *Technical Analysis of the Financial Markets: A Comprehensive Guide to Trading Methods and Applications*. New York Institute of Finance, 1999. ISBN: 0735200661.

[164] Saravanan K and Sasithra S. “Review on Classification Based on Artificial Neural Networks”. In: *The International Journal of Ambient Systems and Applications* 2.4 (Dec. 2014), pp. 11–18.

[165] Rosalind W Picard. “Affective computing: from laughter to IEEE”. In: *IEEE Transactions on Affective Computing* 1.1 (2010), pp. 11–17.

[166] J.A.a Healey and R.W.b Picard. “Detecting stress during real-world driving tasks using physiological sensors”. English. In: *IEEE Transactions on Intelligent Transportation Systems* 6.2 (2005), pp. 156–166. ISSN: 15249050. DOI: 10.1109/TITS.2005.848368.

[167] B. H. Friedman et al. “Validity concerns of common heart-rate variability indices”. In: *IEEE Engineering in Medicine and Biology Magazine* 21.4 (July 2002), pp. 35–40. ISSN: 0739-5175.

[168] D Singh, K Vinod, and SC Saxena. “Sampling frequency of the RR interval time series for spectral analysis of heart rate variability”. In: *Journal of Medical Engineering & Technology* 28.6 (Jan. 2004), pp. 263–272. DOI: 10.1080/03091900410001662350.

[169] Hui-Min Wang and Sheng-Chieh Huang. “SDNN/RMSSD as a Surrogate for LF/HF: A Revised Investigation”. In: *Modelling and Simulation in Engineering* 2012 (2012), pp. 1–8. DOI: 10.1155/2012/931943.

[170] B. J. TenVoorde, Th. J. C. Faes, and O. Rompelman. “Spectra of data sampled at frequency-modulated rates in application to cardiovascular signals: Part 2 evaluation of Fourier transform algorithms”. In: *Medical & Biological Engineering & Computing* 32.1 (Jan. 1994), pp. 71–76. ISSN: 1741-0444.

[171] Jinho Park, Sangwook Lee, and Moongu Jeon. “Atrial fibrillation detection by heart rate variability in Poincare plot”. In: *BioMedical Engineering OnLine* 8.1 (Dec. 2009), p. 38. ISSN: 1475-925X.

[172] R. Martínez et al. “First results in modelling stress situations by analysing physiological human signals”. In: *Proceedings of the IADIS International Conference e-Health*. Ed. by Mário Macedo. July 2012.

[173] Sylvain Laborde, Emma Mosley, and Julian F. Thayer. “Heart Rate Variability and Cardiac Vagal Tone in Psychophysiological Research - Recommendations for Experiment Planning, Data Analysis, and Data Reporting”. In: *Frontiers in Psychology* 08 (Feb. 2017). DOI: 10.3389/fpsyg.2017.00213.

[174] Paul Grossman and Edwin W. Taylor. “Toward understanding respiratory sinus arrhythmia: Relations to cardiac vagal tone, evolution and biobehavioral functions”. In: *Biological Psychology* 74.2 (2007). Special Issue of Biological Psychology on Cardiac Vagal Control, Emotion, Psychopathology, and Health., pp. 263–285. ISSN: 0301-0511. DOI: https://doi.org/10.1016/j.biopsycho.2005.11.014.

[175] Walter B Cannon. “Stresses and strains of homeostasis”. In: *The American Journal of the Medical Sciences* 189.1 (1935), pp. 13–14. ISSN: 0002-9629.

[176] Lu Han et al. “Detecting work-related stress with a wearable device”. In: *Computers in Industry* 90 (Sept. 2017), pp. 42–49. DOI: 10.1016/j.compind.2017.05.004.

[177] P. Hamilton. “Open source ECG analysis”. In: *Computers in Cardiology*. Sept. 2002, pp. 101–104. DOI: 10.1109/CIC.2002.1166717.

[178] C. Y. Chang et al. “Application of support vector regression for phyciological emotion recognition”. In: *2010 International Computer Symposium (ICS2010)*. Dec. 2010, pp. 12–17. DOI: 10.1109/COMPSYM.2010.5685532.

[179] M. S. Sharawi, M. Shibli, and M. I. Sharawi. “Design and implementation of a human stress detection system: A biomechanics approach”. In: *2008 5th International Symposium on Mechatronics and Its Applications*. May 2008, pp. 1–5. DOI: 10.1109/ISMA.2008.4648856.

[180] D. Kulic and E. Croft. “Anxiety detection during human-robot interaction”. In: *2005 IEEE/RSJ International Conference on Intelligent Robots and Systems*. Aug. 2005, pp. 616–621. DOI: 10.1109/IROS.2005.1545012.

[181] L. Guang-yuan and H. Min. “Emotion Recognition of Physiological Signals Based on Adaptive Hierarchical Genetic Algorithm”. In: *2009 WRI World Congress on Computer Science and Information Engineering*. Vol. 4. Mar. 2009, pp. 670–674. DOI: 10.1109/CSIE.2009.120.

[182] J. Wagner, Jonghwa Kim, and E. Andre. “From Physiological Signals to Emotions: Implementing and Comparing Selected Methods for Feature Extraction and Classification”. In: *2005 IEEE International Conference on Multimedia and Expo*. July 2005, pp. 940–943. DOI: 10.1109/ICME.2005.1521579.

[183] H. Cai and Y. Lin. “An Experiment to Non-Intrusively Collect Physiological Parameters towards Driver State Detection”. In: *SAE Technical Paper Series*. SAE International, Apr. 2007. DOI: 10.4271/2007-01-0403.